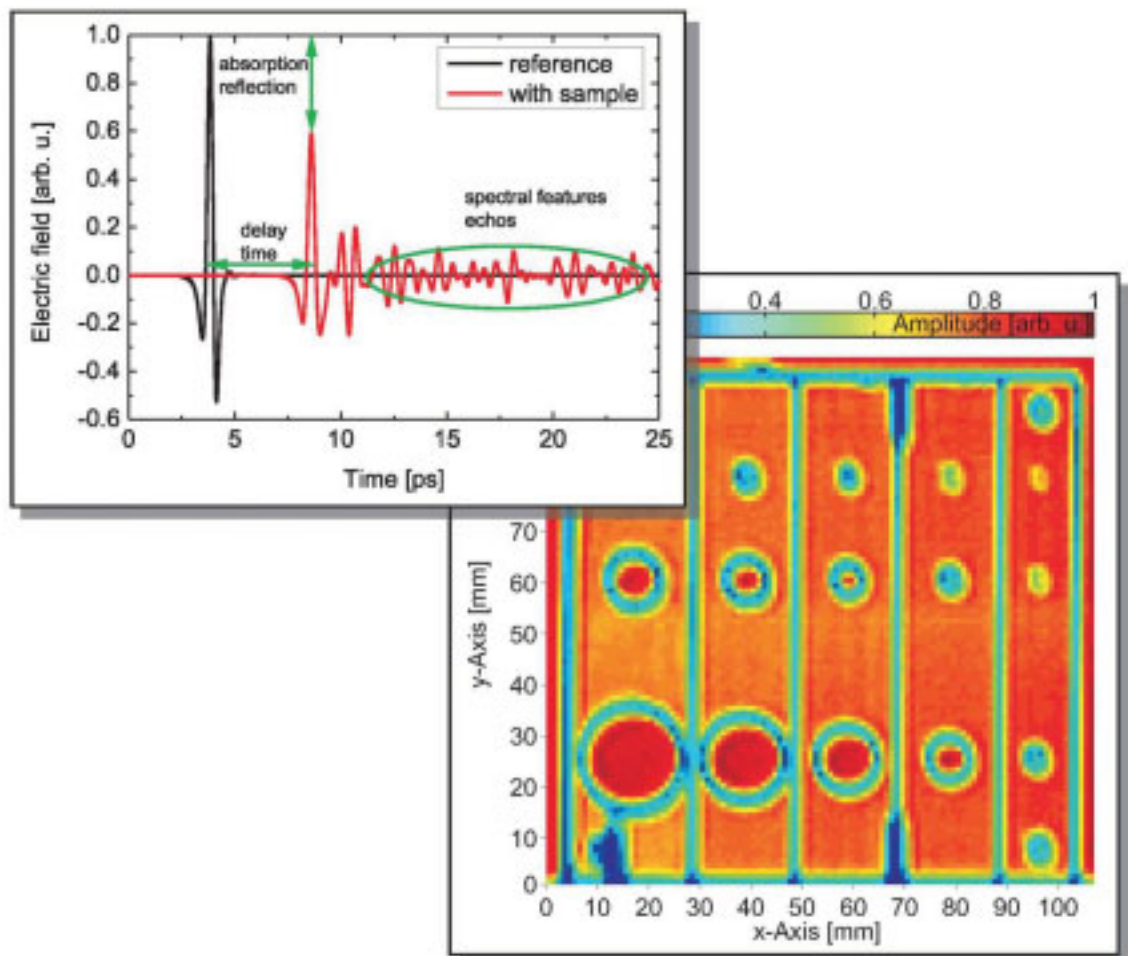Michael Theuer

Terahertz Time-Domain Spectroscopy Systems for Fundamental and Industrial Applications

Cuvillier Verlag Göttingen

Internationaler wissenschaftlicher Fachverlag

Terahertz Time-Domain Spectroscopy Systems for Fundamental and Industrial Applications

Dissertation

Michael Theuer

Vom Fachbereich Physik der Technischen Universität Kaiserslautern
zur Verleihung des akademischen Grades
"Doktor der Naturwissenschaften" genehmigte Dissertation

Betreuer: Prof. Dr. R. Beigang

Zweitgutachter: Prof. Dr. K. Kawase

Datum der wissenschaftlichen Aussprache: 17.10.2008

D 386

Contents

1 Introduction

The terahertz (THz) band between $100\,\text{GHz}$ and $10\,\text{THz}$ is particularly interesting for a wide range of applications since it unifies the properties and advantages of the adjoining spectral ranges, the infrared and the millimeter waves. But unfortunately in this spectral range the optical as well as electronic systems can not offer a sufficient performance in terms of power and sensitivity. So in both approaches, new sources and detectors are developed to expand the accessible electromagnetic spectrum into the THz range.

In this thesis new developments in the field of optical THz systems for THz time-domain spectroscopy (TDS) are investigated using femtosecond pulses for the coherent generation and detection. Starting from previous experiments, mostly carried out by C. Weiß in the group of Prof. R. Beigang at the University of Kaiserslautern, new schemes for THz emitters are elaborated. The main aim is to obtain a THz source with high output power in the frequency range between $100\,\text{GHz}$ and $4\,\text{THz}$ for femtosecond pumped systems. In a cooperation with the RIKEN Institute in Japan, in particular the group of Prof. K. Kawase and C. Otani, an enhancement cavity for the pump radiation is developed. This is an actively stabilized synchronously pumped ring resonator which recycles the unused pump radiation. As THz emitter a lithium niobate crystal in Cherenkov-type geometry is applied. Lithium niobate is particularly well suited as a THz emitter because of its high nonlinearity, high transparency in the near infrared and the well developed poling technique. To guarantee an efficient broadband surface emitting scheme also for longer crystals an attached silicon prism is used as THz output coupler. The enhancement cavity is characterized in terms of properties for the near infrared pump pulses as well as for the emitted THz radiation. Using coherent and incoherent detection the output is compared to other available emitters.

So far most of all optical THz systems are based on Ti:sapphire lasers with wavelengths around $800\,\text{nm}$. In order to apply readily available femtosecond fiber lasers at $1.5\,\mu\text{m}$ wavelength, used e. g. in the telecommunication field, new materials for THz emitters have to be investigated. Here results of various emitters based on different semiconductors are presented. Wavelength dependent measurements up to $2\,\mu\text{m}$ are possible using a CTA-OPO pumped by a tuneable Ti:sapphire laser. The theory of photoconductive surface emission is extended with respect to phase-coupled Hertzian dipoles. The experimental results are verified by numerical simulations.

For the application of THz radiation different TDS systems are realized. With respect to the experimental constraints the devices' layout has to be adapted. Limiting factors like laser power, pump wavelength, flexibility, space consumption and imaging optics are addressed. Portable systems and fiber based systems are constructed. A special emphasis is placed on a THz imaging system, which is used in feasibility studies for

industrial customers. This applied research and development takes place at the Fraunhofer Institute for Physical Measurement Techniques (IPM). Its recently established Dept. of THz Measurement and Systems is located at the Dept. of Physics at the University of Kaiserslautern.

Results of industrial relevant measurements are presented. The recorded THz electric field is typically evaluated in terms of amplitude and phase. This reduces the large amount of recorded data and shows a THz image underlining different properties of the device under test. Potential applications are in the field of non-destructive testing and final inspection (geometry, thickness, coatings, interfaces). Typical examples are layer thickness measurements and entirety checks in the production and packaging process. The detection limit in the time domain is demonstrated for thin layers and calibrated samples.

THz spectroscopy also can give the "spectral fingerprint", an important decision criterion for the sample to be identified (content, substance distribution). Lactose is used as a substitute reference under laboratory conditions. Also real world explosives and poisons are measured. The advantages of THz time-domain spectroscopy compared to cw or passive THz systems are discussed.

THz-TDS can detect signals in reflection as well as in transmission. The used geometry depends on the sample and the experimental restrictions like metallic surfaces or absorbing substances. Therefore, the mentioned inspections are carried out either in direct transmission or in reflection into different angles. This is important for stand-off detection e. g. in safety and security applications. The aim here is to identify hazardous substances at the body of a person or within packages. In principle THz-TDS can spectroscopically identify substances. But real world applications are hampered by system and sample properties. The strongest limitation is given by water vapor absorption in ambient air. The accessible spectral bands are experimentally demonstrated and confirmed by simulations for different parameters like propagation length and humidity. Also the sample properties like surface roughness, interfaces and reflectivity are taken into account. A balanced discussion of the possibilities and limitations for THz stand-off detection is given.

The results of this thesis mark steps towards the acceptance of THz radiation in industrial applications: The introduction of an enhancement cavity together with a better understanding of coherent THz emitters gives rise to THz sources with higher output power. The progress on the components' side allows the THz systems to be used in a real world environment. Finally, the shown imaging and spectroscopic results underline the possibilities of THz-TDS as a valuable technique in the field of non-destructive testing and stand-off detection.

Einleitung

Der Terahertz (THz) Spektralbereich zwischen 100 GHz und 10 THz ist für eine große Anzahl von Anwendungen interessant, da er die Eigenschaften und Vorteile angrenzender Spektralbereiche, nämlich der Infrarot-Strahlung und der Millimeter-Wellen, vereinigt. Jedoch zeigen gerade in diesem Spektralbereich sowohl die optischen als auch elektronischen Systeme unglücklicherweise keine ausreichende Leistungsfähigkeit hinsichtlich Ausgangsleistung und Empfindlichkeit. Von beiden Ansätzen her werden neue Quellen und Detektoren entwickelt, um das zugängliche elektromagnetische Spektrum um den THz Bereich zu erweitern.

In dieser Arbeit werden neue Entwicklungen im Gebiet der optischen THz Systeme untersucht. Dabei wird das Prinzip der Zeitbereichs-Spektroskopie, bei der Femtosekundenpulse zur kohärenten Erzeugung und zum Nachweis verwendet werden, eingesetzt. Aufbauend auf die vorausgehenden Experimente, die im Wesentlichen von C. Weiß in der Arbeitsgruppe von Prof. R. Beigang an der Technischen Universität Kaiserslautern durchgeführt wurden, werden neue Ansätze für THz Quellen ausgearbeitet. Das Hauptziel ist es, eine THz Quelle mit hoher Ausgangsleistung im Frequenzbereich zwischen 100 GHz und 4 THz für durch Femtosekunden-gepumpte Systeme zu erhalten.

In einer Kooperation mit der Arbeitsgruppe von Prof. K. Kawase und C. Otani des RIKEN Instituts in Japan wurde eine Überhöhungs-Kavität für die Pumpstrahlung entwickelt. Diese besteht aus einem aktiv stabilisierten, synchron gepumpten Ringresonator, der die ungenutzte Pumpstrahlung wieder verwertet. Als THz Sender wird ein Lithium Niobat Kristall in Cherenkov-Geometrie verwendet. Um einen effizienten, breitbandig emittierenden Sender auch für lange Kristalle zu erhalten, wurde ein Silizium Prisma als THz Auskoppler verwendet. Somit wird die THz Strahlung direkt unter der Oberfläche erzeugt und dadurch die Materialabsorption deutlich vermindert. Die Überhöhungs-Kavität wird auf ihre Spezifikationen hin untersucht, sowohl im Hinblick auf die Eigenschaften für die Pulse im nahen Infrarot als auch für die ausgesandte THz Strahlung. Diese wird mittels kohärentem und inkohärentem Nachweis detektiert und mit anderen verfügbaren Emittern verglichen.

Bisher basierten die meisten THz Systeme auf einem Titan:Saphir Laser bei einer Wellenlänge von 800 nm. Um jedoch fertig verfügbare Femtosekunden-Faserlaser, wie sie bereits im Telekommunikationsbereich bei 1.5 µm Wellenlänge eingesetzt werden, verwenden zu können, müssen neue Materialen für THz Sender untersucht werden. Ergebnisse von Sendern aus verschiedenen Halbleitern werden präsentiert. Messungen bei variabler Wellenlänge bis zu 2 µm sind durch den Einsatz von durchstimmbaren Titan:Saphir Lasern und eines CTA-OPOs möglich. Die Theorie für photoleitende Oberflächenemission wird um den Aspekt der phasenstarr gekoppelten Dipole erweitert. Die experimentellen Ergeb-

nisse werden durch numerische Simulationen bestätigt.

Unterschiedliche THz Systeme werden zur Anwendung der THz Strahlung werden entwickelt. Unter den gegebenen Randbedingungen muss der Aufbau jeweils angepasst werden. Die begrenzenden Faktoren wie etwa Laserleistung, Pumpwellenlänge, Flexibilität, Platzbedarf und bildgebende Optiken werden ausgeführt. Tragbare und faserbasierte Systeme werden konzipiert. Ein Schwerpunkt liegt auf einem abbildenden System, welches in Machbarkeitsstudien für industrielle Kunden zum Einsatz kommt. Diese anwendungsnahe Forschung und Entwicklung findet am Fraunhofer-Institut für Physikalische Messtechnik (IPM) statt. Die kürzlich eingerichtete Abteilung THz Messtechnik und Systeme befindet sich im Fachbereich Physik an der Technischen Universität Kaiserslautern.

Ergebnisse industriell relevanter Messungen werden gezeigt. Die aufgenommen THz elektrischen Felder werden üblicherweise auf Amplitude und Phase hin ausgewertet. Dies reduziert die große Datenmenge und ermöglicht ein THz Bild, welches verschiedene Eigenschaften des Probekörpers hervorhebt. Potentielle Anwendungen liegen im Gebiet der zerstörungsfreien Materialprüfung und Endkontrolle (Ausmaße, Dicke, Beschichtungen, Grenzflächen). Typische Beispiele sind Schichtdickenmessungen und Vollzähligkeitsprüfungen im Produktions- und Verpackungsprozess. Die Nachweisschwelle im Zeitbereich wird für dünne Schichten anhand kalibrierter Probenkörper bestimmt.

Die THz Spektroskopie kann auch den "spektralen Fingerabdruck" liefern, ein wichtiges Entscheidungskriterium für die vermessene Probe (Inhalt, Wirkstoffverteilung). Milchzucker wird dabei als Austauschstoff unter Laborbedingungen verwendet. Aber auch echte Sprengstoffe und Gifte werden gemessen. Die Vorteile der Zeitbereichs-Spektroskopie im Vergleich zu Dauerstrich oder passiven THz Systemen werden diskutiert.

Die Signale der THz Zeitbereichs-Spektroskopie können sowohl in Reflexion als auch in Transmission detektiert werden. Die verwendete Geometrie hängt von der Probe und den experimentellen Randbedingungen wie etwa metallischen Oberflächen oder absorbierenden Substanzen ab. Deshalb werden die Untersuchungen entweder in direkter Transmission oder Reflexion in unterschiedliche Winkel durchgeführt. Dies ist wichtig für die Ferndetektion, wie sie z. B. in Sicherheitsanwendungen erforderlich ist. Das Ziel dabei ist es, gefährliche Stoffe am Körper einer Person oder in Behältnissen zu erkennen. Grundsätzlich kann die THz Zeitbereichs-Spektroskopie Stoffe durch spektrale Auswertung nachweisen. Aber echte Anwendungen werden durch die System- und Probeneigenschaften beeinträchtigt. Die stärkste Begrenzung stellt die Absorption in Wasserdampf der Umgebungsluft dar. Die zugänglichen spektralen Bänder werden experimentell bestimmt und durch Simulationen mittels Parametern wie Propagationslänge und Luftfeuchte bestätigt. Auch die Probeneigenschaften wie etwa Oberflächenrauhigkeit, Grenzflächen und Reflektivitäten werden berücksichtigt. Eine ausgewogene Diskussion der Möglichkeiten und Grenzen der THz Ferndetektion wird gegeben.

Die Ergebnisse dieser Arbeit markieren Schritte in Richtung der Akzeptanz der THz Strahlung in industriellen Anwendungen. Die Verwendung einer Überhöhungs-Kavität zusammen mit einem weitergehenden Verständnis von kohärenten THz Sendern führt zu THz Quellen mit höherer Ausgangsleistung. Die Entwicklung auf der Seite der Komponenten ermöglicht den Einsatz von THz Systemen in realistischen Umgebungen. Schließlich

unterstreichen die abbildenden und spektroskopischen Ergebnisse die Einsatzmöglich-keiten der THz Zeitbereichs-Spektroskopie als eine nützliche Technik im Bereich der zer-störungsfreien Materialprüfung und Ferndetektion.

2 Fundamentals

Since years most of the electromagnetic spectrum is accessible due to advanced optics and sophisticated electronic sources. For the infrared (IR) and the visible range strong lasers or parametric sources are available since the invention of the laser [1, 2].
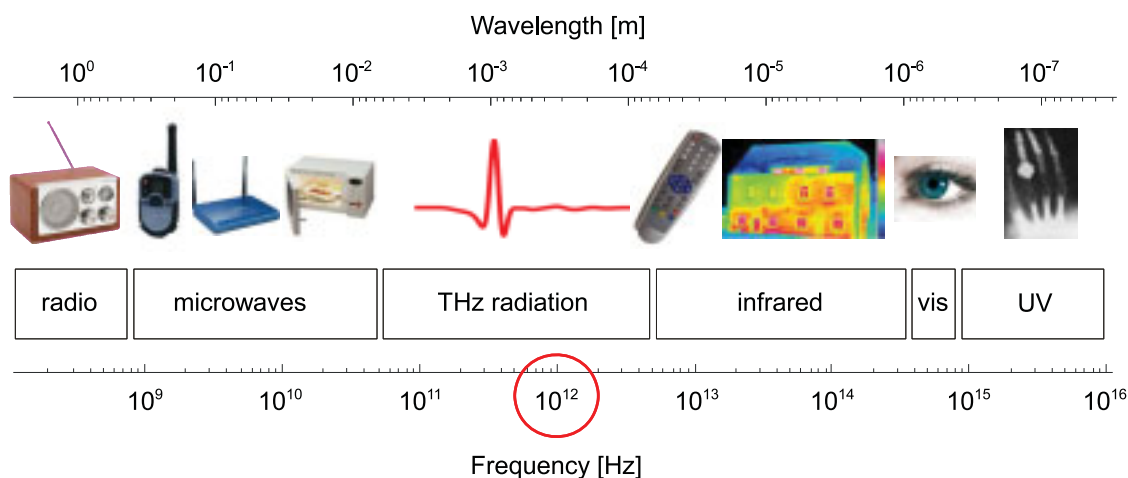

Figure 2.1: Electromagnetic spectrum in units of wavelength and frequency

But the optically accessible wavelength range has been limited towards the long wavelengths, except of some frequency-fixed gas lasers in the far infrared (FIR). On the other side of the electromagnetic spectrum the electronic sources are quite elaborated. But for the frequency range above 100 GHz the output power is rather low. Altogether there was a gap in the accessible electromagnetic spectrum, the so-called terahertz gap in the frequency range between 100 GHz and 10 THz. While both approaches, the photonic and the electronic, expand towards the THz range, for fundamental research at least for linear investigations, the available sensitivity is quite sufficient. For university purposes where cost, energy consumption, size and 24/7-reliability play a minor role compared to industrial requirements, a standard terahertz time-domain spectroscopy (THz-TDS) system is a very good device to address the frequency range between 100 GHz and 4 THz.

However, for real world industrial applications current THz systems have to be improved in terms of power, the detectors in terms of sensitivity and the overall system have to become smaller, cheaper and more reliable. From that point of view also big efforts in fundamental research have to be made to bring the devices in an appropriate condition that a company can sell systems at the free market. So the aim here is to show a

considerable progress towards a running prototype or demonstrator which is state-of-the-art and applicable in industrial processes. So the THz gap can be filled also with applications. It would be very strange if this spectral range would be the only one which is not used for applications.

The within this thesis described research topics use ultrashort femtosecond (fs, 10^{-15} s) pulses in the near infrared (NIR) to generate and detect THz pulses coherently. Because of the substantial progress in the field of nonlinear optics, pulsed fs lasers are accessible. The high peak power, good beam profile and low phase fluctuations at a high repetition rate are the main reasons for the widespread use of ultrashort pulsed lasers. Fs lasers can be operated not only under laboratory conditions but already in industrial turn-key systems in a rough environment.

2.1 Pulse Propagation

Electromagnetic waves are completely characterized by the space and time-dependent electric field $E(x,y,z,t)$. Its sources and temporal evolution are described by the linear Maxwell equations. Therefore the solutions can be applied to all wavelength ranges from the ultraviolet to the far infrared. The physics in this thesis is closely related to the NIR and the THz spectral range. So all notations introduced in the chapter remain valid for both frequency ranges despite showing a large difference in energy per photon by a factor of about 200.

A description of the electric field $E(x,y,z,t) = E(t)$ in the time or frequency domain is equivalent and can be translated using a Fourier transformation [3]

$$E(\omega) = \mathcal{F}\{E(t)\} = \int_{-\infty}^{\infty} E(t)e^{-i\omega t}\,dt \tag{2.1}$$

For convenience reasons also a complex representation of the electric field is common

$$E(t) = \mathcal{E}(t)e^{i\Phi(t)} \tag{2.2}$$

with an envelope of the electric field $\mathcal{E}(t)$ and an oscillating phase $\Phi(t)$ in the time domain. The phase $\Phi(t)$ can be expressed as

$$\Phi(t) = \varphi_0 + \varphi(t) + \omega_\ell t \tag{2.3}$$

This segmentation makes sense because when it comes to wave packets or pulses in most cases only a slowly varying phase $\varphi(t)$ is superimposed to a high frequency oscillating term ω_ℓ (mean or carrier frequency). Then the instantaneous frequency $\omega(t)$ of the pulse is

$$\omega(t) = \frac{\mathrm{d}\Phi(t)}{\mathrm{d}t} = \omega_\ell + \frac{\mathrm{d}\varphi(t)}{\mathrm{d}t} \tag{2.4}$$

Therefore a discussion of the slowly varying phase $\varphi(t)$ is sufficient to describe phenomena like chirp or frequency-shifts occurring due to self-phase modulation (SPM). The constant phase φ_0 is the carrier envelope offset [4] and of no concerns for our kind of experiments. Please note that the concept of envelope and carrier frequency is only valid for pulses which have a bandwidth which is small against the carrier frequency. That may not be the case for ultrashort THz pulses where the bandwidth often exceeds the carrier frequency.

Starting again with the Maxwell equations up to now the spatial coordinates and the vector character were neglected. The Maxwell equations in Cartesian coordinates give for the electric field $\mathbf{E}(x,y,z,t)$:

$$\left(\frac{\partial^2}{\partial x^2} + \frac{\partial^2}{\partial y^2} + \frac{\partial^2}{\partial z^2} - \frac{1}{c^2}\frac{\partial^2}{\partial t^2} \right) \mathbf{E}(x,y,z,t) = \mu_0 \frac{\partial^2}{\partial t^2}\mathbf{P}(x,y,z,t) \tag{2.5}$$

with μ_0 the magnetic permeability of free space and $\mathbf{P}$ the polarization of the medium. This source term $\mathbf{P}$ is the response of the medium and can be decomposed into two parts

$$\mathbf{P}(t) = \mathbf{P}_{\mathrm{L}}(t) + \mathbf{P}_{\mathrm{NL}}(t) \tag{2.6}$$

where $\mathbf{P}_{\mathrm{L}}(t)$ varies linearly with the electric field while $\mathbf{P}_{\mathrm{NL}}(t)$ shows a nonlinear behavior. The first term is responsible for linear losses and gain, diffraction as well as dispersion, while the latter one stands for e. g. sum and difference frequency generation. The nonlinear source term $\mathbf{P}_{\mathrm{NL}}$ will be focussed especially in chapter 4.1 as the reason for THz emission. Restricting eq. 2.5 further to linear polarization and propagation in z-direction brings the reduced wave equation

$$\left(\frac{\partial^2}{\partial z^2} - \frac{1}{c^2}\frac{\partial^2}{\partial t^2} \right) E(z,t) = \mu_0 \frac{\partial^2}{\partial t^2}P_{\mathrm{L}}(z,t) \tag{2.7}$$

A linear response of the medium is related to the dielectric susceptibly $\chi(\omega)$ in the frequency domain by

$$P_{\mathrm{L}}(z,\omega) = \epsilon_0 \chi(\omega) E(z,\omega) \tag{2.8}$$

This together with a Fourier transformed eq. 2.7 gives a differential equation for the electric field in the frequency domain

$$\left(\frac{\partial^2}{\partial z^2} + \omega^2 \epsilon(\omega) \mu_0 \right) E(z,\omega) = 0 \tag{2.9}$$

where $\epsilon(\omega)$ is the dielectric constant defined by $\epsilon(\omega) = [1 + \chi(\omega)] \, \epsilon_0$. A solution of eq. 2.9 is

$$E(z,\omega) = E(0,\omega) e^{-ik(\omega)z} \tag{2.10}$$

with $k(\omega)$ the complex wave vector defined by the refractive index $n(\omega)$

$$k^2(\omega) = \omega^2 \epsilon(\omega) \mu_0 = \frac{\omega^2}{c^2} n^2(\omega) \tag{2.11}$$

Comparable to the decomposition in eq. 2.3 also here $k(\omega)$ is expanded around the carrier frequency ω_ℓ

$$k(\omega) = k(\omega_\ell) + \left. \frac{\mathrm{d}k}{\mathrm{d}\omega} \right|_{\omega_\ell} (\omega - \omega_\ell) + \frac{1}{2} \left. \frac{\mathrm{d}^2 k}{\mathrm{d}\omega^2} \right|_{\omega_\ell} (\omega - \omega_\ell)^2 + \ldots \tag{2.12}$$

The inverse first derivation of the k-vector at the center frequency is also known as the group velocity v_g. It describes the propagation velocity of the envelope of the wave packet

$$v_g = \left(\left. \frac{\mathrm{d}k}{\mathrm{d}\omega} \right|_{\omega_\ell} \right)^{-1} \tag{2.13}$$

The second derivation of k is called the group velocity dispersion (GVD)

$$k_\ell'' = \left. \frac{\mathrm{d}^2 k}{\mathrm{d}\omega^2} \right|_{\omega_\ell} = -\frac{1}{v_g^2} \left. \frac{\mathrm{d}v_g}{\mathrm{d}\omega} \right|_{\omega_\ell} \tag{2.14}$$

This term is responsible for the broadening of a pulse. Typical optical components made of glasses show a positive GVD in the visible and near infrared range. The propagation of an initially bandwidth limited pulse in a dispersive medium extends the pulse duration. Different frequencies travel with unequal phase velocities so that a linear spectral distribution called chirp under the pulse envelope is present. This effect may be compensated by angular dispersion in prisms or grating.

For transmission of pulses in fibers, a special focus has to be set on dispersion. The first because even in low dispersive media the dispersion can add up to large values because the distances are much longer than the extents of lenses or crystals. Even if the linear dispersion is compensated, the third order dispersion (TOD) causes pulse broadening which limits the quality of the transmission. Besides the effects of dispersion, also other

nonlinear effects in fibers have to be accounted for.

If the wave vector $k(\omega)$ contains also an imaginary part, the linear losses α are also accounted for

$$k(\omega) = k_0 + \Delta k(\omega) + i\frac{\alpha(\omega)}{2} \tag{2.15}$$

and the initial electric field $E(\omega,0)$ will suffer losses and phase changes for a given propagation length z.

2.2 Nonlinear Effects

In cases of strong electric fields $E(t)$ which are provided by lasers or focused beams the external electric fields come into the same order of magnitude as the inherent electric fields in the material. Then also nonlinear contributions of the polarization have to be taken into account in eq. 2.5. This is due to the response of the electrons (here assumed to be instantaneous) and their nonlinear potential curve for high energies.

$$P_{\mathrm{NL}}(t) = \epsilon_0\chi^{(2)}E(t)E^*(t) + \epsilon_0\chi^{(3)}E(t)E^*(t)E(t) + \ldots \tag{2.16}$$

The first approximation to quantify the material parameter of the nonlinear response is $\chi^{(2)}$. This term is sufficient for physical phenomena like second harmonic generation (SHG) and difference frequency generation (DFG).

$$P_2(t) = \epsilon_0\chi^{(2)}E(t)E^*(t) \tag{2.17}$$

The simple ansatz $E(t) = E_0 e^{i\omega t}$ leads to

$$P_2(t) = \frac{\epsilon_0\chi^{(2)}E_0^2}{2} + \epsilon_0\chi^{(2)}E_0^2\cos(2\omega t) \tag{2.18}$$

It is obvious from expression (2.18) that a field with twice the frequency as well as a constant DC field is emitted. The latter one is called optical rectification (OR).

Assume that the incident electric field $E(t)$ consists of two superimposed contributions $E(t) = E_1(t) + E_2(t)$ at different frequencies. Then these two waves also interact according to eq. 2.17 in a nonlinear process. The output is a mixture of the sum $(\omega_1 + \omega_2)$ and the difference $(\omega_1 - \omega_2)$ of the participating frequencies (and of course both transmitted fundamental frequencies). Which particular contribution is stronger depends on the phase matching condition because the process is described by a set of coupled differential equations.

3 Terahertz Time-Domain Spectroscopy

In contrast to the electronic approach the photonic THz techniques are based on lasers. Continuous wave lasers, pulsed lasers with nanosecond pulse length as well as ultrashort pulsed lasers in the sub 100 fs regime are used. A big progress has been made towards compact and reliable devices since the realization of the first femtosecond (fs) laser source. Thus, it is now possible to use this photonic high-end technique not only in research but also in real world applications.

The advantages of mode-locked femtosecond laser sources are high peak power and a broadband spectrum. Fourier limited pulses are delivered by solid state Ti:sapphire lasers. Most versions are also tunable in wavelength, sometimes even between 690 nm and 1020 nm. Depending on the particular application and THz setup, some specifications are more important than others. The relevant devices are introduced in this chapter.

3.1 TDS Principle
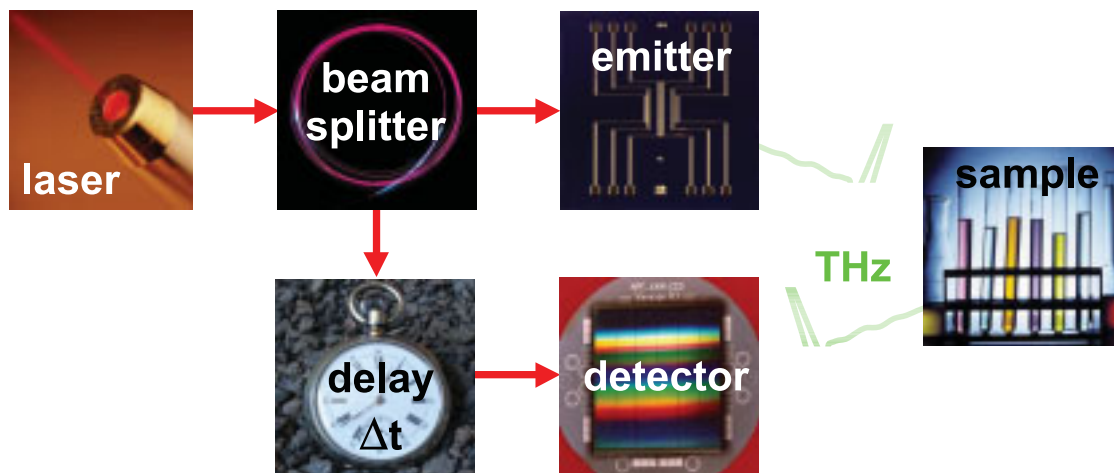
Figure 3.1: Principle of the THz time-domain spectroscopy system (THz-TDS). Major components: laser, emitter, detector and a delay producing device

The basic principle of terahertz time-domain spectroscopy (THz-TDS) is to sample a fast transient slowly by coherent detection (Fig. 3.1). Here the same laser pulse is split into two fractions which are used for the generation of THz radiation in the emitter and to gate the detector, respectively. The pump pulse length and the integration time of

the detector are smaller than the THz pulse length. So the detector can sample the THz pulse with small temporal gates stepwise as a function of delay Δt. The temporal delay is typically caused by a spatial displacement of a mirror. So high frequencies can be sampled. By changing the runtime between pump and detector pulse, the electric field (not only the intensity) can be detected. A following Fourier transformation shows the spectral amplitude and phase. Further on, the repetition rate of the laser is much higher than the inverse pulse length, so the detector is insensitive most of the time. For typical experimental conditions it is only active for $10^{-3}\,\%$ of the time (duty cycle). If during that period the THz pulse is present, the detector gives a signal. Otherwise it only integrates over environmental electromagnetic noise. For the rest of the time it gives only a neutral signal, depending on the type of detector [5]. This reduces the noise of the system considerably.

3.2 Pulse Propagation and Data Processing

Since in THz-TDS systems electric fields are detected, a Fourier transformation can bring the spectral amplitude including intensity and phase. To calculate this with a computer algorithm like the Fast-Fourier-Transform (FFT) procedure it is important to have equally spaced supporting data points in the time domain. This can be assured either by moving the delay line to the appropriate discrete positions (stepwise) or by synchronized readout of the lock-in amplifier and a continuously running linear stage (on-the-flight).

The mathematic algorithm expects 2^n data points. If the data set does not fulfill this condition one can add zeros at the end of the array (zero-filling). But this can bring residuals and changes in the recorded line shape. If the FFT is calculated using Origin® the software will automatically fill up zeros pretending to have a higher spectral resolution.

The mathematical relation of the temporal distance between the data points Δt and the frequency resolution $\Delta\nu$ is given by the number of data points in the time domain N

$$\Delta\nu = \frac{1}{N\Delta t} \tag{3.1}$$

This is the reason for scanning long delay times in the TDS. The longer the scan, the more independent data points can be recorded and thereby the spectral resolution is increased.

According to the Nyquist-Shannon sampling theorem the maximum detectable frequency $\Delta\nu_{\text{max}}$ is

$$\Delta\nu_{\text{max}} = \frac{1}{2\Delta t} \tag{3.2}$$

Higher frequencies can not be detected, they are canceled out by the sampling technique. In the experimental realization this is not a strict cut-off relation but more a steady
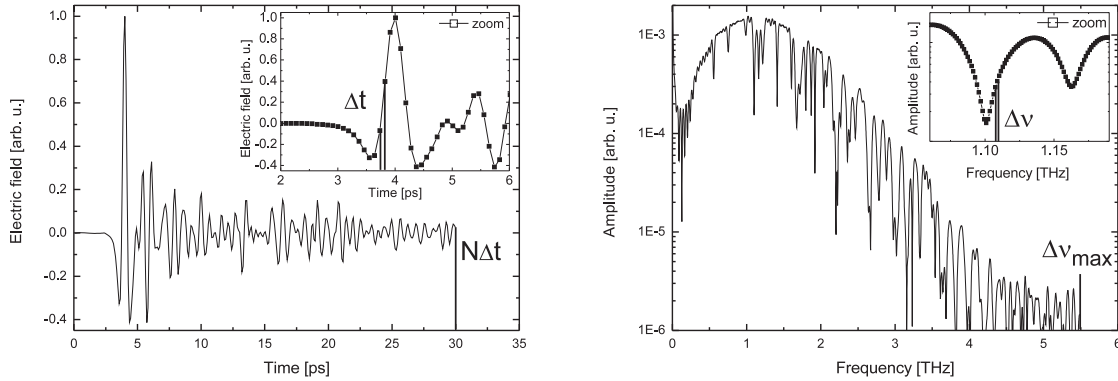
Figure 3.2: Relation between the time and frequency domain: Fourier transformation. The spectral resolution $\Delta\nu$ and the maximum detectable frequency $\Delta\nu_{\mathrm{max}}$ is defined in the time domain by data point spacing Δt and the amount of data points N.

limiting factor for the high frequency limit. If the time constant of the lock-in amplifier is too long or the velocity of the delay line is too fast, the high frequencies are not detectable, limiting the accessible bandwidth despite dense sampling.

If we record the electric field $E_{sample}(\omega)$ with a sample in the THz beam then the complex wave vector $k(\omega)$ will influence the transmitted pulse. But all the characteristics of the combination of emitter and detector as well as the properties of the imaging optics like mirrors and lenses are included in the measured electric field. Also the humidity will show a strong absorption at discrete lines (see chapter 8.6).

Therefore typically a reference $E_{ref}(\omega)$ is recorded without a sample to get rid of all system parameters besides the changes induced by the device under test. A division of these two fields (see eq. 2.10) brings the sample's transmission:

$$T(\omega) = \frac{E_{sample}(\omega)}{E_{ref}(\omega)} = e^{-\frac{\alpha z}{2}} e^{i[k_0 + \Delta k(\omega)]z} \tag{3.3}$$

So for a known propagation length or sample thickness z the material constants refractive index n and absorption coefficient α can be calculated. Further details on the evaluation of the particular parameters with respect to imaging applications are discussed in chapter 8.

3.3 Optics

The most obvious difference between the NIR and THz waves is that typically optical devices like lenses or mirrors have extents larger than the used wavelength for the NIR while in the THz range the wavelength reaches the same order of magnitude like the geometrical dimensions of the devices itself. So much higher precautions have to be taken

into account for the THz waves when it comes to coherence, diffraction or scattering.

As for all optical sources also the THz emitters have an inherent divergency while the detectors show a limited viewing angle. The THz beam path between these two, the more precise: the transfer function, has to be optimized in terms of amplitude, focus diameter, astigmatism, frequency distribution, additional echo pulses and so on.

A surface emitter (chapter 4.2) itself does not need additional optics. The pump beam defines the divergency of the THz beam because it is a diffraction limited source. So if placed in the focus of a mirror, a good beam quality is expected. But for a photoconductive switch (PCS) collimating optics are essential due to the high divergency of the point source and small angle of total internal reflection. Silicon (Si) is very well suited to be used as a substrate for THz transmission optics. The refractive index is quite high ($n_{\mathrm{Si}}^{\mathrm{THz}} = 3.41$ [6]) and it shows only very low dispersion and small absorption. The design of a Si lens is important to increase the angle of view of the emitter and to adjust the THz beam to the application. Different lens layouts are proposed in literature depending on the particular system. Various calculations and simulations as well es experiments have proven this [7–9]. So a good spectral density and a collimated beam with a reduced divergency can be reached.

There is also the possibility to work without a Si lens. But then there are always strong echoes due to multi Fresnel reflections in the substrate. Typically Si has nearly the same refractive index as GaAs ($n_{\mathrm{GaAs}}^{\mathrm{THz}} = 3.59$ [10]) and so only a negligible reflection at the interface occurs. Also sapphire [11] or germanium optics are in use. Anti reflection coatings are difficult to be fabricated for the THz range. The coating layer thicknesses have to be in the wavelength range which is some tens of microns. This is much more than for visible optics. So different techniques are elaborated to produce appropriate optics also for the THz range (Si: [12], Ge: [13]).

Another possibility is to operate the PCS in reflection. This means one illuminates the PCS on its metallized side and detects not the THz radiation that is generated in forward direction but to look at the THz radiation which is emitted back towards the exciting laser beam. Here the dispersion in the PCS is minimized because the THz radiation does not have to propagate through the substrate by the expense that no Si lens can be attached and echoes and divergency problems occur unless otherwise compensated.

The design of all optics is influenced by the large bandwidth of the THz pulse with respect to the center frequency. So the difference in divergency within the THz spectral contributions can be observed, especially for a focussed system [14]. Due to diffraction theory the high frequency part of the THz spectrum can be focussed to a smaller focus than the long wavelengths.

This fact can also be used to restrict the broadband spectrum to a higher center frequency. A pinhole next to the emitter or next to the focus can bring a better spacial resolution [15, 16]. Then the pinhole acts as a frequency filter. The same result can be obtained by evaluation of the THz data in the frequency domain. This would be a kind of software-pinhole allowing the measurement at particular frequency bands. Various attempts have been done to transmit THz pulses on metallic [17] or plastic wave guides [18, 19] to control the propagation. But high losses, dispersion, diffraction and bad

coupling efficiencies limit the possibilities for this approach up to now.

For the THz range only a few techniques are known to produce anti-reflection coatings for optics. Therefore, reflective optics are preferable to transmissive optics if available. The optics used within this thesis are off-axis parabolic mirrors to guide the THz beam. Their advantages are:

- no echo pulses, refractive index steps

- high reflectivity, protected gold coating

- large area, angle of view

The particular used models depend on the device and the required focus. If space is not a problem and a long Rayleigh length is needed, the particular mirror (Melles Griot 02POA017) is an off-axis parabolic with 63.5 mm diameter at a focal distance of 120 mm. The protected gold coating has a reflectivity of better than 95 % in entire THz range.

3.4 Electronic Devices

Typical THz pulses show a spectral distribution between 100 GHz and 4 THz. Compared to commercially available electronic devices and wirings like high-speed network adapters or network cables THz frequencies are a much higher . Today's network standards have stated working frequencies of 100 MHz (Cat-5 standard). A plug like a SMA connector has a bandwidth with a cut-off frequency of 34 GHz. So by using nowadays wires it is impossible to transport signals with THz frequencies. It should be mentioned that there is serious progress in guiding THz pulses on free-space wires [20] or fibers [21] and attempts to use a complete free-space solution for THz communication [22]. Here one further advantage of TDS can be seen: If there is no movement in the time domain (the linear stage is standing still), it is nearly a DC case for the electronics like the preamplifier. So to sample THz frequencies already slow components with bandwidths in the kHz range are sufficient. Of course, to increase the signal-to-noise ratio and to reduce the data acquisition time, high frequency devices are advantageous. The measured signals can be guided in standard wires and BNC cables.

Lock-in Detection

Most of the presented THz signals in this thesis are recorded using a lock-in amplifier. The used model is the Stanford Research SR830. It offers a sensitivity range between 2 nV and 1 V at a frequency response of 100 kHz. The function is as follows: The interested signal is chopped (periodically modulated) and the lock-in amplifier provides at the output the fraction of signal that is modulated with the same frequency canceling out most other frequencies and DC parts. In the experiment this is realized by using a mechanical (optical) chopper for the laser pulses or a modulated bias for the emitter antenna. Only for the enhancement cavity the chopper was used in the THz beam because of electronic

reasons (control circuit). So also weak signals on a high background noise level can be detected. Offset signals and periodic modulations at other frequencies (like the 50 Hz emission from power supplies) are suppressed very accurately. THz antennas are sensitive to the whole electromagnetic spectrum (with a reduced sensitivity) even without illumination. Therefore also the electromagnetic pollution at 50 Hz or the high frequencies of e.g. a fluorescent lamp at up to 100 kHz can also bring a strong signal. That is why the chopping frequency must not be a multiple of the noise frequency.

Amplifier

Despite the high sensitivity of the lock-in amplifier it appeared that an additional preamplifier can increase the signal-to-noise ratio and make the system more stable to environmental influences. The explanation is that it is advantageous to amplify the small currents in the detector spatially very close to the antenna itself. Then afterwards the amplified voltage is transmitted in the longer cable when the additional noise is present. So less environmental noise can be collected because the antenna effect of the cable is minimized.

3.5 Mechanical Components

The most important mechanical device in a time-domain spectroscopy system is the optical delay unit. Like in a Fourier spectrometer it is necessary to scan a signal as a function of delay. Here it is realized using a retro reflector on a moveable stage. A more elegant method would be to use two fs lasers with a slightly detuned repetition rate. Then one laser produces the THz pulses while the other one samples it. This technique is called asynchronous optical sampling (ASOPS) [23]. But here, because of cost and rigidity, a mechanical delay unit producing a time difference by adding a path length was applied.

Linear Stages

The used linear stage is a stepper motor driven device manufactured by Physik Instrumente (PI) in Karlsruhe, Germany. It has the advantage of a high mechanical stability and a good positioning accuracy (bidirectional reproducibility and origin better 1 μm, step size 0.1 μm). So it is possible to measure small changes of time differences which will be of importance later on for timing critical measurements. The maximum scanning range was, depending on the particular model, between 10 cm and 30 cm. This is much more than the typically scanned value of 2 cm, but important for the first alignment of the system and for thick samples. The velocity is limited to a maximum of 20 mm/sec which has to be considered also for the data acquisition time.

Shaker

A faster but less accurate device is a so-called shaker. The here used model is a Scan-Delay 150 manufactured by APE in Berlin, Germany. It contains a retro reflector which can be moved with an amplitude of ± 11.25 mm (150 ps) at a frequency of up to 10 Hz. So 20 data sets can be recorded in one second. The sinusoidal movement of the reflector can only be regarded to be linear in the middle of the scan. So for data points recorded at positions closer to the turning point of the movement the actual position is important. This is useful for thickness measurements where the expected runtime is known, but not sufficient for a high frequency resolution. This allows for the fast data acquisition which is needed for industrial applications. Either by directly monitoring the signal at an oscilloscope or by a fast AD data acquisition card. A chopper, respectively a lock-in amplifier can not be used here. The THz signal is not constant for the time period when the gate is open for typical chopping frequencies.

3.6 Pump Sources

A couple of different laser sources are used in the experiments. They differ in pump output power and stability. The center wavelength and tunability is one further criterion. In the following the laser sources are described as reference for the experiments and systems presented in chapter 7.

SpectraPhysics Tsunami®

The first experiments are carried out using a SpectraPhysics Tsunami® pumped by an argon ion laser. Since the alignment of the optical system concerning the gas laser changes from day to day the reproducibility in terms of pointing stability, center wavelength and pulse duration is rather poor compared to solid state pumped laser systems. Typical values for a Tsunami® pumped by a 10 W pump laser are: 700 nm – 1000 nm center wavelength, > 1.5 W power, < 100 fs pulse length.

SpectraPhysics Mai Tai®

SpectraPhysics Mai Tai® is a wavelength tunable fs Ti:sapphire laser system in one box. It contains the cw frequency doubled (532 nm wavelength) solid state laser and the ultrafast Ti:sapphire part in one temperature stabilized housing. The diodes themselves are located in a power supply connected by an umbilical cable with the laser head. So thermal drifts can be minimized. It's hands free, only allowing to tune the center wavelength between 710 nm and 990 nm in the XF version. This is internally realized by a stepper motor controlled slit and a prism compressor. Also the beam pointing stability is very good and actively stabilized. The maximum average power is 1.9 W at a repetition rate of 80 MHz. The pulse duration is below 100 fs for all operating wavelengths. The HP version even
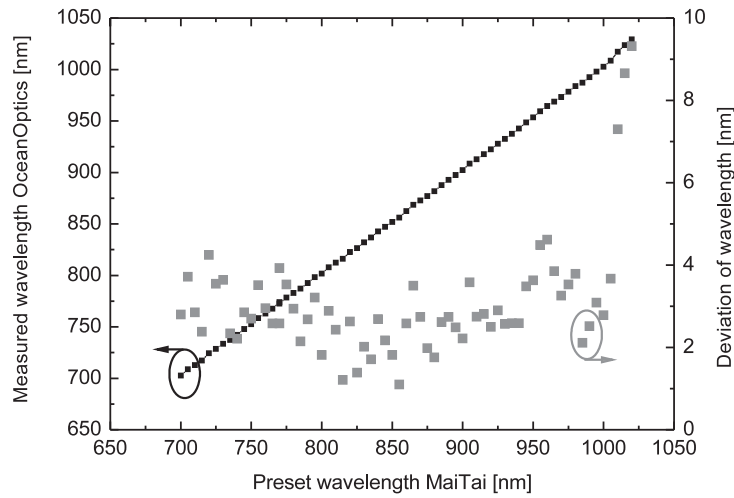
Figure 3.3: Mai Tai® HP wavelength tunability: preset and measured wavelengths and
their deviation

offers a tunability between 690 nm and 1020 nm at an output in the maximum above
2.5 W.

Figure 3.3 shows the wavelength tuning characteristics of a Mai Tai® HP. The values
measured by a calibrated spectrometer (OceanOptics 2000) are plotted versus the wave-
length which was preset at the laser's remote control. A deviation in the range of 4 nm is
seen in the overall tuning range, increasing to the long wavelength limit. If an experiment
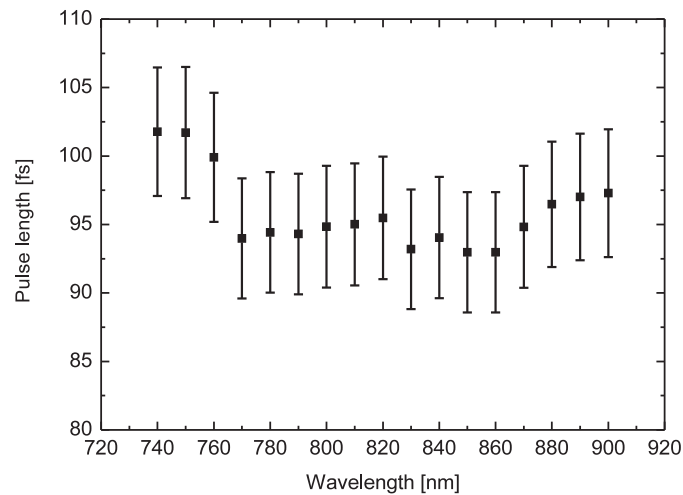is sensitive on the wavelength, this has to be taken into account.

Figure 3.4: Mai Tai® pulse length (FWHM) for different operating wavelengths

The pulse length measured in an interferometric autocorrelation is shown in Fig. 3.4. It

is approx. 100 fs for the entire tuning range. So in terms of pulse length there are no big influences expected caused by the laser when the operating wavelength has to be changed in the experiment.

Coherent® Chameleon XR

This Coherent® laser is comparable to the SpectraPhysics Mai Tai®. It also contains the pump laser and the fs oscillator in one housing while offering a broad tuning range. The specifications for 805 nm are: 1.4 W and 100 fs. Unfortunately it turned out that the pulses were not stable enough for the enhancement cavity (fast repetition rate drifts) so that this laser was only used for other single pass experiments.

Coherent® Vitesse 800

This laser combines a solid state cw pump laser (Verdi®) and a mode-locked Ti:sapphire oscillator into one integrated box. The given specifications are an average power of 800 mW at a fixed center wavelength of 800 nm with a pulse length of less than 100 fs. This model did not contain an additional dispersion control, so the pulses were not Fourier limited. They had a bandwidth of approx. 30 nm while only showing a pulse length of 80 fs.
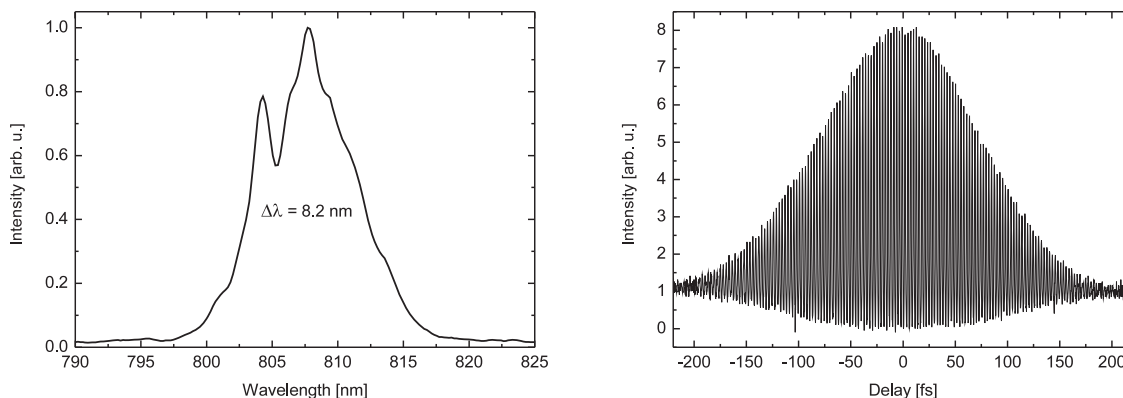
Imra Femtolite F-100

Figure 3.5: Specifications of Imra Femtolite F-100. Left: spectrum, right: interferometric autocorrelation

Imra's Femtolite F-100 is a frequency doubled fiber laser. The fundamental oscillator is operating at approx. 1.55 μm. An internal frequency doubling unit gives an output of more than 110 mW at 808 nm with a pulse length of about 120 fs. The actual specifications depend on the particular model. Figure 3.5 shows the asymmetric output spectrum which is typical for fiber lasers. For industrial applications the major advantage is that it is a turn-key system without requiring a chiller. The pumping diodes just need a fan for cooling, so the needed space is very small and the mean time between failures long. Since

in the cavity the laser light is guided in a fiber there are not much optical components such as mirrors which could be affected by vibrations causing repetition rate changes. Also the pulse-to-pulse stability is higher compared to a Ti:sapphire system.

CTA-OPO

CTA stands for cesium titanyl arsenate. This crystal is a member of the alkali titanyl arsenate group. The CTA fs source is in fact not a laser, it is an optical parametric oscillator (OPO) [24–29]. The main difference to a laser is that there is no inverted medium which has a lifetime of the upper laser level. Here the pump photons delivered by a further fs laser are converted into two photons with smaller energy (parametric process) obeying the energy and momentum conservation law according to a 3-wave mixing process [30]. These two new emitted photons are named signal (higher frequency) and idler (smaller frequency) photon, respectively. The energy conservation for parametric processes is known as the Manley-Rowe relation [31]

$$\frac{\Delta P_{\mathrm{pump}}}{\omega_{\mathrm{pump}}} = \frac{\Delta P_{\mathrm{signal}}}{\omega_{\mathrm{signal}}} = \frac{\Delta P_{\mathrm{idler}}}{\omega_{\mathrm{idler}}} \tag{3.4}$$

Without a cavity this conversion would be just optical parametric generation (OPG). This is in most cases quite inefficient since both, the signal and the idler wave, have to start out of random noise (vacuum fluctuations). So the conversion efficiency is typically low, despite showing no threshold. Therefore a cavity is used to resonate one of the generated waves (called signal or idler resonant) or even both (double resonant). Because the parametric gain is a function of the presence of all three waves much higher conversion efficiencies can be reached in an OPO. But still according to eq. 3.4 the output in terms of photon distribution to signal and idler does not depend on which one is resonant. For the experimental realization the coating and losses in the substrate limit the output in the long wavelength range besides the average power reduction due to the reduced photon energy. Of course, the OPO's oscillation threshold has to be overcome.

The specialities of the used CTA-OPO are versatile: It is a synchronously pumped OPO, which means that the pump pulse and the resonator pulse have to overlap for each round trip. So the cavity length of the OPO and the pump laser have to fit in terms of some microns. Further on, it is a pump tunable OPO using non critical phase matching. The type of phase matching condition changes at the point of degeneration which is reached for a pump wavelength of $\lambda_{\mathrm{pump}} = 778\,\mathrm{nm}$. Here the type switches from type II o-eo (pump ordinary - signal extraordinary, idler ordinary polarized) to type II o-oe. Because the term signal and idler is already defined, these two change the polarization when tuned above the point of degeneration. So it would make more sense to call the output e or o-polarized wave.

As a function of pump wavelength the refractive index for the extraordinary polarized wave varies in the medium very slowly. Therefore it is advantageous to operate the OPO e-resonant, which is idler resonant below and signal resonant above the point of
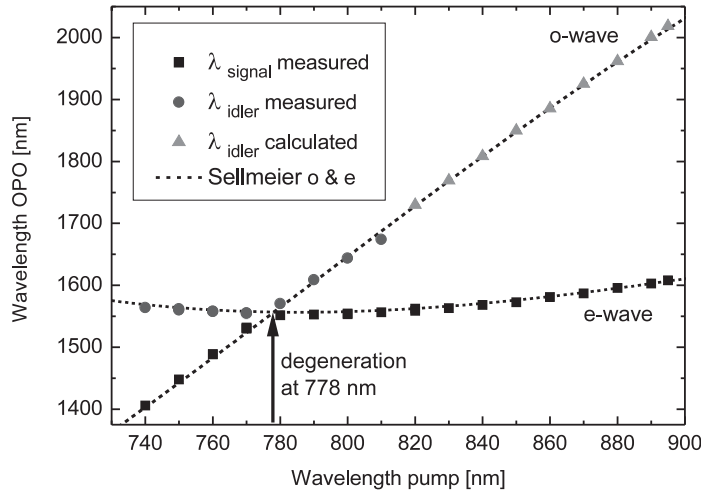
Figure 3.6: Tunability of CTA-OPO: signal and idler wavelength

degeneration. Then one set of mirror is sufficient to access most of the tuning range of the OPO. Especially when it comes to an operation with an idler wave above 1.7 µm the mirror coating is better for a resonant signal wave.

For signal and idler wavelengths below 1.7 µm both are spectrally situated within the broadband reflection coating of the mirrors. Then both waves are circulating. Therefore one has to control which wave is resonant. The most radical way to chose one resonant polarization is to insert a polarizing beam splitter in the resonator. This serves as an output coupler for the deflected polarization. The other more subtle way is to use the dispersion in the CTA crystal. Over the entire tuning range both polarizations have a group velocity difference of 200 fs/mm. So if the output wavelength has to be changed only the pump wavelength has to be adapted and the cavity length to be readjusted. Also a double resonant OPO can be realized by the above mentioned polarizing beam splitter and an additional mirror. Then the condition of synchronously pumping can be fulfilled for the other polarization as well despite the slightly different geometrical resonator length.

The advantage of this particular OPO compared to commercially available OPOs like PPLN or KTP-OPOs is the broad tuning range in the near infrared. No other OPO has such a big tuning range starting at 1.30 µm reaching up to 2.24 µm [32] including the important 1.55 µm wavelength which is used by the telecom industry. The pulse length is quite short (below 200 fs). This is sufficient for testing of THz devices working at any operating wavelength of the OPO.

The achieved output power and the accessible wavelength range of the idler branch is sufficient for the planned THz experiments. Therefore only one set of resonator mirrors and one fixed output coupler is used. The symbols in Fig. 3.6 indicate the wavelength where an applicable output of the OPO is achieved. The accessible spectrometer only shows a signal up to 1.7 µm wavelength. So the signal wave beyond the detection limit was calculated using the energy conservation of the parametric process. The directly

measured as well as the calculated values fit very well to the theoretical curve given by the Sellmeier equation. For further details on the particular OPO see [32, 33].
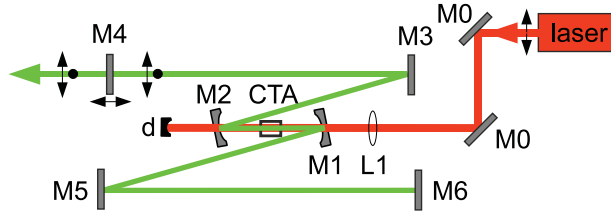

Figure 3.7: Basic CTA-OPO setup: Simple double z linear resonator

The OPO can be set up in different geometries. The most simple one is the one shown in Fig. 3.7. It consists of a set of mirrors M0 which guide the pump pulses from the laser to the OPO. A collimating lens L1 with $f = 100\,\text{mm}$ focusses the pump radiation into the CTA crystal. The curved mirrors M1 and M2 ($R = -100\,\text{mm}$) are transparent for the pump wavelength and high reflective for the signal and idler wave around $1.5\,\mu\text{m}$. For longer wavelengths they get transparent again up to a high transparency at $2.1\,\mu\text{m}$. The mirrors M3, M5 and M6 are also highly reflective for the generated waves in the interval $1.35\,\mu\text{m}$ to $1.6\,\mu\text{m}$. Mirror M4 is a $10\,\%$ output coupler (OC). All cavity mirrors have an auxiliary coating for the frequency doubled Ti:sapphire wavelength ($R > 50\,\%$ for $360\,\text{nm}$ to $420\,\text{nm}$). So the setting up is easier because the SHG in the CTA-OPO can be used to align the resonator.
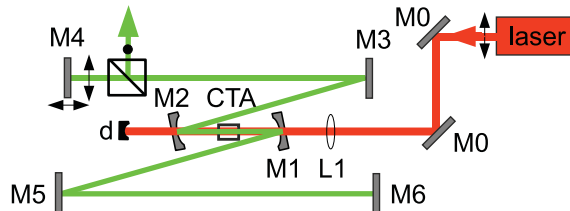

Figure 3.8: CTA-OPO setup for strict single resonant operation

Typically both waves are circulating in the cavity. For the OPO operation this is no problem. The OPO remains single resonant because of the GVD between the two wavelengths. An external polarizing beam splitter (PBS) behind the OC can separate signal and idler wave so that a single wavelength can be accessed. When the PBS is used in the resonator (Fig. 3.8) it acts like a $100\,\%$ OC. The pulse train is separated into two separate paths.

If an output wavelength above $1.7\,\mu\text{m}$ is needed the OPO has to be operated signal resonant. Then the OPO mirrors start getting transparent for the idler wave. Above $1.7\,\mu\text{m}$ the idler wave leaves at mirror M2 gradually as the pump wave also does (Fig. 3.9). Because these two are polarized orthogonally a PBS can separate them spatially. So
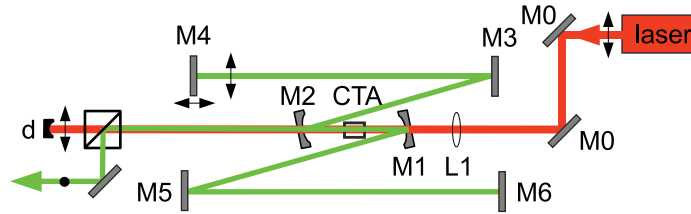
Figure 3.9: CTA-OPO setup for long wavelength operation

an output can be accessed up to $2\,\mu\mathrm{m}$. Since the beam is coupled out at a curved mirror the beam is divergent. An external focussing lens is used to collimate the beam and guide it to the THz setup.
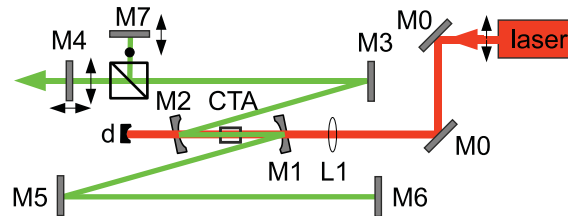

Figure 3.10: CTA-OPO setup for double resonant operation

If in the setup with a PBS inside of the resonator the second wave is also brought back into the cavity synchronously the OPO can operate double resonant (Fig. 3.10). This is sometimes used to reduce the oscillation threshold. But here it causes the OPO to show an unstable output. But for a slightly detuned runtime of both waves a pulse train with adjustable pulse distance can be produced. So depending on the CTA setup and the working point (pump wavelength and power, used OPO polarization, signal or idler) output powers up to $1\,\mathrm{W}$ are achieved.

3.7 Comparison to other THz Systems

In this chapter, the basic principles and components of a THz-TDS system are described. But there are also other manmade sources and detectors besides the ones based on fs lasers. The following listing shall give a first impression on the possibilities and limitations of those systems, especially with respect to the differences compared to THz-TDS. The main classification of THz emitters and detectors are whether they work coherently or incoherently and further on whether they rely on the electronic or optical approach.

Passive Systems

The oldest THz source is a black body radiator. According to Planck's formula

$$B(T,\nu) = \frac{2h\nu^3}{c^2} \frac{1}{e^{h\nu/k_B T} - 1} \tag{3.5}$$

all bodies above a temperature of $10\,\mathrm{K}$ emit THz radiation. So THz radiation is nothing artificial, it always surrounds us. This fundamental principle is still used in thermography for industrial applications.

Complete systems based on passive imaging are available at the market. These map the slight temperature differences which are present at a person's body and correlate it with objects. So metallic "cold" items are detectable under cloth but everything at body temperature does not give a contrast. These systems are based on millimeter waves which limits the spacial resolution of the imaging application. So to be more precisely, it should be called MMW imaging not THz imaging.

To achieve this high sensitivity they need a cooled detector. The high thermal background and the high brightness of e.g. a cup of coffee or a light bulb can reduce the contrast drastically because of saturation and lowered dynamics. But since these systems are passive they are accepted more easily by the public because there is no danger related to a radiation source. Further on, the limited resolution does not concern people. The need of monitoring systems and safety control in contrast to individual privacy is not a topic of this thesis.

Photonic cw THz

Also the photonic cw THz radiation can be detected coherently. Therefore for example two diode lasers with a slightly different wavelength are mixed in a nonlinear element (e.g. a photoconductive switch). The incident waves form a modulated current in the emitter. This beat has the difference frequency between these two pump lasers. The same phase locked process can be used to read out the electric field in the cw case. But here only the phase can be measured modulo $2\,\pi$. This is in most cases sufficient but when absolute delay times are necessary the information content here is reduced compared to a fs TDS.

Photonic Pulsed THz

Also nanosecond pump lasers can be used to generate THz radiation by difference frequency generation. Typical nonlinear media are LN [34] and GaAs [35]. Optic parametric generation (OPG) is observed even in a single pass scheme. An additional resonator can oscillate the signal wave forming an optical parametric oscillator (OPO).

The advantages of the ns pumped systems are manifold. The lasers itself are well developed, show a high pulse energy and allow single mode operation. By additional injection seeding narrow line widths below $100\,\mathrm{MHz}$ and a wide tunability from $0.7\,\mathrm{THz}$ – $2.4\,\mathrm{THz}$ are reported [36, 37]. The observed high pump depletion close to the Manley-Rowe relation proves the high efficiency of THz generation of the parametric process.

Using small Q-switched ns lasers tabletop systems are already available for industrial spectroscopic applications with pyroelectric or bolometric detection [38, 39].

Electronic cw THz

The electronic sources are based on diodes (Schottky diode, Gunn diode) which emit typically in the 90 GHz range. The frequency of this strong fundamental local oscillator is increased into the THz range by a cascaded multiplier chain. While the fundamental oscillator is a cheap emitter with a high power (some 100 mW), the output is considerably reduced by each nonlinear process (frequency doubling, tripling, etc.) into the mW range. The advantages of electronic sources are manifold. The output for low frequencies is quite high, the components are already developed and reliable. The main problem arising here is a sensitive detection. If incoherent detection in a pyrodetector or Golay cell is used the dynamics and refresh rate is quite poor. If on the other side the coherent detection in a mixer is applied the system gets very expensive because a network analyzer is necessary to resolve the signal.

Electron Beam Sources

When a charged particle is accelerated, an electromagnetic wave is emitted. This fundamental principle can be used also to generate THz waves. Synchrotron sources also emit broadband THz radiation. In former times this part of the electromagnetic spectrum was more or less waisted. But in recent times since the need for high brightness THz sources is obvious also this relativistic systems are optimized for an accessible THz beam line. Also the backward wave oscillator (BWO) is based on accelerated electrons in a strong magnetic field. These sources are also commercially available and show an output power of some 10 mW around 100 GHz. Frequency multiplied versions can reach up to 1.5 THz at a reduced power of some mW. The operating wavelength can be tuned by changing the acceleration voltage. Due to the high output power also imaging applications are possible together with pyroelectric detection [40].

THz Gas Lasers

There are also some molecular gas laser which oscillate in the THz range. The most known lasers from that type are the methanol (CH_3OH) and the formic acid (CH_2O_2) lasers. As expected for a gas laser the used laser lines (rotational transitions) are discrete and not tuneable. Unfortunately they have to be pumped by a CO_2 laser. But the high output power of several mW makes them interesting in fundamental research. Commercial versions are available but also expensive.

THz Quantum Cascade Lasers (QCLs)

This electronic sources are common in the mid infrared (MIR) and reach down to the THz range now [41]. As the name already indicates this special kind of laser is based

on a cascaded process of the pump electrons. Unlike for typical lasers where interband recombinations from electrons and holes take place here intraband transitions occur. Assuming an electron above the bandgap of a typical semiconductor the energy difference is much larger than the energy of one THz photon. So the overall quantum efficiency is rather low when only one THz photon per pump photon is emitted. The idea here is to use only a fraction of the pump inversion energy (bandgap energy) to generate one THz photon. The electron with reduced energy can still be used as the upper laser level to emit a second THz photon and so forth. Of course, the lower laser levels have to be depleted by other processes very fast. So each electron can be used a couple of times when the semiconductor hetero structure is designed appropriately. Due to this elaborate layout and fabrication of the semiconductor structure the tunability is very limited.

For applications the high output at high frequencies is very interesting [42]. Unfortunately the QCLs need cryogenic cooling to reduce the thermal energy and to start the lasing process at a THz frequency. Current research tries to achieve operation at higher temperatures. Recently, a THz emission at room temperature was reported using intracavity DFG in a two wavelengths mid IR QCL [43]. The operational mode of a QCL is typically pulsed but also cw lasers are available.

4 THz Emitters

An optical THz emitter converts the pump radiation from the excitation wavelength (typically in the visible or NIR) into THz radiation. Two major kinds of emitters are presented: The first series is based on degenerated difference frequency generation, the so called optical rectification, which is a nonlinear process of second order. The other kind of THz emitters are based on transient photoconductivity. For those it is important to bring electrons above the bandgap and then to accelerate them.

4.1 Optical Rectification

According to chapter 2.2 the nonlinear susceptibility $\chi^{(2)}$ was introduced as a material constant to describe the second order nonlinearity. This gives rise to sum and difference frequency generation of discrete frequencies. If the pump spectrum is broadband this condition is fulfilled for a lot of frequency pairs. So the intuitive description explains the rise of optical rectification (OR) as the degenerated difference frequency between particular frequencies (ω_1, ω_2) within the broadband fs pulse. A Fourier limited pulse at 800 nm center wavelength and 100 fs pulse duration has a spectral width of approx. 4 THz [44]. This already shows the limit of the accessible spectral range for the THz generation using OR. For an efficient conversion into the difference frequency the fundamental laws of energy conservation and impulse conservation have to be fulfilled simultaneously:

$$\omega_1 - \omega_2 - \omega_{\mathrm{THz}} = 0 \tag{4.1}$$

$$\hbar\,\mathbf{k_1} - \hbar\,\mathbf{k_2} - \hbar\,\mathbf{k}_{\mathrm{THz}} = \mathbf{0} \tag{4.2}$$

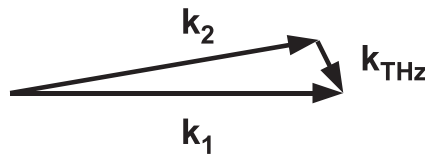Very common is the representation of eq. 4.2 in a k-vector diagram (Fig. 4.1).

Figure 4.1: Phase matching condition in the k-vector diagram

In terms of refractive indices this reads

$$n_1\,\omega_1 - n_2\,\omega_2 - n_{\text{THz}}\,\omega_{\text{THz}} = 0 \tag{4.3}$$

Typically the refractive index in the NIR differs from the refractive index in the THz range very much, e. g. for lithium niobate $n_{\text{LN}}^{\text{NIR}} \approx 2.2$ and $n_{\text{LN}}^{\text{THz}} \approx 5.2$. Therefore by using birefringent refractive index phase matching, i. e. different refractive indices for different polarizations, eq. 4.3 can not be easily fulfilled. In the visible and NIR spectral range, where birefringent phase matching is possible, this technique is used in various OPOs. So different solutions are realized to reach an efficient conversion into the THz range.

In most cases eq. (4.2) can not be satisfied in the phase matching condition which results in a mismatch of $\mathbf{\Delta k}$

$$\mathbf{k_1} - \mathbf{k_2} - \mathbf{k}_{\text{THz}} = \mathbf{\Delta k} \tag{4.4}$$

So typically OR is not phase matched. This results in an inefficient generation since the pump and THz waves are getting out of phase and start to interfere destructively. The length for which the two waves accumulate a phase difference of π is called coherence length $l_c = \frac{\pi}{\Delta k}$.

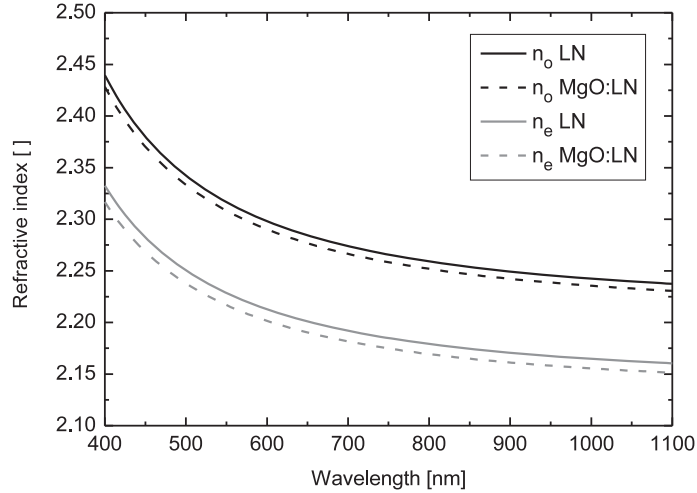## Lithium Niobate as Nonlinear Material

Figure 4.2: Refractive indices of lithium niobate (LN) and magnesium oxide doped lithium niobate (MgO:LN) in the visible and IR [45]

Lithium niobate (LN) is a nonlinear crystal with good-natured mechanical parameters (hardness, hydrophoby, melting point) besides the excellent optical properties [46, 47]. Therefore, this crystal is often used for nonlinear frequency conversion or as a modulator.

Its superiority to other crystals is the reason for a widespread application of this crystal for example in the telecommunication industry. This mass market guarantees the high quality and enduring availability of optical grade LN crystals. That is why for the non-linear generation of THz radiation lithium niobate is used throughout this thesis. Unless otherwise stated the name LN is used synonymously also for the magnesium oxide doped lithium niobate (MgO:LN).

Compared to other available nonlinear crystals, LN is particularly well suited for various applications. The first to mention is the large nonlinear coefficient $d_{33} = 27\,\text{pm/V}$ corresponding to a d_{eff} of $17\,\text{pm/V}$. It is larger than for most other commercially available nonlinear crystals. That is why it is used very often for wavelength conversion like SHG or DFG in various applications and devices.

The refractive index in the IR is plotted in Fig. 4.2. It is approx. 2.2 in the operating wavelength range of typical Ti:sapphire lasers. The curvature indicates that there is considerable dispersion present. The GVD of LN is roughly $500\,\text{fs}^2/\text{mm}$. For broadband pump pulses along with long crystals this has to be taken into consideration.

Because of a transverse optical phonon mode at $7.6\,\text{THz}$ the refractive index increases drastically towards the FIR. This makes birefringent phase matching impossible in the THz range ($n_{\text{LN}}^{\text{THz}} \approx 5.2$). In the tail of this phonon mode the absorption of LN is unfortunately very high in the THz range.
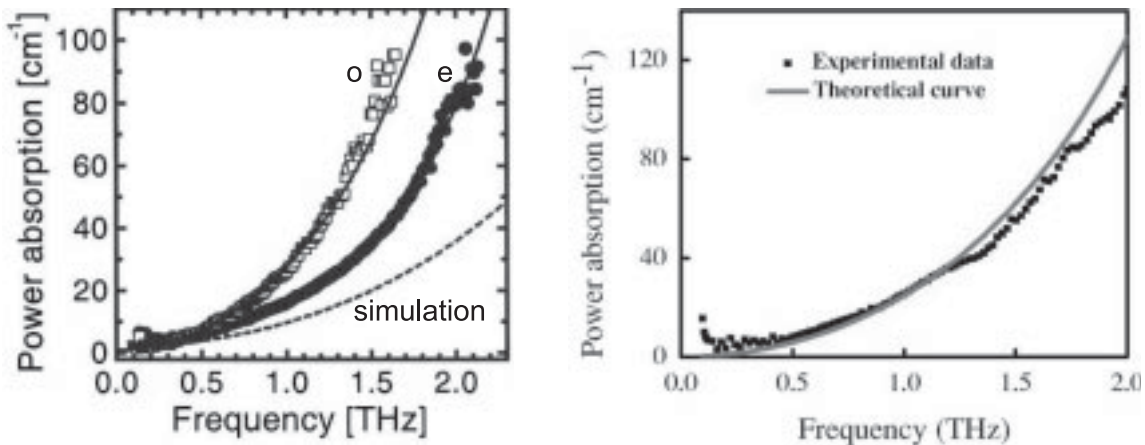

Figure 4.3: Absorption of lithium niobate in the THz range. Left: pure LN according to [48], right: magnesium oxide doped lithium niobate (MgO LN) according to [49]

The absorption coefficient increases from below $10\,\text{cm}^{-1}$ at $0.5\,\text{THz}$ to above $100\,\text{cm}^{-1}$ at $2\,\text{THz}$ (see Fig. 4.3). This is the most limiting factor for a high conversion efficiency from the IR into the THz range. The THz power at the point of generation is quite high, but it is difficult to get it out. One problem is the total internal reflection because of the large refractive index in the THz range, the other one is the mentioned absorption on the way to the emitting crystal facet. Solutions to overcome these difficulties can be found in chapter 4.1.

The losses in the IR are quite small since LN has a high transparency reaching up to $4\,\mu m$ [50]. So also an application of LN in a cavity like an OPO is possible. The high damage threshold is not a limitation neither for strong ns pumped systems nor for the high peak power of fs pulses.

An additional doping with magnesium oxide (MgO) even increases the damage threshold. Also other negative properties are reduced. For example the photorefractive effect in LN is considerably reduced by MgO-doping [51]. This is especially important for fs applications where otherwise beam fanning and perturbations would reduce the performance. So for intracavity applications in the following only MgO-doped LN (1% MgO-doped stoichiometric LN) was used. This does not influence the nonlinear coefficient d_{33} [52], but it affects the losses for the pump wavelength at high peak powers.
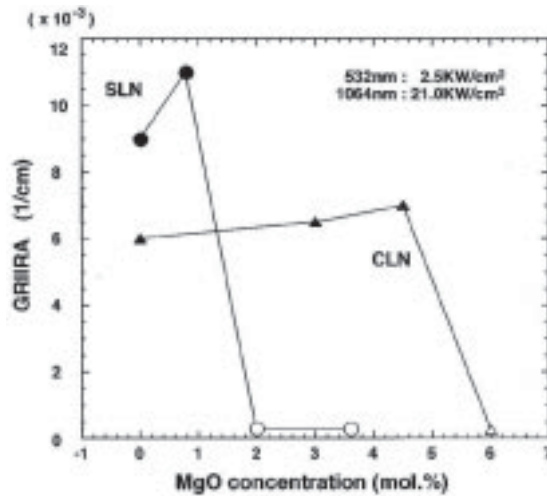

Figure 4.4: Absorption induced by GRIIRA in (MgO)LN according to [53]

The presence of photons at higher energy is expected to reduce the transmission for longer wavelengths. According to the results of Furukawa et al. [53] an affect named bluelight or green-induced infrared absorption (BLIIRA, GRIIRA) according to the inherent second harmonic generation is the reason. Figure 4.4 shows the induced losses by GRIIRA for different doping concentrations and crystal types. Unfortunately, the crystals which are optimal because of the reduced photorefractive effect inhibit a high GRIIRA activity. Also Beyer et al. [54] report on increased losses induced by femtosecond pulses in LN. They attributed it to two-photon absorption in the range of $400\,nm$ pump wavelength. For later mentioned experiments with high peak power this loss mechanisms have to be considered, too.

But still among the ferroelectric crystals LN is the most known and used one. Especially because even large crystals can be poled periodically in a very good and reproducible quality. The high effective nonlinearity leads to high conversion efficiencies even for challenging wavelengths [55]. The concept of quasi-phase matching (QPM) is especially interesting for the THz range where LN has a large refractive index. The poling

period Λ for an emission at $1\,\mathrm{THz}$ is $127\,\mathrm{\mu m}$ (pump wavelength $800\,\mathrm{nm}$) which is easily to be fabricated compared to the short periods below $10\,\mathrm{\mu m}$ for frequency conversion in the visible range.

For pump wavelengths in the mid infrared also periodically poled GaAs is used [56]. Another very interesting crystal from the group of the organic ionic salts is DAST (4-Dimethylamino-N-methyl-4-stilbazolium). It is applied for optical rectification [57] and for efficient DFG sources as an element with very high nonlinearity ($d_{11} = 230\,\mathrm{pm/V}$) [58] also under intracavity conditions [59].
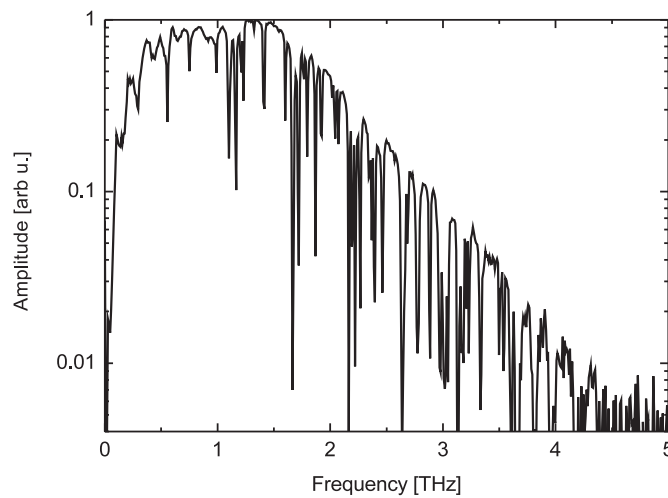
Cherenkov Radiation

Figure 4.5: Broadband spectrum of Cherenkov-type THz generation using optical rectification in lithium niobate

One way to keep all frequency components phase matched was already predicted by Askaryan [60]. This method is known as Cherenkov-type phase matching. It relies on the fact that the envelopes of the generated THz phase fronts are phase matched for a direction Θ_C [44, 61] with respect to the pump propagation

$$\Theta_C = \arccos\left(\frac{n_{\mathrm{NIR}}}{n_{\mathrm{THz}}}\right) \tag{4.5}$$

This kind of phase matching is comparable to Mach's cone in the ultrasonic regime. The source, here the fs pulse, travels faster than the response of the medium. So all generated THz frequencies contribute constructively to the THz pulse. Therefore a broadband pulse is emitted since it is a phase matched scheme for all THz frequencies induced by the broadband fs pump pulse. Recently, this scheme is also reported with DFG in a ns pumped system to achieve a narrow band phase matched output [62].

The problem is that for lithium niobate (LN) the THz emission following the Cherenkov angle $\Theta_C^{\mathrm{LN}} = 65°$ strikes the surface under 25° which is larger than the angle of total internal reflection (TIR) $\Theta_{\mathrm{TIR}}^{\mathrm{LN}} = 11°$ at the boundary between LN and air.

$$\Theta_{\mathrm{TIR}}^{\mathrm{LN}} = \arcsin\left(\frac{n_{\mathrm{THz}}^{air}}{n_{\mathrm{THz}}^{LN}}\right) \tag{4.6}$$

So the THz pulse is reflected internally and stays in the crystal until it is damped by absorption. One way to circumvent the TIR is to use tilted pump pulse fronts [63] to turn the THz phase front with respect to the crystal's surface.

Here we use tight pump focussing and a crystal cut in such a way that the THz wavefront strikes the emitting facet normally. A sketch of the emitter geometry in the so-called Cherenkov cut scheme is shown in the left drawing in Fig. 4.6. The lower beam path points at the problem of TIR. This THz pulse is absorbed in the crystal. The upper part indicates the envelope of the generated phase front which strikes the surface at an angle of 0°.
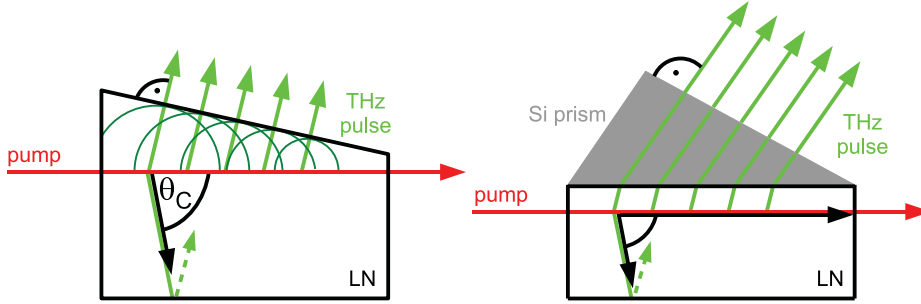

Figure 4.6: Sketch of Cherenkov-type phase matching; left: Cherenkov cut crystal, right: Si prism coupler

Since all THz frequencies remain phase matched for the entire crystal broadband THz radiation is expected. But due to the high absorption in the LN crystal, especially for the high frequency part [48, 49], the output is quite low. Therefore only short crystals can be used. In long crystals the absorption during the extended propagation for the THz wave in the LN is so large that only the last part of the crystal contributes to the emission. This limits the application of longer crystals which would bring higher output. So the interaction length is limited and an effective conversion is not possible.

A short path of the THz beam in the crystal is desired which is the case for a THz generation close to the surface. One solution is to apply a silicon (Si) prism as shown in the right part in Fig. 4.6. The refractive index of Si in the THz range is $n_{\mathrm{THz}}^{Si} = 3.41$ [6, 10, 64, 65]. Therefore Si is ideally suited to reduce the refractive index step between LN and air. So the TIR is prevented and most of the THz power is coupled out while the propagation length is considerably reduced. Also the Fresnel losses are reduced since the refractive index steps take place at two interfaces and not only at one. The Si prism

coupler increases the detected peak maximum of the single-cycle electric field, reaching up to a five times higher intensity [66, 67]. The limiting factor to come closer to the emitting facet is that the edge of the pump beam is not cut away at the entrance facet of the crystal.
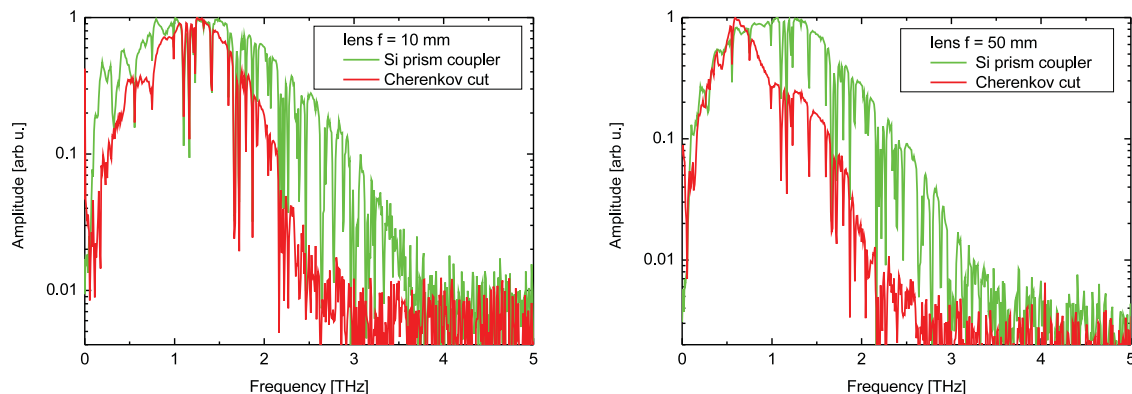

Figure 4.7: THz spectra of a Cherenkov cut crystal compared to a Si prism coupler for different pump foci. Lens left: $f = 10$ mm, right: $f = 50$ mm

Figure 4.7 shows the comparison between a Cherenkov cut and a Si prism coupler scheme [67] under the same experimental conditions (Fig. 4.6). Especially the high frequency part of the THz spectrum above 2 THz is much more pronounced for the emitter using a Si prism coupler arrangement. Two different focussing lenses are used. The tighter focus does not only change the conversion efficiency because of a higher intensity in the focus but also as a consequence leads to a shorter Rayleigh length. This is valid for typical nonlinear generation of light in the NIR or VIS. But for the THz generation it is also a question of transversal interference. This means that THz waves generated at different positions in the y-direction have also a phase difference due to the varying runtime to the detector. If they are out of phase destructive interference will cancel out the particular THz frequency components. Therefore it is important to focus tighter than the shortest THz wavelength to be generated. Thus the harder focussing leads to a more pronounced THz amplitude in the high frequency part even in the Si prism scheme.

A further possibility to couple the THz radiation out of the crystal is a milled grating coupler [68] or the usage of tight focussing under the surface in a periodically poled scheme [69].

Periodically Poled Lithium Niobate (PPLN)

One subtle way to prevent the destructive interference for crystals longer than the coherence length l_c is periodical poling [70, 71]. Every time when pump and THz wave get out of phase due to different velocities the crystal is turned in his orientation by 180°. So the nonlinear coefficient d changes its sign while not affecting the linear refractive index n_{NIR}. Therefore the generation remains phase matched. This can be done by contacting differ-

ent thin pieces of the crystal optically (e. g. gallium arsenide) or by periodic poling. This is an advantage of ferroelectric materials like LN or lithium tantalate where thick and long crystals can be poled in an optically very good quality.
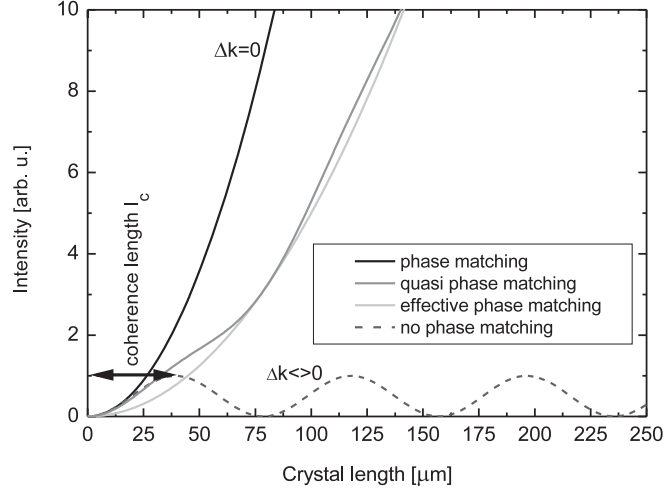

Figure 4.8: Emitted intensities for different kinds of phase matching: perfect, quasi, effective and non phase matching

Figure 4.8 shows the intensity of the generated signal wave as a function of the crystal length which is quite common for e. g. SHG in PPLN. The coherence length l_c is defined as the length for which the pump and signal wave accumulate a phase shift of π. The destructive interference will minimize the output periodically (non phase matched). By changing the crystal's orientation the nonlinear susceptibility changes its sign and therefore the two waves are in phase again. But due to a not optimal phase relation between the turning points, an effective nonlinearity d_{eff} is observed which is reduced compared to the optimal phase matching by a factor of $2/\pi$.

A k-vector $\mathbf{k}_\Lambda$ can be assigned to the poling period. This gives an additional vector term to fulfill the phase matching condition in eq. (4.7) which now reads

$$\hbar\,\mathbf{k_1} - \hbar\,\mathbf{k_2} - \hbar\,\mathbf{k}_{\mathrm{THz}} - \hbar\,\mathbf{k}_\Lambda = \mathbf{0} \tag{4.7}$$

Fulfilling the energy and momentum conservation THz radiation was observed first in forward and backward direction [72, 73] collinear to the pump beam. But this is quite inefficient since the THz wave has to propagate a long way in the absorbing material. The challenge now is to get the wave out of the crystal. The most appropriate way is to focus very tightly under the surface and to observe the THz radiation perpendicular to the propagation direction [69]. In this surface emitting scheme the required additional wave vector component in y-direction comes from the tight focussing. Due to Heisenberg's uncertainty principle [74] a tight restriction in the lateral position leads to a big
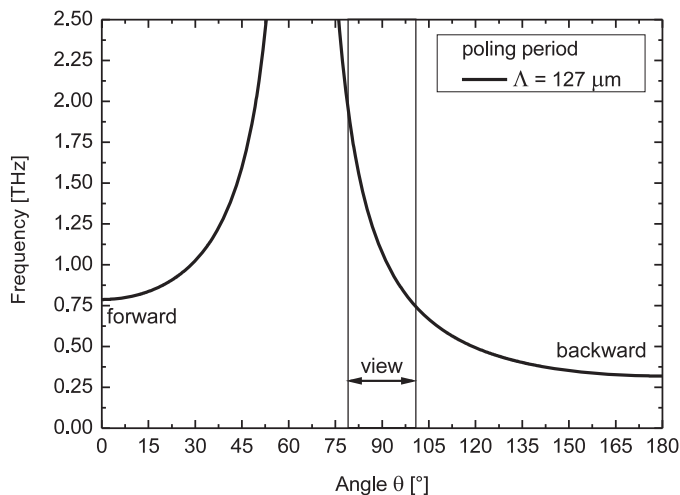
uncertainty in the momentum space.

Figure 4.9: Phase matching in PPLN as a function of internal emission angle Θ

The particular THz frequencies are emitted in different directions according to the phase matching condition. So an observation for different angles Θ will bring different spectral results. Because of the aforementioned TIR an observation in forward and backward direction as well as perpendicular to the pump beam makes sense. The expected frequencies are shown in Fig. 4.9 according to

$$\nu_{\mathrm{THz}} = \frac{c}{\Lambda} \frac{1}{|n_{\mathrm{NIR}} - n_{\mathrm{THz}} \cos \Theta|} \tag{4.8}$$

This leads to a narrow-band multi-cycle THz emission. Please note that the viewing angle is limited by the angle of total internal reflection in LN (indicated as view in the figure) and the viewing angle of the collecting mirror. An interesting possibility now is to change the THz wavelength by adjusting the poling period Λ. A steady tuning was shown by Weiß et al. [75] using a PPLN disc and an observation of the THz emission in forward direction. When rotating the crystal the effective length of the poling period in the projection on the pump beam direction changes. For small deviation angles α from an incidence normal to the poling periods the emitted THz frequency reads

$$\nu_{\mathrm{THz}} = \frac{c}{\Lambda} \frac{\cos \alpha}{|n_{\mathrm{NIR}} - n_{\mathrm{THz}} \cos \Theta|} \tag{4.9}$$

The THz beam pointing stability is quite good in this arrangement. The relative bandwidth changes since as the number of contributing domains do. In the surface emitter arrangement the crystal with an appropriate poling period has to be chosen to get the desired wavelength. The advantage of a PPLN emitter is the higher spectral density in a

narrow frequency band compared to a broadband emitter.

Also the application of fanned-out periodically poled lithium niobate was reported [76]. The crystal is transversally poled with different domain lengths. Depending on which part of the crystal is illuminated through a mask arbitrary terahertz wave forms can be generated.

Aperiodically Poled Lithium Niobate (aPPLN)

Poling of ferroelectric crystals offers a wide range of possibilities for the THz range. It allows the emission of spectrally designed THz pulses [77]. Each cycle can be preset by choosing the particular domain length. In the frequency domain this corresponds to a chirped THz pulse, i. e. a frequency change in time. This might be useful also for THz-pump THz-probe experiments. The first part of the THz pulse pumps one transition while the following would probe the interaction.

4.2 Transient Photoconductivity

For THz emission to occur in a semiconductor there are two processes that have to take place simultaneously. One is to produce free charge carriers, and the other one is to accelerate them. Emitters are divided by the way their charge carriers are accelerated. One possibility is to add an electrode design onto the semiconductor and to bias it [78]. They are called photoconductive antennas or switches (PCS). The term "Auston switch" is also common [78]. The other method, undoubtedly the easier way, is to use the intrinsic acceleration at the surface of a semiconductor [79]. These sources are called (photoconductive) surface emitters.

Photoconductive Switches - Emitters

There are various kinds of photoconductive emitters depending on the geometry of the metallization [80]: dipole [78], strip lines [81], large aperture [82], semi large aperture [83], bow ties [84], spirals [85], or meander shapes [86]. The main idea behind these structures is to enhance the THz generation under different constraints like required bandwidth, available laser power, alignment insensitivity or polarization state.

Figure 4.10 shows a standard layout of a dipole antenna design proposed by D. Grischkowsky et al. [10] based on a scheme invented by Auston [78]. It consists of a substrate made out of semi insulating gallium arsenide (GaAs). The here used metallization is a H-shaped dipole with a spacing between the strip lines called dipole length L_{dipole} of $10\,\mu\mathrm{m}$, $20\,\mu\mathrm{m}$, $40\,\mu\mathrm{m}$ or $60\,\mu\mathrm{m}$. As for a typical Hertzian antenna the dipole length influences the frequency dependent response. This dipole lengths correspond to a high sensitivity in the THz range. The shorter the dipole the more pronounced the high frequency part will be. But also the low frequency part will lose dynamics. The strip lines act as electronic contacts as well as radiation collectors. The gap distance L_{gap} is $5\,\mu\mathrm{m}$ for all dipoles and the extent of the metal lines L_{metal} is $10\,\mu\mathrm{m}$. The large metallized squares in the corners are
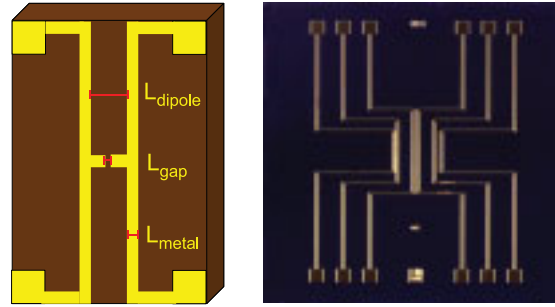
Figure 4.10: Metallization geometry of a typical dipole antenna. Left: sketch, right: processed wafer with 3 antennae

contact pads for wirings which bring the bias to the emitter or the detected current to the amperemeter (see chapter 5.2). The ohmic contact between the semiconducting substrate and the metallization is achieved by annealing. This is important because of photocurrent, heat deposition and structural stability. Typical metallization sequences are either Ge/Au/Ni/Au with 13 nm/26 nm/10 nm/250 nm thickness or Ti on Au (10 nm/250 nm).

Following the intuitive explanation given by Jepsen et al. [87] a simple Drude-Lorentz model is able to describe the radiation emission of a photoconductive switch. The gap itself is much smaller than the generated wavelength (approx. 5 µm) since the frequency of 1 THz corresponds to a wavelength of 90 µm in GaAs. Without illumination the biased switch is just a charged capacitor [88]. The stored electrostatic energy given by $W = \frac{1}{2} C U^2$ is in the range of some pJ. During the period while the fs pulse produces a short-circuit in the gap between the wirings the electrons can flow. Depending on the lifetime of the charge carriers in the substrate the time frame of the charge dynamics is typically increased to approx. 200 fs. For a short timescale the electric field caused by the bias will be completely screened by the generated electron-hole pairs. During that acceleration and deceleration the derivation of the current $j(t)$ defines the THz radiation characteristics. Therefore it is important to describe the evolution of the current in the semiconductor:

$$j = -e\, n_f(t)\, v(t) \tag{4.10}$$

where e is the electron charge, n_f the free charge carriers density and v the average velocity. The movement of the electrons is the main contribution to the current since the holes have a much higher mass.

Let us focus on the time dependency of the different factors in eq. 4.10. The density of the free charge carriers n_f is an interplay between decaying with the timing constant τ_c (trapping time) and generation of new electron hole pairs by the laser pulse $G(t)$:

$$\frac{dn_f}{dt} = -\frac{n_f}{\tau_c} + G(t) \tag{4.11}$$

The Drude-Lorentz model describes the time dependent drift velocity v with a momentum relaxation or scattering time τ_s, the effective mass m^* and the electric field at the position of the carriers E_{mol}:

$$\frac{dv(t)}{dt} = -\frac{v}{\tau_s} + \frac{e}{m^*} E_{mol} \tag{4.12}$$

The electric field at each point can be divided into the externally applied field by the biased metallic contacts (E_{bias}) and the screening field caused by the space charge polarization P_{sc}. The parameter η is a geometrical factor.

$$E_{mol} = E_{bias} - \frac{P_{sc}}{\eta \epsilon} \tag{4.13}$$

Evolving the space charge polarization P_{sc} with a recombination lifetime τ_r yields

$$\frac{dP_{sc}}{dt} = -\frac{P_{sc}}{\tau_r} + j(t) \tag{4.14}$$

By substituting eq. 4.14 in eq. 4.13 and combining the result with eq. 4.12 one gets a differential equation to calculate the aimed dv/dt:

$$\frac{d^2v}{dt^2} + \frac{1}{\tau_s}\frac{dv}{dv} + \frac{\omega_p^2 v}{\eta} = \frac{e\, P_{sc}}{m^*\eta\epsilon\tau_r} \tag{4.15}$$

The parameter $\omega_p^2 = n_f\, e^2/m^*\, \epsilon$, the plasma frequency, was introduced for simplification. The result in eq. 4.15 looks similar to the well known equation of a damped oscillation in mechanics. Therefore, a discussion of the three cases brings the qualitative results of the specific dv/dt:

- $\omega_p \tau_s \ll 1$

- $\omega_p \tau_s = 1$

- $\omega_p \tau_s \gg 1$

The calculated currents for similar experimental conditions are shown in Fig. 4.11. For all three cases, the leading edge of the current is given by the laser pulse and the nearly instantaneous transition of the electrons into the conduction band. In the first case the
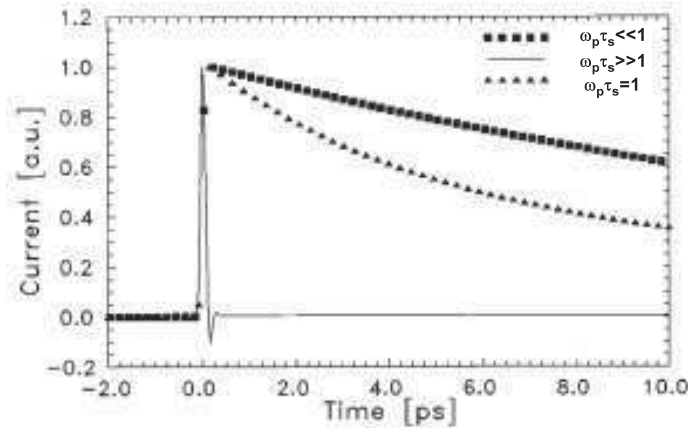
Figure 4.11: Lifetime dependent antenna currents according to [87]

current is dominated by the bias field. Therefore the current decreases linearly in time. This is the behavior for most semiconductors. But for specially designed substrates (e. g. via radiation damage, low-temperature (lt) growing) it is possible to reduce the lifetime and reach the case $\omega_p \tau_s \gg 1$. Here the bias is screened very fast by the molecular field. It is even possible that an electron keeps a higher velocity than expected for the reduced molecular field in the next step. Then the so-called velocity overshoot can be observed which is indicated as a negative current in the plot. This reduces the current on a sub ps timescale leading to an ultrashort current peak with frequency components in the THz range.

Typical photoconductive switches based on (lt-)GaAs are well understood and available in a reliable quality. It is also a component in the fiber-based system (see chapter 7.6), as emitter as well as detector. But they are limited to pump wavelengths below 867 nm to overcome the bandgap. In various publications other InGaAs-substrates are proposed to be operated with the telecom wavelength of 1.55 μm.

The problem of typical InGaAs components is the low dark resistivity of the sample. For an emitter it is important to allow strong biasing without unmodulated currents and large DC offsets. This also brings a big thermal load on the device which limits the performance and life expectancy. A good lt-GaAs antenna with a 5 μm gap has a dark resistivity of some 10 MΩ. InGaAs samples have only resistivities in the kΩ range. Further on, the life time of the charge carriers is typically too long to use the semiconductor also as detector.

These drawbacks of InGaAs can be overcome by different techniques. Various growth techniques, tempering procedures and additional dopants are tested. The most known solutions are heavy-ion irradiation [89], Fe-implantation [90], low-temperature growth [91] and ErAs-nanoparticles [92].

Here results of InGaAs substrates with ErAs nanoparticles (or "nanoislands", called ErAs:InGaAs in the following) are presented. The antenna structures are kindly provided
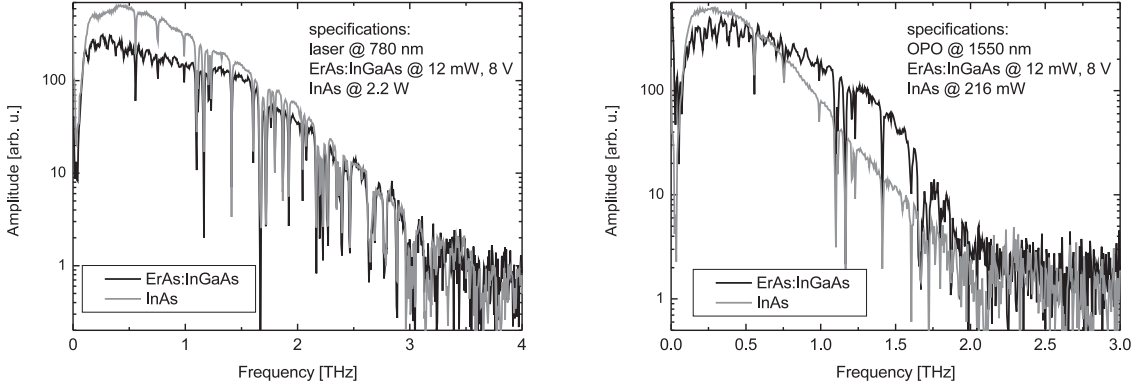
Figure 4.12: InGaAs and InAs emitter pumped at different wavelengths. Left: 780 nm of Ti:sapphire laser, right: 1550 nm of CTA-OPO

by the Max Planck Institute for Solid State Research (Stuttgart, Germany). Their dark resistivity depending on the particular antenna varies between 18 kΩ and 42 kΩ. The charge carrier lifetime is measured to be 220 fs [93] which are basically good premises for THz emitters (and perhaps in the future also for detectors). The performance of dipole antennas based on ErAs:InGaAs is tested with a CTA-OPO system (see chapter 7.2). So the emitter can be driven with a wavelength of 780 nm and closer to the bandgap with for example 1.55 μm wavelength. To compare the output of the biased ErAs:InGaAs chip as reliable reference an InAs surface emitter is chosen. From that emitter it is known that in this operating range the THz output is independent on the pump wavelength. With this source the THz system can be aligned and the appropriate delay also with the CTA-OPO in the emitter arm can be easily found. Figure 4.12 shows the obtained output of the ErAs:InGaAs switch and InAs for the maximum allowed or available parameters, respectively. The left plot is recorded with emitters directly pumped by the Ti:sapphire laser at 780 nm wavelength. For the surface emitter the whole available laser power of 2.2 W are used while the switch was only driven by 12 mW of optical power and biased with 8 V not to damage the device. It can be seen that the cut-off frequency is above 3 THz for both emitters while the surface emitter shows a higher average output. Please note that the surface emitter is pumped by more than 150 times higher optical power and the plot of the InAs emitter is rescaled to the same noise level. The right plot in Fig. 4.12 is recorded with the emitters pumped by the CTA-OPO while the detector wavelength remained the same like in the left plot. So a direct comparison is possible without the influence of the detector. The pump pulses around 1.55 μm have a longer pulse length now (detailed description in [33]). The cut-off frequency is reduced to 2 THz due to the longer pump pulse length. The estimated pulse length of 250 fs corresponds to the detected bandwidth of the surface emitter which is now pumped only with more than 15 times the pump power of the switch. So the overall performance is comparable even with a larger spectral density of the ErAs:InGaAs emitter at 1.5 THz. These studies indicate that also emitters based on InGaAs are in principle suited for broadband THz spectroscopy.
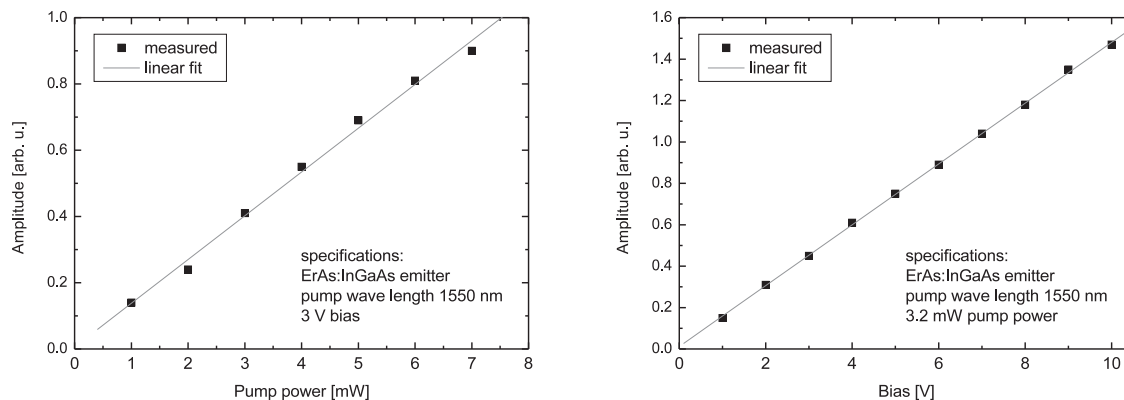
Figure 4.13: THz amplitude of ErAs:InGaAs emitter for different operating parameters. Left: pump power dependency, right: bias dependency

The limiting factor of these series of chips is the expected damage threshold. Due to the still low dark resistivity of the ErAs:InGaAs chip the operating parameters are not as high as for a common GaAs chip. Figure 4.13 shows the behavior for increasing pump power (left) and bias (right) for an ErAs:InGaAs emitter pumped at 1.55 μm wavelength. In this parameter range the emitted peak amplitude is still linear with the pump power and bias. So in principle, if the damage threshold would not be quite low, the output could be considerably increased. Improvements on this topic are in discussion and will further improve the performance. This will offer new possibilities for THz-TDS systems based on telecom wavelengths and the related components.

Photoconductive Surface Emitters

There are also photoconductive THz sources without the need for external biasing. The intrinsic electric field in the semiconductor surface accelerates the charge carriers. These are called surface emitters. Also here the semiconductor is illuminated with light of the appropriate wavelength above the band gap energy. Then the space charge layer of the generated electron hole pairs typically overlaps the intrinsic electric field. This produces a transient photocurrent whose time-variation produces the electromagnetic wave. Since the acceleration time is in the order of magnitude of the optical pulse duration the emission is in the THz range.

Depending on the polarity at the surface Fermi level pinning occurs at the boundary to air. The corresponding band structure in Fig. 4.14 shows the n-type (left) and the p-type distribution (right). This leads to a depletion or enrichment of electrons in the vicinity of the surface, respectively. So a net intrinsic electric field E_d with an orientation perpendicular to the surface is present even without external biasing. Its strength as a function of the position x (depth coordinate) is given by
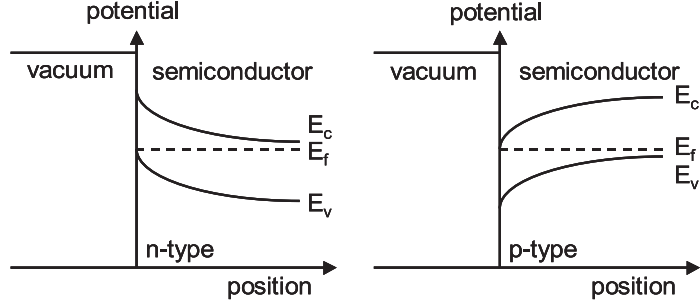
Figure 4.14: Fermi level pinning at the interface between vacuum and semiconductor. Left: n-type, right: p-type semiconductor

$$E_d(x) = \frac{e\,N_d}{\epsilon}\,(d - x) \qquad\qquad (4.16)$$

where $N_d(x)$ stands for the surface defect density and ϵ for the dielectric constant of the used semiconductor. The geometrical extension is

$$d = \sqrt{\frac{2\,\epsilon}{e\,N_d}\left[V - \frac{k\,T}{e}\right]} \qquad\qquad (4.17)$$

while V stands for the height of the Schottky barrier at the surface and $k\,T$ is the thermal energy of the electrons. Typical field strengths for doped semiconductors are some $10\,\frac{kV}{cm}$. The explanation of THz emission is the following: If an electron is pumped into the conduction band and accelerated in the surface depletion field, it forms a dipole with an orientation perpendicular to the substrate's surface.

In literature the influence of the photo-Dember effect [94] is controversially discussed as a significant contribution to the THz emission . This is the phenomenon of different mobilities of the electrons and holes in the substrate. So also effective dipoles are formed when the "clouds" of electrons and holes move with different velocities in the semiconductor. If they are separated this can be regarded as a dipole. Monte-Carlo simulations have shown that for InAs the photo-Dember effect is stronger than the acceleration by surface Fermi level pinning [95].

The emission direction for an extended pump spot can be derived by the interaction of the phase coupled fundamental dipoles. Excitation under an angle will cause the dipoles to oscillate with a different phase to each other with respect to the laser pulse incidence direction. In the far field the envelope of the fundamental waves form a new wave front. According to Huygens' principle the transversal phase which is given by the angled excitation leads to an emission under an angle:
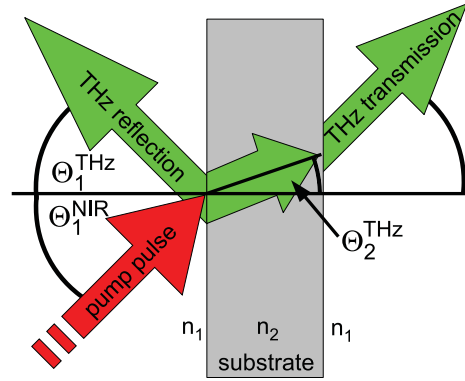
Figure 4.15: Angle nomenclature for basic surface emitter geometries

$$n_1^{\mathrm{NIR}} \sin(\Theta_1^{\mathrm{NIR}}) = n_2^{\mathrm{THz}} \sin(\Theta_2^{\mathrm{THz}}) = n_1^{\mathrm{THz}} \sin(\Theta_1^{\mathrm{THz}}) \tag{4.18}$$

Because the refractive index of air is roughly the same for the THz and the NIR range $(n_1^{\mathrm{NIR}} = n_1^{\mathrm{THz}})$ the angle of the THz emission is the same like for the reflected NIR wave [96]. The THz emission overlaps with the reflected pump spot. This geometry of the THz emitter is called quasi optical reflection (Fig. 4.15):

$$\Theta_1^{\mathrm{NIR}} = \Theta_1^{\mathrm{THz}} \tag{4.19}$$

The part of THz radiation which propagates through the semiconductor is usually not used. Dispersion and losses in the substrate decrease the amplitude remarkably.

The advantage of surface emitters is that they are diffraction limited easy to use THz sources. From eq. 4.19 it is clear that the THz wave co-propagates with the reflected pump beam. This makes the optical pre-alignment of a THz system much easier since IR cards or viewers can be used which are not sensitive in the THz range. Especially for THz imaging systems where a small focus diameter with no astigmatism is crucial the correct alignment of the off-axis parabolic mirrors is easier in this case.

Furthermore there is no need for biasing or collimating optics. The alignment critical pump spot position between electric contacts is replaced by an extended source. Typical pump spot sizes are in the mm range which is directly related to the source diameter of the THz emitter. Here a drift of some microns only slightly changes the amplitude or direction of the generated THz pulse. Especially when beam pointing stability is a problem a surface emitter can compensate for that drift.

When mounted on an heat sink surface emitters can stand a high thermal load. This can be done by attaching the substrate to a metallic holder with heat conducting paste. The higher pump power is necessary since the THz output per mW pump power is less compared to photoconductive switches. But the latter ones already saturate or get dam-

aged by some 10 mW average power. Under this conditions surface emitters are well suited for laboratory setups where a large laser power is available, e. g. delivered by a Ti:sapphire laser. Also for the upcoming high power amplified fs fiber lasers [97] surface emitters are useful devices.

The radiation characteristics in terms of amplitude and divergency are mostly depending on the used semiconductor, pump intensity and spot size. Typical semiconductors are:

semiconductor	InAs	InP	GaAs	GaSb	InSb
carrier concentration [cm^{-1}]	$1.4\,10^{16}$	$1.0\,10^{8}$	$1.0\,10^{6}$	$8.5\,10^{17}$	$1.4\,10^{14}$
THz intensity [%]	100	8.2	4.9	0.8	0.7
bandgap [eV]	0.36	1.27	1.43	0.68	0.17
bandgap [nm]	3444	976	867	1823	7293

Table 4.1: Different semiconductors for THz surface emitters. THz intensities out of [15], bandgap energies in units of eV out of [98]

From Tab. 4.1 it is seen that indium arsenide (InAs) is the strongest THz surface emitter among typical semiconductors. Within the last years there was only a small change of the used semiconductors for surface emission, e. g. indium nitride [99] was proposed for THz generation. But yet no substantial higher output was reported in literature than the one obtained with InAs. Meanwhile the dopant concentration was optimized to enhance the output, so that in the following work only indium arsenide (InAs) was used as substrate, unless otherwise stated. A detailed record of surface emitters and their output power can be found in [100].

The THz output is directly related to the amount of excited oscillating dipoles in the substrate. The more pump power is deposed in the substrate the more free charge carriers can be pumped above the bandgap. So there are some parameters that have to be controlled: Pump intensity and spot size, polarization of the pump radiation (Fresnel reflection) and observation direction.

Typically, the surface emitter is irradiated with all the available pump intensity. Even for average pump powers above 2 W and continuous operation surface emitters do not show degradation or damage. But depending on the applied intensity a saturation of the THz output is observed. For typical pump beam extensions in the range of 1 mm the intensity is lower than the saturation threshold. However, if one needs to come to a tiny pump spot diameter like for THz imaging (see chapter 7.3) the THz output scales sublinearly with the pump power almost until saturation. The left plot in Fig. 4.16 shows the measured THz peak amplitude of an InAs emitter for different pump powers and pump spot diameters. It starts saturating for a spot size of 230 µm and a pump power of 1.2 W which corresponds to an intensity of 2.6 kW/cm^2. So the pump intensity can be varied on a large scale.
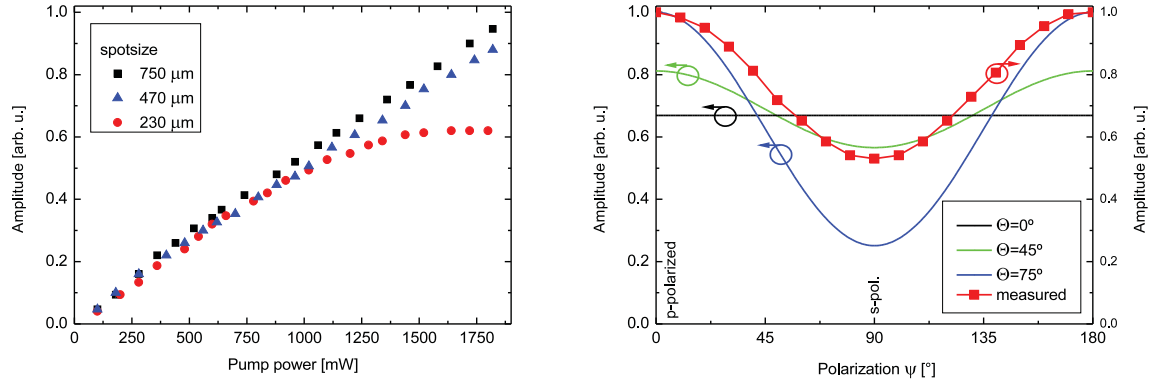
Figure 4.16: Left: linearity of surface emission for different intensities. Right: calculated polarization dependent transmission coefficients (Fresnel) for InAs. As comparison the measured electric field for different polarizations

The higher the pump entry in the substrate, the higher is the THz output. Let us assume that all the pump power that penetrates trough the surface of the semiconductor is responsible for the THz emission, i.e. all power gets absorbed in the vicinity of the substrate. According to Fresnel's laws a fraction of pump power is reflected at the facet. This refractive index step decreases the effectively used pump power [101]. And also the THz radiation is split up into a refracted and a reflected part on the way back at the interface between InAs and air. Fresnel's laws depend on the polarization, the incidence angle and the refractive index step. The right plot in Fig. 4.16 shows the transmission as a function of the polarization angle for different incidence angles. For normal incidence ($\Theta = 0°$) it is obvious that the transmission does not depend on the polarization due to reasons of symmetry. For $75°$, which is the Brewster's angle of InAs (n = 3.71) the overall highest transmission can be reached for p-polarized light ($0°$, $180°$) while for s-polarized light only a small fraction can reach inside the InAs. The typically used geometry of $45°$ shows an intermediate behavior indicating that the polarization has to be controlled and set to p. A measured polarization dependent THz emission shows the polarization dependent tuning curve. The measured amplitude was normalized to the maximum at p-polarization while the Fresnel transmission is kept at absolute values.

The incidence angle dependency is not only caused by Fresnel's law, but also by the dipole emitter characteristics. An oscillating dipole radiates its intensity proportional to $\sin^2(\Theta)$, where Θ is the angle between the oscillation axis and the direction of observation. Because the THz radiation is produced inside of the semiconductor substrate this angle Θ is refracted at the interface to air. So the overall angle dependent THz electric field is

$$E(\Theta_1^{\mathrm{THz}}) \propto \mathrm{T}(\Theta_1^{\mathrm{NIR}})\,\mathrm{T}(\Theta_2^{\mathrm{THz}})\,\sin(\Theta_2^{\mathrm{THz}}) \tag{4.20}$$

$$\propto \frac{tan(\Theta_1^{\mathrm{NIR}} - \Theta_2^{\mathrm{NIR}})}{tan(\Theta_1^{\mathrm{NIR}} + \Theta_2^{\mathrm{NIR}})}\frac{tan(\Theta_2^{\mathrm{THz}} - \Theta_1^{\mathrm{THz}})}{tan(\Theta_2^{\mathrm{THz}} + \Theta_1^{\mathrm{THz}})}\,\sin(\Theta_2^{\mathrm{THz}}) \tag{4.21}$$
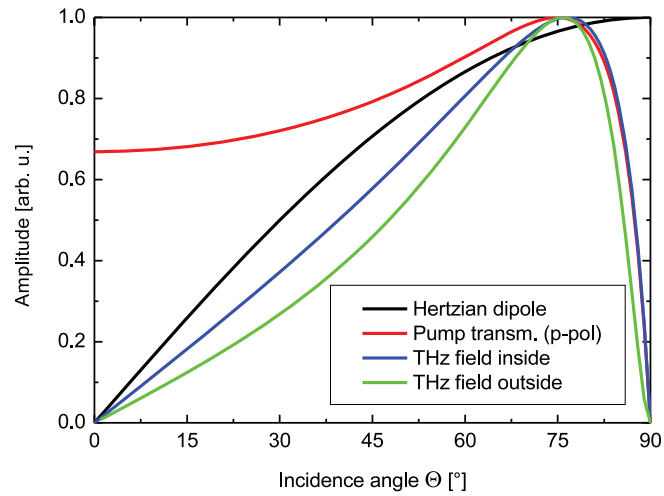
Figure 4.17: Influence of incidence angle for surface emitters: Fresnel conditions and
            dipole emission

To increase the output for a given pump power an applied magnetic field can enhance the
THz output [102]. Since for the observed excited dipoles the main lobe of the emission
is in-plane only the projection of the electric field towards the observation direction is
accessible. A permanent magnetic field can turn the direction of the dipoles' oscillation
in the way that the projection of the electric field shows a higher contribution in the
adequate direction.

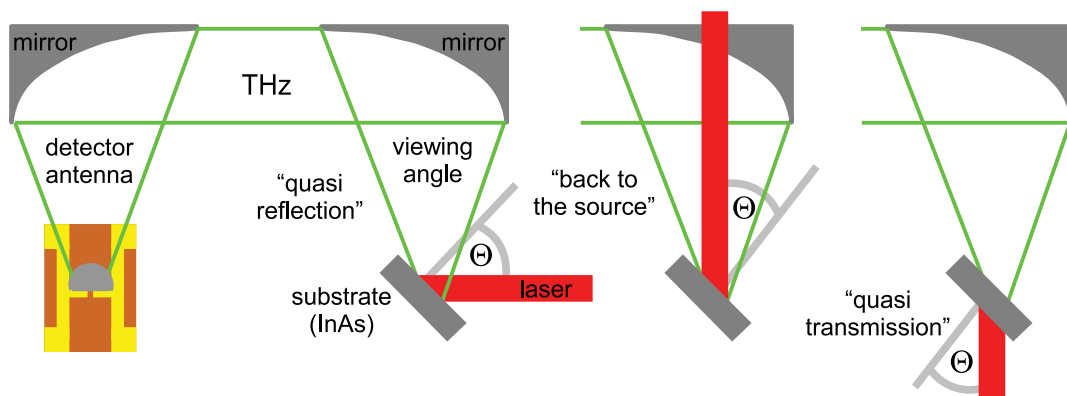## Spot Size and Diffraction

Figure 4.18: Experimental setup of a surface emitter in quasi-reflection, "back to the
            source" and quasi-transmission geometry

The following measurements and simulations are carried out under different questions

and constraints: The first question arises from the need to determine the angle dependent emission characteristics of non-transparent THz surface emitters. The typical geometry which is used by Zhang or Li [96, 103] excites the charge carriers on one side and detects the THz transmission. If the semiconductor is doped this geometry is not applicable. All other geometries working in quasi-reflection require a realignment of the detector and are difficult to be reproduced. Perhaps with fiber based THz emitters the error can be reduced.

The other question is related to imaging applications and the divergency of the emitter. Experimental experiences have shown that it is advantageous to reduce the spot size on the surface emitter to enhance the output at high frequencies by the expense of a reduced average output.

Further on, there is a fundamental question arising from the more than one optical decade extending spectral range within the THz pulse: What happens if the pump spot is larger than the wavelength for the high frequency part of the generated THz spectrum while it is smaller for the low frequency contributions. And if the fundamental dipoles radiate symmetrically with respect to the semiconductor's surface, what fraction of the THz power goes back to the direction of the exciting laser? Also for the materials sciences is there a possibility to determine the orientation of the dipoles within the semiconductor's surface additionally to the field strength?

The setup which is used to answer these questions is drawn in Fig. 4.18. It consists of a standard surface emitter, initially working in quasi optical reflection of $\Theta = 45°$ like indicated in the sketch. If now the emitter is turned in the plane around the incidence point of the laser point on the substrate, the THz emission cone will move out of the viewing angle of $\pm 15°$ of the parabolic mirror. This scheme is called quasi reflection or emission in forward direction.

The other geometry uses a small drilled hole in the mirror to bring the laser pulses to the emitter. So a detection in a direction "back to the laser source" can be realized. This allows to keep the conditions constant just by rotating the semiconductor.

The results of the experiment are shown in the left plot in Fig. 4.19. Simulated electric fields are given for direct comparison and additional verification (right). This calculated values are obtained by a simulation using CST MICROWAVE STUDIO®. This work on numerical solutions of Maxwell's equations is carried out with the kind support of C. Imhof and Prof. R. Zengerle of the Department of Electrical and Computer Engineering at the University of Kaiserslautern [104, 105].

Measurements are carried out just by rotating the substrate around the angle Θ. In the simulation elementary dipoles are used to implement the accelerated electrons at the substrate's surface. It is found out that a number of 20 infinitesimal currents provide a sufficient accuracy for an appropriate model, also as a function of computational time. Concerning the simulations, the angled incidence is implemented by applying a transversal phase difference for the excitation of the dipoles. An integration over $\pm 15°$ is carried out to adapt the results to the viewing angle of the experimental system. The simulated results in Fig. 4.19 and Fig. 4.20 show a good agrement for the maximum and minimum direction of the intensity, respectively. The qualitative discussion depends on the assumed
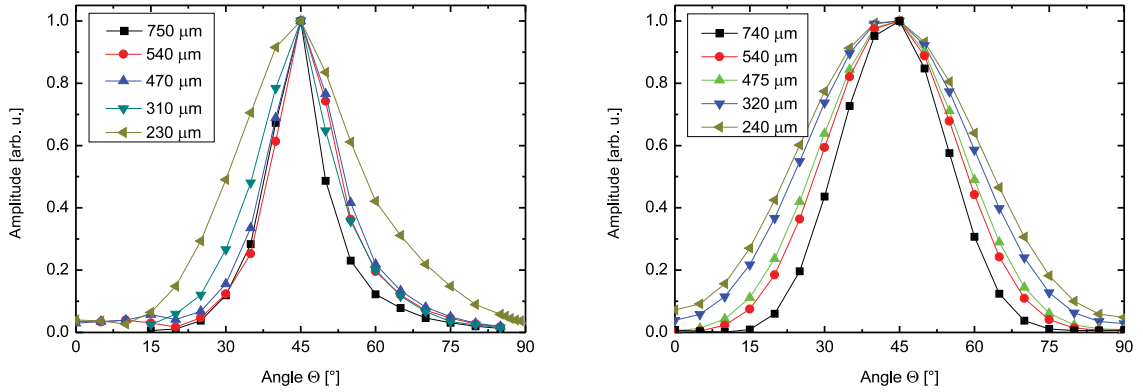
Figure 4.19: Angle of 90° between laser and THz beam (quasi reflection). The amplitude of the electric field as a function of crystal rotation for different pump spot diameters. Left: measurement, right: simulation at 500 GHz

frequency of the broadband THz pulse (here 500 GHz).

By applying a Hertzian dipole model along with Huygens' principle of fundamental waves the phase fronts and therefore the behavior of the emitter can be explained. In the standard 90° geometry the THz emission follows Fresnel's law of reflection. The far field envelope of the THz phase front overlaps with the reflected near-infrared pump beam. For smaller pump spot sizes the THz radiation is refracted to wider angles. So the opening angle is increased. This result is consistent with expectations from previous reports [96, 106]. Saturation effects play a minor role for the used pump beam intensities. Only for a beam diameter of 220 µm the THz electric field was slightly sub proportional to the pump power (see Fig. 4.16).
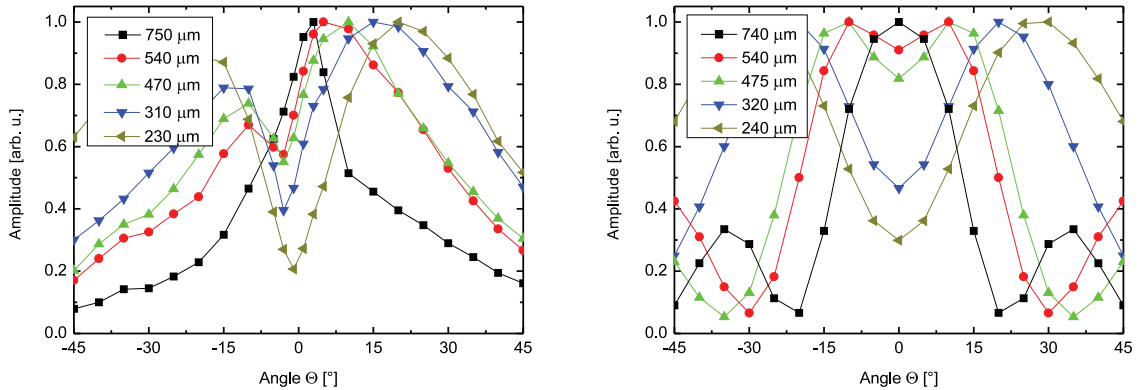

Figure 4.20: Angle of 0° between laser and THz beam "back to the source". The amplitude of the electric field as a function of crystal rotation for different pump spot diameters. Left: measurement, right: simulation at 500 GHz

In the case of "back to the source" geometry a strong dependence of the radiation

characteristics on the pump spot diameter is observed. As can be seen from Fig. 4.20, a widespread pump beam results in a maximum of the generated THz radiation following the quasi-optical reflection (here $\beta = 0°$), whereas the focussed beams exhibit a barbell shaped emission with a minimum in the optical reflection direction. Two maxima (here between $\beta = 5°$ and $\beta = 25°$) are situated nearly symmetrically to the axis of back reflection. The diffraction angle increases for decreasing laser beam diameter.

Classical dipole theory says that a dipole does not irradiate in the direction of the oscillation of its charge carriers. So in the $0°$ geometry an emission normal to the surface is in principal unexpected. However, in this geometry the direction of the constructive interference of the individual oscillators is perpendicular to the boundary. Having in mind that the detection system has a limited angular resolution, smoothing blurs the detailed behavior. But it is still obvious that for smaller spot sizes the similarity to the radiation pattern of one single dipole is larger than the restrictions of the phase fronts. So here the transition between one single Hertzian dipole and the ensemble of phase locked coupled oscillators can be clearly observed. While the single dipole radiates symmetrically to its axis with a minimum in the direction of acceleration the sum of all dipoles shows an emission characteristic in this particular direction. This is in contrast to the typically given expression of the emitted THz intensity of a surface emitter $I_{THz} \sim \sin^2(\Theta)$ with Θ the angle between dipole oscillation and observation direction [96]. For a real surface emitter, this means that it is always an interplay between these two conditions.

The simulation in Fig. 4.20 shows the transition from a single dipole behavior to the ensemble of phase locked oscillators for a frequency of 500 GHz. With increasing spot diameter the two angular maxima move closer to zero until they combine into a single pronounced maximum at $\beta = 0°$. An evaluation for other wavelengths shows a comparable behavior but with less diffraction for higher frequencies. In comparison to the measured values, where the intensity is more emphasized for positive angles, the simulation gives nearly symmetrical results. This is caused by the off-axis shape of the mirrors, the alignment accuracy and the scattering of the pump radiation in the experiment.

InAs emitter pumped at wavelengths up to 2 µm

The developments towards new THz sources for the pump wavelength around 1.5 µm need reliable and calibrated emitters. Therefore the possibilities of a standard InAs emitter are checked with the CTA-OPO as a tunable fs pump source. The obtained results are shown in Fig. 4.21. The overall bandwidth even in the best case is reduced to 3 THz. This is due to the longer pump pulse length in the emitter arm. It is obvious that there is a considerable broadband THz emission up to a pump wavelength of 2 µm. The amplitude reduction is not related to the emitter [107] (the bandgap of InAs is 3.4 µm). This is related to the detector. To be more precise it is the efficiency when the pump wavelength is tuned above the bandgap of the GaAs detector (867 nm) which is the case for an OPO wavelength above 1912 nm. Since the OPO is tuned by the pump wavelength, the Ti:sapphire laser's wavelength has to be changed to reach an idler output close to 2 µm. For the OPO's tuning characteristics see chapter 7.2. The performance of the GaAs
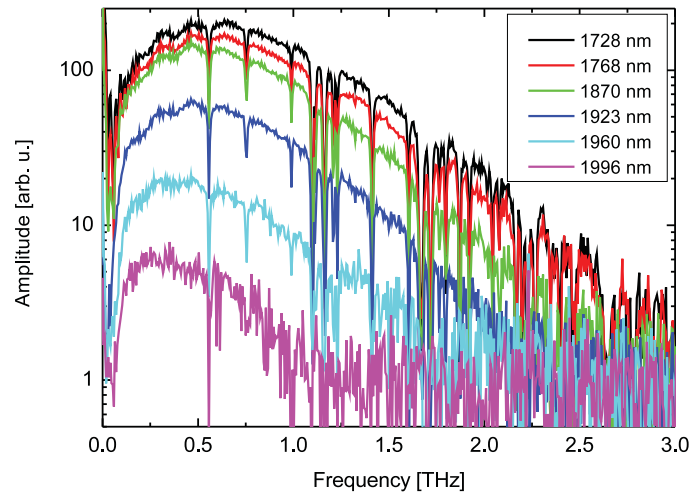
Figure 4.21: InAs surface emitter pumped at wavelengths up to $2\,\mu m$

detector close to the bandgap can be found in chapter 5.2.

Black Silicon

So far silicon has only rarely been used as a material for THz emitters. Because of its small absorption coefficient and low dispersion [108] together with a high refractive index in the THz range ($n_{\mathrm{Si}}^{\mathrm{THz}} = 3.4$) high resistivity silicon is often used as a beam splitter for THz radiation or as a high-refractive lens material attached to a photoconductive switch. THz optics made out of silicon absorb the copropagating infrared radiation sufficiently.
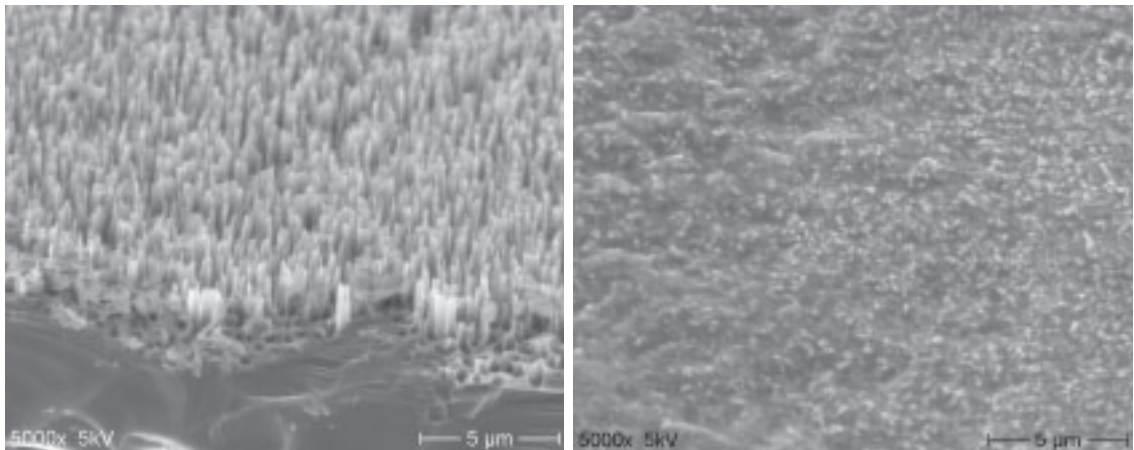

Figure 4.22: Black silicon sample imaged with a scanning electron microscope. Left: black silicon, right: damaged sample

In this chapter black silicon (BS) as an emitter of THz radiation is discussed. BS

has the advantage of an extremely high absorption throughout the visible and infrared spectral region. Due to the black structure, the large penetration depth of silicon being an indirect semiconductor is effectively reduced to a sub-micron range under the surface, independent on the "path" of the absorbed photons (see Fig. 4.22 and Fig. 4.23 left). Multiple reflections lead to an absorption in nanoscopic pillars. The needles are interconnected only via the bulk material at their back end. Therefore BS shows an anisotropy towards the surface (structural asymmetry) which can be used as a polarization effect to generate THz radiation [109].
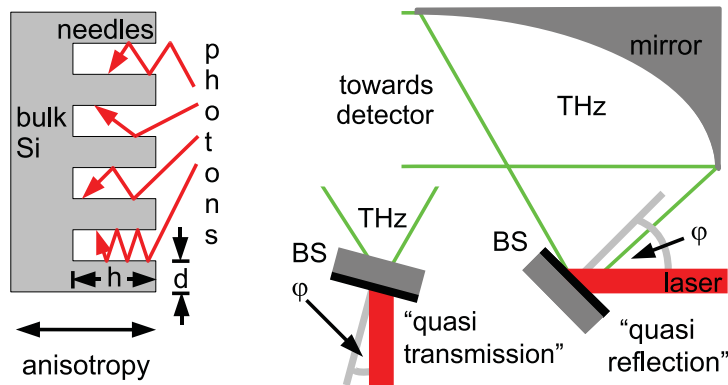

Figure 4.23: Left: possible paths of photons in the needles of black silicon (BS) emitter. Right: experimental setup in quasi transmission and quasi reflection geometry

Indirect semiconductors are not widely used as THz emitters because they only show very weak THz emission compared to other available sources. According to Zhang and Auston [96] this fact is caused by the large absorption length of photons in the surface. As a consequence, the region of the generated free carriers and the acceleration by the surface field do not overlap sufficiently. In order to use an indirect semiconductor like silicon as a THz emitter together with optical excitation it is important to reduce the penetration depth considerably. In the case of BS this is accomplished by multiple reflections within the surface structure (Fig. 4.23 left).

The used BS is a $\langle 1\,0\,0 \rangle$ oriented unintentionally phosphor doped silicon wafer with a conductivity of $2-10\,\Omega\,cm$. The thickness of the sample is $525\,\mu m$. The BS wafer is kindly provided by T. Käsebier from the Institute of Applied Physics at the Friedrich Schiller University of Jena. It was prepared on the cleaned wafers in an inductively coupled plasma via reactive ion etching (SI-500-C, Sentech Instruments, Berlin) for $10\,min$ using sulfur hexafluoride and oxygen [110]. The surfaces are characterized by scanning electron microscopy (SEM) under $45°$ observation (Fig. 4.22 left). The measured dimensions of the needles are $d = 300\,nm$ in diameter and $h = 2\,\mu m$ in height, varying statistically. The tiny needles are very fragile as can be seen on the damaged sample in Fig. 4.22 right. The SEM pictures are kindly prepared by J. Kehrbusch and Prof. Dr. E. Oesterschulze at the University of Kaiserslautern.

The basic experimental setup is shown in Fig. 4.23. The emitters under investigation are measured in a quasi optical reflection geometry, corresponding to $90°$ between pump laser and direction of detection. In addition the emitters were also measured in a quasi transmission geometry (Fig. 4.25 left) to detect the oscillation axis of the THz emitter in a reproducible grazing incidence configuration. Here $\Theta = 0°$ corresponds to incidence normal to the BS wafer, while $\Theta = 90°$ is a grazing incidence configuration. To prevent thermal influences on the measured signals or even damage of the samples the emitters are mounted on a heat sink. The laser beam is not focused and has a diameter of $750\,\mu m$.
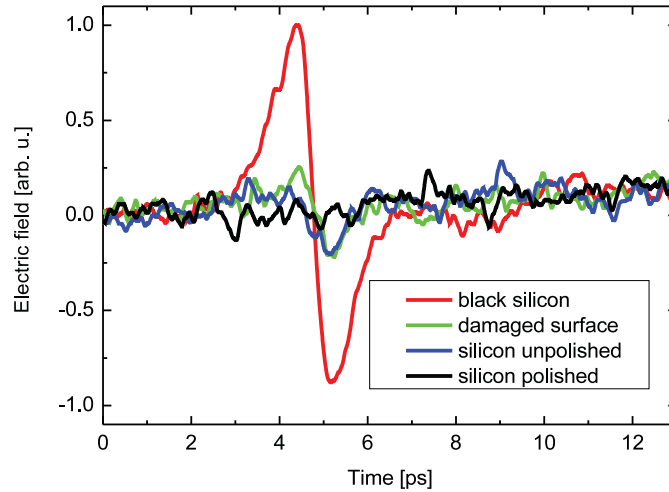

Figure 4.24: Emitted THz electric fields for different surface qualities: black, damaged, unpolished (sawed), polished

When irradiated with ultrashort pulses from the Ti:sapphire laser THz emission is observed from the BS emitter. To make sure that the THz generation is really caused by the surface properties of the silicon sample, the black surface was mechanically damaged. Thereby the structure of the tiny needles was destroyed and the anisotropy towards the surface is removed. A considerable reduction of THz amplitude is measured (Fig. 4.24). The emission from the damaged surface of the BS is comparable to THz emission from a regular unpolished silicon wafer without any surface treatment. The black surface obviously gives rise to an additional polarization in the THz range. Low residual emission is observed also from the sawed unprocessed surface. On the other hand, a polished silicon wafer did not show any detectable THz emission.

In order to determine the direction of the oscillating dipoles a measurement in quasi transmission [103] was performed (Fig. 4.25 left). In this case the black surface faces the laser while the THz optics images the backside of the BS emitter onto the detector. The maximum of the THz emission is observed under grazing incidence (around $\Theta = \pm 70°$) whereas no emission is detected for a perpendicular illumination ($\Theta = 0°$).

The THz emission in silicon under optical excitation is strongly influenced by the surface structure. The orientation axis of the oscillating Hertzian dipole is not perpendicular to
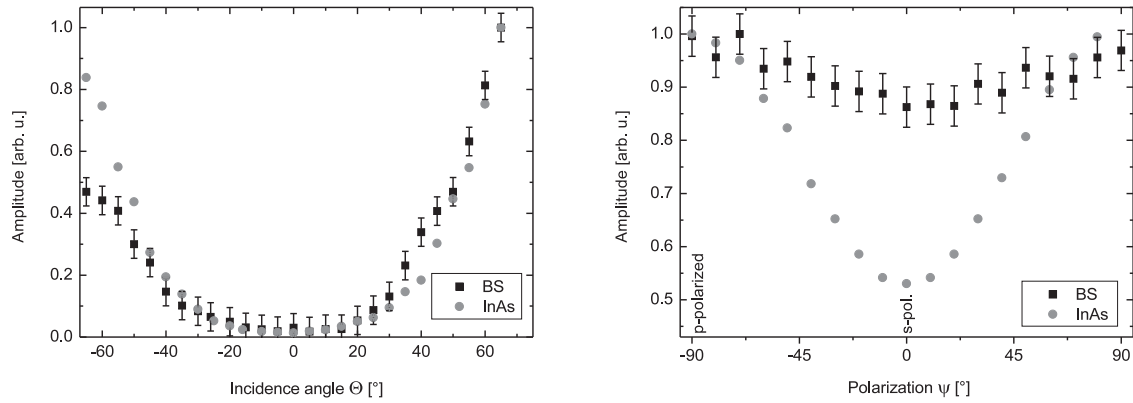
Figure 4.25: Left: angle dependent THz emission from BS and InAs in quasi transmission geometry. Right: THz output for different pump polarizations, both normalized

the surface of the individual needles (in-plain) but normal to the BS wafer.

The right graph in Fig. 4.25 shows the dependence of THz emission from a BS emitter on the incoming beam polarization. The behavior of InAs is added for comparison. Both plots are normalized to 1, despite the approx. 50 times higher output of the InAs emitter. Taking into account the error bars for the measurement the output of BS is almost independent of the pump beam polarization. The controlling wave plate is located as close as possible to the emitter. But slight changes in amplitude may also be caused by a polarization dependent reflection of other optical components.
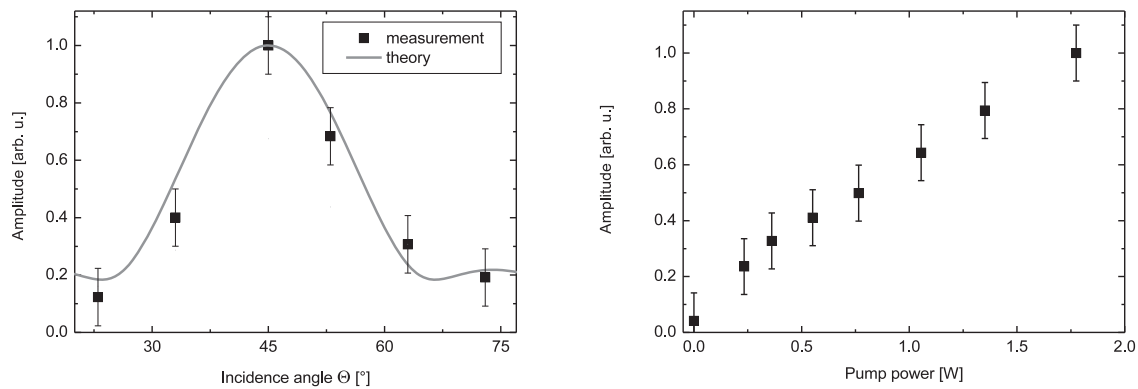
Figure 4.26: Left: THz output of BS for different angles Θ in quasi reflection. Right: Pump power dependence of THz emission in BS

In order to determine the angular emission characteristics of the BS surface emitter the electric field of the generated THz radiation is measured in quasi reflection geometry as a function of rotation angle Θ. A clear maximum around $\Theta = 45°$ is observed which corresponds to the specular reflection of the pump beam comparable to unstructured

surface emitters (see chapter 4.2). The theoretical curve shows the emission characteristics of a diffraction limited THz source calculated with a pump beam diameter of 1060 µm and a THz wavelength of 600 µm. In this plot the integration over a solid angle of $\pm 15°$, the viewing angle of the mirror, is also included.

The emission characteristic in terms of dependence on the pump laser power and emission direction is comparable to the emission of InAs [101, 102]. But for BS the THz amplitude is roughly not sensitive to the polarization of the pump radiation. For InAs this is important because the Fresnel reflection at the surface is polarization dependent. This reduces the effectively absorbed laser power. In the case of BS all the pump power is absorbed independent of the polarization.

The left graph in Fig. 4.26 shows that the emission cone follows the restrictions of Huygens' law since the emission is observed only in the direction of the reflected incident light (quasi optical reflection). The refractive index of air is nearly the same for the NIR and THz range ($n_{\mathrm{air}}^{\mathrm{THz}} \approx n_{\mathrm{air}}^{\mathrm{NIR}}$). So the phase fronts of the fundamental dipoles interfere constructively in the same direction like for the NIR waves. The sub-wavelength structure of the needles has no influence on the THz beam properties like divergency and beam diameter.

As the THz pulse length was in the range of 1 ps no broadband THz spectrum was observed. In semiconductors the penetration depth of NIR photons and the carrier lifetime are strongly dependent on the dopant concentration. An optimization of this parameter will increase the THz output and spectral width of the BS emitter.

Also for other direct semiconductor emitters surface treatment can bring useful advantages: The absorbed laser power is increased which scales linearly with the THz electric field. Also there will be no need for a beam dump like a Teflon disc to absorb the reflected part of the laser power which otherwise could damage other optical components or would increase the noise of the TDS system. As a consequence this reason for additional losses (typically 20 %) in the THz beam path can be removed.

The results demonstrate that in BS the space charge layer and the penetration depth can be designed to be within the same range. Photo-induced carrier separation in the region of the space charge layer is usually faster and less dependent on material defects, so lower grade material might be used if nano-structured surfaces similar to BS are applied. Furthermore, the orientation of the dipole perpendicular to the surface induces an electron movement in the same direction. This effect could be used for solar cell devices by using economic low grade p-doped black silicon in an heterojunction device with e. g. a transparent semiconducting window material [111, 112].

4.3 Comparison of Emitter Output Power

The here discussed emitters have their inherent advantages and limitations. To quantify the efficiency a comparative study is carried out with the three most common emitters: A surface emitter (InAs), LN in the Cherenkov geometry and a 100 µm photoconductive switch (strip line GaAs).
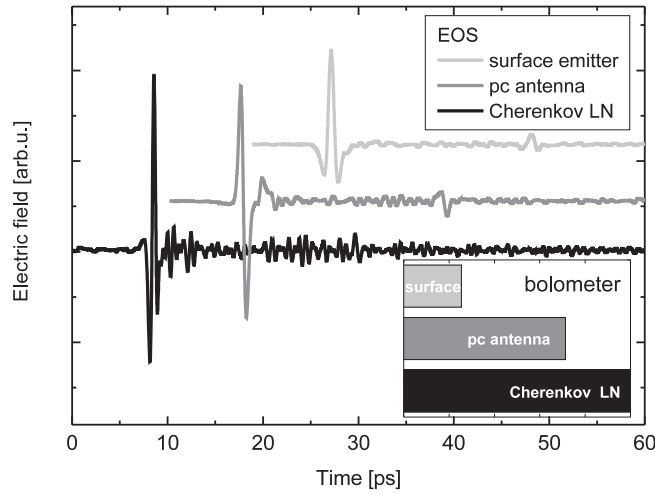
Figure 4.27: Electric fields generated by a surface emitter (InAs), photoconductive antenna and LN in the Cherenkov geometry. Inset: intensity of a bolometric measurement of the same emitters

The electric fields obtained for the maximum available laser power (1.3 W) of the surface and LN emitter are plotted in Fig. 4.27. The photoconductive antenna was driven by 20 mW and biased with 50 V which are the maximum allowed values below the damage threshold. All electric fields were detected with the same EOS setup. Therefore the arbitrary units of the detected electric fields are equal for each measurement within the realignment uncertainties.

It can be seen that the peak output of the LN emitter in the Cherenkov scheme is the strongest, followed by the photoconductive switch and the surface emitter [113]. This is valid for the chosen optimal parameters. If only a weak laser is available, the switch would be much superior to both other emitters. The output electric field here scales linearly with the pump power. So there is some "break-even point" where the switch shows a better performance if the laser power is reduced. For further possibilities to increase the output of LN emitters see chapter 6.

The emitters show a bandwidth up to 4 THz. No fundamental difference in the broadband character is seen. Only slight changes in the center frequency are observed. The statement above on the achieved output is verified by a bolometer measurement (inset in Fig. 4.27). The bolometric detected intensities correspond to the square of the peak electric fields in the EOS measurement.

5 THz Detectors

The lack of sensitive THz detectors made this spectral range to be known as "the THz gap". Within the last decade a lot of efforts in this field brought up new useful devices. The basic ideas here are known and based on e.g. thermal effects or nonlinear interaction. Recent developments are less based on new schemes but more on new semiconductor structures. So here just a short overview of the used detectors is given.

5.1 Incoherent Detectors

Among the incoherent detectors, the THz power meters, there are different devices depending of the THz average power to be detected.

Bolometers are widespread THz power meters. They are very sensitive at weak THz powers but unfortunately they need to be cooled down to cryogenic temperatures (liquid nitrogen and helium) to achieve the operating temperature which is below 4 K. Only then the sensitivity of the detector is given. It requires a heat sink to detect very small portions of thermal changes as it is caused by absorbed radiation. The principle is based on thermally induced resistivity change of an absorber which is detected as a voltage. So the THz intensity can be measured.

The detector itself can also detect IR and MMW radiation. So special vacuum windows and far infrared filters are used to block the neighboring frequency bands except for the THz waves. The optics simultaneously collect the THz radiation out of a bigger solid angle and guide the THz radiation together with a metallized horn, the so called Winston cone [114], towards the detector's chamber. Coming from astronomy, bolometers are typically used to detect incoherent radiation. So it is more likely to be applied in strong ns pumped systems rather than in fs pumped systems.

At weak THz powers a Golay cell is another possible detector. Coming from IR spectroscopy it relies on the gas expansion caused by heat exposition. So when THz radiation is absorbed in a gas chamber the expansion causes a membrane to move. This can be detected optically with a very high accuracy. Golay cells have only a few manufacturers so the accessibility is limited and the price is high. Also the environmental influences on the signal are quite strong, so for an industrial application it is not the device of choice. But under laboratory conditions it is used to compare the absolute output power of different emitters.

Recently, the performance of pyroelectric detectors was considerably improved. Most pyrodetectors are based on lithium tantalate. Here a change in temperature gives rise to a spontaneous polarization which can be detected at the surface of the crystal. The SNR

of a Golay cell is still better, but a pyrodetector has a faster response time and is more rigid.

The coherent detection offers a lot of advantages compared to the incoherent methods, especially the determination of the phase. Along the coherent sensors two major techniques are widespread: The detection in a photoconductive antenna or by electro-optical sampling. Each technique has its advantages and limitations. Depending on the application and availability of the particular detector, both techniques can address a broadband THz pulse with a good signal to noise ratio. For a direct comparison between these two, also under experimental constraints, see e. g. [115, 116].

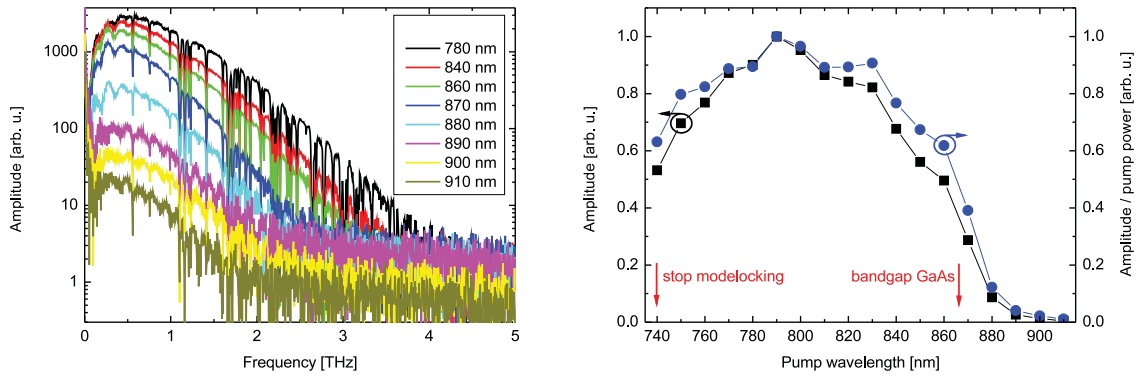## 5.2 Photoconductive Switches - Detectors

Figure 5.1: GaAs detector for different pump wavelengths. The performance is reduced at short wavelengths due to laser instability and for longer wavelength due to the bandgap of GaAs at 867 nm.

Under some conditions the same photoconductive switch which was used as an emitter in chapter 4.2 can be used also as a detector. The main difference for a detector is the need for a short carrier lifetime (scattering time τ_s, trapping time τ_c). For GaAs this is realized in the production process by introducing defects in a thin layer on the top of the substrate. Then the same antenna layout (see Fig. 4.10) is adequate for a sensitive detector. The critical parameter is related to this thin layer which defines the performance of the detector. For 800 nm pump wavelength the design of such lifetimes is very elaborated using a low-temperature grown (lt-)GaAs layer on a GaAs wafer. For other pump wavelengths, especially the telecommunication wavelength around 1.5 µm, still a lot of research is necessary to have a semiconductor with an appropriate bandgap and performance also for detection. Different approaches based on indium gallium arsenide are reported. They differ in the way the lifetime reduction is reached: Either by low-temperature growth [91], Fe implantation [117], ion-irradiation or erbium arsenide (ErAs) nano islands [93, 118]. But still the overall performance is inferior to lt-GaAs. Further development will bring big advantages for the industrial application of THz-TDS because

then cheap fiber based solutions will be available. So still this topic is of interest for various fields also in fundamental questions. In the here presented systems lt-GaAs is used.

The best working point of a Ti:sapphire laser which is in the middle of his gain maximum at 780 nm as well as the wavelength of a frequency doubled fiber laser (around 800 nm) are both well suited to gate a GaAs switch. Its performance is quite constant for pump wavelengths which have photon energies above the bandgap of the GaAs substrate (867 nm). Starting at 860 nm pump wavelength the detected amplitude and bandwidth is reduced (Fig. 5.1 left plot). In this experiment the pump power on the detector was kept constant. But the average power of the pump laser on the InAs emitter changed due to the tuning curve of the laser. To compensate for that slight change, the THz amplitude was divided by the pump power to achieve a pump power independent comparison of the detected amplitude (Fig. 5.1 right plot). The THz amplitude scales linearly with the pump power so this fact is not the reason for the reduced performance. The pulse duration did not show a considerable change within this spectral range. Rather the coating of the polarization optics is expected to contribute to the reduced performance for shorter wavelength. Weak back reflections cause the laser to show instabilities which are not present for a free-running laser. So at this end of the wavelength range of the laser, the stopped modelocking limits the tuning. This has to be considered when the pump wavelength has to be changed in the experiment like for the CTA-OPO system.

5.3 Electro-Optical Sampling (EOS)

Typical antenna detectors show a major drawback: a spectrally dependent response for different THz frequencies. A dipole antenna for example has an optimal frequency response for twice the dipole length, strongly decaying for higher frequencies. A detector with a flat very broadband frequency response would offer big advantages. Furthermore, a 1D or 2D detector array based on an antenna geometry is difficult to fabricate. The detectors would become very expensive due to the high amount of consumed wafer and difficulties in production process. Also a single beam for each pixel would be necessary to illuminate only the gap. Recently, a scheme solving the problem by micro optics was proposed [119]. But still, an easy to set up large detector would be superior to standard Auston detectors.

Electro-optical sampling (EOS) is a THz detection scheme based on the linear electro-optic effect (Pockels' effect) [120]. A slowly varying electric field (THz pulse) changes the refractive index ellipsoid in the sensor crystal causing birefringence [121]. This can be probed by a second ultrashort pulse in the visible or NIR. With respect to the polarization plane the latter changes its polarization which is proportional to the THz electric field. So a cross-correlation between the THz and optical pulse can be measured [122].

Depending on the probe wavelength and detection bandwidth different sensor crystals are used. For the Ti:sapphire pumped systems around 800 nm wavelength zinc tellurite (ZnTe) crystals show the best performance while for longer wavelengths gallium phosphide
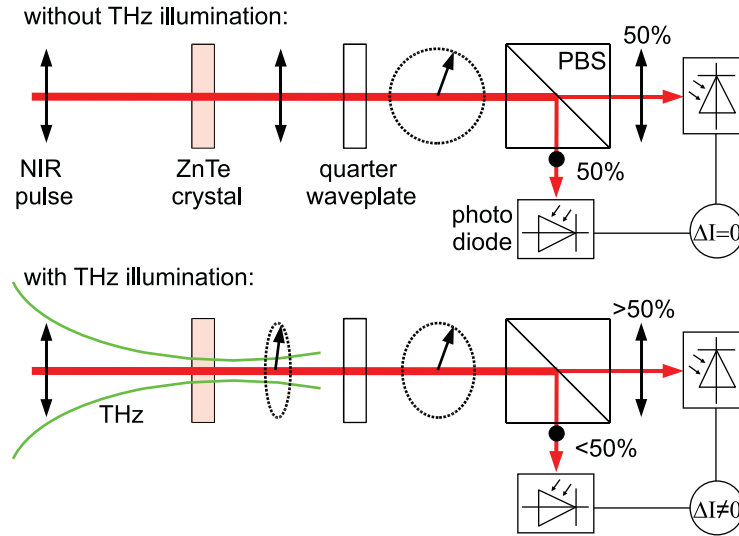
Figure 5.2: Balanced EOS setup with and without THz illumination

(GaP) shows a better signal. Reaching up to the mid infrared, also gallium selenite is reported [123]. The performance strongly depends on the velocity matching between the THz and probe pulse. If these two get out of phase the signal for this frequency will be averaged out in the crystal. This fact, the dispersion, and the pump pulse length limit the detection bandwidth. With such sensors ultrabroadband THz radiation detection has been demonstrated [124].

The main idea behind EOS is to transfer the information from the THz range to the visible or infrared, where sensitive and cheap detectors are available. The Pockels' effect maps the THz electric field to a phase retardation of the NIR beam. A quarter wave plate adds a further phase shift of $\pi/2$ so that a polarizing beam splitter (PBS) separates two polarizations with nearly the same intensity. The detected signal is the difference in the intensity between these two arms. A differential detector consisting of two cheap and slow photodiodes measures the different intensities of the two polarization components. So fast THz transients can be sampled. This allows the application of EOS in a setup where the one pixel detector (2 photodiodes) is replaced by a line or array detector. So THz cameras can be build up if enough laser power is available [125]. Recently, the combination of THz-TDS together with THz triangulation was reported [126]. This allows for the realtime imaging including the depth information without the need to know the refractive index of the sample.

To understand the exact polarization behavior assume a case where no THz field is present. A linearly polarized NIR pulse will propagate through the ZnTe remaining linearly polarized. The quarter wave plate produces circularly polarized light. The PBS separates both polarizations equally so that difference in intensity at both photodiodes is zero. If now a THz pulse co-propagates at the same time with the NIR pulse the latter one will show an elliptical polarization. Dependent on the handedness of the NIR pulse

the intensity will be increased in one particular arm, detecting the THz electric field.
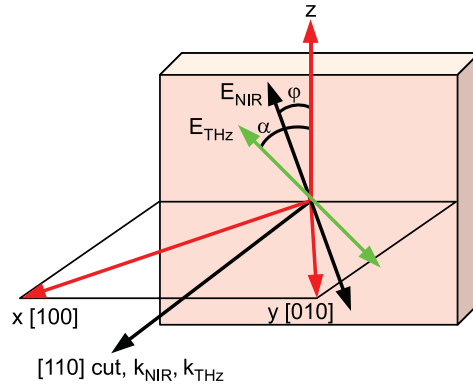

Figure 5.3: Orientation of the crystal axis and polarizations in an EOS scheme

Figure 5.3 shows the the orientation of the crystal's axis and the possible polarizations: The used crystal is a [110]-cut ZnTe. The THz and the NIR pulse draw an angle of α and φ to the [001]-axis within the crystal's plane, respectively. Following the results of Planken et al. [127] the change in intensity at the balanced photodiodes is given by:

$$\Delta I(\alpha, \varphi) = I_0 \frac{\omega_{NIR}\, n^3 E_{\text{THz}}\, r_{41} L}{2c} (\cos \alpha\, \sin 2\varphi + 2 \sin \alpha\, \cos 2\varphi) \tag{5.1}$$

where α and φ are the polarization orientations, L is the crystal length, I_0 is the probe intensity and ω_{NIR} is the angular frequency of the probe pulse. The best signal can be obtained for a parallel or orthogonal polarization between the THz and NIR pulse ($\alpha = \varphi$ and $\alpha = \varphi + 90°$). The in-plain [001]-crystal axis is unfortunately not indicated for most commercial crystals. Therefore a rotation around the [110]-axis is carried out to obtain the maximum THz peak signal.
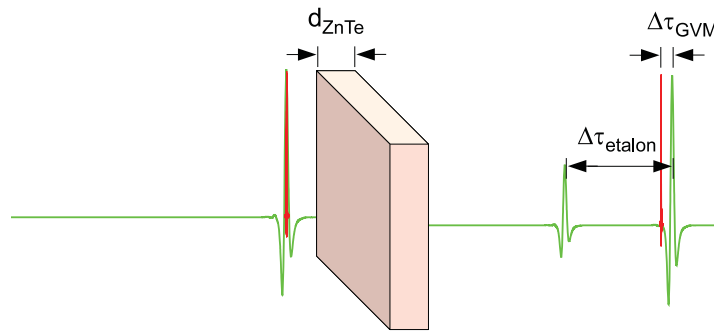

Figure 5.4: Influence of ZnTe sensor crystal in EOS: GVM and echo pulses

In principle the signal should be proportional to the crystal length L. To understand the limitations Fig. 5.4 shows the two main difficulties that play the major role for the crystal

choice: The group velocity mismatch (GVM) and the echo pulses. The echoes arise due to etalon effects caused by internal reflection [124, 128] mostly of the THz wave, fractionally also of the NIR pulse. The temporal separation $\Delta\tau$ of the first echo relative to the main pulse is $\Delta\tau = 2n_{\mathrm{group}}^{\mathrm{THz}} d_{\mathrm{ZnTe}}/c$. For typical detector crystals of thickness $d_{\mathrm{ZnTe}} = 1\,\mathrm{mm}$ the corresponding echo will appear for $\Delta\tau \approx 20\,\mathrm{ps}$. This limits the accessible spectral resolution very much. But the etalon effects can be easily removed by adding a thick inactive [100]-cut crystal behind the sensor crystal. Because the linear properties of both crystals are the same no interface is observed. The cut along the inactive axis prevents the influence of additional birefringence. So if a high spectroscopic resolution is needed a $2\,\mathrm{mm}$ thick [100] ZnTe ("dummy") is attached to the sensor crystal (see Fig. 5.5). Another possibility would be to use a wedged ZnTe crystal or an anti-reflection coated surface.
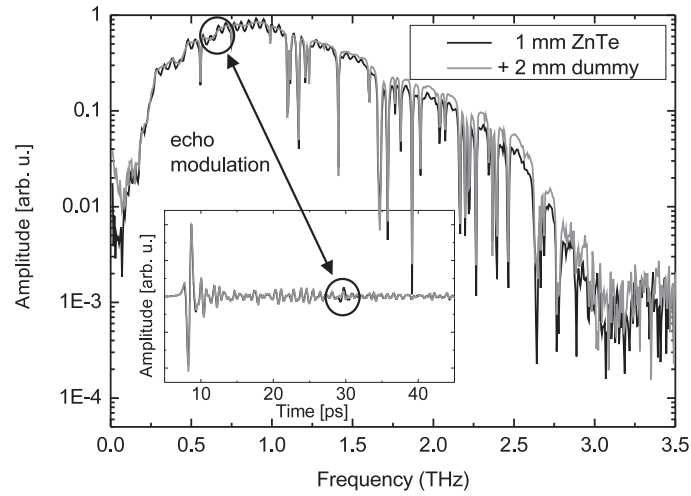

Figure 5.5: The echo in ZnTe (here $20\,\mathrm{ps}$ behind the main pulse) modulates the spectrum. An attached thick dummy crystal shifts the echo to longer times.

The second problem due to GVM is more difficult to deal with. The accessible bandwidth is a function of probe pulse duration and wavelength, the crystal type and its thickness. As the GVM increases for thicker sensor crystals a very thin crystal would be desirable. In this case not much GVM can be accumulated between the THz and NIR pulse and $\Delta\tau_{\mathrm{GVM}}$ which is quasi the internal averaging time remains small. But a short crystal also only slightly turns the polarization for the balanced detection (see eq. 5.1). So the signal-to-noise ratio will fall for short crystals. Therefore a compromise has to be chosen between large signal and high bandwidth. So typical crystal thicknesses start below $200\,\mathrm{\mu m}$ up to $2\,\mathrm{mm}$ depending on the application [129].

6 Enhancement Cavity

In chapter 4.1 the basic principles of THz generation in nonlinear media is explained. Even for a LN emitter with a high nonlinear coefficient the conversion efficiency is quite small. Typical reported values are photon conversion efficiencies of 10^5:1. Because the crystal's transmissivity in the NIR is quite high, most of the pump power is still available after one single pass through the crystal. Usually more than 95% of pump power is present behind the crystal for appropriate anti-reflection coatings of the facets. In a single pass setup this transmitted radiation is damped. The new proposed improvement of the conversion efficiency is to recycle the transmitted pulses in an additional resonator. A multi pass pumping scheme would just extend the effective crystal length but not increase the available pump power which is important for the nonlinear process of THz generation. The problems of lithium niobate sources which were explained in chapter 4.1 like absorption of THz waves, dispersion, need for a small beam waist etc. would accumulate in a multi pass setup.
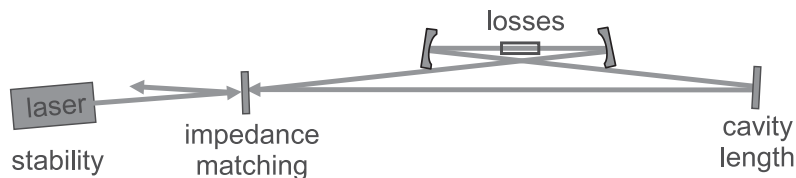
6.1 Cavity Layout

Figure 6.1: Enhancement cavity requirements: stable laser, impedance matching, cavity length and low losses

The chosen resonator is designed to oscillate the pump wavelength. Therefore it's not possible to use a standard laser mirror or OPO arrangement. The main problem is to get the power into the resonator cavity. There are no mirrors which are transparent in one direction and high reflective in the other one for the same wavelength. Unlike in the laser case where there are mirrors which are transparent for the pump wavelength while being high reflective for the stimulated wavelength. This is possible since the latter one is shifted to longer wavelengths. Even for OPOs operating far away from degeneration this is possible using dichroic mirrors. The only way to solve this problem is to use an interferometric cavity like a Fabry-Perot etalon and to place the crystal in this cavity. This resonator, the so called enhancement cavity (EC), has to fulfill different criteria.

Otherwise no enhancement will be reached and the pump power is rejected from the first cavity mirror.

The maximum possible enhancement factor A for the pump power is given by [130]

$$A = \frac{1 - R}{\left(1 - \sqrt{R(1 - L)}\right)^2 + 4\sqrt{R(1 - L)} \ sin^2 (\delta/2)} \tag{6.1}$$

where L is the EC's round trip losses, R is the reflectivity of the EC incoupling mirror and δ is the phase difference between two following pulses. $A = 1$ corresponds to the single pass value for the pump intensity or the THz electric field, respectively. Since optical rectification is a second order nonlinear process, the enhancement factor for the intensity of the pump A_{pump} and the THz electric field A_{THz} should be the same.

An intuitive explanation is to regard the EC as a Fabry-Perot which has to be kept on resonance. For that assumption under optimal conditions the etalon causes no losses and shows a transmission of 1. Here we are not interested in a high transmission but regard the crystal as loss similar to an output coupler for the cavity.

Resonator Geometry

As two following pump pulses have to interfere at the entrance mirror of the cavity to get the power into the resonator the repetition rate of the EC is already fixed. It has to fit exactly to the repetition rate of the pump laser [131]. In terms of cavity length this means a ring cavity with a length of approx. $L_{\mathrm{EC}} \approx 3.75\,\mathrm{m}$ for a pump laser operating at a repetition rate of $80\,\mathrm{MHz}$. This extent is realized in a doubly folded bow-tie ring geometry. The nonlinear crystal is placed in the beam waist between two identical spherical mirrors with a curvature of $R = -100\,\mathrm{mm}$ or $R = -200\,\mathrm{mm}$. The distance between the curved mirrors was roughly $R + (n_{\mathrm{LN}}^{\mathrm{NIR}} - 1) \cdot L_{\mathrm{LN}}$, with $n_{\mathrm{LN}}^{\mathrm{NIR}}$ the refractive index of lithium niobate for the pump wavelength and L_{LN} the geometric length of the crystal.

The incoupling mirror was placed on a manually driven linear stage to preset the cavity length and to adapt it to different laser repetition rates and crystals. This adjustment allows to fulfill the condition of synchronous pumping known from the synchronously pumped OPOs. Here a length accuracy in terms of pump pulse length counts. For a $100\,\mathrm{fs}$ long pump pulse this means a required length accuracy of $30\,\mathrm{\mu m}$. Once adjusted this condition remains fulfilled since thermal drifts etc. do not accumulate that much. If the attached resonator is to short or too long short multiple pulses are circulating in the cavity. Figure 6.2 shows the THz pulses which are emitted in such a length detuned scheme recorded by EOS. The main pulse is caused only by the classical transmitted intensity through the pump mirror and the echoes are decaying with the resonator losses. In this figure the EC's length is chosen to short. That is why the echo pulses arrive earlier at the detector. For a longer resonator the echoes would coincide with the water fringes. The aim of the interferometric EC is to concentrate all contributions into one stronger THz pulse.
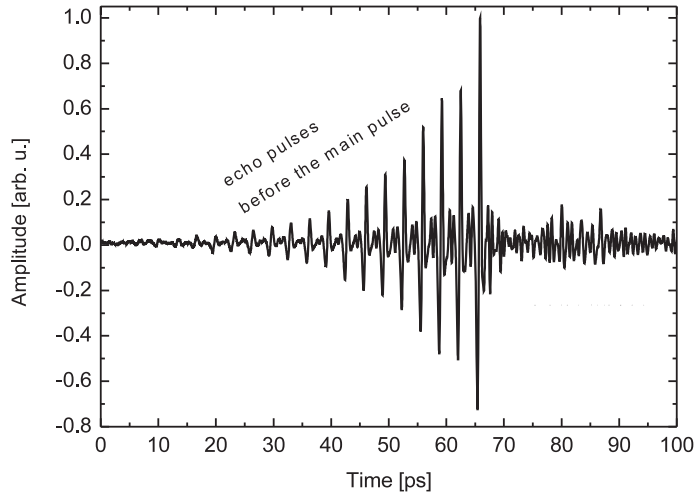
Figure 6.2: Multi THz pulses for a length mismatched cavity, the echo pulses arrive before the main pulse. Afterwards water fringes follow.

Impedance Matching

According to eq. 6.1 the EC's losses and the input coupler reflectivity determine the enhancement factor in the resonant case ($\delta = 0$). The first step is to minimize the cavity round trip losses. All cavity mirrors have a reflectivity higher than 99.95 % unless otherwise referred. Most of the cavity losses are caused by the LN crystal. The nonlinear medium contributes surface losses despite appropriate coatings and volume losses due to nonlinear processes like SHG. Therefore a ring cavity is chosen to reduce the round trip losses L by a factor of two for a given repetition rate of the EC. The other advantage of a ring cavity is that there are no optics perpendicular to the pump beam. Like for OPOs it is important not to bring the fs laser out of mode-locking operation. In the case of the EC this is even more crucial because the back reflection of the first cavity mirror can reach up to 100 % of the pump power. This would damage the laser unless very strong attenuating optical diodes are used. But this would broaden the pump pulses by dispersion.

To get the whole pump power through the high reflective mirror, the impedance matching condition has to be fulfilled. Otherwise the pump power will be fractionally reflected from the incoupling mirror even in the resonance condition $\delta = 0$. In the impedance matched case, when the cavity round trip losses equal the transmission of the incoupling mirror ($L = 1 - R$) all the pump power can pass through the mirror into the cavity. A deviation from this optimal case will make a fraction of the pump power be reflected from the cavity. Figure 6.3 shows this effect for different cavity mirrors as a function of cavity losses. The theoretically possible maximum enhancement factor A as a function of cavity losses for impedance matching is $1/L$.
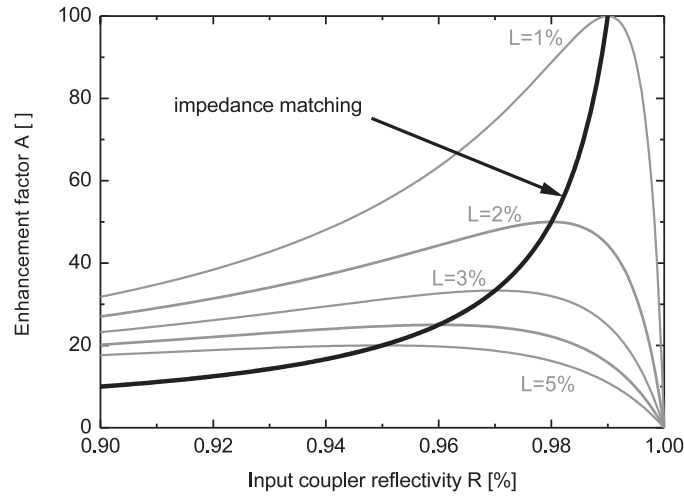
Figure 6.3: EC theoretically possible enhancement factors A for different round trip losses L
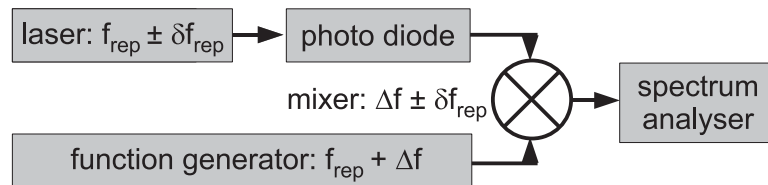

Figure 6.4: Setup for detection of repetition rate drifts. A mixer is used to down-convert the frequency range.

Stability

Since the EC is a Fabry-Perot etalon, interferometric stability is required. This means that the EC's length has to be kept on a constructive interference for the electric field, i. e. phase difference $\delta = 0$. Only in this condition the laser pulses reach inside the cavity. This is a very strict requirement, because it is equal to a length drift of less than a fraction of the pump wavelength within some milliseconds. For that not only a mechanically stable EC is needed, also a pump laser with a constant repetition rate is required. Mechanical vibrations have oscillation frequencies in the kHz range. So a resonance frequency of e. g. a vibrating mirror holder, a cooling fan or chiller will cause the laser itself to be too unstable to drive a following EC. The first rough test whether a laser has a humming is to lay the hand on the fs oscillator's chassis. If a mechanical vibration is sensible, the laser is not applicable to EC's.

Some vibration sources had to be attenuated or removed. Of course a vibration sensor can detect this more accurately but needs a friction-locked mechanical connection. On the optical side the repetition rate drift can be detected using a spectrum analyzer. The used setup to detect the laser stability is shown in Fig. 6.4. The laser pulses are detected with
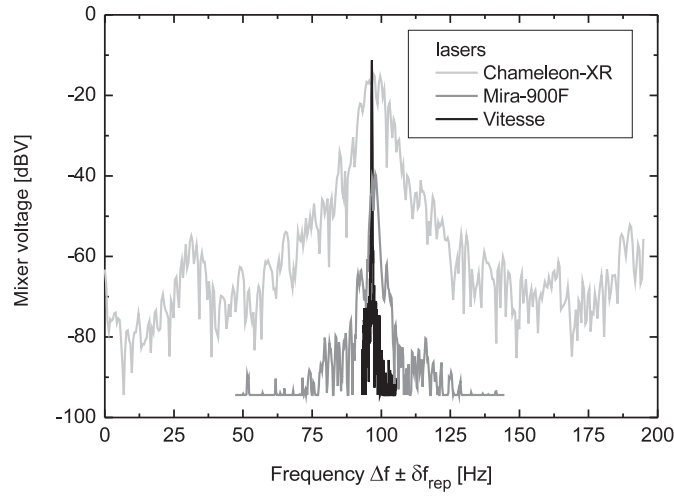
Figure 6.5: Repetition rate drift of different pump lasers

a fast photodiode. The signal is located around a center frequency $f_{rep} \approx 80\,\text{MHz}$. The deviation δf_{rep} is small against f_{rep}. A function generator preset at frequency $f_{rep} + \Delta f$ shows a slightly different but known frequency compared to the laser. For a detuning of $\Delta f \approx 100\,\text{Hz}$ the results of the mixed signal obtained for different lasers are shown in Fig. 6.5. The signal is centered around Δf while the sharpness of the signal gives a hint to the mechanical noise which can be observed by small repetition rate changes of the laser output.
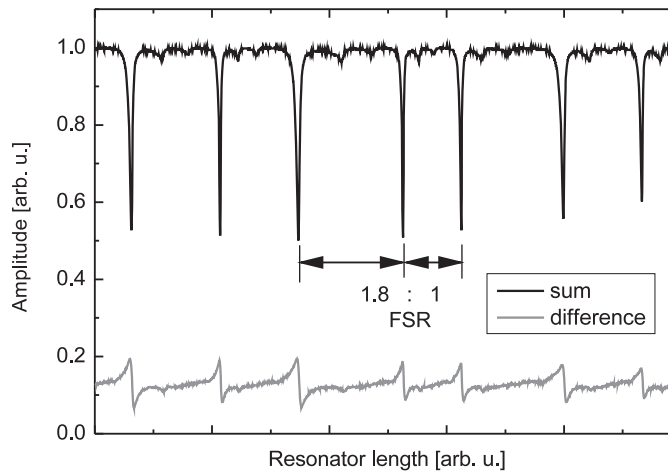

Figure 6.6: Stability of Mai Tai® laser. Jumping interference fringes indicate repetition rate jitters.

The repetition rate jumps can be clearly seen in Fig. 6.6 at the example of a Mai Tai® laser. The shown values are described in chapter 6.3. An easy to understand explanation is

that here the free spectral range (FSR) recorded by a scanning Fabry-Perot interferometer (FPI) is displaced. As indicated in the plot the FSR spacing seems to vary. This is related to the mechanical noise of the pump laser. The problem could be solved by switching all vibration sources off. In particular, for a Mai Tai® laser these are: The dry air purging unit for the fs cavity and the fan on the control board in the laser housing. Then the FSR is constant. The fringes' position is only moving due to thermal drifts.
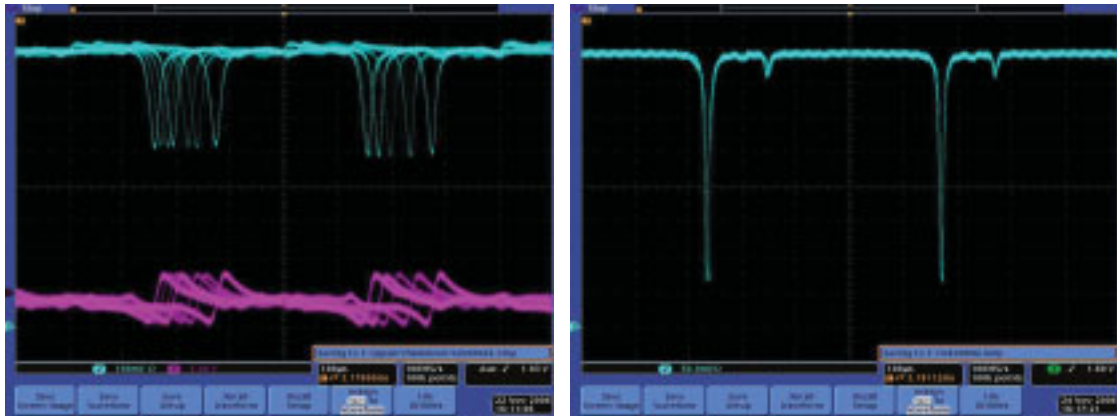

Figure 6.7: Stability of lasers. Left: Chameleon, jumping interference fringes indicate repetition rate jitter. Right: Helium Neon laser, fringes persist at the same position.

For the initially planned Coherent® laser Chameleon it turned out that the cavity can not be stabilized on that reference. Figure 6.7 shows the fringes (FSR) for a scanning FPI on an oscilloscope with luminescence. Unfortunately the resonances of the Chameleon laser jump unpredictable. To be sure that the noise is caused by the laser itself and not by the EC or induced mechanical vibrations a cw helium neon laser (HeNe) is used to check the stability of the EC. The interference fringes of the HeNe laser persist at the same position. This is a clear indication that the chosen components are mechanically stable enough to allow for an enduring locking scheme.

Thus, some lasers have to be excluded from being a pump source for the EC. But still the cavity itself is free running. That is why thermal drifts of optics or even air movement can bring the EC out of resonance.

6.2 Free Running Resonator

In the following the first experimentally obtained results are presented. Because the experiments are carried out in Japan and Germany various lasers are used. They differ in power, stability, pulse duration and wavelength. The particular pulse sources are described in chapter 3.6. Also different detectors are used to measure the THz radiation. Here the emphasis is placed on reproducibility and signal-to-noise ratio for a reference system. So only relative electric fields or intensities are given.

The first step to check to the possibilities of an enhancement cavity for THz generation is to use a free running cavity with a bolometer detector (chapter 5.1). The detector's response time can not follow the high repetition rate of the laser and THz pulses, respectively. So it integrates over all pulses and environmental noise without any useable signal. Thus, a mechanical chopper has to be used to modulate the signal with some 10 Hz to detect the difference in voltage with and without THz illumination.

The particularly used bolometer is a 4 K Si bolometer manufactured by Infrared Laboratories. The ex works given calibration constant is $2.77 10^5$ V/W. But due to additionally used PE filters to block scattered pump radiation, a varying coupling efficiency and a temperature dependent sensitivity, the calibration of bolometer voltage to mW of THz power is only a rough estimation. Some µW of THz power are feasible for most kinds of checked emitters.
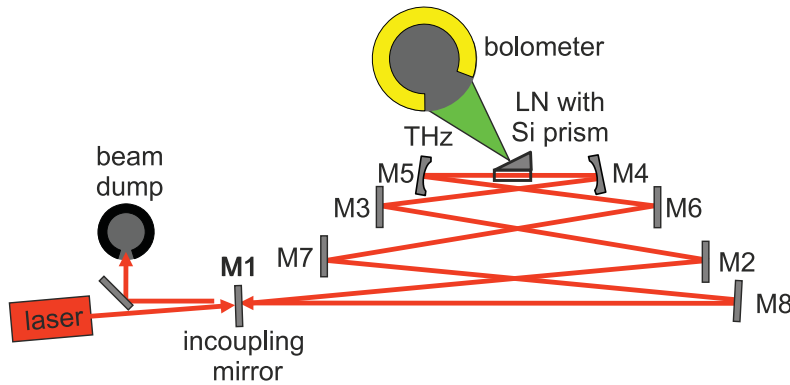

Figure 6.8: Setup of a free running EC with bolometric THz detection

Figure 6.8 shows a sketch of an unstabilized or free running enhancement cavity. It consists of a fs laser source (in the following measurement Coherent® Mira), a bolometer, a 5 mm long MgO:LN crystal with attached Si prism for the generation of Cherenkov radiation and the resonator itself. The latter is set up with an incoupling mirror with a reflectivity of 95 % to be in the range of impedance matching. The mirrors are all high reflective. Two curved mirrors with curvature radius of 100 mm form a beam waist in the crystal.

To compare the output of the EC with the single pass signal the incoupling mirror was removed to illuminate the LN with 100 % pump radiation. Figure 6.9 shows the chopper gate and the single pass output. The single pass THz signal follows the shape of the chopper signal with a phase depending on the electronics. Then the EC is closed by introducing the mirror and nearly no power reaches inside the cavity. When fulfilling the condition of synchronously pumping a strong blue "blinking" of the crystal can be observed. The reason is non phase matched second harmonic generation. This coincides with a noticeable THz signal detected by the bolometer. Due to the mechanical chopping with 110 Hz only the leading edge of the THz signal can be detected. The blinking of the THz signal is attributed to cavity length drifts which change the resonance condition
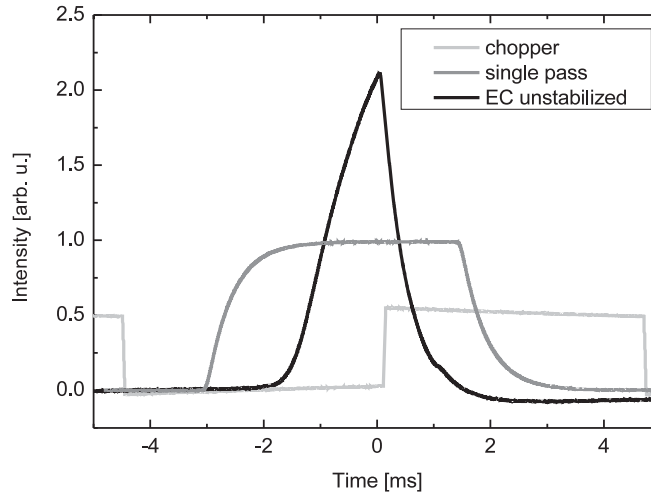
Figure 6.9: THz intensity of a single pass emitter and an unstabilized enhancement cavity

$\delta = 0$ within milliseconds. On timescales of the build-up time of the cavity (some tens of round trips correspond to less than one microsecond) the cavity remains on resonance. So what actually is observed here for some tens of milliseconds is the response function of the bolometer's electronic circuit. Its specification is given for a chopping frequency of up to 110 Hz. But it can be stated for sure is that the THz output exceeds the single pass intensity at least by a factor of 2 [67]. But for a more detailed investigation and description a stabilized setup is inescapable. At this point a spectroscopic detection in a TDS setup makes no sense since the signal on the detector is not constant enough. Even long integration constants would not bring a reproducible spectral amplitude.

6.3 Actively Stabilized Resonator

The challenge now is to set up a cavity stabilization which has a short response time to readjust the cavity length. It has to compensate the long term thermal drifts as well as the fast laser drifts. In principle there are two common stabilization schemes: The Pound-Drever-Hall [132] and the Hänsch-Couillaud [133] stabilization technique.

The Pound-Drever-Hall stabilization uses an induced modulation of the laser to discriminate whether the reference cavity (OPO, Fabry-Perot, enhancement cavity, etc.) is to long or to short. This sign can be determined by a small frequency change of the laser, perhaps induced by a current modulation of the diode) or an external phase modulator which changes the frequency. But this technique based on an active modulation is expected to have a higher noise in terms of intracavity power. Therefore the Hänsch-Couillaud scheme is chosen since it is self-referencing without the need for an additional noise source.

A Hänsch-Couillaud (HC) stabilization analyzes the reflection of the first EC mirror. The information on the sign and amount of cavity length detuning is already present

in this pulse. The principle behind the HC scheme is ellipsometry. Comparable to an EOS sensor (see chapter 5.3) the same optical and electronical components are used. The explanation is as follows:

The reflection of the EC's pump mirror consists of two contributions. One is the direct back reflection from the first surface, the second one is the part of intensity which leaves the cavity here. In the optimal case of resonance ($\delta = 0$), the reflection vanishes. If there is a little length difference between laser and EC, these two pulses have a different run time. Thus, they are separated in time with a defined phase difference.

To exploit the highest nonlinear coefficient d_{33} in LN the polarization of the pump beam is chosen along the z-axis of the crystal. This is s-polarized (out of plane) in the HC scheme (see Fig. 6.8 or 6.13). A minimal detuning, in most cases unintended and below the measurement accuracy, will produce a deviation from the pure s-polarization. Then there are two projections of the pump polarization with respect to the crystal's z-axis. The one parallel to it will see higher losses due to the larger nonlinear coefficient, the other one will see a smaller nonlinearity. Other possible reasons are angle dependent surface losses at optical boundaries. So the two polarizations suffer different losses in the cavity. Thus the polarization axis is turned with respect to the pump polarization.

In summary the two pulses, the direct reflection and the pulse which leaves the cavity, have a phase difference due to a different runtime and an unequal polarization. The superposition of these two contributions leads to elliptically polarized light if there is a phase difference ($\delta \neq 0$) or to linear polarization for an accurate cavity length ($\delta = 0$). The handedness of the ellipticity is defined by the sign of cavity length detuning.

The overlapping pulses propagate through a $\lambda/4$ wave plate and a PBS cube. This separates the two polarizations towards two nearly equally biased photodiodes. The phase detuning of the attached EC now leads to a varying intensity in the two arms depending on the sign of drift.

The electronic closed loop consists of a commercially available PID circuit (TEM Messtechnik, Hannover, Germany) which controls a moveable mirror mount. By changing the voltage on the piezo actuator the cavity length can be re-adjusted with a very high accuracy. A linear scan of the piezo actuator and the corresponding signals are shown in Fig. 6.10. On the x-axis the scanning distance of the piezo is given. On the y-axis the sum and the difference of the two balanced photodiodes are plotted. The sum corresponds to the reflected pump intensity, i.e. the intensity that does not reach inside of the cavity. It can be seen that the sum signal is quite constant besides some small sharp lines or fringes. These are the points where the EC length fits to the repetition rate of the laser. Besides the condition of synchronously pumping which is manually preset here also the EC is on an interferometric resonance. The fringes spacing is equal to half of the pump wavelength.

The difference of the intensity incident at the two photodiodes is proportional to the cavity length detuning. The most important part of the difference signal is the steep inclinations which coincides with the fringe in the sum. The zero crossing of the dispersion shaped signal is located at the minimum of the sum signal. So a small deviation of the sum brings a large signal in the difference. The overall stabilization response frequency is a few
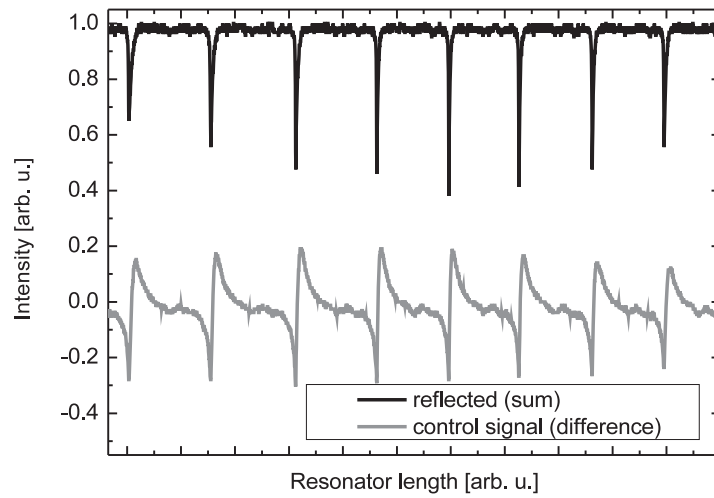
Figure 6.10: HC circuit control signals: Reflected (sum) intensity and control signal (difference) as a function of cavity length

kHz. The limitation is mostly attributed to the resonance frequency of the mechanical system (piezo, mirror) and less to electronic reasons.
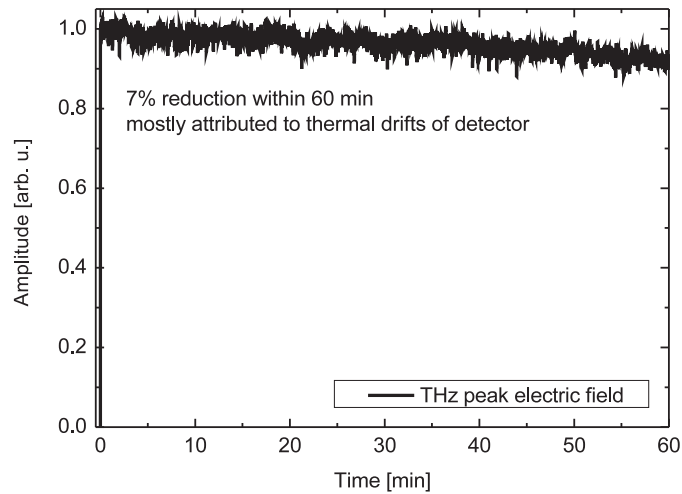
Figure 6.11: Long term stability of THz amplitude for the HC stabilized EC. Reduction mostly attributed to thermal drifts of the detector.

For the mechanical components of the EC in particular the mirror holders and the breadboard very rigid hardware is chosen. Therefore the overall thermal drift under typical laboratory conditions is much smaller than the amplitude of the piezo actuator. So the system can be kept on resonance for hours. Figure 6.11 shows the emitted THz amplitude for a LN emitter in the resonant case. For the experimental setup see Fig. 6.13.

Within one hour the amplitude reduces by 7%. This is not attributed to the electronic circuit or the emitter, this is more related to thermal drifts in the detector arm. So the realized setup can also compensate for the long term drifts of the EC.

Figure 6.12: Intracavity signal with and without stabilization

If the HC circuit would jump out of cavity locking, then the THz amplitude would not gradually go down, but instantaneously fall down to 5% of the single pass amplitude which is the transmission of the first mirror. This corresponds to approx. 1% of the here presented amplitude in resonance. It is expected that the cavity still has a high frequency noise because it is still a control circuit which lags 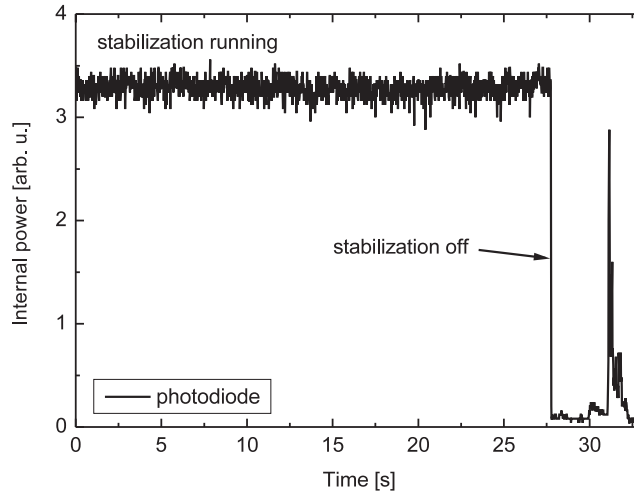behind the drifts. The induced noise in the system and the influences on the THz amplitude will be discussed later in this chapter.

The first check of the THz emission in an actively stabilized enhancement cavity could be carried out with an easy-to-use bolometer. It is easy to operate since is does not require a correct timing of a second detector pulse like for a coherent detector. The bolometric detection will be used again to compare different emitters, especially in terms of output power. But for an optimization of the system it is not the detector of choice. The measurement time is limited to a couple of hours until the bolometer needs a refill of cryogenics. Also the spectral behavior is important to know because the influences of the system on the pump pulses (length, phase, beam profile) also affect the broadband THz emission. Therefore an EOS setup is operated at the same time as explained in chapter 5.3.

An EOS setup is used to detect the THz electric fields with a spectroscopic resolution. The probe beam is directly separated behind the laser before the EC. This detector arm is more susceptible to thermal drifts compared to the actively stabilized EC. So the overall setup consists of the EC itself, HC control circuit and the THz detector. The last two both contain nearly the same optical components since both are based on balanced ellipsometry. With this setup reliable and reproducible measurements are possible also
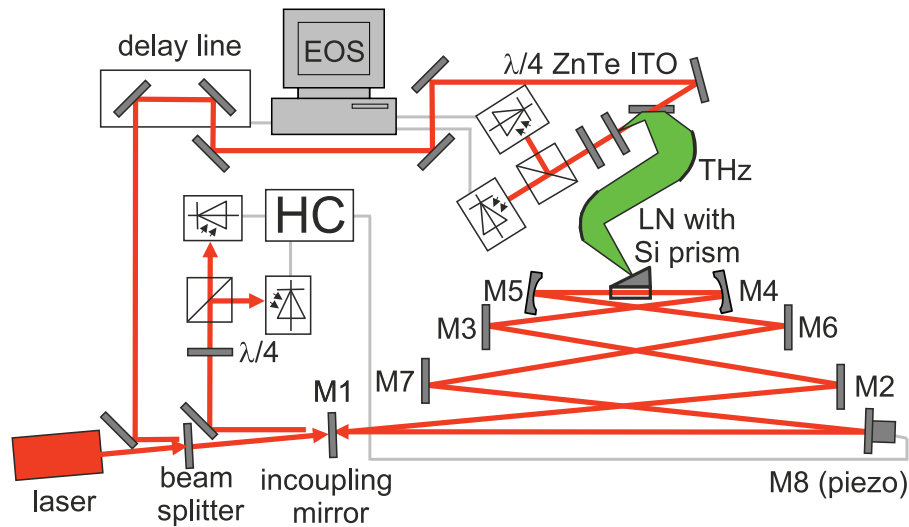
Figure 6.13: Actively stabilized EC setup with EOS detector [134]

on daily timescales.

Since for the EOS a lock-in technique is needed to achieve a high signal-to-noise ratio the THz signal needs a modulation. Typically the laser is switched optically. But here not to bring the electronic circuit out of operation the THz beam itself is chopped.

Results of EC

The aforementioned stabilized EC setup is successively pumped by different laser sources. The particular specifications can be found in chapter 3.6.

EC pumped by IMRA

With this laser a stable locking is easily possible. Since fiber lasers have only few solid state optics, it is less sensitive to mechanical vibrations. This is proven by the steady positioned and equally spaced fringes of the EC resonances (Fig. 6.14).

To detect the short term noise of the EC respective its control unit the internal power is measured (Fig. 6.15). The system never looses the lock point completely, the power does not show indications for mode hops. The intracavity power fluctuations are faster than typical integration constants of EOS systems in the 100 ms range. Therefore, the noise with kHz frequencies does only slightly contribute to the THz system noise.

The THz electric field detected in an actively stabilized EC resonance is shown in Fig. 6.16. The amplitude of the single pass scheme is plotted as comparison. The used IMRA frequency doubled fiber laser does only provide a weak output of 110 mW. Thus, the spectral width and peak output of the nonlinear THz emitter in the single pass scheme is substandard. The peak amplitude can be increased by the application of an enhancement cavity by a factor of 7. The given data in Fig. 6.16 show a typical enhancement factor of
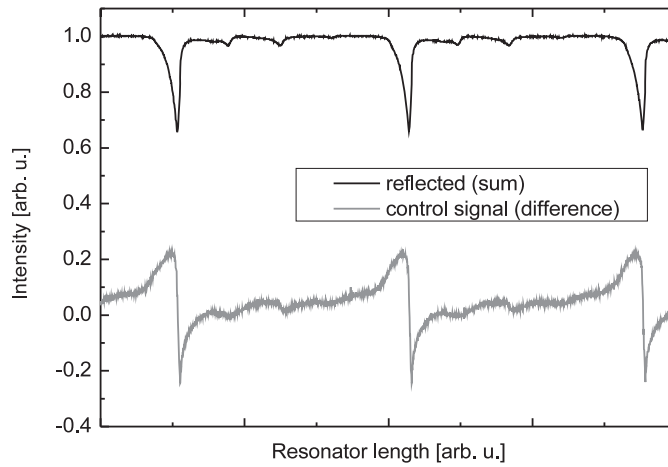
Figure 6.14: Stabilization signal of the EC pumped by an IMRA fiber laser for a scan of cavity length
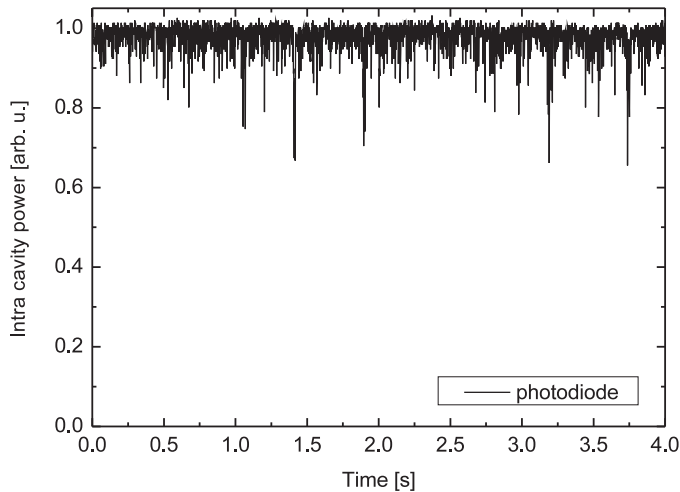
Figure 6.15: Noise of intracavity pump power of the EC pumped by an IMRA fiber laser

5 for the electric field. Due to above mentioned pump intensity fluctuations the signal-to-noise ratio (SNR) is not 5 times higher. The single pass SNR is determined to be 97 compared to 410 in the resonant case. This is a significant improvement for the application of cheap, small and rigid fiber lasers in THz-TDS systems.

EC pumped by Mai Tai®

By small modifications at the Mai Tai® laser's housing the noise was considerably reduced. Then the HC circuit could follow the resonances. With a solid state Mai Tai® laser a higher pump power in the single pass scheme is already available. But with a stabilized EC a
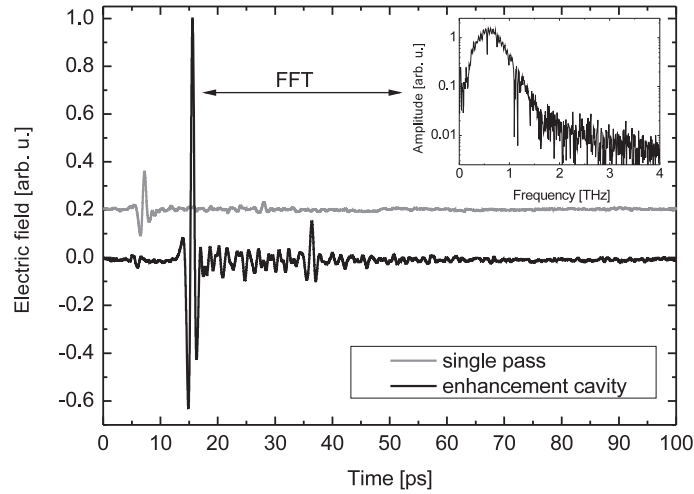
Figure 6.16: Emitted THz electric fields (single pass vs. resonant case) from an EC
pumped by an IMRA fiber laser. Inset: Spectral amplitude of the EC source

much higher pump power becomes achievable which is not applicable in single pass. So
the nonlinear process of THz generation is expected to be much more efficient.
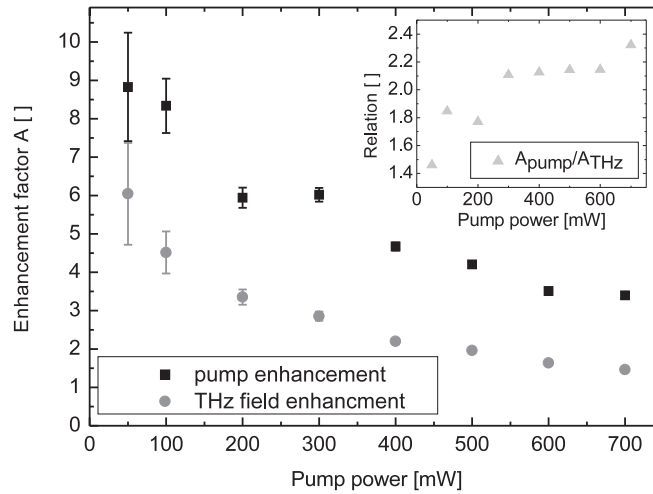
Figure 6.17: Enhancement factors of EC (Mai Tai®) for the pump and THz electric field
at different pump powers (6 mm crystal length)

Figure 6.17 shows the archived enhancement factors for different pump powers. The
pump power is preset by a variable attenuator consisting of a $\lambda/2$ wave plate and a
polarizing beam splitter cube. So it is guaranteed that only the laser power is changed
while keeping the pulse length and polarization constant.

It turns out that the enhancement factor A_{pump} starts to decay from 9 for low pump

power below $100\,\mathrm{mW}$ down to a factor of 4 for the maximum available pump power. Obviously the corresponding THz enhancement factor A_{THz} which ideally should have the same value is smaller. The relation $A_{\mathrm{pump}}/A_{\mathrm{THz}}$ is plotted in the inset. It starts at 1.46 increasing up to above 2. The reason that it does not start at 1 is related to the cavity transversal mode. Despite the single pass values were recorded with the same focussing element (curved mirror), the beam diameter and divergence is different for the closed cavity. Then the THz generation may be shifted to a different position in the crystal or show a different beam waist. As explained in chapter 4.1 for a strong THz source based on LN the propagation in LN and the hard focussing is very important. Even with manual realignment the relation can not be improved. A further reduction of the THz amplitude arises due to dispersion and self phase modulation (SPM). The first one can easily be compensated while the other one is strongly dependent on peak power. The measured intracavity pulse length (Fig. 6.18) and the increasing difference of the two measured enhancement factors support the appearance of SPM.

In the single pass scheme, the dispersive broadening of the pump pulse in some millimeters of LN is not of concern. But when it comes to a multi pass setup, the dispersion length can add up to some centimeters in LN. Assuming round trip losses of 5% statistically each circulating pump photon propagates 20 times through the crystal. The pulse will show a dispersive broadening and as a consequence generate a reduced THz emission. The average power will remain the same (neglecting the different impedance matching condition) but the peak power will be reduced which is a drawback for nonlinear processes.

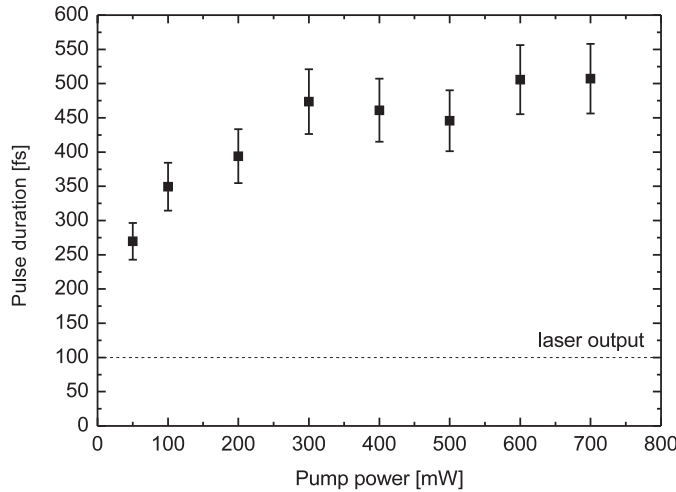**Figure 6.18:** Intracavity pulse duration for different pump powers

To compensate for the additional dispersion specially designed Gires-Tournois interferometer (GTI) mirrors are used to compensate at least the linear part of dispersion [135] caused by the crystal. The number of used mirrors depends on the crystal length that has to be accounted for. Typically, all 5 plain HR mirrors were Gires-Tournois

interferometer (GTI) mirrors made by Layertec with a negative dispersion of $-550\,$fs per reflection in the wavelength interval between $780\,$nm and $805\,$nm. Thus, a large amount of dispersion can be compensated. But the usage of GTI mirrors only allows for the discrete stepwise compensation. No steady dispersive tuning is possible like it is known from prism compressors. The implementation of an additional internal compressor would increase the alignment difficulties, especially in the ring resonator. Also the resonator's round trip losses would be increased which is the limiting factor for the EC.

An autocorrelation setup which is used to measure the pulse length required a change of optics in the EC. Since the available leakage reflexes were too weak to be used for an autocorrelation measurement one of the GTI mirrors was exchanged by an output coupler with a transmission of 1% and a dispersion of $< 20\,$fs^2. So these values vary from the real conditions. But already here the influences of SPM for higher pump powers are observable (see Fig. 6.18).
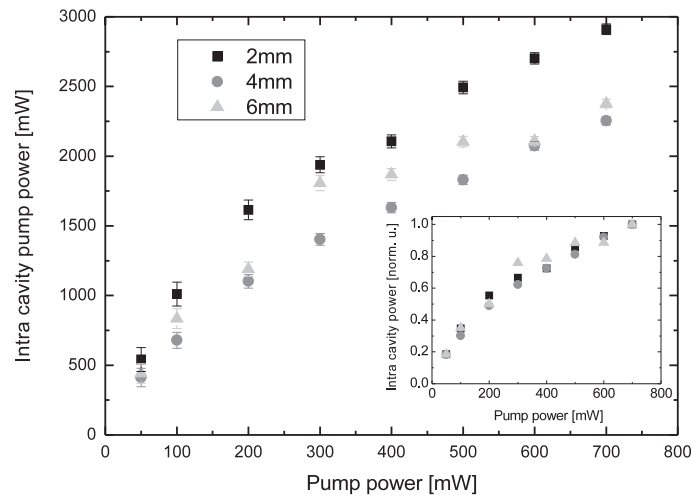
Figure 6.19: Intracavity pump power of the EC pumped by an Mai Tai® solid state laser for different crystal lengths. Inset: All power values normalized to the value for $700\,$mW

Besides residual contributions of uncompensated dispersion and SPM the strongest limitations are the losses in LN. Figure 6.19 shows the archived enhancement factor for a crystal length of $2\,$mm, $4\,$mm and $6\,$mm, respectively. There is no clear principle difference between the enhancements for different crystal lengths. This may be related to the Rayleigh length of the beam waist in the cavity. If it is much shorter than the crystal length then the losses are concentrated in the focus with high intensity and no losses are added for longer crystals. To guide the eye, in the inset the enhancement was normalized to the individual maximum. A clear saturation behavior is evident.

EC pumped by Vitesse

From the very first measurement the Vitesse laser seems to be very stable. The active cavity stabilization can easily lock on it. So here enhancement measurements were possible at a high pump power.
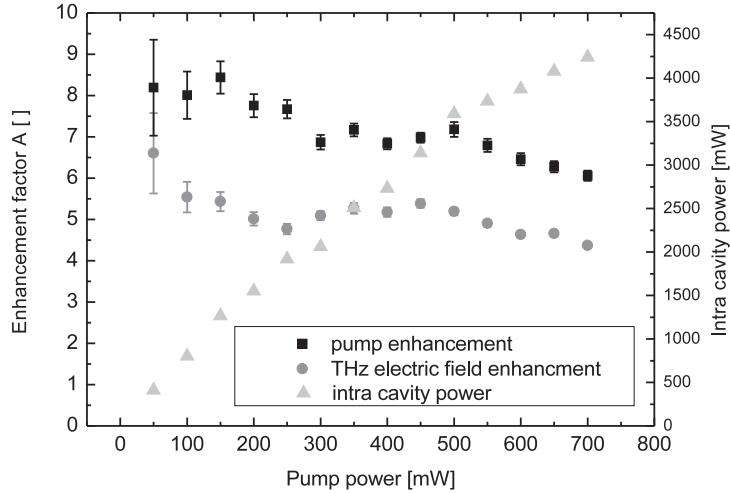
Figure 6.20: Enhancement factors of EC (Vitesse) for the pump and THz electric field at different pump powers (6 mm crystal length)

Typical enhancement factors for different pump powers are plotted in Fig. 6.20. The pump enhancement factor A_{pump} starts above 8 for low pump power gradually decaying down to 6 at the full pump power. The THz electric field enhancement factor A_{THz} is smaller than the pump enhancement factor A_{pump} (approx. 2 points). The deviation is constant over the whole pump power range as expected for a nonlinear process of second order. This indicates that only an offset compared to the single pass case is seen. The pulse duration and beam shape in the cavity do not affect the THz generation negatively. The intracavity power which is the product of the pump power and the pump enhancement factor A_{pump} is plotted as comparison. A slight saturation can also been observed here. It is remarkable which very high intracavity pump power can be achieved. More than 4 W of ultrashort pulses are available for THz generation. This is much more than a Ti:sapphire oscillator can provide. Fortunately, the LN crystal can stand this high power. But it shows some increased losses for high peak power.

The enhancement factors in the cavity are measured as a function of the intracavity peak power density (Fig. 6.21). This was estimated from the calculated intracavity beam waist diameter of $20\,\mu m$, the measured pump power enhancement A_{pump} and the pulse duration of $100\,fs$. So in the cavity up to $80\,GW/cm^2$ can be expected in the peak maximum. To determine the crystals behavior for this operating parameters the focus in a the single pass setup is chosen very tight to reach the same power densities with less average power. It is obvious that the losses are constant for pump power densities below $30\,GW/cm^2$.
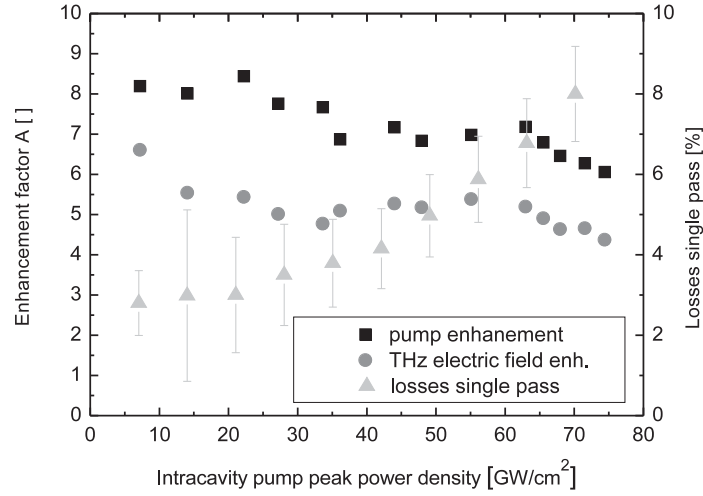
Figure 6.21: Enhancement factors of EC (Vitesse) for the pump and THz electric field at
different pump peak power densities and crystal losses (6 mm crystal length)

Then a quadratical behavior starts which increases the losses up to 8%. This is the main
reason for decreased enhancement at high pump power according to eq. 6.1.

6.4 Discussion of EC

The losses in LN are related to different factors as discussed in chapter 4.1. The pump
power which is accessible using an EC is much higher than the typical pump power for
single pass oscillator pumped systems. But unfortunately under conditions which are re-
quired for efficient THz generation (hard focussing, high peak power) also parasitic effects
strongly contribute to the losses in the crystal. The largest contribution is either directly
or indirectly caused by SHG. This non phase matched frequency doubling is described by
the same nonlinear coefficient $\chi^{(2)}$. Above a peak power density of $30\,\mathrm{GW/cm^2}$ a signif-
icant increase of the single pass losses is observed. This strongly limits the performance
of the system.

   According to results of Furukawa et al. [53], the BLIIRA effect should be sufficient
high for our doping of 1% magnesium oxide in lithium niobate. Also Beyer et al. [54]
reported on increased losses induced by fs pulses in LN. They attributed it to two-photon
absorption in the range of $400\,\mathrm{nm}$ pump wavelength. Compared to their measurements
our crystal is longer ($6\,\mathrm{mm}$ vs. $1\,\mathrm{mm}$) and MgO-doped so also here a strong inherent
second harmonic generation is expected to induce additional losses.

   The accessible parameters in eq. 6.1 are addressed and improved. The first important
factor is the interferometric stability δ for the EC with respect to the pump source. Since
a cw measurement clearly indicates that the EC itself is very stable the optimization has
to be done at the lasers side. Some lasers had to be excluded, some others showed a stable
output. The remaining vibrations and thermal drifts were steadily actively compensated

by a HC control unit. So the reduction of the enhancement factor A caused by the phase mismatch in the resonance can be neglected. Only weak additional noise is present in the system which reduces the SNR of the THz system or has to be filtered out by the integration time of the lock-in amplifier. But the higher pump power more than compensates for that.

The impedance matched case ($L = 1 - R$) is reached by an appropriate input coupler mirror. The deviation of the maximum enhancement factor for a difference of the input coupler mirror's optimal reflectivity R (e.g. 1%) is not so critical like increased losses by the same amount. Especially for high losses, the enhancement as a function of mirror's reflectivity R is very smooth (see Fig. 6.3).

What finally turned out to be the most limiting factor was the cavity's losses in the LN crystal. As mentioned above the responsible physical reasons for the higher losses induced by fs pulses are also increased for an optimized THz output. The SHG corresponds to the same nonlinear coefficient as the THz optical rectification also does. Other effects are increased by the high power density required for THz generation. Therefore only slightly improvement was reached by reducing the focus diameter. The crystal losses are reduced in that case but also the THz output is lowered.

On the material side on LN, an improvement is difficult to achieve. The accessible types of LN were tested. Unfortunately, not much suppliers are available at the market to check different kinds of crystals. Without MgO-doping only a single pass scheme was possible. Then the transversal beam profile gets so fanned and perturbed that a steady state operation is not possible. Heating up the crystal to reduce the losses, perhaps without MgO doping, would be a possibility to reduce the photorefractive effect. But also here it turns out that the higher the crystal's temperature the higher the losses in the THz range get [51].

Other kinds of nonlinear materials are either not applicable for that pump wavelength range, do not have a high transmission in the NIR or simply have a small nonlinear coefficient. Lithium tantalate would also be an option for a THz emitter [136]. But the pump power needs to be higher to get the same output like with a single pass LN emitter due to the small nonlinear coefficient in lithium tantalate. Further on, the photorefractive effects and the losses in the THz range are the same for this crystal. GaAs would offer a very high nonlinearity [96]. But since pumping below the two photon absorption is required, typical Ti:sapphire systems can not be used [35].

This restrictions limit the type of applicable crystals to LN up to now. But the stabilization scheme itself could be easily adapted to other pump wavelength ranges. Perhaps with a fiber laser emitting at $1.5\,\mu m$ a valuable system could be arranged. In that case, the most critical part would be the sensitive THz detection.

Intra Laser Cavity THz Generation

The most obvious upgrading of the femtosecond pumped EC would be to bring the Ti:sapphire laser and the EC together in one device. This means an Ti:sapphire oscillator with a second beam waist where the nonlinear crystal is located. Then the condition of

interferometric stability is inherently given. The phase matching and the output coupler are replaced by the losses in the lithium niobate crystal.

A lot of attempts have been carried out to get a homemade sub 10 fs Ti:sapphire laser [137] into steady mode locking operation with different LN crystals in the resonator. But even with an elaborated dispersion control using chirped mirrors and a prism compressor the Kerr lens was not stable enough. For external hits on a mirror an increased SHG in LN is observed which is an indication for pulsed operation. But no THz output was observed.

Without the LN crystal but with the second beam waist the Ti:sapphire laser was mode locking stably with pulses below 55 fs length [138]. Perhaps an active mode locker could make this setup run with the second beam waist.

Nanosecond System

Not only the material side could significantly improve the performance of an EC by reducing the losses, also the basic idea of fs pump pulses has to be reconsidered. A lot of THz parametric generators or oscillators are pumped by ns pump sources [34]. The principle of the EC can also be used for the ns pump pulses. Then the pulse length is longer with respect to the cavity round trip time. So the condition of synchronously pumping is replaced by a nearly cw pulse overlapping with itself. Typical ns sources have a lower peak power compared to fs systems. In this case nonlinear losses caused by the high peak power of fs pulses are reduced considerably. On the other hand the enhancement cavity still allows for a high conversion efficiency possibly resulting in high THz output power.

In this experiment the EC is stabilized to the 1064 nm pump laser. First results using PPLN indicate that this concept operates very efficient [139, 140]. Especially because also cascaded processes are observed. Injection seeding can reduce the oscillation threshold and the spectral bandwidth.

7 THz-TDS Systems

In this chapter the layout of different THz systems is described. The decision criteria why particular components are chosen for each setup are given. The systems are made for different purposes: Simple transmission measurements, automated imaging, components characterization under different parameters, or measurements outside of the laboratory at a customer's place. The required portability and flexibility is the reason for updates or revisions of already established setups. But it is not only to change a THz mirror to switch from a collimated THz beam to a focussed one. Also transmission and reflection schemes differ in their behavior very much. These criteria strongly influence the layout of THz systems via the components which are included in every TDS system:

- a fs laser source

- a THz emitter

- a THz detector

- a delay producing unit (mostly linear stage)

- optics which guide the pump pulses

- optics which guide the THz pulses

- electronics to amplify and filter the recorded signals

- software for data acquisition and system control

- software for data evaluation and display

7.1 Standard TDS System

A standard TDS system (according to Fig. 3.2) is a setup that was designed to be operated firmly standing on an optical table under laboratory conditions. Pumped by a Ti:sapphire laser it offers a very high flexibility for the choice of components: Surface emitters, photoconductive switches or nonlinear crystals can be used as emitters because a high pump power is available. They are interchangeable with each other by adjusting the mirrors and the pump power. THz detection is realized with photoconductive switches or by electro-optical sampling. Because space abounds on the optical table rigid optic holders are used. This allows for a fast change in the pump beam path in terms of length, direction or polarization. So a large variety of components (e.g. emitters, detectors, electronics) can be tested with such a system.
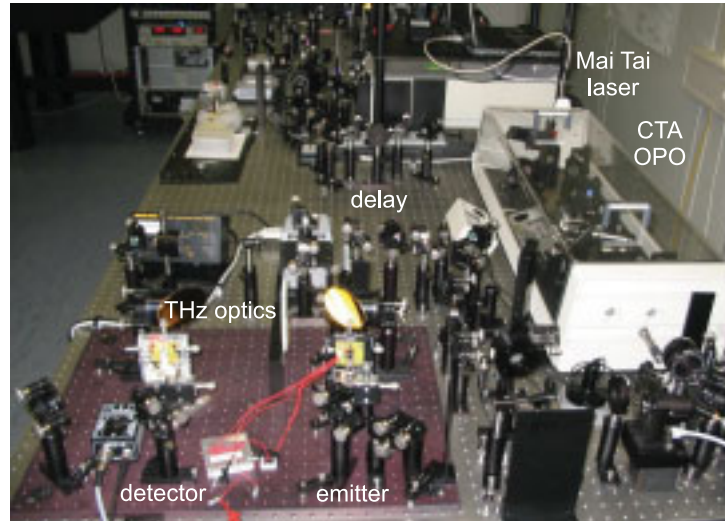
7.2 CTA System

Figure 7.1: Setup of the CTA-OPO pumped THz-TDS system

The CTA-TDS system (Fig. 7.1) is the most flexible of all systems in terms of accessible pump output wavelength. A standard TDS system can not be used to test the new generation of THz emitters which are designed for a pump wavelength of 1.5 µm. Of course the photon energy of a Ti:sapphire laser is sufficient to bring electrons above the bandgap in such devices. But the carrier lifetime is also wavelength dependent. It is expected that the lifetime will increase for photon energies which are much higher than the bandgap energy. The reason is that before recombination some transitions have to occur inside the conduction band first. So a widely tunable OPO which extends the accessible wavelength range of a Ti:sapphire laser is needed. The CTA-OPO is very well suited for such purposes as shown in chapter 3.6.

The fundamental pump is a Ti:sapphire laser (Mai Tai® HP) with a tunability between 690 nm and 1040 nm. The appended CTA-OPO extends the accessible wavelength range up to above 2 µm. A fraction of the Ti:sapphire pump power is split away before entering the OPO. To have all possibilities in the emitter and detector arm the time delays, respective the beam paths, are chosen for a nearly equivalent runtime of both NIR wavelengths. The beam path of the fundamental pump is folded to compensate for the OPO runtime. A flipping mirror can switch between the beams delivered by the fs laser and and the CTA-OPO.

So the emitters can be gated with different wavelengths. This is important for the characterization of components. In particular since antennas based on GaAs with a large bandgap (867 nm) are sufficiently understood and developed, new devices with a smaller bandgap can be described with a known reference. In this way normalized values with respect to a standard component can be given.
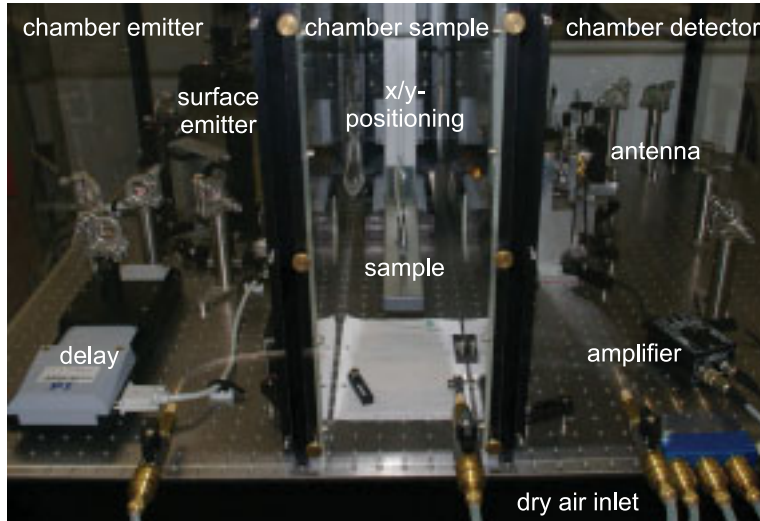
7.3 Transmission Imaging System

Figure 7.2: Setup of the THz transmission imaging system

Since the setups described within this thesis are single pixel systems, only one point on the sample can be tested with one single TDS scan. For imaging applications, the sample or the THz path have to be moved relative to each other. The chosen solution is to use a scanning imaging scheme where the sample is moved on an automated xy-stage. Figure 7.2 shows a photograph of the transmission imaging system.

Some ulterior motives for the design of the system are the following: The most obvious is the plastic box covering the system. So broadband spectroscopy with pure dry air or discrete humidities is possible. Furthermore, the air flow keeps the optics clean and reduces the thermal gradient during the day. The posts and optic holders are completely made of stainless steal where possible. So also thermal restraints and mechanical tensions between materials with different thermal extension coefficients are considerably reduced. The used emitter is a n-type InAs surface emitter. A focussing lens demagnifies the pump beam diameter on the THz source. This reduces the source diameter (see chapter 4.2) and optimizes the divergency with respect to the imaging optics. So smaller foci can be realized and the high frequency part of the THz spectrum is enhanced. The noise level of the system can be reduced by appropriate grounding and shielding of the amplifiers. An additional bandpass filter was used to reduce the 50 Hz noise and the high frequency offset which was sometimes present in the building. This combination of small steps towards a stable system along with the reliable Mai Tai® XF laser allowed for long enduring measurements. Overall, the system keeps running with different samples for months without realignment. For results obtained with this system and the achieved lateral resolution see chapter 9.1.

7.4 Reflection Imaging System
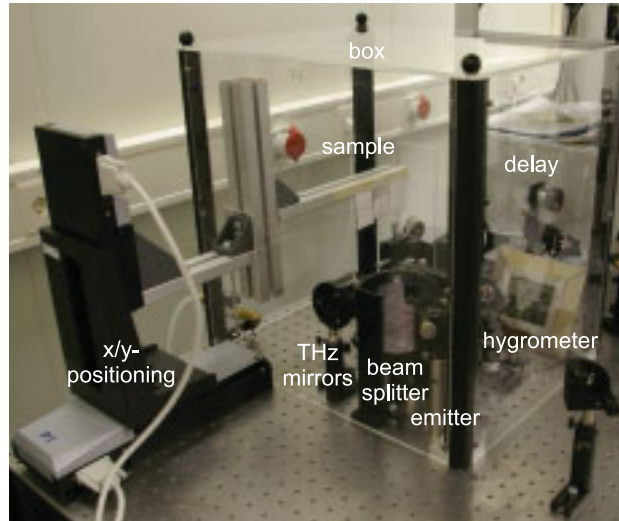
Figure 7.3: Setup of the THz Reflection Imaging System

THz reflection spectroscopy can be carried out in different geometries. There are various possibilities of angles between illumination and detection direction of the THz system and the orientation of the surfaces' normal, respectively. The geometry of $0°$ between emitter and detector is typically most interesting since it corresponds to a direct reflection back to the emitter.

The experimental difficulty is how to guide the THz beam. One way is to use a transceiver (combination of transmitter and receiver) with respect to the surface normal of the sample. But then one faces the electronic and optical problem of two gating pulses at the antenna and the tricky alignment of the THz optical system for the pulses propagating into both directions. The easier solution is to use a beam splitter for the THz radiation. Then a fraction of the intensity (ideally 50%) is transmitted through the beam splitter, the rest remains unused. On the way back from the sample the fraction of intensity which gets reflected at the beam splitter is used. So in the optimal case of a 100% reflecting sample, 25% of the THz intensity reach the detector. The beam splitter used here is a 10 mm thick Si wafer. The Fresnel reflection amplitude for an incidence at an angle of $45°$ is approx. 20%. So the transmission and reflection is not optimal. But since the variety of THz optics is limited, the Si beam splitter is a good compromise. To reduce the THz focus diameter, a horn-like tip is used to guide the beam to the sample.

On the other hand the sample's surface plays a major role for the detected signal. Depending on the orientation either a direct reflection or diffuse scattering is detected. So the adjustment of the sample in the THz focus strongly influences the detected signal.

7.5 Portable System

Figure 7.4: Setup of the Portable TDS System
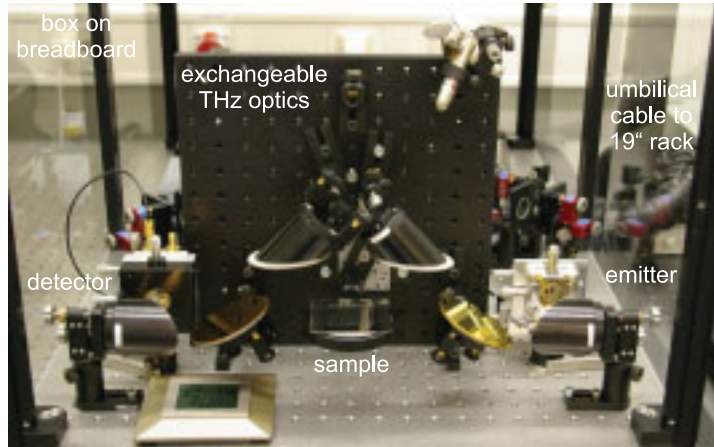
The first step to make a system portable is to make it compact. The optical table is replaced by a breadboard (60 cm times 90 cm) which can be transported by two persons. The Ti:sapphire laser is exchanged by a frequency doubled fiber laser (Imra Femtolite F-100). This renders the chiller, the strong diode laser and the big power supply unnecessary. These two facts already bring a lot of consequences for the entire setup: The used mechanical components have to be miniaturized which is no problem using commercially available parts. Due to the limited pump power, surface emitters can not be reasonably used anymore. With this low delivered power only a photoconductive switch can be operated as an emitter. An arising problem for the space consumption is the THz beam path if a focus is needed. Either the THz focus is located outside of the breadboard or the THz beam is turned up out of the optical plane. The realized setup shown in Fig. 7.4 keeps the whole THz beam path on the breadboard in order to allow the system to be covered by a box for dry air purging. The optics between the emitter and detector are mounted on an exchangeable baseplate. So the setup can be switched between reflection and transmission geometry very easily. All the electronics like the lock-in amplifier, laser power supply, controllers and the computer fit into a small 19"-rack. The only required supply is a standard 240 V power outlet and, if needed, a dried air supply. This offers the possibility to measure at customers' places also outside of laboratory conditions. Without the portable system the presented measurements of explosives would not have been possible since it is forbidden to carry the samples out of the producing institute. A transportation in a van did not affect the alignment of the system nor the THz signal. But due to thermal drifts and mechanical requirements when changing the optics realignment through a skilled operator is still necessary. Also the data acquisition and evaluation is still carried out manually with respect to the sample's properties. So the development of a hands-free system is still necessary to access the real-world market.
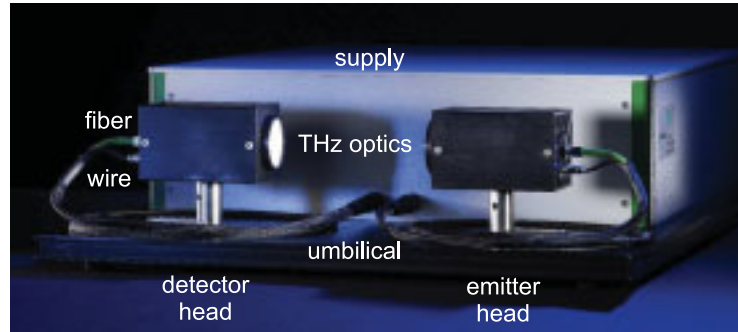
7.6 Fiber Based System

Figure 7.5: Photograph of fiber based system

The system which is the closest to the real world application is the fiber based system (see Fig. 7.5). Typical TDS systems use free space propagation to guide the fs pulses from the laser to the emitter and detector. This can easily be done using standard components like mirrors, lenses and polarization optics. But once aligned the system is fixed and the angle between emitter and detector can not be changed easily. For example a scattering experiment under different angles would not only be time consuming in the arrangement but also not be reproducible in terms of relative THz amplitudes. The fiber guided pulse transmission offers a high flexibility for the positioning of the emitter and detector heads. The setup can be designed completely eye-safe, mechanically, thermally and environmentally independent of the place of application.

The main difficulty of a fiber based system is how to transmit the fs pulses from the laser to the semiconducting chip without pulse distortions [141, 142]. Depending on the fiber length an initially Fourier limited pulse with approx. 100 fs pulse duration will be dispersively broadened in the fiber until it reaches some tens of ps. Such pulses can not be used for broadband THz-TDS anymore [143]. So an elaborate dispersion management is necessary.

The used fiber is a single mode polarization maintaining fiber. It has a positive material dispersion at the wavelength of the used IMRA fiber laser ($800\,\text{nm} \pm 4\,\text{nm}$). The reason for that particular choice is not the absorption which is usually crucial for the telecommunication light transmission over kilometers of fiber. Here the chromatic dispersion is the limiting factor concerning the broadband transmission. Therefore, a single mode fiber with polarization maintaining property is needed. This allows for flexible point-to-point transmission of the fs signal. Otherwise polarization mode dispersion would lead to additional pulse broadening or even double pulses.

There are two main contributions for the broadening of pulsed signals with high peak power in fibers: The chromatic dispersion and the nonlinear effects. The first one can mostly be compensated by negative angular dispersion in a prism or grating compressor. The other one is much more tricky to compensate.
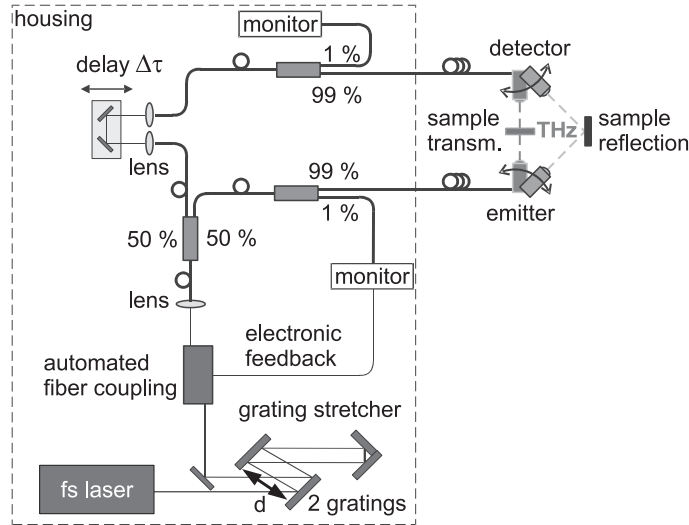
Figure 7.6: Layout of the fiber based system consisting of a fs laser, dispersion management, automated fiber coupling, free-space delay line and measurement heads

A simplified scheme of the fiber based system can be seen in Fig. 7.6. The most important part is the dispersion management unit. Here it is realized using a reflection grating compressor. The particular grating (line density $1200\,\text{mm}^{-1}$, blaze wavelength $1000\,\text{nm}$ at $36.8°$) shows an angular dispersion of $0.67\,\text{nm/mrad}$. It is located before the fiber line to pre-chirp the pulses by a strong negative dispersion. So the high peak power of the ultrashort laser pulse is coming up only at the end of the fiber. Other used key components are the automated fiber coupling (piezo mounted mirrors with feedback loop) and the measurement heads. The latter ones are hand-held and allow for a flexible alignment in a reflection or transmission geometry.

Figure 7.7 shows the pulse length of a pulse with $6\,\text{mW}$ average optical power after the propagation through a $2\,\text{m}$ long fiber. For a distance of $d \approx 175\,\text{mm}$ between the gratings the minimum pulse length τ_{min} is reached. This is the working point for the following measurements. Of course, the distance d is a function of the used fiber, optical power and fiber length. It is first adjusted by an autocorrelation measurement and then optimized online with the THz signal.

A comparison between the interferometric autocorrelations of the laser pulses before the stretcher and after propagation over $2\,\text{m}$ of fiber are plotted in Fig. 7.8. It is obvious that the stretcher can pre-compensate the following dispersion in the fiber very well. The measured pulse durations only change from $93\,\text{fs}$ to $95\,\text{fs}$. So for the here chosen arrangement and specifications a nearly distortionless transmission can be guaranteed.

The grating stretcher can compensate for the linear part of dispersion caused by the fiber. But for longer fibers also the third order dispersion (TOD) influences the pulse duration in a parasitic way. Figure 7.9 shows this behavior for different fiber lengths L_{fiber}. The accumulated TOD increases the minimally achievable pulse length. Since
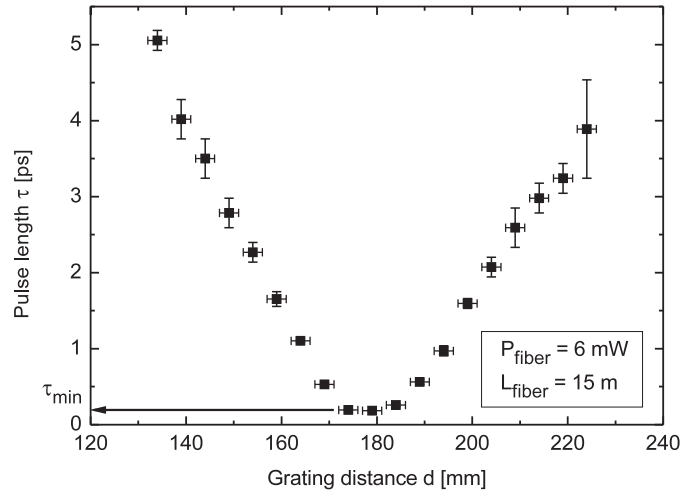
Figure 7.7: Dispersion compensation with grating stretcher. By changing the grating distance d the dispersion can be controlled and the minimal pulse length $\tau_{\min}$ is set.
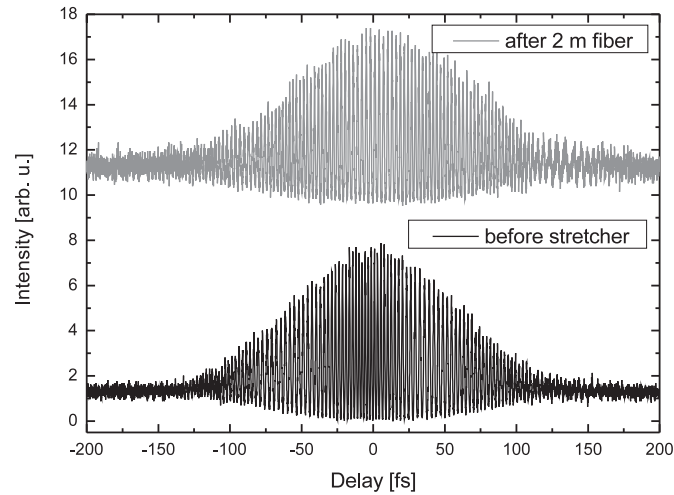
Figure 7.8: Measured interferometric autocorrelation of the pulses in the fiber transmission line. Bottom: before the stretcher (93 fs), top: after the fiber (95 fs), offset added for clarity

the pulse duration is directly correlated to the detectable THz bandwidth, a longer fiber will reduce the accessible bandwidth. But still, fiber lengths of up to 10 m are feasible with this technique. For longer fibers the bandwidth will be reduced, unless the TOD is compensated as well.

In this measurement only some mW of optical power are propagating. This is sufficient to gate a photoconductive switch (see chapter 4.2). Depending on the chosen antenna
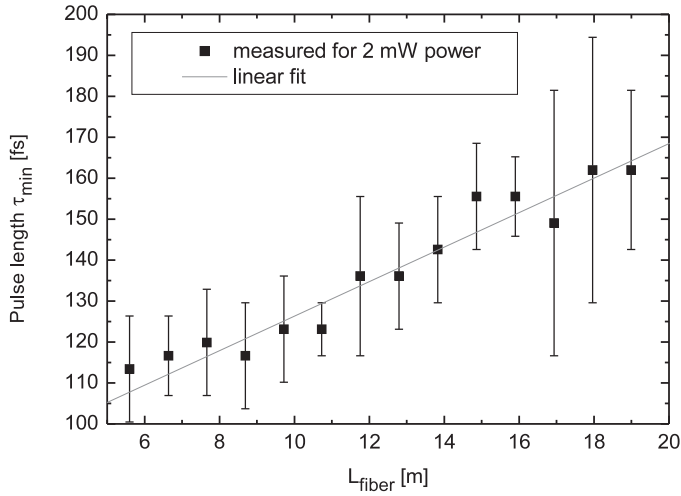
Figure 7.9: Measured minimal pulse length τ_{min} for different fiber lengths L_{fiber}. The stretcher is always readjusted for the shortest possible pulse length.
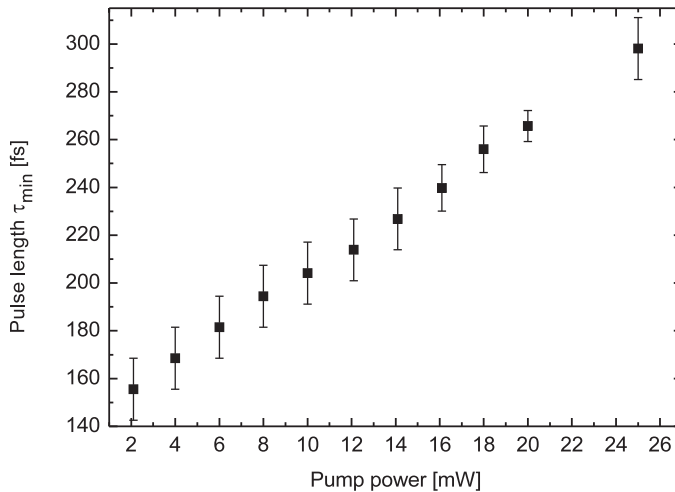
Figure 7.10: Measured minimal pulse length τ_{min} at different pump powers

geometry, also a higher power is allowed until the performance saturates or the device is damaged. So sometimes more optical power is needed at the end of the fiber.

The behavior for a larger pump power in the fiber is measured in Fig. 7.10. It is obvious that for increasing optical power the pulse length τ_{min} is extended with a steep slope. This is attributed to nonlinear effects in the fiber, mostly self-phase modulation (SPM). The induced phase change can not be compensated with the chosen simple grating compressor. But still the realized setup can operate up to a couple of meters at low optical power. A spectral bandwidth of above 3 THz with a good SNR is obtained.

Further on, the data acquisition time is drastically reduced by a rapid scanning delay

line in the time domain. Data sets with high spectroscopic resolution can be recorded with a repetition rate of 200 Hz [144, 145]. An online spectroscopic evaluation is possible and makes this system more than comparable to other commercially available THz-TDS systems.

8 Data Evaluation
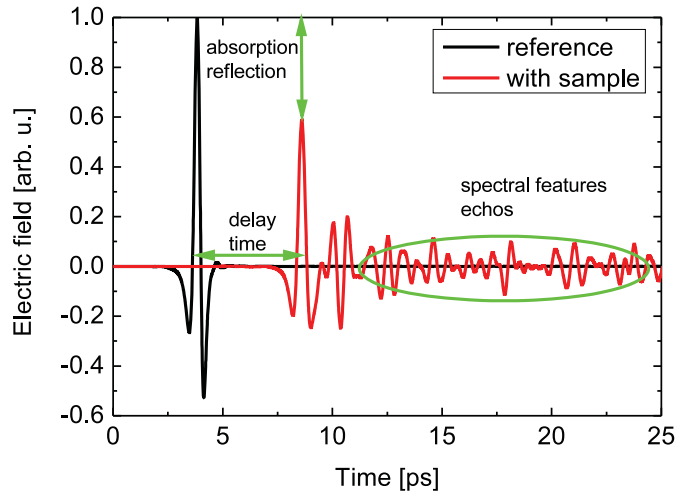
Figure 8.1: Data evaluation in the time domain brings the amplitude and delay information. A Fourier transformation is needed for spectral evaluation.

The principle of THz-TDS is already known from chapter 3.1. A typical recorded THz pulse, respective its electric field is shown in Fig. 8.1. Now it is the question which physical or, in most cases, optical properties are of interest. A good overview of the possibilities of data evaluation can be found in [146]. The most common algorithms of data evaluation operate in the time domain. Depending on whether the measurement is carried out in transmission or reflection the explanation differs.

In a transmission measurement one just records a data set and compares the change of data by inserting the sample. So the relative reduction in amplitude corresponds to absorption, Fresnel losses or scattering. The change in delay of the main peak maximum is a measure for the added optical thickness which is the product of refractive index and geometrical thickness. An evaluation in the frequency domain will measure absorption or scattering, but not only integrated over the entire used THz spectrum but also for some single frequencies or spectral bands.

In the frequency domain the transmission function $T(\omega)$ of a plain sample with refractive index $n = n(\omega)$ in the THz range and extinction coefficient κ is given by

$$T(\omega) = \frac{E_{\text{sample}}}{E_{\text{ref}}} = \frac{4(n + i\kappa)}{(n + 1 + i\kappa)^2} \, exp\left[i\frac{(n-1)\,\omega}{c}\,d\right] exp\left[-\frac{\kappa\,\omega}{c}\,d\right] \tag{8.1}$$

The terms account for the boundary losses at the two interfaces between sample and air and the lossy propagation in the bulk sample. Scattering in the sample or diffraction at edges are not included. So by appropriate choice of the reference waveform with e. g. an empty sample holder or different sample thicknesses can reduce the artifacts.

Depending on the sample or experimental demands some measurements have to be carried out in reflection and not in transmission mode. Also these can access the amplitude and delay in the time domain. But here the amplitude is influenced by much more factors: The interface, coating, alignment and surface roughness. The interface or boundary defines the amount of reflected and transmitted light. This may be a metal coating showing a high reflectivity or a styrofoam block with a very weak reflection. Also all interfaces with a difference in refractive indices cause a reflection according to Fresnel's law. The delay time when the THz main peak is detected is related to the runtime it takes the THz pulse to pass from the emitter to the detector. A variation of the positioning of the sample in the direction of THz propagation will increase or reduce the time delay unlike in a THz transmission measurement [147]. Also spectroscopic data can be recorded in reflection. This may be wavelength dependent scattering at a rough surface or spectral absorption bands. Since the absorption coefficient and the refractive index are related via the Kramers-Kronig relation, it is sufficient to measure one of this quantities with a spectral resolution.

8.1 Amplitude

To find the maximum amplitude, one has to keep in mind that a variation of thickness in transmission and a movement of the sample in reflection changes the time position of the maximum. Some proposed TDS systems do not use a scanning delay line during the measurement. If the sample needs to have an accurate thickness, then a deviation of the appropriate thickness will change the runtime and thereby reduce the measured THz amplitude. This technique may be sufficient for some niche applications, but for most of the samples with inner structure or layered surfaces a scan in the time domain is necessary.

Assume a recorded electric field consisting of N discrete data points in the time domain $E(0)$, $E(t_1)$,..., $E(t_N)$. The amplitude algorithm just looks at all data points and remembers the largest one (without loss of generality $E(t_{\text{max}})$). Then this value is saved as the maximum value. Sometimes when a phase jump is observed at an additional boundary it makes sense to look for the absolute value of the amplitude. This amplitude change here is not spectrally resolved. So broadband characteristics are detected weighted with the spectral power distribution of the emitter.

Up to now this consideration is valid only for one single pixel. If we now move the

sample in x and y-direction stepwise, and record a complete signal in the time domain for each position, we come to an array of electric fields. For m points in the x and n in the y-direction, this is a $m \times n$ matrix with N entries $E_{11}(t),\ldots, E_{mn}(t)$.

A typical recorded waveform has a file size of $100\,\text{kB}$ on the hard disk. For a data set with 100×100 supporting points on the sample there is a data volume of $1\,\text{GB}$. This is a size which is difficult to handle. If all 100×100 electric fields are saved as single files it even causes problems for FAT-formatted hard disks. NTFS file systems can handle the amount but are still very slow in performance. So it's the best solution to merge all single files into one big indexed file or MATLAB® $m \times n \times N$ matrix.

In imaging applications for each data point the amplitude maximum has to be found separately. The result is written into an output matrix, the amplitude transmission of the sample. This data evaluation reduces the volume of the data set drastically and it visualizes the interesting features of the sample.

THz-TDS is also a tomographic measurement technique. Each time frame for a fixed time delay t_fix gives a slice of the sample at a defined depth. If these single frames $E_{11}(t_\text{fix}),\ldots, E_{mn}(t_\text{fix})$ are considered as frames of a movie one can scroll through the sample like in a real tomographic measurement. Since the complete time dependent electric field is available for each pixel of the sample, no further detector or cutting plane is necessary.

To guarantee an artefact-free evaluation system, parameters like thermal expansion, optical stability, current humidity or sample tilting have to be accounted for or removed by software.

8.2 Delay Time

If during the evaluation of the maximum amplitude $E(t_\text{max})$ also the delay time of the amplitude t_max is saved then the delay time matrix is generated straightforward. This time difference of the THz maximum corresponds to the phase difference.

If the refractive index n_THz of the sample is known, the delay information can be rescaled to a thickness d_sample of the device under test (DUT). In a transmission measurement this is just the relation of optical thickness given by

$$d_\text{sample} = \frac{c\,\Delta t}{n_\text{THz} - 1} \tag{8.2}$$

where Δt is the time difference with and without sample. In the experiment either a reference without sample is recorded before the imaging starts or the frame is chosen in the way that at least one pixel is next to the sample. This is the preferred option because this is the closest to the real experimental conditions.

The reflection measurement is self referencing. If the sample is transparent for THz radiation there will be a front side reflex due to the refractive index step between air and sample. It is followed by an echo pulse from the next interface, may this be the edge of

the sample (again refractive index step sample–air) or a further material with different refractive index. From the temporal spacing Δt between these two pulses the thickness of the layer can be determined by

$$d_{\mathrm{sample}} = \frac{c\,\Delta T}{2\,n_{\mathrm{THz}}} \tag{8.3}$$

Equations 8.2 and 8.3 are only valid if the sample is perpendicular to the THz beam. In a transmission measurement otherwise the refraction at the interface and the projection of the real thickness with respect to the propagation direction is measured. But for small incidence angles this error can be neglected. For the reflection setup it is similar for the timing information but completely different for the maximum amplitude which does not find the way to detector in a misaligned system.

Sometimes experimental constraints make reflection measurements under an angle of Θ between the THz incidence and the surface normal necessary. The angle of the detection is kept in the direct reflection. But still the different runtimes of the phase fronts and their refraction at the boundary have to be included in the calculation. So the formula for a reflection measurement under the angle Θ reads

$$d_{\mathrm{sample}} = \frac{c\,\Delta T}{2\,n_{\mathrm{THz}}\,\cos[\arcsin(\sin(\Theta)/n_{\mathrm{THz}})]} \tag{8.4}$$

To get a high depth resolution a mechanically stable system is necessary. The reproducibility of the delay line (here better than $1\,\mu\mathrm{m}$) is one fundamental limitation of the accuracy. The other one is given by the THz pulse length. A rough estimation of a $1\,\mathrm{ps}$ long pulse with a SNR of 1000 offers in a linear approximation (sawtooth) distinguishable data points with a separation of $1\,\mathrm{fs}$ which corresponds to a resolution $0.3\,\mu\mathrm{m}$ in free space. But this accuracy can not be reached without further precautions.

Because it is mathematically easier here just the maximum of the THz peak is used for data evaluation. If the steep trail of the electric field or the zero-crossing would be evaluated an even higher depth resolution would be possible. But then other problems would show stronger influences and the software data preparation would get very complex and be a task of image reconstruction.

8.3 Spectral Information

If an electric field is recorded with sufficient scanning interval the spectral information can show the THz "fingerprint" of the sample. In transmission this is for most samples absorption at discrete frequencies and extended absorption bands. Depending on the sample a broadband scattering background can be superimposed e.g. for powder with grain sizes in the wavelength range. The absorption is displayed in arbitrary units. A plot in absolute absorption coefficients is only possible if the absorption length is known

and the surface Fresnel losses are excluded.

Here the evaluation is done by the eye. A comparison with reference databases can distinguish known substances. Machine implemented solutions are also possible. Pattern analysis at only a few frequencies and their relation is already sufficient to distinguish between substances even if interfaces reduce the performance [148]. The principle of chemometrical methods which is know from other wavelength ranges, especially the IR, can be implemented as well.

For the application spectroscopic resolution is only required if the content has to be determined. Unfortunately the spectroscopic resolution increases the data acquisition time in standard TDS systems. Fast systems with a shaking or rotating delay device are proposed as TDS systems with a high spectral resolution [144, 145]. Also asynchronous optical sampling allows for online spectroscopic measurements [23]

8.4 Region of Interest (ROI)
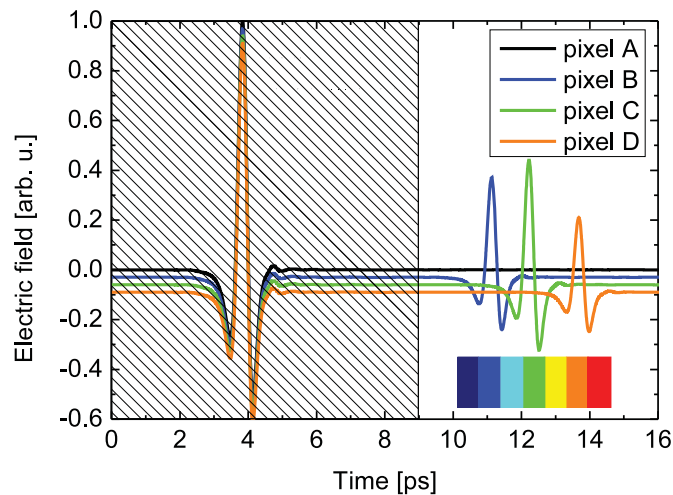
Figure 8.2: A region of interest in the time domain can reduce artifacts by choosing the right timing window.

The specified algorithms show how to reduce the large amount of data to get one single matrix. There are two different possibilities to enhance the interesting part of a THz image. The most obvious is to choose a region of interest (ROI). Then the grayscales or the colorbars can be adjusted to give the maximum contrast to the particular feature. If for example in a strongly absorbing sample the normalized transmission is nearly zero while at a pixel next to the sample it is one, the colorbar should not be in the range of $[0 \ldots 1]$ but in e.g. $[0 \ldots 0.1]$. Then the structures in the sample are emphasized while without the ROI only a two color black and white image would be seen.

A big benefit of THz-TDS compared to cw systems is that here also a ROI can be preset also in the time domain. This can be realized either during the measurement by

choosing a small scanning window or afterwards by skipping time windows during the evaluation. This possibility is described in Fig. 8.2. It shows three pulses which are shifted a little bit in amplitude for clarity. This is a signal which is quite common for THz reflection measurements. The strong peak at 4 ps is caused by the first front surface. The following echoes emerge at the rear side surface of the sample. The front surface is flat and homogenous while the sample has a varying thickness and an unknown boundary to the next sample or holder. The standard algorithms would get stuck at the pre-pulse. So the amplitude and the time information would show no dynamics. If the time window is chosen according to the sample (skip of the first pulse) then the emphasis is laid on the second pulse sequence which geometrically corresponds to the layer thickness or the back surface of the sample.

8.5 Measurement Time

The measurement time of THz imaging and spectroscopic applications is up to now the most limiting factor in comparison to other measurement techniques. Since in this thesis mostly conventional linear stages are applied, the data acquisition time is still quite long.

In the raster imaging setup there are two related times which one has to consider to calculate the overall measurement time. The first is the positioning of the sample itself, the other one is related to the movement of delay axis. For an imaging measurement three axes and the lock-in amplifier have to be controlled and clocked synchronously. So for the initialization, positioning of the axis and waiting for the integration constant at the lock-in amplifier needs approx. five seconds per pixel. That is some kind of offset which has to be added independent of the data acquisition time itself. In a simple amplitude or delay mode where only one millimeter has to be scanned, the measurement time does not contribute to the time per pixel that much. Unlike for spectroscopic measurements, which require a slow scanning velocity and a long integration constant, where five minutes can be assumed per pixel.

8.6 Humidity: Simulation and Experiment

For real-world applications besides system parameters also environmental parameters have to be included in the data evaluation. The most disturbing influence in the broadband THz spectroscopy is humidity [149]. There are strong rotational transitions above 500 GHz which must be accounted for. Free-space THz spectra show absorption from these water molecular lines unless the THz path is purged with dry air or nitrogen which is not always possible. Therefore precise knowledge of the absorption accumulated in ambient air is indispensable [150].

Vapor absorption lines are very strong, however, since the properties of the atmosphere are known to the operator of the THz setup, these effects can be arithmetically removed unless the signal falls below the signal-to-noise ratio. Since the absorption lines are strong and narrow, the calculation must be precise. We have checked various models well-known
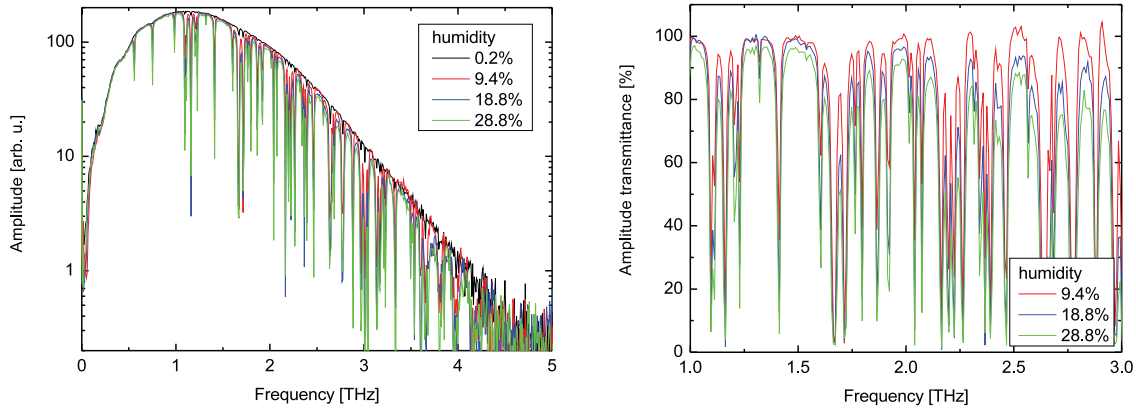
Figure 8.3: Measurement of water vapor absorption at different humidities

in meteorology covering the infrared and the microwave region of the electromagnetic spectrum. By extending the models into the THz region, an accurate description of the measured spectral absorption is reached [151, 152].

A typical measurement for different humidities is shown in Fig. 8.3. Here no sample is in the THz beam. The propagation length is 1 m in free-space. The transmission is calculated by a division through the reference at 0.2% humidity which is the lowest reachable value for the used air dryer and already below the measurement accuracy of 1% of the used hygrometer. Obvious is the first water absorption line at 560 GHz and the dense absorptions above 1.5 THz. As expected, the absorption depth is increased for higher humidities. The values above 100% are related to an offset caused by thermal drifts. Some open "operating windows" are present limiting the accessible bandwidth. But also within these windows of high transmission there is still a reduced amplitude. Transmission does not increase up to 100%. In some simulation algorithms this overall reduced amplitude reduction is described as an virtual strong absorbtion at an arbitrary high frequency. This tail then takes influence corresponding to an humidity dependent offset.

The overall average amplitude reduction is shown in Fig. 8.4. The narrow band absorption at frequencies of the emitters maximum spectral density and the overall reduction take influence on the received THz amplitude. So also the spectral amplitude at frequencies within the operating windows above 1 THz suffers losses. The humidity dependent measurement with a propagation length of only 1 m already shows the challenge for THz stand-off identification under real world conditions. With broadband THz radiation distances of up to 5 m seem feasible. For longer ranges free-space THz techniques are challenging.

To evaluate limitations of THz stand-off detection a numerical model named linefit of the Forschungszentrum Karlsruhe (Germany) is used [153]. It was developed in the Institute for Meteorology and Climate Research for the IR spectral range and extended towards the THz frequency band.
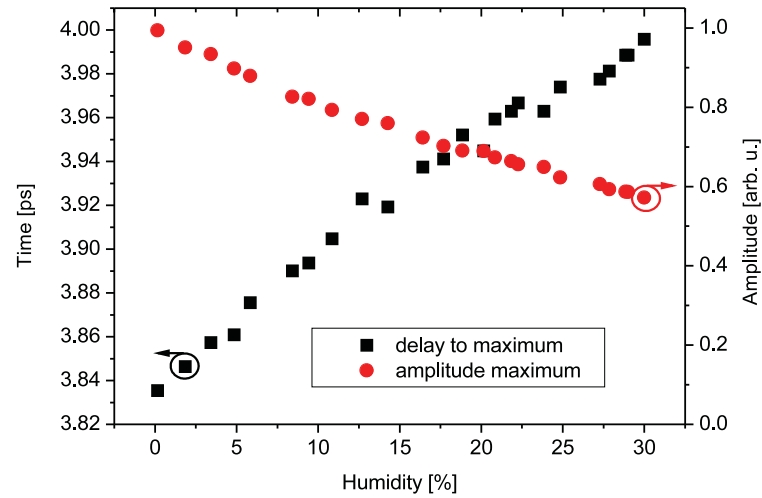
Figure 8.4: Measured amplitude reduction and delay changes at different humidities
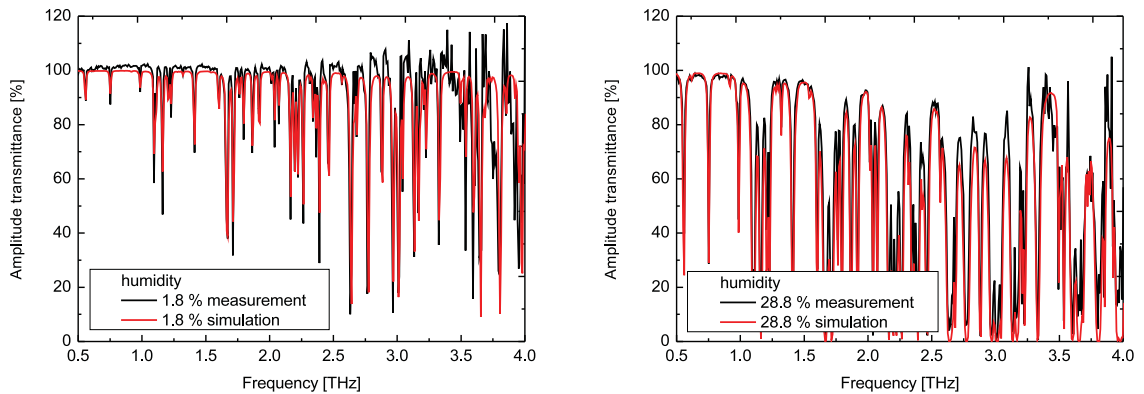
Figure 8.5: Measured and simulated amplitude transmission for different humidities and a fixed THz path length of 1 m. Left: 1.8% humidity, right: 28.8%

The correlation between the simulation and measurement is checked for various humidities. In the experiment the fixed THz beam path in the sealed-off chamber of the transmission imaging setup is 1 m long. The simulations are carried out with the same parameters (humidity, propagation length, temperature, air pressure, frequency resolution). Figure 8.5 shows exemplarily two comparable plots at low and high humidity (left 1.8% and right 28.8%). For both values the plots show a good agreement in the position, depth and line shape of the absorption. The overall amplitude transmission in the experiment sometimes reaches above a value of 100%. This is related to inconsistencies of the references caused by thermal drifts of the optical components. When calculating the reference division especially at high frequencies even small deviations cause a large change of the signal. So the error increases for higher frequencies which explains the larger difference between simulation and experiment. It is assumed that the simulation

is closer to the physical conditions than the noisy experiment can detect it. Within the accuracy the influence of air pressure and temperature is not affecting the absorption for typical conditions. Now that the simulation is calibrated with respect to the experiment in the THz range, the limitations of broadband THz stand-off detection under various humidities and path length can be estimated.
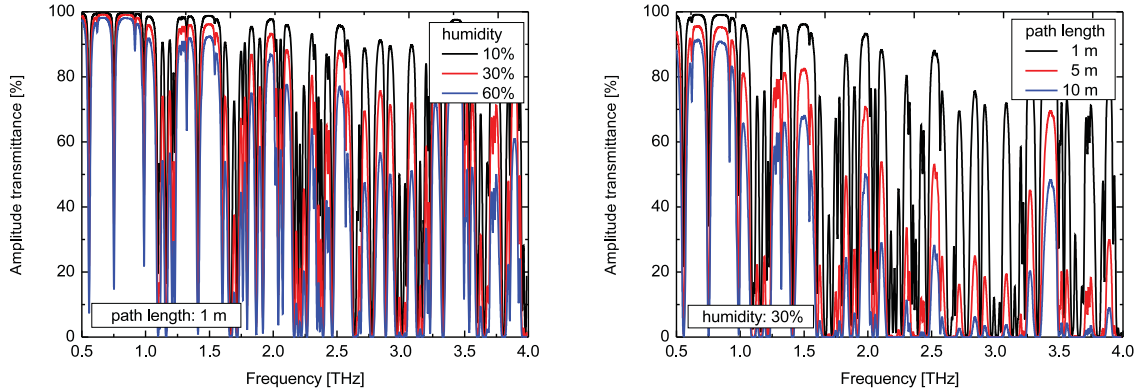
Figure 8.6: Simulated amplitude transmission for different humidities and THz path lengths. Left: 1 m path length fixed and humidity variable, right: 30% humidity fixed and path length variable

In Fig. 8.6 simulations for higher humidities (left) and longer distances (right) are shown [151, 152]. Already 1 m path length which corresponds to a stand-off distance of only 50 cm for a humidity of some 10% reduces the performance of the THz system. Especially in the high frequency part above 2.5 THz the absorption lines are so dense that also the average transmission is low in this window. Keeping the reduced SNR of typical TDS systems in this frequency range in mind the accessible bandwidth is limited to approx. 2 THz.

But even if the humidity is kept on a moderate level (here 30%) the possible operating distance remains short. For a single pass distance of 5 m still 20% of the THz amplitude will pass through the air, even if no sample is in the beam. So here it is obvious that only a few meters are feasible for THz stand-off detection.

9 Industrial Applications

In the field of non-destructive testing the whole accessible electromagnetic spectrum is used to gather information on the device under test. Some first applications arose also for the THz frequencies which unify some specific features known from the neighboring spectral ranges. This is the high transparency of dielectrics which is typical for the microwaves and the spectral characterization via fingerprints like carried out with IR radiation. Furthermore, with THz-TDS systems tomographic measurements with one single detector can be performed by using the relative time delay of the THz pulses or their echoes. These features are very interesting for detecting shape, geometry, content, active substance distribution, thickness, layer sequence, density and so on. Depending on the sample's material THz-TDS can detect these values in transmission or reflection. Different algorithms of data evaluation display the desired parameters.

Another commercial but also challenging application is related to the safety and security sector. There are no devices for the stand-off detection of explosives like TNT, RDX or C4 available. Worldwide different sensors are tested to show the possibilities of the particular detection techniques. This may be laser-induced optical breakdown spectroscopy (LIBS), molecularly imprinted polymers (MIPs) or neutron activation. None of those has reached widespread market acceptance because the devices are insufficiently developed, too expensive, dangerous to humans or simply not accepted by the public. So this is a niche where THz radiation will have to show its strength.

But also the THz radiation itself has some physical properties which limit the possibilities. The first is that THz radiation gets nearly completely reflected at every metal. So it is e.g. not possible to detect anything within a metallic packaging or within the interior of a car. Like for the microwaves even unpolished surfaces show a very good reflectivity for the THz frequencies. This can be used to detect small deposits on metallic layers. The second problem is that water has a strong absorption in the THz range. Liquid water is nearly opaque for THz frequencies since very broadband absorption bands are present. But also water vapor shows rotational transitions in the THz range like all polar molecules. These absorption features limit the stand-off distance to some meters, but can also be used to trace gases or measure the water content very precisely (see chapter 8.6).

The advantageous properties of THz radiation are manyfold. The benefits from the microwave and the IR spectral region are unified in the THz band. But why there are so few THz applications in industrial operation or in our everyday life? It is one thing to demonstrate that THz radiation can solve a problem. But to compete with other elaborate techniques already established at the market is another step. Under laboratory conditions where required space, cost, measurement time, power consumption, and reliability play a minor role, the THz spectral range is prospering for years (e.g. gas analysis [154–157]).

But for industrial applications a lot more research and development on the system side is necessary. And vice versa, the needs from the applications also bring up new topics for the fundamental research.

A lot of potential applications are proposed on topics like telecommunication, material science and non-destructive testing. Among these, some are quite known to the public like applications in medicine [158], biology [159], electronic circuit testing [160], drug detection [148], security applications [161], and testing of industrial objects in general [162]. But the first real world application of THz radiation was in the field on non-destructive testing in the aerospace industry.

After the disaster of the space shuttle Columbia in 2003, NASA was not allowed to relaunch their space shuttles due to problems with the insulation foam of the fuel tank (sprayed-on foam insulation). Inhomogeneities, air intrusions and debonds could not be controlled and measured accurately with conventional measurement techniques up to then. As a consequence, the spare parts could get loose during take-off or re-entry in the atmosphere and damage the outer cladding of the shuttle. This was expected to have caused the disintegration. So there was the urgent need for a new measurement technique which can detect above mentioned failures accurately. Also other techniques were tested with prepared samples containing willingly introduced damages. The comparison between the THz image [163] and other detection techniques including x-ray backscattering and ultrasonics showed that THz detection can compete with other established technologies. This gave the deciding factor for the THz technique. In the first step for NASA cost did not play any role. Only the result counted, to find the failures and to launch the space shuttle again.

That was a publicly funded project, but to bring a THz system to a real world industrial market the system has in most cases to guarantee the following specifications:

- recording, evaluation and presentation of data

- reliability, 24/7 operation, hands-off

- semi-skilled operator sufficient, better stand-alone, computer controlled

- low space requirements

- insensitive to environmental influences (humidity, temperature, air pressure, etc.)

The specifications of different THz-TDS systems were discussed in chapter 7. Now the aim is to demonstrate that THz technology can solve the particular task. It will show the possibilities of THz radiation for various applications.

If the device under test (DUT) is two-dimensional the THz imaging setup is used. For spectroscopic measurements or single pixel measurements the automated positioning of the sample in the beam path is not necessary. Then also the other setups are used, depending on availability.

9.1 Calibrated Test Samples (BAM)

Figure 9.1: Test samples for THz non-destructive testing provided by BAM

The German Federal Institute for Materials Research and Testing (Bundesanstalt für Materialforschung und -prüfung, BAM) supplies testing samples (Fig. 9.1) for THz non-destructive testing (NDT). They are already calibrated and specially fabricated as testing samples (device under test, DUT). So THz images of these DUTs are recorded to check the possibilities of THz-NDT and the specifications of the assembled THz imaging systems, respectively. The electric field for each pixel is recorded by one of the scanning TDS systems introduced in chapter 7. A subsequent data evaluation (see chapter 8) reduces the large amount of data and displays the particular feature.

Transmission

The samples which are used to determine the resolution of the THz transmission imaging setup are made of white polyethylene (PE) and red polyvinyl chloride (PVC). PE has a refractive index of 1.46 in the THz range and does not show high absorption or dispersion. Therefore, PE is an ideally suited material for THz transmission measurements especially because it is cheap and easy to prepare. Teflon (PTFE) would also be a good material for such kind of samples, but the raw Teflon is quite expensive and under some conditions it can melt during machining. The PVC samples show a higher absorption than the PE plates. This is a negative feature of the PVC itself and the added dyestuffs.

The first calibration sample BAM 1 is shown in Fig. 9.2. The layout of the 100 mm times 100 mm large PE sample can be seen in the photograph. The sketch gives the dimensions of the drilled holes. They are drilled through the wedged PE plate in a series with 1 mm steps (diameter 1 mm to 20 mm). The 4 holes at the edges are just for mounting. The

(a) Photograph

(b) Transmitted THz amplitude

(c) Sketch
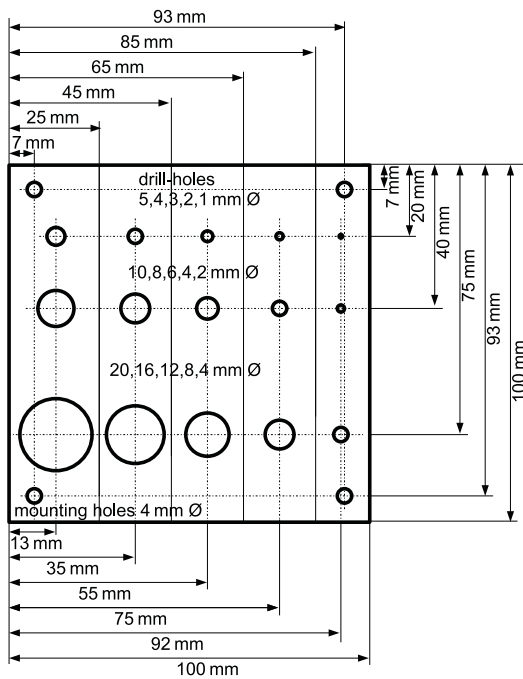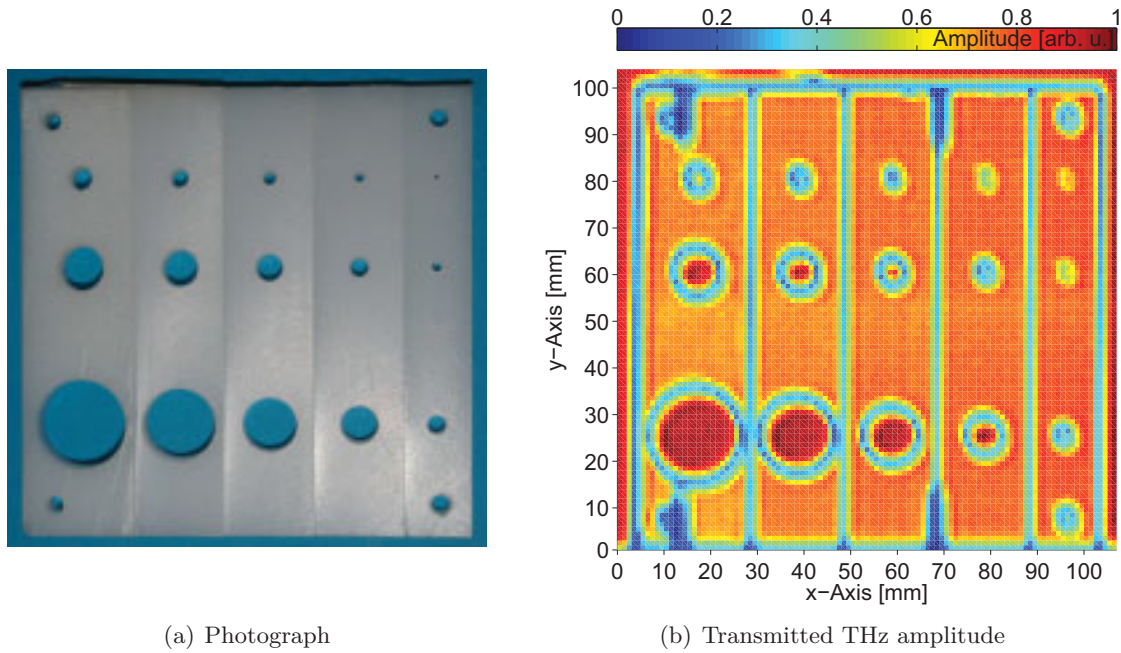
setting	value
$x_\text{steps} \times y_\text{steps}$	108×104
Δx [mm]	1
Δy [mm]	1
Δt [ps]	26.6
v_stage [µm/s]	500
ν_sampling [Hz]	64
t_int [ms]	30
t_meas [h]	25

(d) Measurement settings

Figure 9.2: PE sample BAM 1 with drilled holes for the THz-NDT. Comparison between THz transmission image (amplitude mode) and sample geometry [164]

measurement settings are given here as an example also to other measurements. The table lists the settings of the two imaging axes, the delay axis and the data acquisition of the lock-in amplifier, respectively.

To show the lateral resolution of the THz transmission setup the amplitude of the electric field transmitted through the sample in a false color illustration is displayed. The color bar is chosen in a linear scale. Red pixels show a high transmission like next to the sample and within the holes. The blue data points represent pixels with low transmission like at the edges of the holes. Since the sample is located in the THz beam waist (focus) of the setup, also small structures can be seen when the THz spot moves with respect to sample [165]. The THz amplitude displays the drilled holes in the DUT and its outer geometry in the two lateral directions. Even the smallest hole with 1 mm in diameter is detected. The thickness of the wedged sample does only slightly influence the transmitted amplitude. Each flat point on the DUT has an amplitude transmissivity of approx. 70 %. The stepwise structure of the bulk sample can not be seen in the amplitude display mode since most of the amplitude reduction is caused by Fresnel losses at the boundaries and not by absorption in the volume. So a change in thickness is insensible in the transmitted amplitude. Only at the steps themselves vertical lines can be seen over the entire sample. The reason is that a fraction of the THz pulse travels through the thick sample while the rest of the beam already sees a thinner piece. Because this way of data evaluation displays the overall highest amplitude at one time, this splitting up reduces the amplitude in the worst case by a factor of $\sqrt{2}$. If the integrated transmitted energy would be observed this feature could be removed except for the scattering losses at the edges.

But for the sample BAM 1 the same information content could also be recorded with a camera operating in the visible. Here neither the advantages of the timing information nor some particular THz properties are needed. For a similar sample the possibility to penetrate dielectrics is the advantage of THz waves in contrast to techniques relying on visible light. For sample BAM 2 the holes were not drilled through the PE, but blind holes were placed at the same positions (see Fig. 9.3). Here a THz transmission image is recorded, too. The amplitude transmission is shown for the interesting region of the sample.

Here the same explanation with the edges and the pulse splitting brings the contrast at the surface of the rim of the blind holes. For the smallest holes the detected shape is more circular (doughnut shaped) than point-shaped. This is caused by diffraction at the edge and the aforementioned double pulses for geometries in the range of the THz spot size. In the middle of some larger holes even the highest intensity can be detected. This may be attributed to the refraction and scattering of THz radiation at the edge of the sample.

This sample shows that in an application where hidden holes or air intrusions have to be found in plastics the same kind of imaging can find deviations down to a diameter of at least 1 mm. The holes do not have to be located at the surface of the DUT. Also in a layered sample or an homogeneous device failures can be found.

The THz image of a PVC sample (BAM 3) with the same geometry as BAM 1 shows a reduced overall transmission of approx. 10 %. This fact also reduces the contrast in the

(a) Photograph
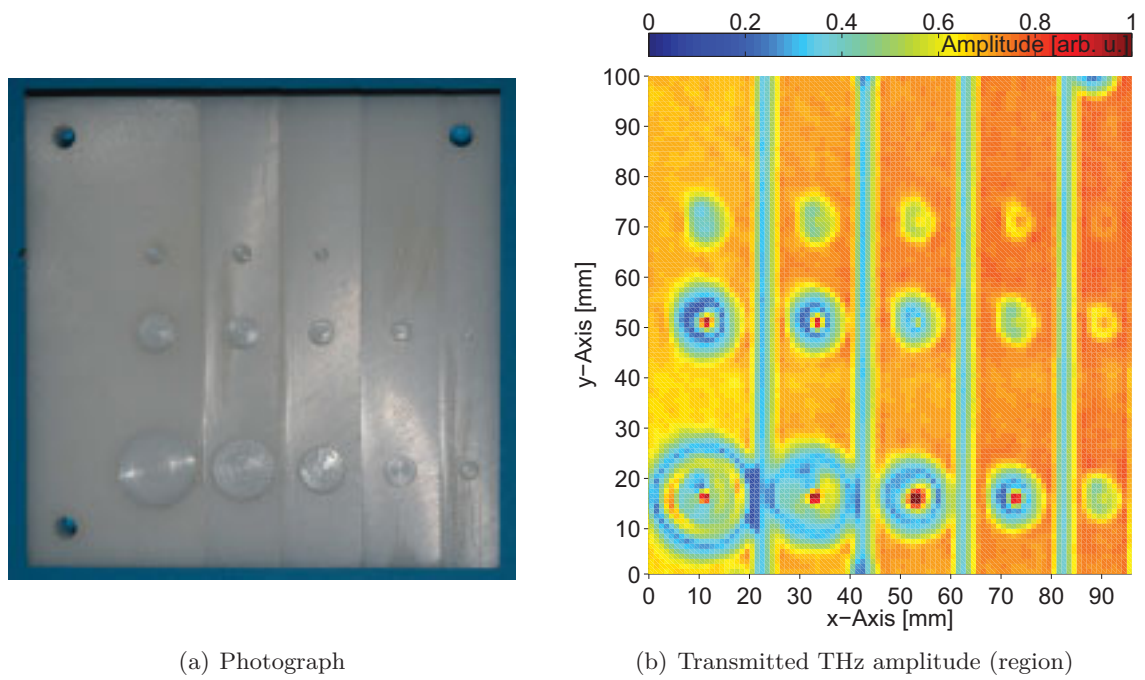
(b) Transmitted THz amplitude (region)

Figure 9.3: PE sample BAM 2 with blind holes for the THz-NDT. Comparison between THz transmission image (amplitude mode) and sample geometry

(a) Photograph

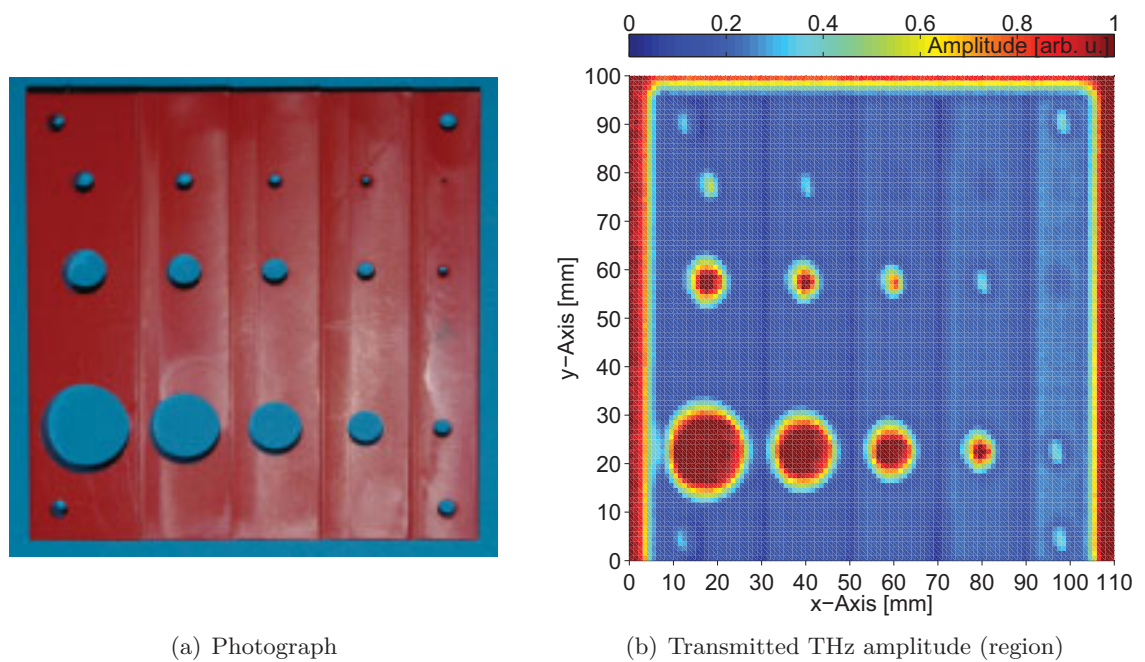(b) Transmitted THz amplitude (region)

Figure 9.4: PVC sample BAM 3 with drilled holes for the THz-NDT. Comparison between THz transmission image (amplitude mode) and sample geometry

holes. Especially the high frequency part of the THz spectrum is absorbed. This reduces the center frequency and thereby increases the THz focus diameter in the sample. The smallest holes here can just be assumed as shadows because most of the dynamic range is spent at the step between air and sample. An appropriate color bar can improve the performance. An automated change of the sensitivity of the the lock-in amplifier would also bring a higher resolution for the digital signal.

(a) Delay time of THz peak maximum   (b) Sketch
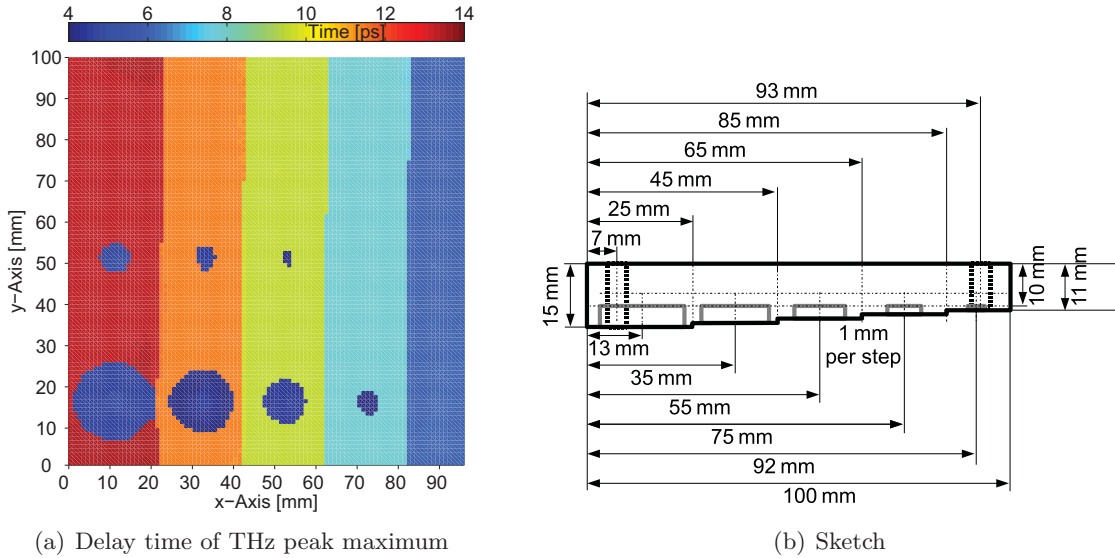
Figure 9.5: PE sample BAM 2 with blind holes for the THz-NDT. Comparison between THz transmission image (delay time mode) and sample geometry

The additional benefit which can be gained by a THz-TDS system compared to other techniques is the delay time information. For the same data set, which is evaluated in terms of amplitude in Fig. 9.3, the delay information in picoseconds is plotted in Fig. 9.5. It is obvious that the stepwise structure can be clearly resolved according to the geometry in the sketch. The caused delay Δt is given by the refractive index and the thickness of the sample d_{DUT} by $\Delta t = (n_{\mathrm{THz}} - 1)\, d_{\mathrm{DUT}}$.

So the time axis can be directly calibrated in terms of thickness if the refractive index is known. Otherwise, in a calibration measurement with a sample of known thickness, the refractive index can be easily determined. This means there is no need for a further scan to record thickness information on a DUT. The data set which already contains tomographic information is available.

Here the steps are quite distinguishable from each other. But not all drilled holes can be seen. The evaluated pixel information is just the time delay for the THz pulse maximum. Next to a small hole, most of the THz pulse passes by the dent and the time information will be the same like for an homogeneous plate. That is why the holes below a diameter of 6 mm are not directly resolved in the time delay mode. For these pixels the maximum of the THz amplitude is recorded for a delay time corresponding to the bulk sample.

The following peak in the electric field, caused by the fraction of THz intensity passing through the hole, is not taken into account in this kind of display mode. For the sample BAM 1 the holes down to a diameter of 4 mm are detected.

(a) Delay time of THz peak maximum   (b) Delay time in reduced time window
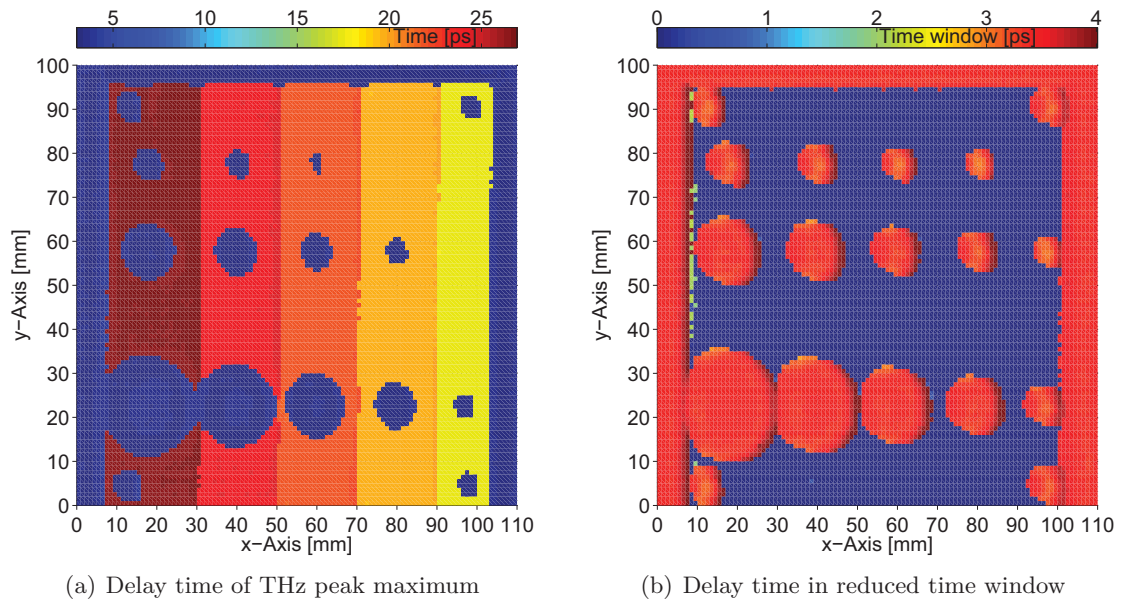
Figure 9.6: PVC sample BAM 3 with drilled holes for the THz-NDT. Comparison between THz transmission image (delay time mode) of full data set and reduced time window

A further increase in contrast can be reached if the time range is truncated the way that only the interesting region is in the scanning range. This can be done mechanically in the measurement by shortening the travel distance of the delay line. Of course, this can also be done by shortening the data set afterwards by software. A comparison between the full data set and reduced time window is shown in Fig. 9.6. The thinnest step of the sample brings a time delay Δt of 13 ps. Now the time range is reduced to 4 ps so that delay time including the plate's delay is out of the frame. So only within the holes the delay time is in the scanning range and brings an amplitude and defined delay time of the maximum. For all points of the DUT where an additional delay is caused, it will not find a real maximum (indicated by blue 0 ps in the plot).

This is a possibility only offered by a THz-TDS system, e. g. a cw THz system could deliver THz radiation with the same wavelength, but not offer a detection in a particular time window. Also interference within the sample would cause artifacts.

Reflection

For reflection measurements samples with a sequential metallization on a plastic plate are available. An image of the reflected THz amplitude of the DUT BAM 4 next to a

(a) Reflected THz amplitude
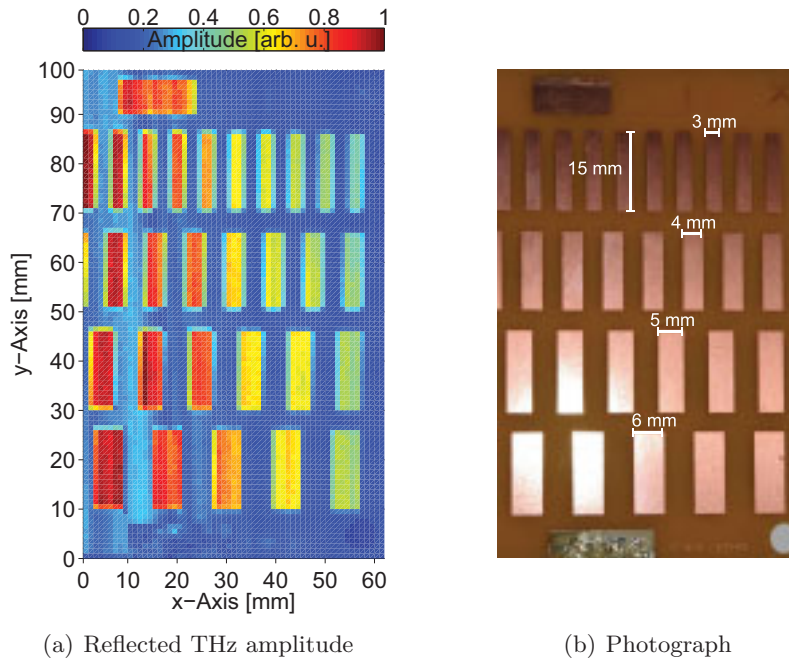
(b) Photograph

Figure 9.7: Plastic sample BAM 4 with metallized pads for the THz-NDT. Comparison between THz reflection image (amplitude mode) and sample geometry

dimensioned photograph can be seen in Fig. 9.7. All metal pads down to a size of 3 mm and their shape could be resolved.

It is remarkable that the amplitude of the reflection of the metallization seems to change linearly with the scan. That is actually not the case. Rather the movement of the sample and the change of positioning in the direction of THz radiation is responsible. If the sample is not directly in the focus, the spot will not be optimally mapped to the detector and this results in an amplitude reduction of the reflected signal. The kind of used metal and the surface roughness are less important for the strength of the signal. It is more important to keep the sample perpendicular to the beam and the deviation of the focus minimal.

The time image in Fig. 9.8 underlines this statement. It is obvious that the runtime to the main back reflection (first surface) varies in an interval of 15 ps. This is not due to a curved surface of the sample but related to the tilted clamping of the sample's mount. This corresponds to a sample movement of 2.25 mm out of the focus along the direction of the THz beam.

But still the thin metal coating can be seen also as a difference in delay. The visual evaluation can resolve the steps at the edges of the pads. A linear fit of the offset delay towards both imaging axis could remove the inclination. Please note that a reflection system has no reference runtime or easy to reproduce reference spectrum. What one can do is to place a polished metal plate with micrometer alignment screws exactly into the
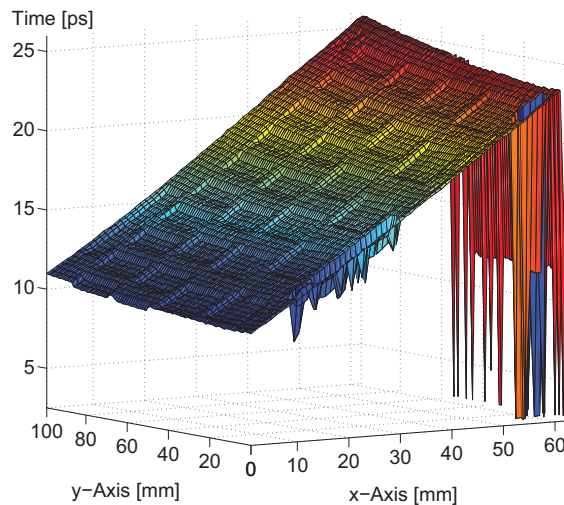
Figure 9.8: Plastic sample BAM 4 with metallized pads for the THz-NDT. THz reflection
image (delay time mode)

focus and record a reference electric field. But still the focus and angle deviation, the
curved metal surface and the surface roughness will change the signal. This is in contrast
to a transmission measurement more subject to errors.

9.2 Thin Film Measurement

Industrial production processes often require an accurate determination of the thickness
of a sample, layer, or coating. Ordinary techniques require either a mechanical contact or
work with optical reflexes typically in the visible or IR. Sometimes none of the standard
techniques is applicable, perhaps because of the sensitive surface of a wet sample, strong
scattering environment of a curved surface or a non-metallic sample. Then a thickness
measurement using THz radiation can offer some useful advantages.

Recently Hils et al. [166] reported on THz cw profilometry carried out at 600 GHz. They
achieved a depth resolution of 0.5 μm verified by an interferometer in the visible. This is
already a very good result keeping in mind that the within this thesis used linear stages
have only a bidirectional reproducibility of 1 μm. Within a linear scan the mechanical
step size is 0.1 μm. So if someone wants to come to such a high resolution already other
factors like mechanical stability, thermal drifts, and sample positioning start to create
offsets.

Transmission

The discussion of the results obtained with the BAM samples 1–3 is extended now to
samples with thickness changes below the THz wavelength. If the sample and the holder
allow a THz transmission measurement the thickness change is easily detectable. Scotch
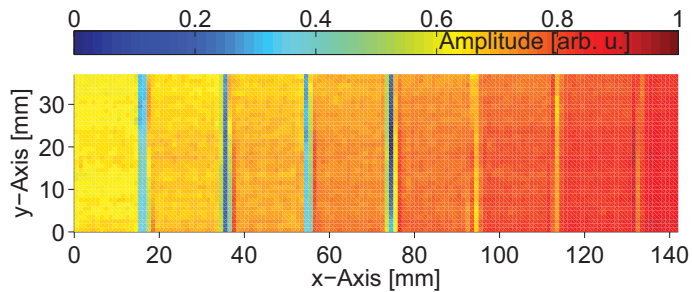
(a) Transmitted THz amplitude
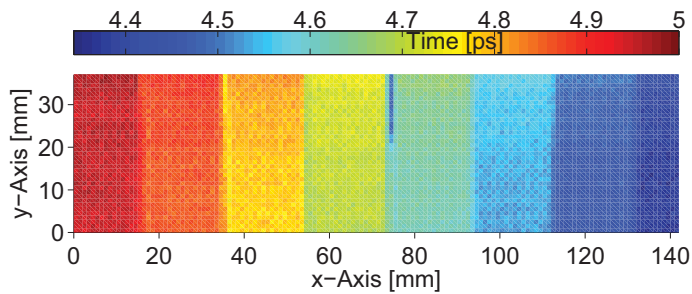
(b) Delay time of THz peak maximum
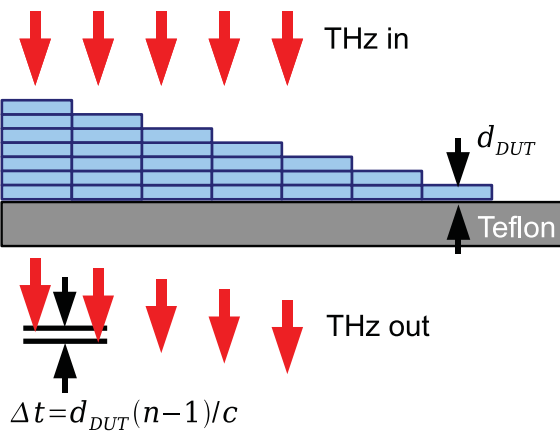
(c) Sketch

Figure 9.9: Thin film measurement in transmission. The reference is a Teflon plate. Step-wise layers of Scotch tape are attached on top.

tape layers are attached to a Teflon holder to represent layers with different thicknesses. So the same stepwise geometry like for the BAM samples (see sketch in Fig. 9.5) is realized but with a smaller pitch.

Figure 9.9 shows the THz amplitude transmission and the corresponding delay time through the 2 mm thick Teflon plate and the plastic layers. For $x = 140$ mm only the pure Teflon part is in the beam while for $x = 0$ mm already 7 Scotch tape layers are added. Each step is detected also in the transmitted amplitude as a reduction (e. g. $x = 17$ mm or $x = 74$ mm). This is caused by the pulse splitting due to the different delay time within the THz spot diameter. So only the steps itself are detected clearly but the relative amplitude reduction can only be roughly determined. The absorption in the plastic layers is too small to allow a quantitative predication. Although the amplitude is slightly reduced for smaller x values, the contrast at the steps is much more pronounced than the added losses for longer absorption lengths.

The same data set like in the measurement before is used but evaluated in terms of delay time of the peak maximum. Obviously is that the delay time rises 0.6 ps for 7 layers of Scotch tape. Please note that the gap at $x = 74$ mm is also seen in the delay time mode since here a real gap is between the layers and so the amplitude of one layer less is displayed. These results are already satisfying the eye, but a zoom into the raw data underlines the high accuracy and limitations more precise.
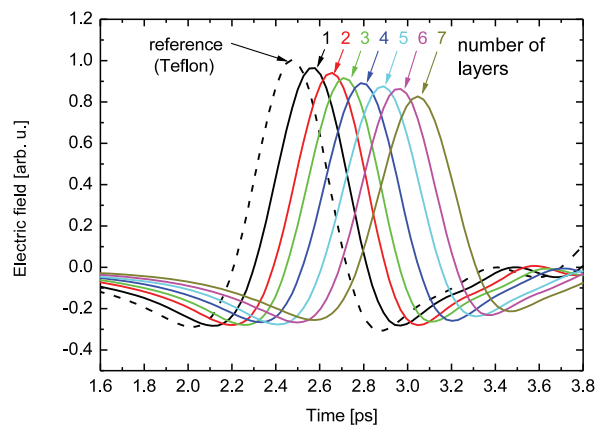
Figure 9.10: Thin film measurement in transmission. The reference is a Teflon plate. Stepwise layers of Scotch tape are attached on top.

The optically measured layer thickness (under the assumption of $n_{\mathrm{plastik}}^{\mathrm{THz}} = 1.5$) is 49 µm. This is very close to the mechanically measured thickness with a deviation of only 2 µm. In the first moment it sounds strange to measure a thickness of less then a hundredth of the wavelength. But this is consistent also with typical experimental experiences: If the delay line is moved stepwise towards the maximum of the amplitude even slight changes below 2 µm are detectable as an amplitude change at the lock-in amplifier.

Reflection

Measurement of thin layers in reflection is of exceptional interest for the production of coated surfaces. An accurate control of the accumulated layer thickness is difficult to be realized with conventional techniques if the surface of the sample is very hot or still wet. During the drying process while measurements in contact would damage the coating THz TDS can directly give a fast feedback signal to the production line [167, 168]. For paint layers and functional coatings contact-free tomographic measurements can determine the thickness.

Most industrial metallic surfaces are coated. This may be car lacquer, a finished pipe or even the color on a potato chips bag. A slight deviation of the optimal thickness will make the metal corrode or increase the paint consumption and thereby the cost and drying time.

These samples give optimal conditions if the additional layer itself is transparent for the THz waves. As a substitute to check the limits of the reflection setups the same Scotch tape layers were attached on a metallic plate.

(a) Delay time of THz peak maximum (b) Sketch
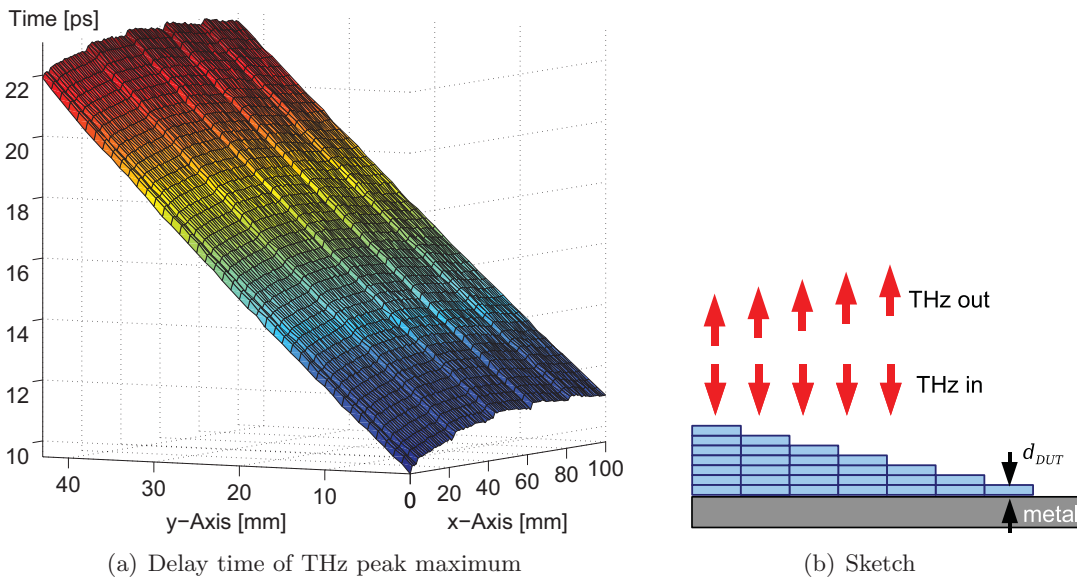
Figure 9.11: Thin film measurement under 90° reflection. THz reflection image (delay time mode) and sample geometry

Figure 9.11 shows the time delay image of such an aluminum plate with zero to four layers of Scotch tape in the scanning range. Since this evaluation mode only displays the time of the peak maximum here the runtime to the reflection of the metallic plate is plotted. The edges of the tapes are seen here, but a clear structure like in the transmission measurement is not observed. This is because the metal plate is mounted not completely perpendicular to the beam. Already slight geometric misalignments of the sample holder will show a big inclination in this mode (comparable to Fig. 9.8). So a data evaluation

without further data processing is difficult. But what can be stated for sure is that each step can be resolved already in the given plot.
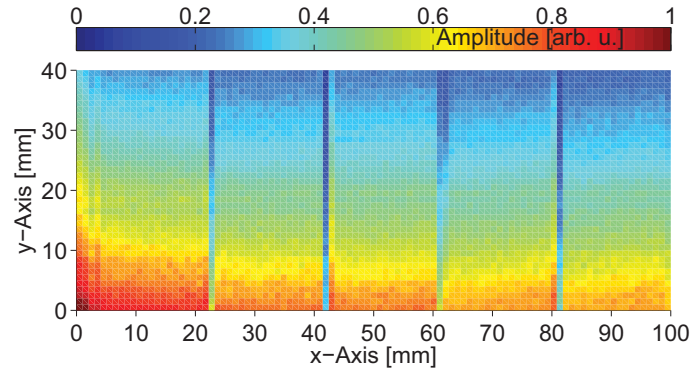
Figure 9.12: Thin film measurement under 90° reflection. THz reflection image (amplitude mode)

(a) Delay time of THz peak maximum

(b) Sketch
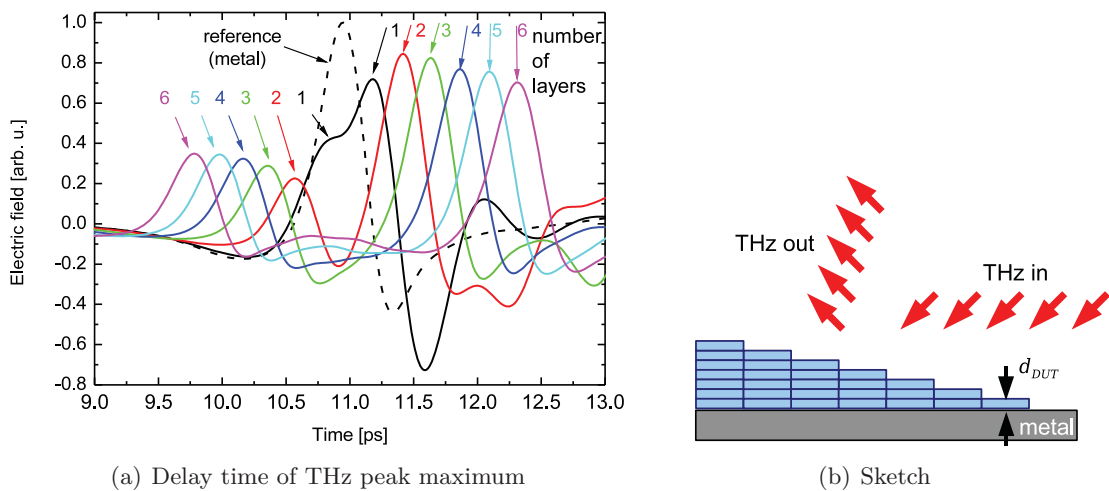
Figure 9.13: Thin film measurement under 45° reflection. The reference is a metallic plate. Stepwise layers of Scotch tape are glued on top. Recorded electric fields in reflection and sample geometry

This mentioned behavior also causes problems for the maximum amplitude as it can be seen in Fig. 9.12. If the sample moves out of the focal plane also the maximum of the detected electric field will be drastically reduced. So for a this kind of reflection measurement either a data processing has to adapt the amplitude with respect to the delay time or a good positioning of the sample has to be guaranteed. For samples with strong curvature or steps this means even that the geometric structure has to be known in advance as an input parameter to the imaging system.

An accurate sample positioning can be realized in the portable TDS system (see chapter

7.5). One of its exchangeable optics boards allows for a reflection under 45° with a vertically guided THz beam. So the sample can be kept horizontally and the corresponding position is reproducible. The detected electric fields of the aforementioned metallic plate with Scotch tape layers are shown in Fig. 9.13.

This easy kind of evaluation which just measures the time shift of the peak gets unprecise below an overall thickness of 15 μm as other measurements with coated foils have shown. Then the edge of the front facet reflex overlaps the main pulse from the metallic plate similar to the first layer in Fig. 9.13. The delay time of the local maximum caused by the first peak shifts because it overlaps with the steep tail of the main pulse. Numerical algorithms can calculate the layer thickness more accurately, both in the time domain and in the frequency domain.

9.3 Non-Destructive Testing of Ceramics

For various industrial applications ceramic materials have a range of specific properties which fundamentally distinguish them from other materials. The field ranges from electronics, plant construction, machining tools to even medical prostheses. The special design as functional or technical ceramics offers a lot of properties that can be selectively influenced by the composition of the raw materials and the sintering process.

Extreme hardness, resistance to corrosion, low weight, heat stability, high electrical insulating capacity and a good physiological compatibility distinguish technical ceramics. The structural design and the defined microstructure determines the mechanical and physical material parameters. At the same time, it also represents a weakness in this class of materials. Ceramics are considered fragile to compensate for minor structural defects by means of elastic and plastic deformation. The error tolerance in manufacturing high-performance ceramics is correspondingly low.

Consequently, precise and consistent test procedures are demanded which are capable of detecting the pores, inclusions, cracks or inhomogeneities reliably. Established methods of materials testing such as optical, acoustic, magnetic, electrical or electromagnetic techniques can be employed for testing high-performance ceramics. Key factors in selecting the process alongside reliability are speed and ease of integration into the production process. This offers a possibility to apply THz-NDT.

In principle, both the reflection as well as transmission mode are well suited to find interfaces, air intrusions and geometries within a massive bulk piece or a layered ceramic coating. The high refractive index in the THz range (around 3 depending on the particular type of ceramic material) brings a large contribution to the back reflection at every boundary. Further on, the absorption of most ceramics is quite low in the THz range.

To check the possibilities of an accurate thickness measurement of the THz-TDS a step wedge made of ceramics is used. The minimum thickness of the sample is 2 mm. The delay time plot in Fig. 9.14 shows that even the smallest step with a height below 100 μm can be resolved. Of course, the large refractive index of the ceramic sample in the THz range (around 3 for typical bulk ceramics) is advantageous for high-accuracy thickness

(a) Delay time of THz peak maximum

(b) Photograph
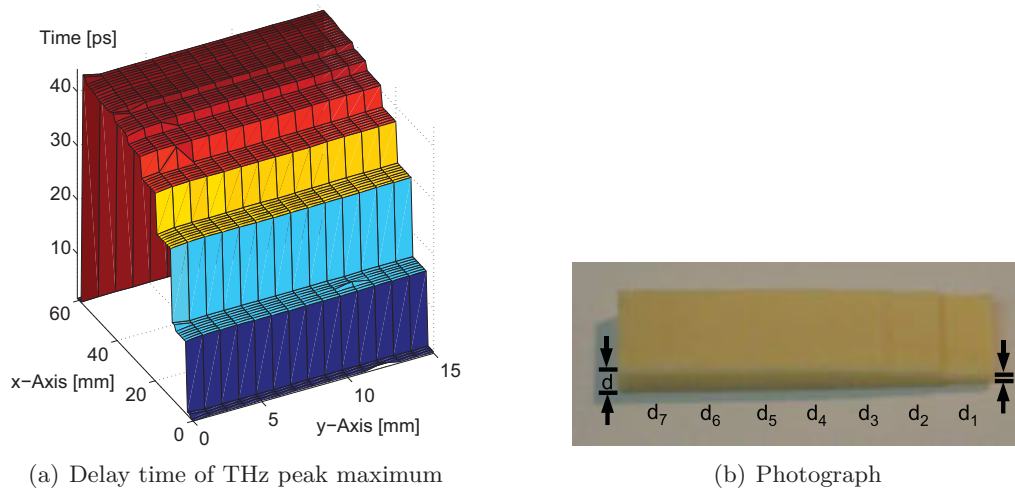
Figure 9.14: Ceramic sample "step wedge" as a testing sample of an industrial customer. Comparison between THz transmission image (delay time mode) and sample geometry

measurements [169]. This and the low losses underline the suitability of THz technologies for the industrial quality inspection.

(a) Transmitted THz amplitude: drilled holes (cavities)

(b) Sketch: drilled holes (cavities)
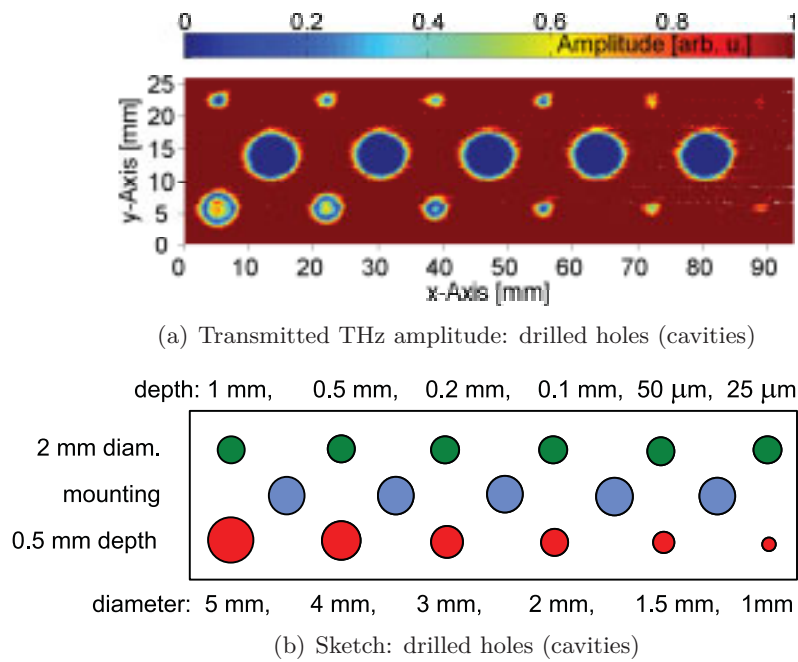
Figure 9.15: Ceramic sample with drilled holes for the THz-NDT. THz transmission image (amplitude mode) and sample geometry
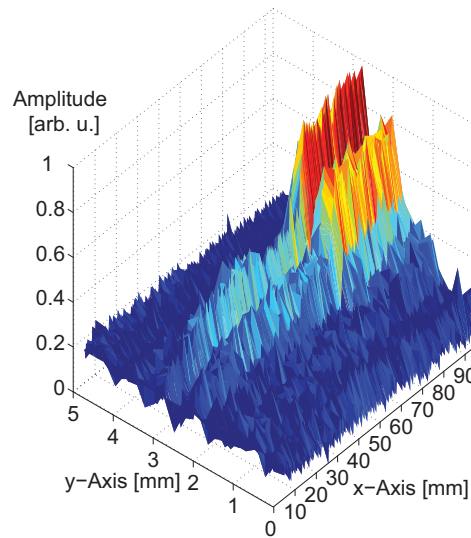
Figure 9.16: Ceramic sample with sawed gap for the THz-NDT. THz transmission image (amplitude mode)

Air intrusions or holes within massive ceramic bodies are checked with a prepared ceramic plate. It is composed of two similar plates (like a sandwich) where small holes and a sawed bar with varying thickness and depth are located in the interior of the DUT. So this is a good substitute for a real sample with small production failures in the volume. Figures 9.15 and 9.16 show the THz transmission image in the amplitude mode. Even the smallest drilling with a depth of only $25\,\mu m$ at a diameter of $2\,mm$ is detected. For the sawed gap a 3D view of the amplitude shows the position while the depth of the fault is difficult to be evaluated. The geometrical depth of the gap varies between $1\,mm$ down to $25\,\mu m$. Please note that there is only one cut with two edges. That is why the THz image shows two distinct lines for only one single cut. But still it is remarkable that failures much below the THz wavelength can be detected. The THz spot diameter is convoluted with the samples structure. So also structures with smaller lateral dimensions are resolvable. The absolute position can only be determined within an accuracy of the THz wavelength. But for most applications of the industrial NDT it is sufficient to know that the DUT has a failure. Its precise location is nice to know, but not critical in the first step.

A gear-shaped component part as it appears in a real-world production process is imaged in Fig. 9.17. The above mentioned thickness and outer geometry can be clearly seen in the evaluation of the time delay. But the amplitude mode shows even more information: On the right ($y = 15\,mm$) and bottom side ($x = 13\,mm$) of the DUT there are indications for material failures like a fault or crack. This may be attributed to increased scattering or thickness fluctuations of the sample with an extent smaller than the THz wavelength. On the homogeneous background of the flat body this can be detected.

THz-NDT of composite ceramics is looking for debonding or delamination of one of

(a) Transmitted THz amplitude   (b) Delay time of THz peak maximum   (c) Photograph

Figure 9.17: Ceramic sample "gear" as a real world spare part of an industrial customer. Comparison between THz transmission image (amplitude and delay time mode) and sample geometry

(a) Delay time of THz peak maximum   (b) Photograph

Figure 9.18: Composite ceramic device as a testing sample of an industrial customer. Detected electric field in reflection and sample geometry

the components. Solving this problem using THz tomography requires an elaborate data conditioning. A lot of industrial ceramics are in contact with metallic surfaces or, like in the here 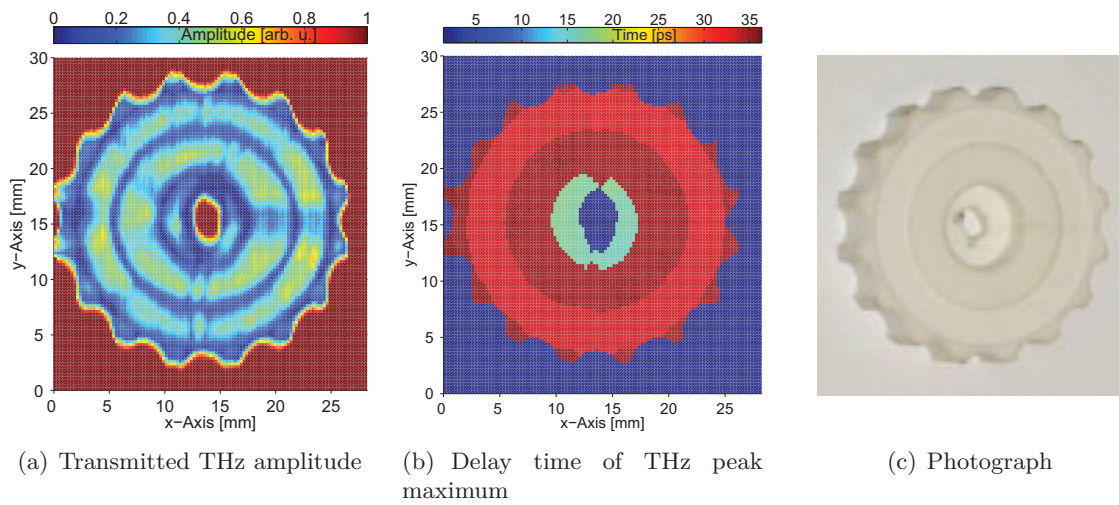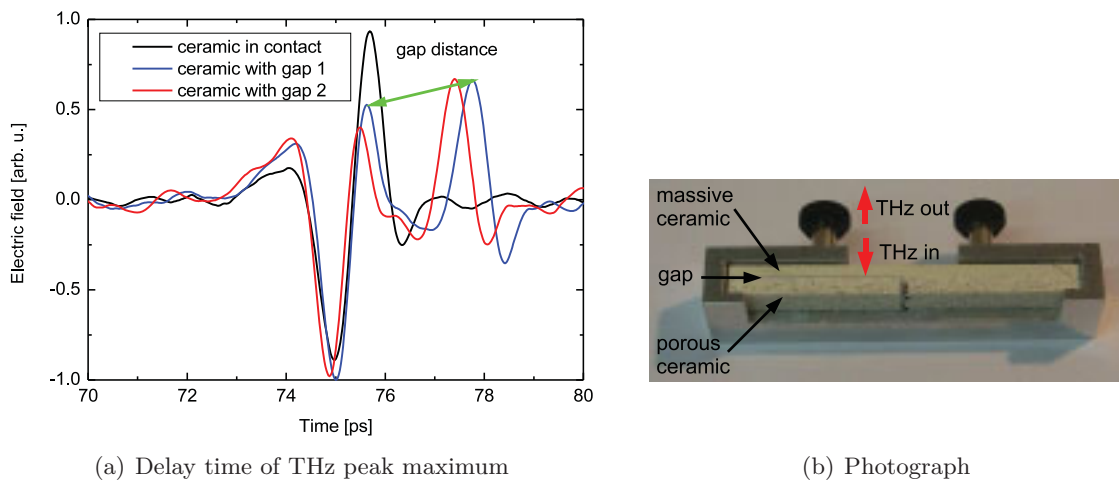checked sample, consist of a porous part. The latter one shows very high looses in the THz range due to pores with diameters in the range of the wavelength. So scattering will reduce the transmitted amplitude so drastically that the peak amplitude is in the range of the noise level of the THz system. So a measurement must be carried out in reflection geometry.

The particular sample and the recorded electric field is shown in Fig. 9.18. The sample is positioned with the homogenous part of the composite facing the THz optics. So for a delamination check the THz pulse has to pass through the part with a good transparency, gets reflected at the boundary (interface ceramics-ceramics or ceramics-air), and passes the homogenous part for a second time. The plotted electric field is already zoomed to the particular interface in terms of corresponding delay time. The choice of the appropriate time window is very important to detect an image of the boundary.

If the two ceramic composites are in contact there will be a reflection at the boundary due to the different refractive indices or a bad surface conditioning of the porous sample. If now the composites form an air gap in between the two boundaries this can be seen in reflection: One is caused by the refractive index step between homogenous ceramic to air and a second one from the boundary air to porous ceramic. The delay between these two pulses is a quantity for the spacing distance between the surfaces. The here evaluated pixels show a gap of 300 µm. Also the first Fresnel reflection at 75.5 ps is reduced due to a change of refractive index step. This already gives a signal if the two pulses can not be completely separated. So the increasing air gap can be quantitatively measured.

As a result, it is possible to uncover structures inside of a three-dimensional body. These outcomes can be extended also to other non-conducting materials which show a sufficient transmission in the THz range like most common dielectrics. The same measurement technique is also tested for glued plastic parts. The glue itself changes the refractive index step similar to an immersion fluid or causes losses due to material absorption. The particular contrast depends on the individual optical properties of the components.

9.4 Final Inspection of Packaging

Another big market is the final inspection of products. THz spectroscopy has already proven to be able to identify contents by spectroscopy and determine coatings of tablets by tomography [170, 171]. The here given further example arises from the requirements in the field of pharmaceutical production and packaging.

For a company selling high-class goods it is very important that the products have a reliable quality. Especially in the pharmaceutical sector it is important to guarantee a specific content without contaminations. Chemical methods are well elaborated and available at the market, so that this point is not of concern here. If it is possible to take a sample and analyze it, then chemical methods are the ones of choice. But still the packaging process is a possible application for THz imaging.

(a) THz transmission original DUT

(b) THz transmission DUT with defects

(c) Photograph of original DUT

(d) Photograph of DUT with defects
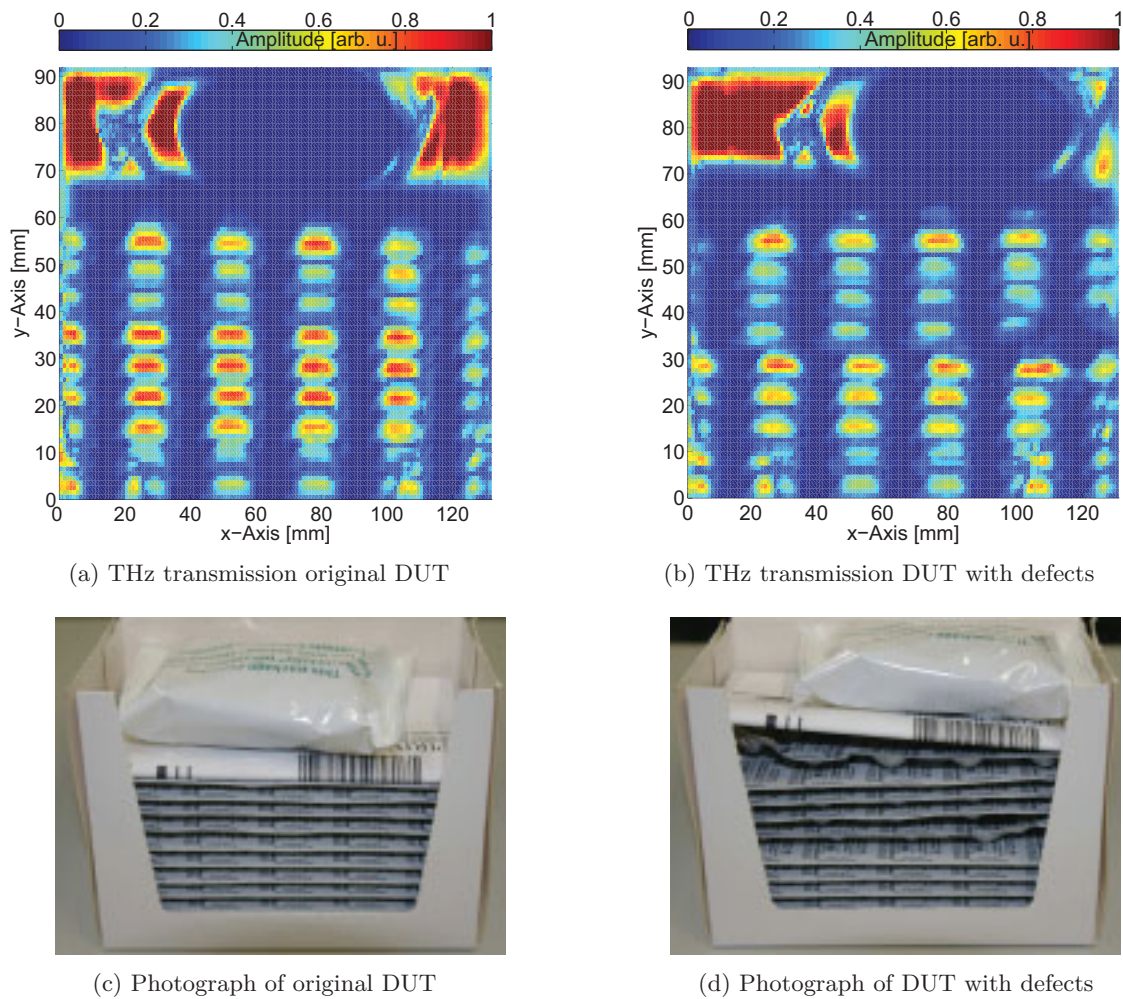
Figure 9.19: THz-NDT of blister packages. Paperboard package containing layers of tablet blisters and an inhaler with a paper instruction leaflet on top

During the production process the transportation and packaging can be controlled using photoelectric barriers and cameras in the visible. But at the very end of the production line, when the final product is stored in the cardboard container, the cameras can not look inside through the closed package.

At the here tested item made by Boehringer Ingelheim Pharma GmbH & Co. KG the content is not under suspect. It is a cardboard container with a layered sequence of tablet blisters. Within this metallic containers the tablets themselves are placed. On the top of the package an inhaler and the paper instruction leaflet are stored (see Fig. 9.19). The amount of content could perhaps be assumed by the weight of the package. But a feature which is very important is the first view when the customer opens the package. Bends or misplaced contents, even if they do not negatively effect the agent, make the

product look damaged. This prejudice will stay in the mind of the customer and remain as repercussions on the brand. Therefore companies try to avoid this manufacturing defect in the sense of a good corporate appearance.

The first photograph and corresponding THz amplitude transmission image show an undamaged package. This data set one would take as reference in image processing. It is opened to take a photograph but was closed when the THz image was recorded. So the conditions like in a real world measurement is kept. In the THz image horizontal yellow to red lines correspond to the blisters. The bright spots correspond to the space between the tablets in the side view while the blue pixel represent nearly no transmitted THz amplitude. This is the case when the tablet respectively its metallic package is in the THz beam. So even for the 8 cm wide box the lateral resolution is sufficient. By purpose the Raleigh length of THz beam in the transmission imaging system is quite long. The chosen THz mirrors have a long focal length compared to other setups.

Above the blisters the paper leaflet and the inhaler can be seen in as blue areas. The bright red pixels correspond to empty space in the box. So the position of the inhaler and the blisters can be seen. The most important fact is the positioning of the blisters with respect to each other. It is obvious that there is a step in the periodicity which indicates a problem during the packaging process. Also the two bends are detected: One on the left underneath the paper leaflet and the other one right in the middle within the blisters. These large blue areas are caused by the absence of THz transmission because the metallic foil is misplaced.

9.5 Spectroscopic Identification

Most of the mentioned applications can be carried out with a data set in the time domain. Then the single cycle THz pulse is recorded and evaluated. This only requires a short scan of the delay line and allows for a fast data acquisition. With some well prepared samples (constant optical thickness) it is even sufficient to keep the delay line standing still and just detect the deviation of the amplitude at a constant delay time.

But if an identification is needed then spectroscopy is required. Some THz systems change the frequency of the emitter and measure at different preset frequencies. For the THz-TDS and the broadband emitters it requires a longer scan in the time domain to achieve a spectral resolution. Of course it depends on the aimed application: For gas sensing for example narrow lines have to be detected while for scattering at solid samples broadband structures are expected.

An often used reference for THz spectroscopy (besides the water absorption lines) is lactose. Lactose (also referred to as milk sugar) has distinct absorption lines in the THz range (Fig. 9.20). Because it is chemically harmless lactose is often used as a substitute for dangerous substances like drugs, explosives or poisons. Also for the here presented results the system performance checks and feasibility tests are carried out with lactose until for the final step the real substance is measured.

The here presented absorption coefficient is derived out of a transmission measurement
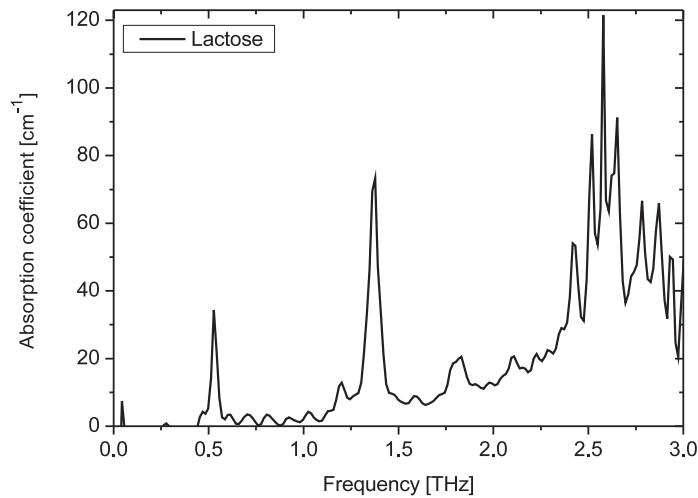
Figure 9.20: Measured absorption coefficient of lactose

with respect to the reference and the sample thickness. This already shows the main difficulty: Besides the need to know the accurate sample thickness, the sample preparation starts to play an important role for the detected signal. For the powder samples there is the possibility to fill up a container. Then the density may vary and mechanical knocks at the holder can change the measured amplitude, affecting the absorption. Pressed pellets are more reproducible. They can be manufactured with a defined pressure and reproducible shape. But unfortunately most of the pellets are fragile and not mechanically stable. To make them more sticky polyethylene (PE) powder is added to the sample's powder. This dilutes the concentration and may be also of importance to enhance the SNR for an optimal sample thickness. Depending on the aimed frequency range, this varies [172]. For e. g. the low frequency range below 500 GHz, where the transmission is roughly 1, it is advantageous to use a thick sample to detect a change in transmission. But the same thick sample will show no transmission at the middle and high frequency part of the available THz spectrum (above 2 THz). Then the transmitted field for this frequency is too low and the error bar of the calculated absorption immense.

If the sample has to be stored in a box, perhaps because it is a liquid or volatile sample, then the container should of course be transparent for the THz waves and show a refractive index quite close to the sample's one. Also the thickness should be chosen that the etalon effects do not modulate the THz spectrum within the scanning range. But also sometimes it is advantageous to put a sample within an even holder to reduce the scattering losses at the sample's surface. Especially if no pellets are available the flat surface reduces the scattering losses in transmission as well as in reflection measurements. So by an appropriate sample preparation the accessible spectral range can be considerably extended.

Spectroscopic Detection of Substances within Packages
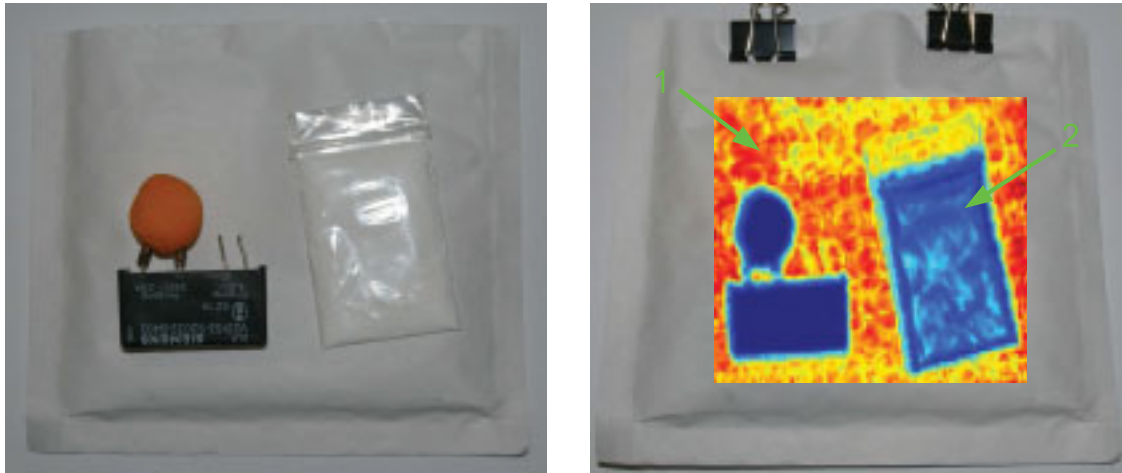
(a) Photograph of opened letter bomb dummy

(b) Closed letter bomb dummy, overlay: THz amplitude transmission
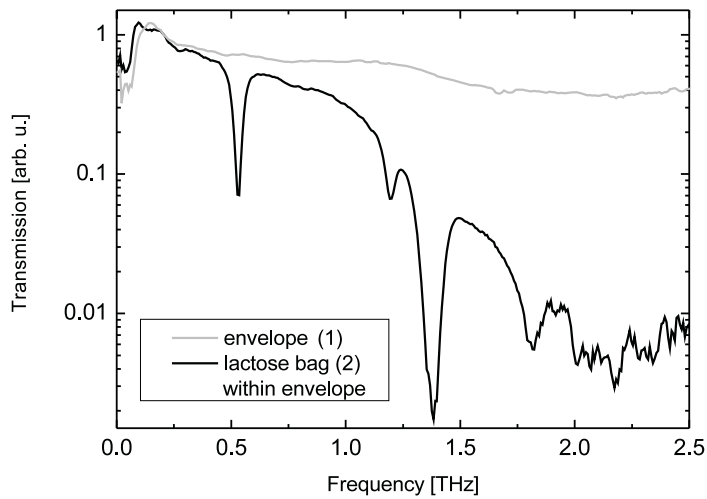
(c) Amplitude transmission at the two marked pixels

Figure 9.21: Letter bomb dummy for spectroscopy within packages. A standard padded envelope with an electronic chip and a PE bag containing lactose powder. The transmission at the second pixel clearly shows the absorption lines of lactose.

The substance identification using THz spectroscopy has attracted a big interest in various safety and security applications. Here really the specific advantages of THz radiation – a sufficient penetration and the spectral selectivity – make this wavelength range superior to all other spectral ranges [173, 174].

To show the fundamental principle a dummy letter bomb is prepared and measured. The contents can be seen in Fig. 9.21. A standard padded envelope (paper with plastic honeycomb pattern) is filled with an electronic device (chip as fuze) and a PE bag with lactose. This might also be any other substance with a signature in the THz range. The packaging in a plastic bag and the delivery per mail is not uncommon for typical scenarios e.g. in the field of drug delivery [148, 175]

In the THz transmission image the outer shape of the content can be clearly seen. Even the transparent PE bag gives enough contrast. To allow for a spectroscopic evaluation of the data set, a long time range of the electric field is scanned (133 ps). This data set was non only used to derive the amplitude transmission but also converted into the frequency domain to calculate a spectral absorption. The transmission at one pixel on the envelope and one on the lactose bag is plotted. The broadband absorption at high frequencies for the envelope itself shows no distinct abortions only broadband characteristics. This is in contrast to the clear absorptions caused by the lactose powder. So a content evaluation by comparison with a THz absorption data base can be carried out with the same data set. Please note that the data acquisition time for spectroscopy is larger than for standard imaging applications. The here recorded image needed approx. 5 min per pixel. Recently, the data acquisition rate is considerably improved for spectroscopic applications to up to 250 pixels per second [144].

Detection in Transmission

What kinds of substances have a significant absorption in the THz range? This can not be answered in general. For gases the polar molecules show a real finger-print absorption in the THz range. But for solids it depends on the particular substance. A rough estimation is that small molecules show a broadband absorption while large molecules exhibit absorption bands. Large molecules tend to bend themselves as a whole molecule. This resonance frequency is typically in the THz range. Different numerical calculations on molecules are reported, but the number of involved atoms increase the computational time so drastically that only for small molecules model calculations are available.

Most of the energy-rich substances used as ingredient at the production of explosives show a characteristic absorption in the THz range [177]. This offers a large potential for the THz stand-off detection [173, 174, 178]. Figure 9.22 shows the measured absorption of RDX in the THz range exemplarily for other explosives and related compounds. The data set was recorded with the portable THz-TDS system at the Fraunhofer ICT in Karlsruhe. From the fundamental view this is just an absorbing substance. That is why performance checks can also be carried out with lactose powder. But an accurate knowledge of the absorption spectra of various explosives is crucial for the setup of a data base. So unknown recorded data can be compared with reference spectra and identified as the particular substances.

Various applications related to toxic substances could also be solved by THz spectroscopy. Figure 9.23 shows the transmission through sealed-off packages of lindane and PCB which are carcinogen poisons. The here presented spectra just serve as a glimpse
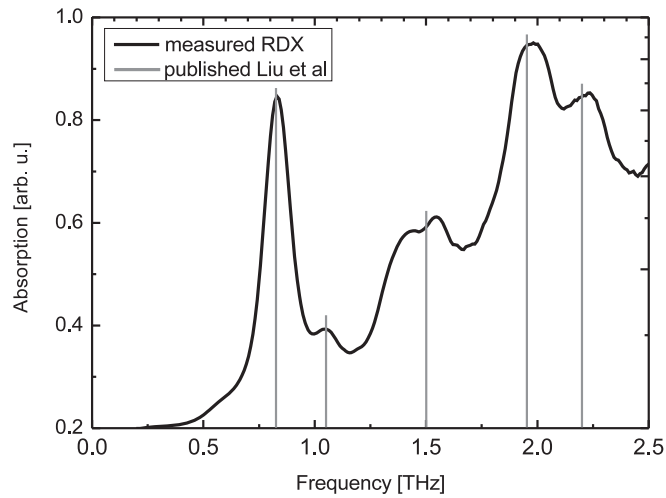
Figure 9.22: Measured absorption of RDX in transmission; published values taken from Liu et al [176]
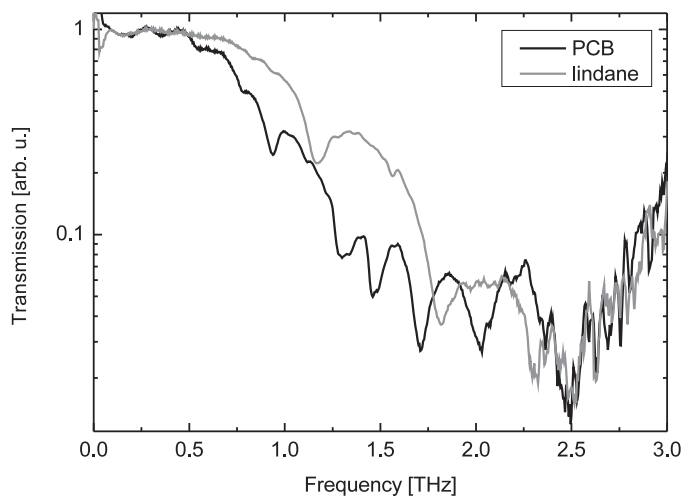
Figure 9.23: Measured transmission through a sealed-off package containing lindane or PCB

of the large potential of THz spectroscopy for the detection of chemical, biological and explosive hazardous substances [150].

Detection in Reflection

The detection of substances in transmission is not possible in all scenarios. If the content is packed within a metallic container, THz radiation does not reach the sample. So additional detection techniques have to be used to find metallic contents at the suspicious

object. This can be cheaply done using a metal detector. But other applications require a spectroscopic detection in reflection. Also passive or cw THz system can be applied for stand-off imaging. But to really identify contents tuneable or broadband THz radiation has to be used.
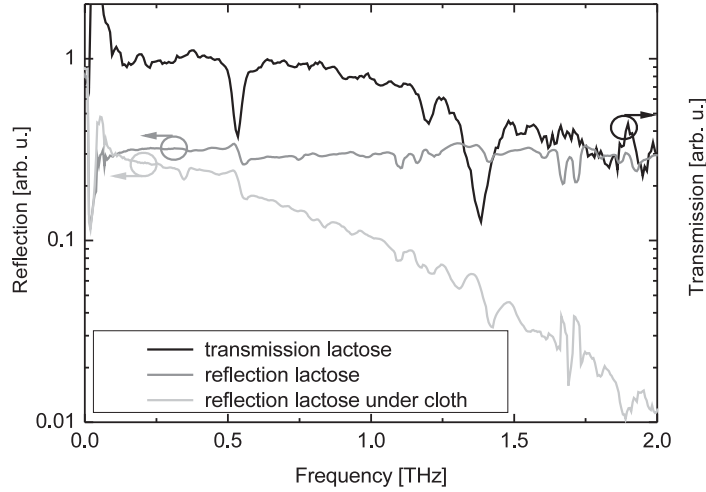
Figure 9.24: Measured reflectivity of lactose

According to Jepsen et al. [179] the relation between the reflected electric field from the sample surface E_{DUT} to the reference field E_{ref} is given by

$$\frac{E_{\text{DUT}}}{E_{\text{ref}}} = |r| \, exp\,(i\phi) = \frac{(n + i\kappa) - 1}{(n + i\kappa) + 1} \tag{9.1}$$

with n the real and κ the complex index of refraction of the DUT. Then the absorption coefficient α can be estimated by

$$\alpha = \frac{2\omega}{c} \frac{2\,|r|\,sin\,\phi}{1 + |r|^2 - 2\,|r|\,cos\,\phi} \tag{9.2}$$

The interrelationship between the real and imaginary part of the refractive index is mathematically based on the Kramers-Kronig relations. To show this in the experiment the measured THz reflectivity of lactose is plotted in Fig. 9.24 together with the transmitted amplitude. Especially at the absorption peaks at $0.5\,\text{THz}$ and $1.4\,\text{THz}$ it is obvious that an absorption peak in transmission causes a dispersion shaped behavior in the reflected signal. This is expected because the reflected amplitude has also a contribution caused by the absorption coefficient. This fact might be of importance for the stand-off detection of explosives in reflection [180].

To bring the experiment closer to real world conditions an arbitrary T-shirt is brought

into the beam path. So the THz pulses have to pass the cloth, get reflected at the sample and pass the cloth a second time. But still the dispersion shaped signal is seen. The deviation for larger frequencies is caused by scattering and absorption in the T-shirt.

A lot of types of clothes are measured in transmission. None of them shows spectral characteristic features. Only the accessible broadband range of the THz pulse is reduced. This underlines the statement that is does not make sense to reach for even higher THz frequencies [181, 182]. The band above 4 THz gets nearly completely absorbed in ambient air and is very sensitive to absorption and scattering.

In particular the applications in reflection have to account for a lot of environmental influences (see chapter 8.6) and sample properties. Among these the surface flatness and roughness influence the scattering conditions. The reflected intensity strongly varies between specular reflection and diffuse scattering [151, 152, 183]. This has to be taken into account in the discussion of the possibilities for THz stand-off detection.

A topic which is not emphasized in this thesis is the compatibility in the morals department. THz radiation can collect data on any target that is observed. In the newspapers people are frightened by showing naked persons "stripped" by THz radiation. Starting from the microwave regime the spatial resolution of these images get better towards the THz range but still do not have a detailed resolution for larger stand-off distances. Whether the public opinion will accept such observations and who is allowed to handle the recorded data will have to be discussed elsewhere.

THz and Arts

A THz application which attracted a large public media attention is the application of THz-NDT to find hidden art objects [184, 185]. Here the properties of THz radiation are advantageous compared to other adjacent wavelengths ranges: THz radiation can penetrate plaster, cement or wood to interact with underlaying color pigments of pictures which were painted over. Also the tomographic information is useful to determine the depth of the second color layer. The particular color pigments may be even detected using spectroscopic THz imaging.

The first step is to investigate representative uncovered paintings. If in this simplified scheme identification of color pigments and the detection of the layered structure is possible, then the next level of difficulty is to do this in reflection and look for real hidden images and their pigments or mechanical structures. So cavities or anomalies can be indicators for hidden wall paintings. So the THz-TDS might be able to uncover hidden frescoes and mural paintings which were over-coated in time of iconoclasm. The detection method has to be non-destructive, non-invasive and spatially precise. The requirements pose a challenge which could be met with THz technology [186, 187].

To know what part of a painting can give a detectable indication it is important to know how the structure of a painting typically looks like (see Fig. 9.25): Starting with a canvas on wood, the ground coating is the first layer. Then the color pigments are superimposed. Different layers of glaze and varnish cover the art against environmental influences like dirt or moisture. The individual layer thickness varies from $20\,\mu m$ to $100\,\mu m$.

(a) Painting structure according to Forth (Crete, Greece) [187]   (b) Measured color pigments
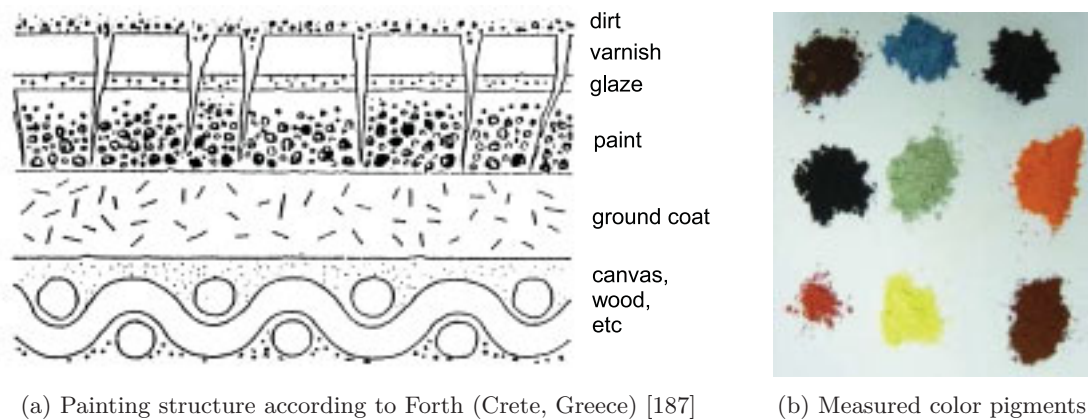
Figure 9.25: THz-NDT offers possibilities to uncover hidden art objects. Principal investigations are carried out with paintings and the pure color pigments.
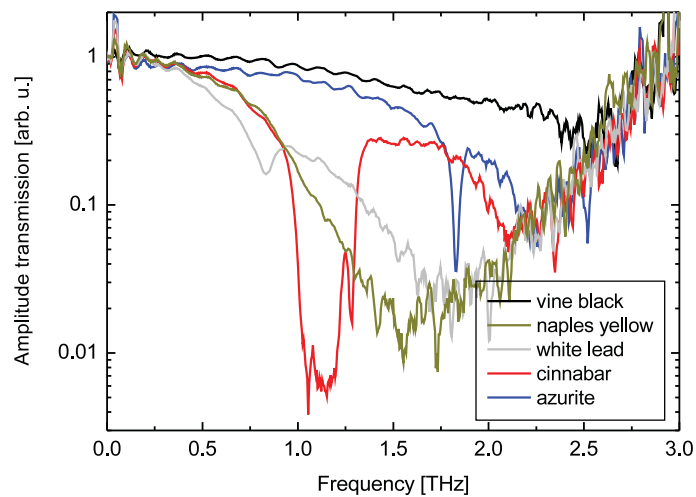
Figure 9.26: Absorption of different color pigments

Different color pigments are measured in transmission. A teflon container with a 1 mm thick countersink is used to store the powder. This minimizes the echoes in the transmission measurement and allows for a reproducible evaluation of the absorption without etalon effects. Also surface losses are minimized because of the reduced refractive index step and the scattering losses by pressing the powder into a plain surface. The results shown in Fig. 9.26 indicate that some color pigments show spectral absorption features. These are white lead $(2PbCO_3 - Pb(OH)_2)$, cinnabar (HgS) and azurite $(2CuCO_3 - Cu(OH)_2)$. The particular absorption of these three pigments is distinguishable from the others. They only show an increased loss for higher frequencies due to scattering. The grain size of the powder limits the accessible high frequency range in this measurement which explains the broadband structure of vine black (pure elemen-

tal carbon, soot) and naples yellow $(Pb(SbO_3)_2 - Pb_3(Sb_3O_4)_2)$. So in a transmission measurement, the particular pigments can be mapped if the substance shows a "THz fingerprint".

(a) Transmitted THz amplitude (b) Delay time of THz peak maximum (c) Photograph
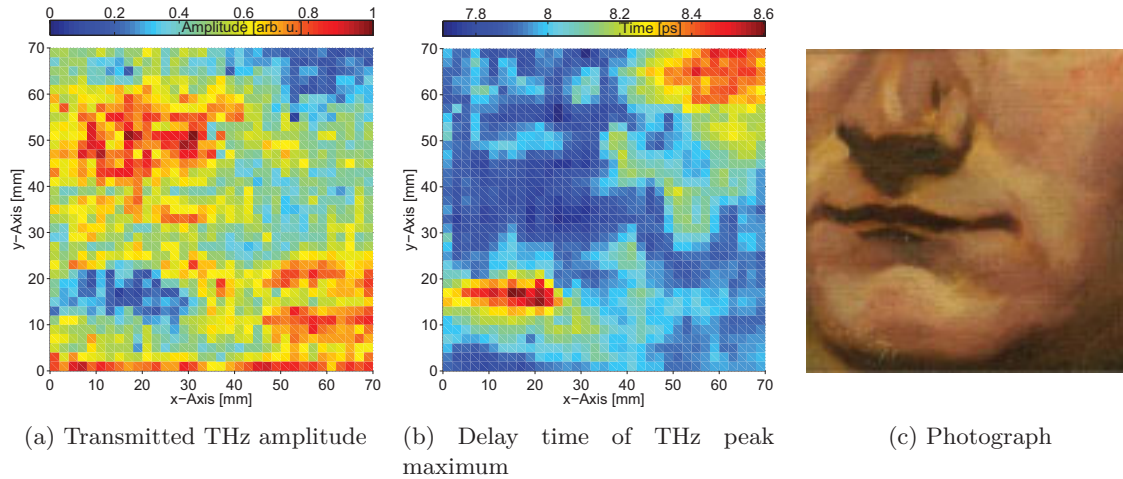
Figure 9.27: Canvas painting for the THz-NDT of art objects. Comparison between THz transmission image (amplitude and delay time mode) and photograph [187]

The results of a THz imaging scan of a real painting on canvas can be seen in Fig. 9.27. It shows the transmitted THz amplitude, the corresponding runtime and the photograph of the sample. The evaluation of the amplitude shows a low transmission at the position of the bright area of the chin ($x = y = 15$ mm). So here either the color application is thicker compared to the neighboring areas or the used white color pigment has a higher absorption. The delay time mode at this points shows a longer runtime. So here the painter just used a larger amount of color. The behavior at the darker areas of the nostrils ($x = 20$ mm, $y = 50$ mm) and their shadow is different. The amplitude transmission is high there, but the runtime is not minimal (approx. bright blue with $\Delta t = 8.0$ ps). So here a color pigment was used with a low absorption in the THz range. This two examples show already the main problem of the data evaluation in this system: In the transmission measurement the absorption and the thickness change both. A data evaluation in a "normalized absorption" display mode would emphasize the features. Assuming a constant refractive index for all pigments and regarding the canvas completely plain and homogenous, one could normalize the amplitude with respect to the delay time. Then the delay time is proportional to the absorption length, and together with Beer-Lambert's law of absorption, the absolute absorption can be calculated.

The data set of Fig. 9.27 is recorded with a lateral resolution of only 2 mm times 2 mm to keep the measurement time in an acceptable range. Each pixel also allows for a spectroscopic evaluation. The best contrast displaying the face also in the THz range is a sliced plot in the time and frequency domain similar to a THz movie. So the coordinates are steadily tuned until the maximum contrast is reached. This video files are available,

but already show the problem of the large data set. If electric fields are recorded with a corresponding high spectral resolution the amount of data is immense. The storage and handling of this data sets even brings today's computers to their limit. So a special care has to be taken on the data management.

10 Summary

The topic of this thesis are new sources and complete systems in the terahertz (THz) frequency band. Especially this particular spectral range of the electromagnetic spectrum – around a frequency of 1 THz corresponding to a wavelength of 300 µm – is very interesting for a wide range of fundamental and industrial applications.

The basic principle of time-domain spectroscopy is applied in all measurements. Femtosecond laser pulses are used to generate THz radiation in different emitters. The same laser pulse gates a broadband THz detector coherently. A mechanical delay line causes a time shift between the two fractions of the laser pulses and therefore allows for the sampling of the fast THz transients.

Three types of emitters for femtosecond pumped systems are applied and developed further. Nonlinear THz sources based on lithium niobate crystals are used in the Cherenkov scheme to generate broadband THz radiation by optical rectification. An attached silicon prism to the crystal's emitting facet is able to increase the average output as well as high frequency components of the THz spectrum. Various emitters are characterized in the single pass scheme.

To increase the efficiency of the nonlinear process the available pump radiation is resonated in an enhancement cavity. This is realized in an synchronously pumped ring cavity containing the lithium niobate crystal as THz emitter. An active feedback circuit is applied to keep the cavity length locked on an interferometric resonance. The Hänsch-Couillaud stabilization is able to keep the cavity on a constructive resonance for hours. So slow slope drifts of the pump laser repetition rate and the enhancement cavity itself are compensated for. Thermal drifts and air movements affecting the round trip time of the cavity are canceled out.

In this scheme pump enhancement factors above 8 corresponding to a THz intensity enhancement of more than 25 are measured. The particular values depend on the losses induced by the fs pulses in the lithium niobate crystal. So also frequency doubled fiber lasers with low average power can be used to pump nonlinear THz emitters efficiently.

New photoconductive materials are inspected and evaluated. Standard Ti:sapphire setups are used as well as a CTA-OPO system with longer pump wavelengths of up to 2 µm. Among these photoconductive emitters some are gated with pump pulses centered at the important 1.5 µm telecom wavelength. Especially from the photoconductive switches made out of indium gallium arsenide a large impact on the price and reliability of THz systems is expected.

Also photoconductive surface emitters are discussed. Various emission geometries (quasi reflection, quasi transmission, back to the source) are realized and measured. The results are verified by simulations using CST MICROWAVE STUDIO®. Black silicon as

a new nano structured surface emitter is proposed. Its needles absorb the whole pump power and generate an anisotropy towards the surface which gives rise to THz emission unlike for non-structured bulk silicon samples.

Depending on the intended application different TDS systems are designed and assembled. The standard TDS systems which are common for fundamental research are set up on optical tables under laboratory conditions. They are sufficient for fundamental investigations and flexible at component testing. Depending on the specimen, setups working in transmission or reflection are used. An automated scanning of the sample under test allows to gather also imaging information.

Towards a system which can be operated under industrial conditions the first step is to realize a portable system. This requires some changes of the layout and the employment of a compact fiber laser. Measurements at industrial customers are carried out with this system also outside of the laboratory.

But the most flexible setup in terms of the THz alignment is the fiber based system. It is assembled with a fiber transmission line to guide the fs pulsed from the laser to the THz emitter and detector heads. This system together with a fast delay line allows for online spectroscopic measurements also in industrial environments. Drifts of optics are strongly reduced by a fiber coupled solution compared to a free space propagation. Also the alignment is kept constant by a glued connection between the fiber and the photoconductive switch. This system guarantees the typical requirements for an industrial system and can be applied for the non-destructive testing e.g. for final inspection or in security applications.

The potential range of applications can be roughly divided into imaging and spectroscopic measurements. But for both a large amount of data has to be handled either to record the electric field for a lot of pixels on the sample or because of the need for a high frequency resolution. So different mathematical algorithms have to be applied to reduce the amount of recorded data and to display the particular feature of the device under test. Typical evaluation modes are the amplitude transmission and reflection mode as well as the delay time evaluation.

The lateral and temporal limitations of THz-TDS systems are determined. The achieved resolution depends on the sample, optics and the appropriate best-fitting mode of data evaluation. On flat and homogenous samples structures with an extension down to 25 μm are distinguishable. But the absolute spacial resolution is still in the range of the wavelength – typically one millimeter. Thickness measurements in the delay time mode are much more accurate. Even thin layers with a thickness of only 10 μm are clearly seen. The absolute determination of thicknesses with an accuracy of some microns is shown. This allows for a high-resolution tomographic measurement. Influences of the system and the sample properties on the measured signals are determined. Environmental influences like humidity are taken into account for stand-off applications.

The advantages and limitations of THz radiation in the field of non-destructive testing are discussed with respect to other frequency bands. Absorption, Fresnel losses and scattering bring the contrast in the detected THz amplitude. This gives information on inner and outer geometries like interfaces, cavities or foreign bodies. Also defects,

delaminations and substance distributions are measured at various types of samples. The highest accuracy is reached for thickness measurements where sub-wavelength structures are resolved.

It is shown that the THz spectral range can unify the properties of the adjoining spectral ranges – the microwaves and the infrared. Measurements in transmission for transparent samples as well as in reflection for metallic or layered samples have proven that there are applications which can be carried out more accurately by THz-TDS compared to other techniques. Under some experimental constraints THz tomography contains more information than typical intensity images taken in the visible or by using microwave radiation. Since these techniques are already at the market for a quite long time, they are well elaborated and the systems fully developed. But still the results of this thesis offer new possibilities to the real world application of pulsed THz radiation.

Bibliography

[1] SCHAWLOW, A. L.; TOWNES, C. H.: Infrared and Optical Masers. In: *Phys. Rev.* 112 (1958), Dec, No. 6, p. 1940–1949

[2] MAIMAN, T.: Stimulated Optical Radiation in Ruby. In: *Nature* 187 (1960), p. 493–494

[3] DIELS, J.; RUDOLPH, W.: *Ultrashort laser pulse phenomena: fundamentals, techniques, and applications on a femtosecond time scale.* Academic Press, San Diego, 2006

[4] HOLZWARTH, R.; UDEM, T.; HÄNSCH, T. W.; KNIGHT, J. C.; WADSWORTH, W. J.; RUSSELL, P. S. J.: Optical Frequency Synthesizer for Precision Spectroscopy. In: *Phys. Rev. Lett.* 85 (2000), Sep, No. 11, p. 2264–2267

[5] EXTER, M.; GRISCHKOWSKY, D.: Characterization of an optoelectronic terahertz beam system. In: *Microwave Theory and Techniques, IEEE Transactions on* 38 (1990), No. 11, p. 1684–1691

[6] EDWARDS, D.: Silicon. In: *Handbook of Optical Constants of Solids I, ED Palik, ed.(Academic, 1985)* (1985), p. 547–553

[7] RUDD, J. V.; MITTLEMAN, D. M.: Influence of substrate-lens design in terahertz time-domain spectroscopy. In: *J. Opt. Soc. Am. B* 19 (2002), No. 2, 319–329

[8] FILIPOVIC, D.; GEARHART, S.; REBEIZ, G.: Double-slot antennas on extended hemispherical and elliptical silicon dielectric lenses. In: *Microwave Theory and Techniques, IEEE Transactions on* 41 (1993), No. 10, p. 1738–1749

[9] DOU, W.; ZENG, G.; SUN, Z.: Pattern prediction of extended hemispherical-lens objective-lens antenna system at millimetre wavelengths. In: *Microwaves, Antennas and Propagation, IEE Proceedings* 145 (1998), No. 4, p. 295–298

[10] GRISCHKOWSKY, D.; KEIDING, S.; EXTER, M.; FATTINGER, C.: Far-infrared time-domain spectroscopy with terahertz beams of dielectrics and semiconductors. In: *J. Opt. Soc. Am. B* 7 (1990), No. 10, 2006

[11] FATTINGER, C.; GRISCHKOWSKY, D.: Terahertz beams. In: *Applied Physics Letters* 54 (1989), No. 6, 490-492

[12] GATESMAN, A.; WALDMAN, J.; JI, M.; MUSANTE, C.; YAGVESSON, S.: An anti-reflection coating for silicon optics at terahertzfrequencies. In: *Microwave and Guided Wave Letters, IEEE [see also IEEE Microwave and Wireless Components Letters]* 10 (2000), No. 7, p. 264–266

[13] KAWASE, K.; HIROMOTO, N.: Terahertz-Wave Antireflection Coating on Ge and GaAs with Fused Quartz. In: *Appl. Opt.* 37 (1998), No. 10, 1862–1866

[14] HUNSCHE, S.; FENG, S.; WINFUL, H.; LEITENSTORFER, A.; NUSS, M.; IPPEN, E.: Spatiotemporal focusing of single-cycle light pulses. In: *Journal of the Optical Society of America A* 16 (1999), No. 8, p. 2025–2028

[15] WEISS, C.: *Untersuchung und Anwendung neuartiger Methoden zur Erzeugung von Terahertz-Strahlung*, University of Kaiserslautern, Diss., 2001

[16] MITROFANOV, O.; LEE, M.; HSU, J. W. P.; PFEIFFER, L. N.; WEST, K. W.; WYNN, J. D.; FEDERICI, J. F.: Terahertz pulse propagation through small apertures. In: *Applied Physics Letters* 79 (2001), No. 7, 907-909

[17] GALLOT, G.; JAMISON, S. P.; MCGOWAN, R. W.; GRISCHKOWSKY, D.: Terahertz waveguides. In: *J. Opt. Soc. Am. B* 17 (2000), No. 5, 851–863

[18] MENDIS, R.; GRISCHKOWSKY, D.: Plastic ribbon THz waveguides. In: *Journal of Applied Physics* 88 (2000), No. 7, 4449-4451

[19] HAN, H.; PARK, H.; CHO, M.; KIM, J.: Terahertz pulse propagation in a plastic photonic crystal fiber. In: *Applied Physics Letters* 80 (2002), No. 15, 2634-2636

[20] WANG, K.; MITTLEMAN, D. M.: Guided propagation of terahertz pulses on metal wires. In: *J. Opt. Soc. Am. B* 22 (2005), No. 9, 2001–2008

[21] CARLITO S. PONSECA, J.; POBRE, R.; ESTACIO, E.; SARUKURA, N.; ARGYROS, A.; LARGE, M. C.; EIJKELENBORG, M. A.: Transmission of terahertz radiation using a microstructured polymer optical fiber. In: *Opt. Lett.* 33 (2008), No. 9, 902–904

[22] MÖLLER, L.; FEDERICI, J.; SINYUKOV, A.; XIE, C.; LIM, H. C.; GILES, R. C.: Data encoding on terahertz signals for communication and sensing. In: *Opt. Lett.* 33 (2008), No. 4, 393–395

[23] BARTELS, A.; DEKORSY, T.: Terahertz-Spektroskopie mit High-Speed ASOPS (THz Spectroscopy Based on High-Speed ASOPS). In: *tm-Technisches Messen* 75 (2008), No. 1, p. 23–30

[24] KINGSTON, R.: Parametric amplification and oscillation at optical frequencies. In: *Proc. IRE* 50 (1962), p. 472

[25] GIORDMAINE, J. A.; MILLER, R. C.: Tunable Coherent Parametric Oscillation in LiNbO$_3$ at Optical Frequencies. In: *Phys. Rev. Lett.* 14 (1965), Jun, No. 24, p. 973–976

[26] FALLNICH, C.; RUFFING, B.; HERRMANN, T.; NEBEL, A.; BEIGANG, R.; WALLENSTEIN, R.: Experimental investigation and numerical simulation of the influence of resonator-length detuning on the output power, pulse duration and spectral width of a cw mode-locked picosecond optical parametric oscillator. In: *Applied Physics B: Lasers and Optics* 60 (1995), No. 5, p. 427–436

[27] DRIEL, H.: Synchronously pumped optical parametric oscillators. In: *Applied Physics B: Lasers and Optics* 60 (1995), No. 5, p. 411–420

[28] KLEIN, M. E.; LEE, D.-H.; MEYN, J.-P.; BOLLER, K.-J.; WALLENSTEIN, R.: Singly resonant continuous-wave optical parametric oscillator pumped by a diode laser. In: *Opt. Lett.* 24 (1999), No. 16, 1142–1144

[29] GALE, G. M.; CAVALLARI, M.; HACHE, F.: Femtosecond visible optical parametric oscillator. In: *J. Opt. Soc. Am. B* 15 (1998), No. 2, 702–714

[30] DEMTRÖDER, W.: *Laser Spectroscopy, Basic Concepts and Instrumentation.* 3. Springer, 2003

[31] MANLEY, J.; ROWE, H.: Some General Properties of Nonlinear Elements-Part I. General Energy Relations. In: *Proceedings of the IRE* 44 (1956), No. 7, p. 904–913

[32] KÖHLER, B.: *Untersuchung der physikalischen Eigenschaften eines modengekoppelten optisch parametrischen Oszillators aus CTA zur Erzeugung von ultrakurzen Lichtimpulsen im Spektralbereich von* 1300 nm *bis* 2200 nm, University of Kaiserslautern, Diplomarbeit, 1995

[33] DÖRRING, J.: *Untersuchung der physikalischen Eigenschaften eines modengekoppelten optisch parametrischen Oszillators aus CTA zur Erzeugung von Femtosekunden-Lichtimpulsen im Spektralbereich von* 1300 nm *bis* 2200 nm, University of Kaiserslautern, Diplomarbeit, 1995

[34] KAWASE, K.; SHIKATA, J.; ITO, H.: Terahertz wave parametric source. In: *Journal of Physics D: Applied Physics* 34 (2001)

[35] VODOPYANOV, K.; LEVI, O.; KUO, P.; PINGUET, T.; HARRIS, J.; FEJER, M.; GERARD, B.; BECOUARN, L.; LALLIER, E.: Optical parametric oscillation in quasi-phase-matched GaAs. In: *Optics Letters* 29 (2004), No. 16, p. 1912–1914

[36] KAWASE, K.; SHIKATA, J.; IMAI, K.; ITO, H.: Transform-limited, narrow-linewidth, terahertz-wave parametric generator. In: *Applied Physics Letters* 78 (2001), No. 19, 2819-2821

[37] Kawase, K.; Minamide, H.; Imai, K.; Shikata, J.; Ito, H.: Injection-seeded terahertz-wave parametric generator with wide tunability. In: *Applied Physics Letters* 80 (2002), No. 2, 195-197

[38] Sato, A.; Kawase, K.; Minamide, H.; Wada, S.; Ito, H.: Tabletop terahertz-wave parametric generator using a compact, diode-pumped Nd:YAG laser. In: *Review of Scientific Instruments* 72 (2001), No. 9, 3501-3504

[39] Hayashi, S.; Minamide, H.; Ikari, T.; Ogawa, Y.; Shikata, J.; Ito, H.; Otani, C.; Kawase, K.: Output power enhancement of a palmtop terahertz-wave parametric generator. In: *Appl. Opt.* 46 (2007), No. 1, 117–123

[40] Dobroiu, A.; Yamashita, M.; Ohshima, Y. N.; Morita, Y.; Otani, C.; Kawase, K.: Terahertz Imaging System Based on a Backward-Wave Oscillator. In: *Appl. Opt.* 43 (2004), No. 30, 5637–5646

[41] Köhler, R.; Tredicucci, A.; Beltram, F.; Beere, H.; Linfield, E.; Davies, A.; Ritchie, D.; Iotti, R.; Rossi, F.: Terahertz semiconductor-heterostructure laser. In: *Nature* 417 (2002), No. 6885, p. 156–159

[42] Bründermann, E.; Havenith, M.; Scalari, G.; Giovannini, M.; Faist, J.; Kunsch, J.; Mechold, L.; Abraham, M.: Turn-key compact high temperature terahertz quantum cascade lasers: imaging and room temperature detection. In: *Opt. Express* 14 (2006), No. 5, 1829–1841

[43] Belkin, M. A.; Capasso, F.; Xie, F.; Belyanin, A.; Fischer, M.; Wittmann, A.; Faist, J.: Room temperature terahertz quantum cascade laser source based on intracavity difference-frequency generation. In: *Applied Physics Letters* 92 (2008), No. 20, 201101

[44] Kleinman, D.; Auston, D.: Theory of electrooptic shock radiation in nonlinear optical media. In: *Quantum Electronics, IEEE Journal of* 20 (1984), No. 8, p. 964–970

[45] CASIX: *Lithium Niobate Crystal Series.* Fuzhou, Fujian 350014, China: CASIX INC., 2008. `http://www.casix.com/product/prod_cry_linbo3.html`

[46] L'huillier, J.; Torosyan, G.; Theuer, M.; Avetisyan, Y.; Beigang, R.: Generation of THz radiation using bulk, periodically and aperiodically poled lithium niobate–Part 1: Theory. In: *Applied Physics B: Lasers and Optics* 86 (2007), No. 2, p. 185–196

[47] L'huillier, J.; Torosyan, G.; Theuer, M.; Rau, C.; Avetisyan, Y.; Beigang, R.: Generation of THz radiation using bulk, periodically and aperiodically poled lithium niobate–Part 2: Experiments. In: *Applied Physics B: Lasers and Optics* 86 (2007), No. 2, p. 197–208

[48] SCHALL, M.; HELM, H.; KEIDING, S.: Far Infrared Properties of Electro-Optic Crystals Measured by THz Time-Domain Spectroscopy. In: *International Journal of Infrared and Millimeter Waves* 20 (1999), No. 4, p. 595–604

[49] GUO, H. C.; LIU, W. M.; TANG, S. H.: Terahertz time-domain studies of far-infrared dielectric response in 5 mol In: *Journal of Applied Physics* 102 (2007), No. 3, 033105

[50] MYERS, L. E.; ECKARDT, R. C.; FEJER, M. M.; BYER, R. L.; BOSENBERG, W. R.: Multigrating quasi-phase-matched optical parametric oscillator in periodically poled LiNbO 3. In: *Opt. Lett.* 21 (1996), No. 8, 591

[51] PALFALVI, L.; HEBLING, J.; KUHL, J.; PETER, A.; POLGAR, K.: Temperature dependence of the absorption and refraction of Mg-doped congruent and stoichiometric LiNbO[sub 3] in the THz range. In: *Journal of Applied Physics* 97 (2005), No. 12, 123505

[52] XUE, D.; BETZLER, K.: Influence of optical-damage-resistant dopants on the nonlinear optical properties of lithium niobate. In: *Applied Physics B: Lasers and Optics* 72 (2001), No. 6, p. 641–645

[53] FURUKAWA, Y.; KITAMURA, K.; ALEXANDROVSKI, A.; ROUTE, R.; FEJER, M.; G.FOULON: Green-induced infrared absorption in MgO doped $LiNbO_3$. In: *Applied Physics Letters* 78 No. 14 (2001)

[54] BEYER, O.; MAXEIN, D.; BUSE, K.; STURMAN, B.; HSIEH, H.; PSALTIS, D.: Femtosecond time-resolved absorption processes in lithium niobate crystals. In: *Optics Letters* 30 (2005), No. 11, p. 1366–1368

[55] RUEBEL, F.; HAAG, P.; L'HUILLIER, J. A.: Synchronously pumped femtosecond optical parametric oscillator with integrated sum frequency generation. In: *Applied Physics Letters* 92 (2008), No. 1, 011122

[56] LEE, Y.-S.; HURLBUT, W. C.; VODOPYANOV, K. L.; FEJER, M. M.; KOZLOV, V. G.: Generation of multicycle terahertz pulses via optical rectification in periodically inverted GaAs structures. In: *Applied Physics Letters* 89 (2006), No. 18, 181104

[57] ZHANG, X.-C.; MA, X. F.; JIN, Y.; LU, T.-M.; BODEN, E. P.; PHELPS, P. D.; STEWART, K. R.; YAKYMYSHYN, C. P.: Terahertz optical rectification from a nonlinear organic crystal. In: *Applied Physics Letters* 61 (1992), No. 26, 3080-3082

[58] KAWASE, K.; HATANAKA, T.; TAKAHASHI, H.; NAKAMURA, K.; TANIUCHI, T.; ITO, H.: Tunable terahertz-wave generation from DAST crystal by dual signal-wave parametric oscillation of periodically poled lithium niobate. In: *Opt. Lett.* 25 (2000), No. 23, 1714–1716

[59] Shibuya, T.; Akiba, T.; Suizu, K.; Uchida, H.; Otani, C.; Kawase, K.: Terahertz-Wave Generation Using a 4-Dimethylamino-N-methyl-4-stilbazolium tosylate Crystal Under Intra-Cavity Conditions. In: *Appl. Phys. Express* 1 (2008), p. 042002

[60] Askaryan, G.: Cerenkov radiation and transition radiation from electromagnetic waves. In: *Soviet Phys JETP* 15 (1962), p. 943–946

[61] Auston, D.; Cheung, K.; Valdmanis, J.; Kleinman, D.: Cherenkov Radiation from Femtosecond Optical Pulses in Electro-Optic Media. In: *Physical Review Letters* 53 (1984), No. 16, p. 1555–1558

[62] Suizu, K.; Shibuya, T.; Akiba, T.; Tutui, T.; Otani, C.; Kawase, K.: Cherenkov phase-matched monochromatic THz wave generation using difference frequency generation with a lithium niobate crystal. In: *Opt. Express* 16 (2008), No. 10, 7493–7498

[63] Stepanov, A. G.; Hebling, J.; Kuhl, J.: Efficient generation of subpicosecond terahertz radiation by phase-matched optical rectification using ultrashort laser pulses with tilted pulse fronts. In: *Applied Physics Letters* 83 (2003), No. 15, 3000-3002

[64] Loewenstein, E. V.; Smith, D. R.; Morgan, R. L.: Optical constants of far infrared materials. 2: Crystalline solids. In: *Appl. Opt.* 12 (1973), No. 2, 398

[65] Randall, C. M.; Rawcliffe, R. D.: Refractive indices of germanium, silicon, and fused quartz in the far infrared. In: *Appl. Opt.* 6 (1967), No. 11, 1889

[66] Theuer, M.; Torosyan, G.; Beigang, R.; Maki, K.; Kawase, K.: Terahertz radiation from a MgO:LiNbO$_3$ crystal using a femtosecond pumped enhancement cavity. In: *Infrared and Millimeter Waves and 13th International Conference on Terahertz Electronics* 2 (2005), p. 636–637

[67] Theuer, M.; Torosyan, G.; Rau, C.; Beigang, R.; Maki, K.; Otani, C.; Kawase, K.: Efficient generation of Cherenkov-type terahertz radiation from a lithium niobate crystal with a silicon prism output coupler. In: *Applied Physics Letters* 88 (2006), No. 7, 071122

[68] Kawase, K.; Sato, M.; Taniuchi, T.; Ito, H.: Coherent tunable THz-wave generation from LiNbO$_3$ with monolithic grating coupler. In: *Applied Physics Letters* 68 (1996), No. 18, 2483-2485

[69] Weiss, C.; Torosyan, G.; Avetisyan, Y.; Beigang, R.: Generation of tunable narrowband surface-emitted THz-radiation in periodically poled Lithium Niobate. In: *Opt. Lett.* 26 (2001), No. 8, p. 563–565

[70] ARMSTRONG, J.; BLOEMBERGEN, N.; DUCUING, J.; PERSHAN, P.: Interactions between Light Waves in a Nonlinear Dielectric. In: *Physical Review* 127 (1962), No. 6, p. 1918–1939

[71] FEJER, M. M.; MAGEL, G. A.; JUNDT, D. H.; BYER, R. L.: Quasi-phase-matched second harmonic generation - Tuning and tolerances. In: *IEEE Journal of Quantum Electronics* 28 (1992), November, p. 2631–2654

[72] LEE, Y.; MEADE, T.; PERLIN, V.; WINFUL, H.; NORRIS, T.; GALVANAUSKAS, A.: Generation of narrow-band terahertz radiation via optical rectification of femtosecond pulses in periodically poled lithium niobate. In: *Applied Physics Letters* 76 (2000), p. 2505

[73] WANG, T. D.; LIN, S. T.; LIN, Y. Y.; CHIANG, A. C.; HUANG, Y. C.: Forward and backward terahertz-wavedifference-frequency generations from periodically poled lithium niobate. In: *Opt. Express* 16 (2008), No. 9, 6471–6478

[74] HEISENBERG, W.: Über quantentheoretische Umdeutung kinematischer und mechanischer Beziehungen. In: *Zeitschrift für Physik A Hadrons and Nuclei* 33 (1925), No. 1, p. 879–893

[75] WEISS, C.; TOROSYAN, G.; MEYN, J.; WALLENSTEIN, R.; BEIGANG, R.; AVETISYAN, Y.: Tuning characteristics of narrowband THz radiation generated via optical rectification in periodically poled lithium niobate. In: *Optics Express* 8 (2001), No. 9, p. 497–502

[76] DANIELSON, J. R.; AMER, N.; LEE, Y.-S.: Generation of arbitrary terahertz wave forms in fanned-out periodically poled lithium niobate. In: *Applied Physics Letters* 89 (2006), No. 21, 211118

[77] LEE, Y.-S.; NORRIS, T. B.: Terahertz pulse shaping and optimal waveform generation in poled ferroelectric crystals. In: *J. Opt. Soc. Am. B* 19 (2002), No. 11, 2791–2794

[78] AUSTON, D. H.; CHEUNG, K. P.; SMITH, P. R.: Picosecond photoconducting Hertzian dipoles. In: *Applied Physics Letters* 45 (1984), No. 3, 284-286

[79] ZHANG, X.-C.; DARROW, J. T.; HU, B. B.; AUSTON, D. H.; SCHMIDT, M. T.; THAM, P.; YANG, E. S.: Optically induced electromagnetic radiation from semiconductor surfaces. In: *Applied Physics Letters* 56 (1990), No. 22, 2228-2230

[80] RUDD, J. V.; JOHNSON, J. L.; MITTLEMAN, D. M.: Cross-polarized angular emission patterns from lens-coupled terahertz antennas. In: *J. Opt. Soc. Am. B* 18 (2001), No. 10, 1524–1533

[81] KATZENELLENBOGEN, N.; GRISCHKOWSKY, D.: Efficient generation of 380 fs pulses of THz radiation by ultrafast laser pulse excitation of a biased metal-semiconductor interface. In: *Applied Physics Letters* 58 (1991), p. 222

[82] DARROW, J. T.; HU, B. B.; ZHANG, X.-C.; AUSTON, D. H.: Subpicosecond electromagnetic pulses from large-aperture photoconducting antennas. In: *Opt. Lett.* 15 (1990), No. 6, 323

[83] ZHAO, G.; SCHOUTEN, R.; VALK, N.; WENCKEBACH, W.; PLANKEN, P.: A terahertz system using semi-large emitters: noise and performance characteristics. In: *Physics in Medicine and Biology* 47 (2002), No. 21, p. 3699–3704

[84] TANI, M.; MATSUURA, S.; SAKAI, K.; NAKASHIMA, S.: Emission characteristics of photoconductive antennas based on low-temperature-grown GaAs and semi-insulating GaAs. In: *Appl. Opt.* 36 (1997), No. 30, 7853–7859

[85] BROWN, E.; SMITH, F.; MCINTOSH, K.: Coherent millimeter-wave generation by heterodyne conversion in low-temperature-grown GaAs photoconductors. In: *Journal of Applied Physics* 73 (1993), p. 1480

[86] DREYHAUPT, A.; PETER, F.; WINNERL, S.; NITSCHE, S.; WAGNER, M.; SCHNEIDER, H.; HELM, M.; KOHLER, K.: Leistungsstarke Emitter und einfach handhabbare Detektoren für die Terahertz-Time-Domain-Spektroskopie (Powerful Emitters and Easy-to-Use Detectors for Terahertz-Time-Domain Spectroscopy). In: *tm-Technisches Messen* 75 (2008), No. 1, p. 3–13

[87] JEPSEN, P.; JACOBSEN, R.; KEIDING, S.: Generation and detection of terahertz pulses from biased semiconductor antennas. In: *J. Opt. Soc. Am. B* 13 (1996), No. 11, p. 2424

[88] PEDERSEN, J. E.; LYSSENKO, V. G.; HVAM, J. M.; JEPSEN, P. U.; KEIDING, S. R.; RENSEN, C. B. S.; LINDELOF, P. E.: Ultrafast local field dynamics in photoconductive THz antennas. In: *Applied Physics Letters* 62 (1993), No. 11, 1265-1267

[89] CHIMOT, N.; MANGENEY, J.; JOULAUD, L.; CROZAT, P.; BERNAS, H.; BLARY, K.; LAMPIN, J. F.: Terahertz radiation from heavy-ion-irradiated $In_{0.53}Ga_{0.47}As$ photoconductive antenna excited at 1.55 μm. In: *Applied Physics Letters* 87 (2005), No. 19, 193510

[90] SUZUKI, M.; TONOUCHI, M.: Fe-implanted InGaAs terahertz emitters for 1.56 mu m wavelength excitation. In: *Applied Physics Letters* 86 (2005), No. 5, 051104

[91] TAKAZATO, A.; KAMAKURA, M.; MATSUI, T.; KITAGAWA, J.; KADOYA, Y.: Detection of terahertz waves using low-temperature-grown InGaAs with 1.56 mu m pulse excitation. In: *Applied Physics Letters* 90 (2007), No. 10, 101119

[92] DRISCOLL, D. C.; HANSON, M. P.; GOSSARD, A. C.; BROWN, E. R.: Ultrafast photoresponse at 1.55 mu m in InGaAs with embedded semimetallic ErAs nanoparticles. In: *Applied Physics Letters* 86 (2005), No. 5, 051908

[93] OSPALD, F.; MARYENKO, D.; KLITZING, K.; DRISCOLL, D. C.; HANSON, M. P.; LU, H.; GOSSARD, A. C.; SMET, J. H.: 1.55 μm ultrafast photoconductive switches based on ErAs:InGaAs. In: *Applied Physics Letters* 92 (2008), No. 13, 131117

[94] DEMBER, H.: Über eine photomotorische Kraft in Kuperoxydul-Kristallen. In: *Phys. Z.* 32 (1931), p. 554–556

[95] JOHNSTON, M. B.; WHITTAKER, D. M.; CORCHIA, A.; DAVIES, A. G.; LINFIELD, E. H.: Simulation of terahertz generation at semiconductor surfaces. In: *Phys. Rev. B* 65 (2002), Mar, No. 16, p. 165301

[96] ZHANG, X.; AUSTON, D.: Optoelectronic measurement of semiconductor surfaces and interfaces with femtosecond optics. In: *Journal of Applied Physics* 71 (1992), p. 326

[97] MATTHÄUS, G.; SCHREIBER, T.; LIMPERT, J.; NOLTE, S.; TOROSYAN, G.; BEIGANG, R.; RIEHEMANN, S.; NOTNI, G.; TÜNNERMANN, A.: Surface-emitted THz generation using a compact ultrashort pulse fiber amplifier at 1060 nm. In: *Opt. Commun.* 261 (2006), No. 1, p. 114–117

[98] KITTEL, C.: *Einführung in die Festkörperphysik*. 14. Oldenbourg Wissenschaftsverlag, 2004

[99] PRADARUTTI, B.; MATTHÄUS, G.; BRÜCKNER, C.; RIEHEMANN, S.; NOTNI, G.; NOLTE, S.; CIMALLA, V.; LEBEDEV, V.; AMBACHER, O.; TÜNNERMANN, A.: InN as THz emitter excited at 1060 nm and 800 nm. In: *Millimeter-Wave and Terahertz Photonics* 6194 (2006), No. 1, 61940I

[100] MALEVICH, V.; ADOMAVIČIUS, R.; KROTKUS, A.: THz emission from semiconductor surfaces. In: *Comptes rendus-Physique* (2008)

[101] ONO, S.; TSUKAMOTO, T.; KAWAHATA, E.; YANO, T.; OHTAKE, H.; SARUKURA, N.: Terahertz Radiation from a Shallow Incidence-Angle InAs Emitter in a Magnetic Field Irradiated with Femtosecond Laser Pulses. In: *Appl. Opt.* 40 (2001), No. 9, p. 1369–1371

[102] WEISS, C.; WALLENSTEIN, R.; BEIGANG, R.: Magnetic field enhanced generation of THz radiation in semiconductor surfaces. In: *Appl. Phys. Lett.* 77 (2000), p. 4160

[103] LI, M.; SUN, F. G.; WAGONER, G. A.; ALEXANDER, M.; ZHANG, X.-C.: Measurement and analysis of terahertz radiation from bulk semiconductors. In: *Applied Physics Letters* 67 (1995), No. 1, 25-27

[104] THEUER, M.; IMHOF, C.; TOROSYAN, G.; ELLRICH, F.; ZENGERLE, R.; BEIGANG, R.: Experimental Investigation and Simulation of THz Surface Emission Characteristics. In: *EOS Annual Meeting 2008, Paris, France, 29th September 2008 - 2nd October 2008* (2008)

[105] THEUER, M.; IMHOF, C.; TOROSYAN, G.; ELLRICH, F.; ZENGERLE, R.; BEIGANG, R.: Pump Beam Diameter Dependent Terahertz Generation from Surface Emitters - Experiment and Simulation. In: *The Joint 33th International Conference on Infrared and Millimeter Waves (IRMMW-THz2008), Pasadena, California, USA, 15-19. Sept. 2008* (2008)

[106] HILBK-KORTENBRUCK, F.; BOLIVAR, P. H.; MARTINI, R.; PELLEMANS, H. P. M.; KURZ, H.: Time-resolved detection of far-field THz-radiation patterns: spatially restricted coherence of surface field THz emitters. In: *Terahertz Spectroscopy and Applications II* 3828 (1999), No. 1, 315-318

[107] SUZUKI, M.; TONOUCHI, M.; FUJII, K.; OHTAKE, H.; HIROSUMI, T.: Excitation wavelength dependence of terahertz emission from semiconductor surface. In: *Applied Physics Letters* 89 (2006), No. 9, 091111

[108] DAI, J.; ZHANG, J.; ZHANG, W.; GRISCHKOWSKY, D.: Terahertz time-domain spectroscopy characterization of the far-infrared absorption and index of refraction of high-resistivity, float-zone silicon. In: *J. Opt. Soc. Am. B* 21 (2004), No. 7, 1379–1386

[109] HOYER, P.; THEUER, M.; BEIGANG, R.; KLEY, E.-B.: Terahertz emission from black silicon. In: *Applied Physics Letters* 93 (2008), No. 9, 091106

[110] STUBENRAUCH, M.; FISCHER, M.; KREMIN, C.; STOEBENAU, S.; ALBRECHT, A.; NAGEL, O.: Black silicon − new functionalities in microsystems. In: *J. Micromech. Microeng.* 16 (2006), No. 6, p. S82–S87

[111] HOYER, P.; BABA, N.; MASUDA, H.: Small quantum-sized CdS particles assembled to form a regularly nanostructured porous film. In: *Appl. Phys. Lett.* 66 (1995), p. 2700

[112] KÖNENKAMP, R.; HOYER, P.; WAHI, A.: Heterojunctions and devices of colloidal semiconductor films and quantum dots. In: *J. Appl. Phys.* 79 (1996), p. 7029

[113] THEUER, M.; MOLTER, D.; MAKI, K.; OTANI, C.; L'HUILLIER, J. A.; BEIGANG, R.: Terahertz generation in an actively controlled femtosecond enhancement cavity. In: *Applied Physics Letters* 93 (2008), No. 4, 041119

[114] WINSTON, R.: Light Collection within the Framework of Geometrical Optics. In: *J. Opt. Soc. Am.* 60 (1970), No. 2, 245

[115] CAI, Y.; BRENER, I.; LOPATA, J.; WYNN, J.; PFEIFFER, L.; STARK, J. B.; WU, Q.; ZHANG, X. C.; FEDERICI, J. F.: Coherent terahertz radiation detection: Direct comparison between free-space electro-optic sampling and antenna detection. In: *Applied Physics Letters* 73 (1998), No. 4, 444-446

[116] PARK, S.-G.; MELLOCH, M. R.; WEINER, A. M.: Comparison of terahertz waveforms measured by electro-optic and photoconductive sampling. In: *Applied Physics Letters* 73 (1998), No. 22, 3184-3186

[117] SUZUKI, M.; TONOUCHI, M.: Fe-implanted InGaAs photoconductive terahertz detectors triggered by 1.56 mu m femtosecond optical pulses. In: *Appl. Phys. Lett.* 86 (2005), No. 16, 163504

[118] OSPALD, F.; MAYENKO, D.; DRISCOLL, D. C.; HANSON, M. P.; LU, H.; GOSSARD, A. C.; MANGENEY, J.; THEUER, M.; JONUSCHEIT, J.; SMET, J. H.: Characterization of ultrafast $In_{0.53}Ga_{0.47}As$ optoelectronic materials by pulsed excitation of photoconductive switches. In: *EOS Annual Meeting 2008, Paris, France, 29th September 2008 - 2nd October 2008* (2008)

[119] PRADARUTTI, B.; MÜLLER, R.; MATTHÄUS, G.; FREESE, W.; RIEHEMANN, S.; NOTNI, G.; NOLTE, S.; TÜNNERMANN, A.: Multichannel THz line detection by a microlens array excited photoconductive antenna array. In: *The Joint 33th International Conference on Infrared and Millimeter Waves (IRMMW-THz2008), Pasadena, California, USA, 15-19. Sept. 2008* (2008), p. 1–2

[120] VALDMANIS, J.; MOUROU, G.: Subpicosecond electrooptic sampling: Principles and applications. In: *Quantum Electronics, IEEE Journal of* 22 (1986), No. 1, p. 69–78

[121] VALK, N. C. J.; WENCKEBACH, T.; PLANKEN, P. C. M.: Full mathematical description of electro-optic detection in optically isotropic crystals. In: *J. Opt. Soc. Am. B* 21 No. 3 (2004)

[122] WU, Q.; ZHANG, X.-C.: Free-space electro-optic sampling of terahertz beams. In: *Applied Physics Letters* 67 (1995), No. 24, 3523-3525

[123] KÜBLER, C.; HUBER, R.; TÜBEL, S.; LEITENSTORFER, A.: Ultrabroadband detection of multi-terahertz field transients with GaSe electro-optic sensors: Approaching the near infrared. In: *Applied Physics Letters* 85 (2004), No. 16, 3360-3362

[124] LEITENSTORFER, A.; HUNSCHE, S.; SHAH, J.; NUSS, M.; KNOX, W.: Detectors and sources for ultrabroadband electro-optic sampling: Experiment and theory. In: *Applied Physics Letters* 74 (1999), p. 1516

[125] JIANG, Z.; ZHANG, X.: Terahertz imaging via electrooptic effect. In: *Microwave Theory and Techniques, IEEE Transactions on* 47 (1999), No. 12, p. 2644–2650

[126] HERRMANN, M.; BEIGANG, R.: Real-Time THz Imaging of Large Objects based on the Triangulation Method. In: *Infrared Millimeter Waves and 14th International Conference on Teraherz Electronics, 2006. IRMMW-THz 2006. Joint 31st International Conference on* (2006), p. 191–191

[127] PLANKEN, P.; NIENHUYS, H.; BAKKER, H.; WENCKEBACH, T.: Measurement and calculation of the orientation dependence of terahertz pulse detection in ZnTe. In: *Journal of the Optical Society of America B* 18 (2001), No. 3, p. 313–317

[128] TURCHINOVICH, D.; DIJKHUIS, J.: Performance of combined 100–110 ZnTe crystals in an amplified THz time-domain spectrometer. In: *Optics Communications* 270 (2007), p. 96–99

[129] HAN, P. Y.; ZHANG, X.-C.: Coherent, broadband midinfrared terahertz beam sensors. In: *Applied Physics Letters* 73 (1998), No. 21, 3049-3051

[130] ASHKIN, A.; BOYD, G.; DZIEDZIC, J.: Resonant optical second harmonic generation and mixing. In: *Quantum Electronics, IEEE Journal of* 2 (1966), No. 6, p. 109–124

[131] JIANG, J.; HASAMA, T.: Synchronously pumped femtosecond optical parametric oscillator based on an improved pumping concept. In: *Optics Communications* 220 (2003), No. 1-3, p. 193–202

[132] DREVER, R.; HALL, J.; KOWALSKI, F.; HOUGH, J.; FORD, G.; MUNLEY, A.; WARD, H.: Laser phase and frequency stabilization using an optical resonator. In: *Applied Physics B: Lasers and Optics* 31 (1983), No. 2, p. 97–105

[133] HÄNSCH, T.; COULLIAUD, B.: Laser frequency stabilization by polarization spectroscopy of a reflecting reference cavity. In: *Optics Communications* 35 (1980), No. 3, p. 441–444

[134] MOLTER, D.; THEUER, M.; TOROSYAN, G.; BEIGANG, R.; MAKI, K.; KAWASE, K.: Actively stabilized synchronously pumped Enhancement Cavity for THz Generation. In: *Infrared and Millimeter Waves and 15th International Conference on Terahertz Electronics, 2007. IRMMW-THz 2007. Joint 32st International Conference on* (2007), p. 462–463

[135] MOLL, K.; JONES, R.; YE, J.: Nonlinear dynamics inside femtosecond enhancement cavities. In: *Optics Express* 13 (2005), No. 5, p. 1672–1678

[136] YU, N. E.; KANG, C.; YOO, H. K.; JUNG, C.; LEE, Y. L.; KEE, C.-S.; KO, D.-K.; LEE, J.; KITAMURA, K.; TAKEKAWA, S.: Simultaneous forward and backward terahertz generations in periodically poled stoichiometric LiTaO[sub 3] crystal using femtosecond pulses. In: *Applied Physics Letters* 93 (2008), No. 4, 041104

[137] LINZ, N.: *Kerr-Linsen modengekoppelter sub* 10 fs *Titan-Saphir Laser*, University of Kaiserslautern, Diplomarbeit, 2004

[138] FOHR, F.: *Neue Methoden zur Erzeugung Breitbandiger THz-Strahlung mit Ultrakurzen Laserpulsen*, University of Kaiserslautern, Diplomarbeit, 2007

[139] MOLTER, D.; THEUER, M.; BEIGANG, R.: A pump enhanced ns-OPO for THz generation. In: *The Joint 33th International Conference on Infrared and Millimeter Waves (IRMMW-THz2008), Pasadena, California, USA, 15-19. Sept. 2008* (2008)

[140] MOLTER, D.; THEUER, M.; BEIGANG, R.: A pump enhanced ns-OPO for THz generation. In: *EOS Annual Meeting 2008, Paris, France, 29th September 2008 - 2nd October 2008* (2008)

[141] ELLRICH, F.; WEINLAND, T.; THEUER, M.; JONUSCHEIT, J.; ; BEIGANG, R.: Fiber-Coupled THz TDS System. In: *International Forum on Terahertz Spectroscopy and Imaging, Kaiserslautern, Germany, 4.-5. March 2008* (2008)

[142] ELLRICH, F.; WEINLAND, T.; THEUER, M.; JONUSCHEIT, J.; BEIGANG, R.: Fasergekoppeltes Terahertz-Spektroskopiesystem (Fiber-coupled Terahertz Spectroscopy System). In: *tm - Technisches Messen* 75 (2008), No. 1, 14-22

[143] INOUE, R.; OHNO, Y.; TONOUCHI, M.: Development of Fiber-Coupled Compact Terahertz Time-Domain Spectroscopy Imaging Head. In: *Japanese Journal of Applied Physics* 45 (2006), No. 10A, p. 7928–7932

[144] ELLRICH, F.; MOLTER, D.; WEINLAND, T.; THEUER, M.; JONUSCHEIT, J.; BEIGANG, R.: 200 Hz Rapid Scan Fiber-coupled Terahertz Time Domain Spectroscopy System. In: *The Joint 33th International Conference on Infrared and Millimeter Waves (IRMMW-THz2008), Pasadena, California, USA, 15-19. Sept. 2008* (2008)

[145] ELLRICH, F.; MOLTER, D.; WEINLAND, T.; THEUER, M.; JONUSCHEIT, J.; BEIGANG, R.: Fast Scanning 200 Hz Fiber-coupled Terahertz Time Domain Spectroscopy System. In: *EOS Annual Meeting 2008, Paris, France, 29th September 2008 - 2nd October 2008* (2008)

[146] HERRMANN, M.; TANI, M.; SAKAI, K.: Display modes in time-resolved terahertz imaging. In: *Jpn. J. Appl. Phys* 39 (2000), No. 6254, p. 336

[147] NASHIMA, S.; MORIKAWA, O.; TAKATA, K.; HANGYO, M.: Measurement of optical properties of highly doped silicon by terahertz time domain reflection spectroscopy. In: *Applied Physics Letters* 79 (2001), No. 24, 3923-3925

[148] KAWASE, K.; OGAWA, Y.; WATANABE, Y.; INOUE, H.: Non-destructive terahertz imaging of illicit drugs using spectral fingerprints. In: *Opt. Express* 11 (2003), No. 20, 2549–2554

[149] EXTER, M. P.; FATTINGER, C.; GRISCHKOWSKY, D.: Terahertz time-domain spectroscopy of water vapor. In: *Opt. Lett.* 14 (1989), No. 20, 1128

[150] THEUER, M.; WOHNSIEDLER, S.; HERRMANN, M.; TOROSYAN, G.; JONUSCHEIT, J.; BEIGANG, R.: Terahertz Sensor for Stand-off Identification of Chemical, Biological

and Explosive Hazardous Substances. In: *Safety & Security Systems in Europe, Potsdam, Germany, 19th June 2008 - 20th June 2008* (2008)

[151] WOHNSIEDLER, S.; THEUER, M.; HERRMANN, M.; ISLAM, S.; JONUSCHEIT, J.; BEIGANG, R.; HASE, F.: Influences of Real-World Conditions on Terahertz Stand-Off Detection: Simulation and Experiment. In: *The Joint 33th International Conference on Infrared and Millimeter Waves (IRMMW-THz2008), Pasadena, California, USA, 15-19. Sept. 2008* (2008)

[152] WOHNSIEDLER, S.; THEUER, M.; HERRMANN, M.; ISLAM, S.; JONUSCHEIT, J.; BEIGANG, R.; HASE, F.: Terahertz Stand-Off Detection: Simulation and Experiment. In: *EOS Annual Meeting 2008, Paris, France, 29th September 2008 - 2nd October 2008* (2008)

[153] HASE, F.; BLUMENSTOCK, T.; PATON-WALSH, C.: Analysis of the Instrumental Line Shape of High-Resolution Fourier Transform IR Spectrometers with Gas Cell Measurements and New Retrieval Software. In: *Appl. Opt.* 38 (1999), No. 15, 3417–3422

[154] JACOBSEN, R. H.; MITTLEMAN, D. M.; NUSS, M. C.: Chemical recognition of gases and gas mixtures with terahertz waves. In: *Opt. Lett.* 21 (1996), No. 24, 2011

[155] MITTLEMAN, D.; JACOBSEN, R.; NEELAMANI, R.; BARANIUK, R.; NUSS, M.: Gas sensing using terahertz time-domain spectroscopy. In: *Applied Physics B: Lasers and Optics* 67 (1998), No. 3, p. 379–390

[156] CHEVILLE, R. A.; GRISCHKOWSKY, D.: Far-infrared foreign and self-broadened rotational linewidths of high-temperature water vapor. In: *J. Opt. Soc. Am. B* 16 (1999), No. 2, 317–322

[157] WEISS, C.; VIEHL, E.; THEISS, C.; TOROSYAN, G.; WEINACHT, M.; BEIGANG, R.; WALLENSTEIN, R.: Einsatz breitbandiger THz-Strahlung in der Gasanalyse (Broadband THz-Radiation for Gas Analysis). In: *tm - Technisches Messen* 68 (2001), No. 9, 388–399

[158] SIEGEL, P.: Terahertz technology in biology and medicine. In: *Microwave Theory and Techniques, IEEE Transactions on* 52 (2004), Oct., No. 10, p. 2438–2447. – ISSN 0018–9480

[159] MARKELZ, A.; ROITBERG, A.; HEILWEIL, E.: Pulsed terahertz spectroscopy of DNA, bovine serum albumin and collagen between 0.1 and 2.0 THz. In: *Chemical Physics Letters* 320 (2000), No. 1-2, p. 42–48

[160] YAMASHITA, M.; OTANI, C.; KAWASE, K.; NIKAWA, K.; TONOUCHI, M.: Non-contact inspection technique for electrical failures in semiconductor devices using a laser terahertz emission microscope. In: *Applied Physics Letters* 93 (2008), No. 4, 041117

[161] APPLEBY, R.; ANDERTON, R.: Millimeter-Wave and Submillimeter-Wave Imaging for Security and Surveillance. In: *Proceedings of the IEEE* 95 (2007), No. 8, p. 1683–1690

[162] MITTLEMAN, D.; HUNSCHE, S.; BOIVIN, L.; NUSS, M.: T-ray tomography. In: *Optics Letters* 22 (1997), No. 12, p. 904–906

[163] KARPOWICZ, N.; ZHONG, H.; ZHANG, C.; LIN, K.-I.; HWANG, J.-S.; XU, J.; ZHANG, X.-C.: Compact continuous-wave subterahertz system for inspection applications. In: *Applied Physics Letters* 86 (2005), No. 5, 054105

[164] THEUER, M.; TOROSYAN, G.; ELLRICH, F.; JONUSCHEIT, J.; BEIGANG, R.: Terahertz-Bildgebung in industriellen Anwendungen (Terahertz Imaging in Industrial Applications). In: *tm - Technisches Messen* 75 (2008), No. 1, 64-70

[165] MORITA, Y.; DOBROIU, A.; KAWASE, K.; OTANI, C.: Terahertz technique for detection of microleaks in the seal of flexible plastic packages. In: *Optical Engineering* 44 (2004), p. 019001

[166] HILS, B.; THOMSON, M. D.; LÖFFLER, T.; SPIEGEL, W.; WEG, C.; ROSKOS, H. G.; MAAGT, P.; DOYLE, D.; GECKELER, R. D.: Terahertz profilometry at 600 GHz with 0.5 μm depth resolution. In: *Opt. Express* 16 (2008), No. 15, 11289–11293

[167] GELTNER, I.; HASHIMSHONY, D.; ZIGLER, A.: Detection and electrical characterization of hidden layers using time-domain analysis of terahertz reflections. In: *Journal of Applied Physics* 92 (2002), p. 203

[168] YASUI, T.; YASUDA, T.; SAWANAKA, K.; ARAKI, T.: Terahertz paintmeter for noncontact monitoring of thickness and drying progress in paint film. In: *Applied Optics* 44 (2005), No. 32, p. 6849–6856

[169] ELLRICH, F.; THEUER, M.; TOROSYAN, G.; JONUSCHEIT, J.; BEIGANG, R.: Thin-Film Measurements with THz-Radiation. In: *The Joint 33th International Conference on Infrared and Millimeter Waves (IRMMW-THz2008), Pasadena, California, USA, 15-19. Sept. 2008* (2008)

[170] FITZGERALD, A.; COLE, B.; TADAY, P.: Nondestructive analysis of tablet coating thicknesses using terahertz pulsed imaging. In: *Journal of Pharmaceutical Sciences* 94 (2005), No. 1, p. 177–183

[171] SHEN, Y.; TADAY, P.: Application of Terahertz pulsed imaging for three-dimensional non-destructive inspection of pharmaceutical tablet uniformity. In: *Infrared and Millimeter Waves, 2007 and the 2007 15th International Conference on Terahertz Electronics. IRMMW-THz. Joint 32nd International Conference on* (2007), p. 404–405

[172] WITHAYACHUMNANKUL, W.; FISCHER, B. M.; ABBOTT, D.: Material thickness optimization fortransmission-modeterahertz time-domain spectroscopy. In: *Opt. Express* 16 (2008), No. 10, 7382–7396

[173] BEIGANG, R.; THEUER, M.; JONUSCHEIT, J.: Terahertz Sensor for stand-off detection of explosives. In: *Future Security, Karlsruhe, Germany, 12.-13. Sept. 2007* (2007)

[174] BEIGANG, R.; THEUER, M.; TOROSYAN, G.; JONUSCHEIT, J.: Terahertz Reflection Spectroscopy for Stand-Off Detection of Explosives. In: *XXIX URSI General Assembly, Chicago, Illinois, USA, 7 to 16 August 2008* (2008)

[175] OTANI, C.; SASAKI, Y.; HOSHINA, H.; YAMASHITA, M.; OKAZAKI, G.; KAWASE, K.: Development of a prototype apparatus for inspecting illicit drugs inside envelopes. In: *Infrared Millimeter Waves and 14th International Conference on Teraherz Electronics, 2006. IRMMW-THz 2006. Joint 31st International Conference on* (2006), p. 173–173

[176] LIU, H.-B.; CHEN, Y.; BASTIAANS, G. J.; ZHANG, X.-C.: Detection and identification of explosive RDX by THz diffuse reflection spectroscopy. In: *Opt. Express* 14 (2006), No. 1, 415–423

[177] BURNETT, A.; FAN, W.; UPADHYA, P.; CUNNINGHAM, J.; EDWARDS, H.; KENDRICK, J.; MUNSHI, T.; HARGREAVES, M.; LINFIELD, E.; DAVIES, A.: Broadband terahertz time-domain and Raman spectroscopy of explosives. In: *Proceedings of SPIE* 6549 (2007), p. 654905

[178] THEUER, M.; JONUSCHEIT, J.; BEIGANG, R.: Terahertz-Spektroskopie zur Detektion von Explosivstoffen. In: *Workshop zur Detektion von Explosivstoffen, Karlsruhe, Germany, 13.-14. Feb. 2007* (2007)

[179] JEPSEN, P.; FISCHER, B.: Dynamic range in terahertz time-domain transmission and reflection spectroscopy. In: *Optics Letters* 30 (2005), No. 1, p. 29–31

[180] DIKMELIK, Y.; FITCH, M.; LEAHY-HOPPA, M.; OSIANDER, R.: Examining explosive residues on surfaces with terahertz technology. In: *Proceedings of SPIE* 6549 (2007), p. 65490I

[181] BJARNASON, J. E.; CHAN, T. L. J.; LEE, A. W. M.; CELIS, M. A.; BROWN, E. R.: Millimeter-wave, terahertz, and mid-infrared transmission through common clothing. In: *Applied Physics Letters* 85 (2004), No. 4, 519-521

[182] JACOBS, E.; GRIFFIN, S.: Modeling and characterization of cloth at sub-millimeter wavelengths. In: *Proceedings of SPIE* 6549 (2007), p. 654904

[183] ORTOLANI, M.; LEE, J. S.; SCHADE, U.; HÜBERS, H.-W.: Surface roughness effects on the terahertz reflectance of pure explosive materials. In: *Applied Physics Letters* 93 (2008), No. 8, 081906

[184] Fukunaga, K.; Ogawa, Y.; Hayashi, S.; Hosako, I.: Terahertz spectroscopy for art conservation. In: *IEICE Electronics Express* 4 (2007), No. 8, p. 258–263

[185] Jackson, J.; Mourou, M.; Whitaker, J.; Duling, I.; Williamson, S.; Menu, M.; Mourou, G.: Terahertz imaging for non-destructive evaluation of mural paintings. In: *Optics Communications* 281 (2008), No. 4, p. 527–532

[186] Panzner, M.; Grosse, T.; Liese, S.; Klotzbach, U.; Beyer, E.; Theuer, M.; Koehler, W.; Leitner, H.: Potential of THz-Time Domain Spectroscopy in Object Inspection for Restoration. In: *LACONA VII Madrid, 17-21 September 2007* (2007)

[187] Panzner, M.; Theuer, M.; Beigang, R.; Schmidt, A.; Leitner, H.; Köhler, W.; Klotzbach, U.; Beyer, E.: Application of THz Technology for the Investigation of Art Objects. In: *International Forum on Terahertz Spectroscopy and Imaging, Kaiserslautern, Germany, 4.-5. March 2008* (2008)

[188] Beigang, R.; Torosyan, G.; Rau, C.; Pradarutti, B.; Theuer, M.: Photonic THz radiation for applications in fundamental and applied research. In: *Applied Electromagnetics and Communications, 2005. ICECom 2005. 18th International Conference on* (2005), 1–4

[189] Maki, K.; Theuer, M.; Kawase, K.; Otani, C.: Enhancement of terahertz wave generation via optical rectification by using an external cavity. In: *Autumn Japan Society of Applied Physics, 9a-P6-3, Tokushima univ., Tokushima, Japan, 7-11 Sep. (2005)* (2005), No. 3, p. 958

[190] L'huillier, J.; Torosyan, G.; Theuer, M.; Beigang, R.: Nonlinear generation of terahertz radiation in bulk, periodically and aperiodically poled lithium niobate. In: *ECAPD'8, 8th European Conference on Applications of Polar Dielectrics, Metz (France), 5-8 Sep. 2006* (2006)

[191] Theuer, M.; Molter, D.; Torosyan, G.; Beigang, R.; Maki, K.; Kawase, K.: Actively Controlled Enhancement Cavity For Terahertz Generation. In: *Infrared Millimeter Waves and 14th International Conference on Terahertz Electronics, 2006. IRMMW-THz 2006. Joint 31st International Conference on* (2006), p. 387–387

[192] Maki, K.; Theuer, M.; Kawase, K.; Beigang, R.; Otani, C.: Generation of Terahertz Radiation by using Ultrafast Laser Pumping and an Enhancement Cavity. In: *9th International Symposium on Contemporary Photonics Technology (CPT2006), Tokyo (Jan. 11-13 2006)* (2006)

[193] Theuer, M.; Torosyan, G.; Ellrich, F.; Jonuscheit, J.; Beigang, R.: THz Imaging for Non-Destructive Testing. In: *International Forum on Terahertz Spectroscopy and Imaging, Kaiserslautern, Germany, 4.-5. March 2008* (2008)

[194] BEIGANG, R.; THEUER, M.; ELLRICH, F.; TOROSYAN, G.; JONUSCHEIT, J.: THz Imaging and Spectroscopy for Nondestructive Testing. In: *XXIX URSI General Assembly, Chicago, Illinois, USA, 7 to 16 August 2008* (2008)

[195] THEUER, M.; TOROSYAN, G.; MOLTER, D.; RAU, C.; BEIGANG, R.; MAKI, K.; OTANI, C.; KAWASE, K.: Improved Terahertz Conversion Efficiency and Spectral Features of Cherenkov Radiation from a Lithium Niobate Crystal with Attached Silicon Prism Coupler. In: *International Forum on Terahertz Spectroscopy and Imaging, Fraunhofer IPM & VDI, 1-2. March 2006* (2006)

[196] L'HUILLIER, J.; RAU, C.; BEIGANG, R.; TOROSYAN, G.; THEUER, M.: Generation of Terahertz Radiation using Bulk, Periodically and Aperiodically Poled Lithium Niobate. In: *International forum on Terahertz Spectroscopy and Imaging, Fraunhofer IPM & VDI, 1-2. March 2006* (2006)

[197] L'HUILLIER, J.; TOROSYAN, G.; THEUER, M.; BEIGANG, R.: Nonlinear generation of terahertz radiation in bulk, periodically and aperiodically poled lithium niobate. In: *Infrared Millimeter Waves and 14th International Conference on Terahertz Electronics, 2006. IRMMW-THz 2006. Joint 31st International Conference on* (2006), p. 131–131

[198] ELLRICH, F.; THEUER, M.; TOROSYAN, G.; JONUSCHEIT, J.; BEIGANG, R.: Thin-Film Measurements with Ultra Short THz Pulses. In: *EOS Annual Meeting 2008, Paris, France, 29th September 2008 - 2nd October 2008* (2008)

A Publications

Within the scope of research related to the topic of the PhD thesis the following papers were published and conference contributions were given:

Papers

[67] THEUER, M.; TOROSYAN, G.; RAU, C.; BEIGANG, R.; MAKI, K.; OTANI, C.; KAWASE, K.: Efficient generation of Cherenkov-type terahertz radiation from a lithium niobate crystal with a silicon prism output coupler. In: *Applied Physics Letters* 88, No. 7, 071122 (2006)

[46] L'HUILLIER, J.; TOROSYAN, G.; THEUER, M.; AVETISYAN, Y.; BEIGANG, R.: Generation of THz radiation using bulk, periodically and aperiodically poled lithium niobate–Part 1: Theory. In: *Applied Physics B: Lasers and Optics* 86, No. 2, p. 185–196 (2007)

[47] L'HUILLIER, J.; TOROSYAN, G.; THEUER, M.; RAU, C.; AVETISYAN, Y.; BEIGANG, R.: Generation of THz radiation using bulk, periodically and aperiodically poled lithium niobate–Part 2: Experiments. In: *Applied Physics B: Lasers and Optics* 86, No. 2, p. 197–208 (2007)

[164] THEUER, M.; TOROSYAN, G.; ELLRICH, F.; JONUSCHEIT, J.; BEIGANG, R.: Terahertz-Bildgebung in industriellen Anwendungen (Terahertz Imaging in Industrial Applications). In: *tm - Technisches Messen* 75, No. 1, 64-70 (2008)

[113] THEUER, M.; MOLTER, D.; MAKI, K.; OTANI, C.; L'HUILLIER, J. A.; BEIGANG, R.: Terahertz generation in an actively controlled femtosecond enhancement cavity. In: *Applied Physics Letters* 93, No. 4, 041119 (2008)

[142] ELLRICH, F.; WEINLAND, T.; THEUER, M.; JONUSCHEIT, J.; BEIGANG, R.: Fasergekoppeltes Terahertz-Spektroskopiesystem (Fiber-coupled Terahertz Spectroscopy System). In: *tm - Technisches Messen* 75 (2008), No. 1, 14-22

[109] HOYER, P.; THEUER, M.; BEIGANG, R.; KLEY, E.-B.: Terahertz emission from black silicon. In: *Applied Physics Letters* 93, No. 9, 091106 (2008)

Conference Presentations

[188] Beigang, R.; Torosyan, G.; Rau, C.; Pradarutti, B.; Theuer, M.: Photonic THz radiation for applications in fundamental and applied research. In: *Applied Electromagnetics and Communications, 18th International Conference on*, 1–4 (2005)

[66] Theuer, M.; Torosyan, G.; Beigang, R.; Maki, K.; Kawase, K.: Terahertz radiation from a MgO:LiNbO$_3$ crystal using a femtosecond pumped enhancement cavity. In: *Infrared and Millimeter Waves and 13th International Conference on Terahertz Electronics* 2, p. 636–637 (2005)

[189] Maki, K.; Theuer, M.; Kawase, K.; Otani, C.: Enhancement of terahertz wave generation via optical rectification by using an external cavity. In: *Autumn Japan Society of Applied Physics, 9a-P6-3, Tokushima univ., Tokushima, Japan, 7-11 Sep. (2005)*, No. 3, p. 958 (2005)

[190] L'huillier, J.; Torosyan, G.; Theuer, M.; Beigang, R.: Nonlinear generation of terahertz radiation in bulk, periodically and aperiodically poled lithium niobate. In: *ECAPD'8, 8th European Conference on Applications of Polar Dielectrics, Metz (France), 5-8 Sep. 2006* (2006)

[191] Theuer, M.; Molter, D.; Torosyan, G.; Beigang, R.; Maki, K.; Kawase, K.: Actively Controlled Enhancement Cavity For Terahertz Generation. In: *Infrared Millimeter Waves and 14th International Conference on Terahertz Electronics, 2006. IRMMW-THz 2006. Joint 31st International Conference on*, p. 387–387 (2006)

[192] Maki, K.; Theuer, M.; Kawase, K.; Beigang, R.; Otani, C.: Generation of Terahertz Radiation by using Ultrafast Laser Pumping and an Enhancement Cavity. In: *9th International Symposium on Contemporary Photonics Technology (CPT2006), Tokyo (Jan. 11-13 2006)* (2006)

[178] Theuer, M.; Jonuscheit, J.; Beigang, R.: Terahertz-Spektroskopie zur Detektion von Explosivstoffen. In: *Workshop zur Detektion von Explosivstoffen, Karlsruhe, Germany, 13.-14. Feb. 2007* (2007)

[193] Theuer, M.; Torosyan, G.; Ellrich, F.; Jonuscheit, J.; Beigang, R.: THz Imaging for Non-Destructive Testing. In: *International Forum on Terahertz Spectroscopy and Imaging, Kaiserslautern, Germany, 4.-5. March 2008* (2008)

[187] Panzner, M.; Theuer, M.; Beigang, R.; Schmidt, A.; Leitner, H.; Köhler, W.; Klotzbach, U.; Beyer, E.: Application of THz Technology for the Investigation of Art Objects. In: *International Forum on Terahertz Spectroscopy and Imaging, Kaiserslautern, Germany, 4.-5. March 2008* (2008)

[194] BEIGANG, R.; THEUER, M.; ELLRICH, F.; TOROSYAN, G.; JONUSCHEIT, J.: THz Imaging and Spectroscopy for Nondestructive Testing. In: *XXIX URSI General Assembly, Chicago, Illinois, USA, 7 to 16 August 2008* (2008)

[174] BEIGANG, R.; THEUER, M.; TOROSYAN, G.; JONUSCHEIT, J.: Terahertz Reflection Spectroscopy for Stand-Off Detection of Explosives. In: *XXIX URSI General Assembly, Chicago, Illinois, USA, 7 to 16 August 2008* (2008)

[105] THEUER, M.; IMHOF, C.; TOROSYAN, G.; ELLRICH, F.; ZENGERLE, R.; BEIGANG, R.: Pump Beam Diameter Dependent Terahertz Generation from Surface Emitters - Experiment and Simulation. In: *The Joint 33th International Conference on Infrared and Millimeter Waves (IRMMW-THz2008), Pasadena, California, USA, 15-19. Sept. 2008* (2008)

[144] ELLRICH, F.; MOLTER, D.; WEINLAND, T.; THEUER, M.; JONUSCHEIT, J.; BEIGANG, R.: 200 Hz Rapid Scan Fiber-coupled Terahertz Time Domain Spectroscopy System. In: *The Joint 33th International Conference on Infrared and Millimeter Waves (IRMMW-THz2008), Pasadena, California, USA, 15-19. Sept. 2008* (2008)

[140] MOLTER, D.; THEUER, M.; BEIGANG, R.: A pump enhanced ns-OPO for THz generation. In: *EOS Annual Meeting 2008, Paris, France, 29th September 2008 - 2nd October 2008* (2008)

Conference Poster Contributions

[195] THEUER, M.; TOROSYAN, G.; MOLTER, D.; RAU, C.; BEIGANG, R.; MAKI, K.; OTANI, C.; KAWASE, K.: Improved Terahertz Conversion Efficiency and Spectral Features of Cherenkov Radiation from a Lithium Niobate Crystal with Attached Silicon Prism Coupler. In: *International Forum on Terahertz Spectroscopy and Imaging, Fraunhofer IPM & VDI, 1-2. March 2006* (2006)

[196] L'HUILLIER, J.; RAU, C.; BEIGANG, R.; TOROSYAN, G.; THEUER, M.: Generation of Terahertz Radiation using Bulk, Periodically and Aperiodically Poled Lithium Niobate. In: *International forum on Terahertz Spectroscopy and Imaging, Fraunhofer IPM & VDI, 1-2. March 2006* (2006)

[197] L'HUILLIER, J.; TOROSYAN, G.; THEUER, M.; BEIGANG, R.: Nonlinear generation of terahertz radiation in bulk, periodically and aperiodically poled lithium niobate. In: *Infrared Millimeter Waves and 14th International Conference on Terahertz Electronics, 2006. IRMMW-THz 2006. Joint 31st International Conference on*, p. 131–131 (2006)

[173] BEIGANG, R.; THEUER, M.; JONUSCHEIT, J.: Terahertz Sensor for stand-off detection of explosives. In: *Future Security, Karlsruhe, Germany, 12.-13. Sept. 2007* (2007)

[134] MOLTER, D.; THEUER, M.; TOROSYAN, G.; BEIGANG, R.; MAKI, K.; KAWASE, K.: Actively stabilized synchronously pumped Enhancement Cavity for THz Generation. In: *Infrared and Millimeter Waves and 15th International Conference on Terahertz Electronics, 2007. IRMMW-THz 2007. Joint 32st International Conference on*, p. 462–463 (2007)

[186] PANZNER, M.; GROSSE, T.; LIESE, S.; KLOTZBACH, U.; BEYER, E.; THEUER, M.; KOEHLER, W.; LEITNER, H.: Potential of THz-Time Domain Spectroscopy in Object Inspection for Restoration. In: *LACONA VII Madrid, 17-21 September 2007* (2007)

[141] ELLRICH, F.; WEINLAND, T.; THEUER, M.; JONUSCHEIT, J.; ; BEIGANG, R.: Fiber-Coupled THz TDS System. In: *International Forum on Terahertz Spectroscopy and Imaging, Kaiserslautern, Germany, 4.-5. March 2008* (2008)

[150] THEUER, M.; WOHNSIEDLER, S.; HERRMANN, M.; TOROSYAN, G.; JONUSCHEIT, J.; BEIGANG, R.: Terahertz Sensor for Stand-off Identification of Chemical, Biological and Explosive Hazardous Substances. In: *Safety & Security Systems in Europe, Potsdam, Germany, 19th June 2008 - 20th June 2008* (2008)

[139] MOLTER, D.; THEUER, M.; BEIGANG, R.: A pump enhanced ns-OPO for THz generation. In: *The Joint 33th International Conference on Infrared and Millimeter Waves (IRMMW-THz2008), Pasadena, California, USA, 15-19. Sept. 2008* (2008)

[151] WOHNSIEDLER, S.; THEUER, M.; HERRMANN, M.; ISLAM, S.; JONUSCHEIT, J.; BEIGANG, R.; HASE, F.: Influences of Real-World Conditions on Terahertz Stand-Off Detection: Simulation and Experiment. In: *The Joint 33th International Conference on Infrared and Millimeter Waves (IRMMW-THz2008), Pasadena, California, USA, 15-19. Sept. 2008* (2008)

[169] ELLRICH, F.; THEUER, M.; TOROSYAN, G.; JONUSCHEIT, J.; BEIGANG, R.: Thin-Film Measurements with THz-Radiation. In: *The Joint 33th International Conference on Infrared and Millimeter Waves (IRMMW-THz2008), Pasadena, California, USA, 15-19. Sept. 2008* (2008)

[198] ELLRICH, F.; THEUER, M.; TOROSYAN, G.; JONUSCHEIT, J.; BEIGANG, R.: Thin-Film Measurements with Ultra Short THz Pulses. In: *EOS Annual Meeting 2008, Paris, France, 29th September 2008 - 2nd October 2008* (2008)

[145] ELLRICH, F.; MOLTER, D.; WEINLAND, T.; THEUER, M.; JONUSCHEIT, J.; BEIGANG, R.: Fast Scanning 200 Hz Fiber-coupled Terahertz Time Domain Spectroscopy System. In: *EOS Annual Meeting 2008, Paris, France, 29th September 2008 - 2nd October 2008* (2008)

[118] OSPALD, F.; MAYENKO, D.; DRISCOLL, D. C.; HANSON, M. P.; LU, H.; GOSSARD, A. C.; MANGENEY, J.; THEUER, M.; JONUSCHEIT, J.; SMET, J. H.: Characterization of ultrafast $In_{0.53}Ga_{0.47}As$ optoelectronic materials by pulsed excitation of photoconductive switches. In: *EOS Annual Meeting 2008, Paris, France, 29th September 2008 - 2nd October 2008* (2008)

[104] THEUER, M.; IMHOF, C.; TOROSYAN, G.; ELLRICH, F.; ZENGERLE, R.; BEIGANG, R.: Experimental Investigation and Simulation of THz Surface Emission Characteristics. In: *EOS Annual Meeting 2008, Paris, France, 29th September 2008 - 2nd October 2008* (2008)

[152] WOHNSIEDLER, S.; THEUER, M.; HERRMANN, M.; ISLAM, S.; JONUSCHEIT, J.; BEIGANG, R.; HASE, F.: Terahertz Stand-Off Detection: Simulation and Experiment. In: *EOS Annual Meeting 2008, Paris, France, 29th September 2008 - 2nd October 2008* (2008)

B Acknowledgment

During the years of the presented research I was given the possibility to work with many great and complaisant persons. Here I would like to mention at least some of them:

The first I would like to thank Prof. R. Beigang for the interesting topic of this thesis and the possibility to carry out the experiments in his group. Despite his crowded time schedule with his university group and his prospering Fraunhofer Department he always kept an open ear for my individual ideas and questions.

With the support of Prof. K. Kawase I had the chance to research at the RIKEN Institute in Japan on a high international level. During the stay in the team of Dr. C. Otani I learned very much on laser and THz physics. I had fruitful discussions with all group members, so I do not want to underline one particular person. This time will persist in my mind as an important cultural and friendly impression.

In Kaiserslautern I had very nice colleagues. We reached our aims together in teamwork. With some of them I had more points in common.

All I know about THz I was taught by Dr. G. Torosyan. His friendly manner and experimental skills keep the unit together. I really believe he can see THz waves!

My roommate Dr.-Ing. F. Ellrich who had to undergo my bad mood in the morning, became a good friend of mine. The topics while having a cup of coffee were related to physics and the "real life". We will see whether the successor on my seat wants to listen the same music.

Many of the experimental results related to the enhancement cavity were obtained by Dipl.-Phys. D. Molter. His determined interest and comprehension in physics are remarkable. I hope I gave him all the support he needed during his diploma thesis and I am sure he will write an excellent PhD thesis.

A fast research would not be possible without the non-scientific members in our group: The secretary Mrs U. Rein-Rech kept my head free of problems with the beloved administration. The two technicians Mr H.-J. Feurich and Mr J. Heiderich helped me in questions of electronics and mechanics. If a device will take you weeks to repair, the technician can do it to the very next morning.

The best thanks go to my family and friends. Especially to Dipl.-Met. S. Wohnsiedler. She does not only worry about the diet coke I drink, but she is my balance in everyday life. Also my parents never lost hope on their "first-born". They finally accepted the fact that I did not take any reasonable job. Thank you for enduring support!

C Curriculum Vitae

Personal Data

Michael Theuer
Bornheimer Str. 6
76829 Landau (Germany)
E-Mail: michael@theuer.name

born on 26th of November 1978 in Landau/Pfalz

Education

08/1985–07/1989	elementary school in Landau-Dammheim
08/1989–07/1998	secondary school (Max-Slevogt-Gymnasium in Landau)

Studies

10/1998–09/2004	experimental physics at the University of Kaiserslautern
09/2003–09/2004	diploma thesis in the group of Prof. R. Beigang entitled *Online-Characterization of Ultrashort Laser Pulses in Intensity and Phase* degree: diploma in physics
09/2004–10/2008	postgraduate at the University of Kaiserslautern

Professional Experience

10/2004–04/2005	stay abroad in Japan at the RIKEN Institute with Prof. K. Kawase
05/2005–11/2006	Fraunhofer-Institute for Physical Measurement Techniques
12/2006–10/2008	researcher at the University of Kaiserslautern
since 10/2008	postdoc at the University of Kaiserslautern

Landau/Pfalz, 17th of October 2008